ISSN 0915-6348

NATIONAL INSTITUTE FOR FUSION SCIENCE

Proceedings of 9th IAEA Technical Meeting on "Energetic Particles in Magnetic Confinement Systems" 9 to 11 November 2005, Hida Earth Wisdom Center, Takayama, Japan

K. Toi (Ed.)

(Received - Apr. 10, 2006)

NIFS-PROC-63 Apr. 2006

RESEARCH REPORT
NIFS-PROC Series

TOKI, JAPAN

Proceedings of 9th IAEA Technical Meeting on

"Energetic Particles in Magnetic Confinement Systems"

9 to 11 November 2005.

Hida Earth Wisdom Center, Takayama, Japan

edited by K. Toi

Abstract

The 9th IAEA technical meeting on "Energetic particles in Magnetic Confinement Systems" was held from 9 November to 11 November 2005 at Takayama, Japan. This meeting was organized by National Institute for Fusion Science, Toki, Japan. Over 60 participants attended this international meeting. 16 invited talks, 13 oral talks and 24 posters were presented. In this meeting, the present status of experimental and theoretical studies on energetic ions and runaway electrons in various magnetic confinement geometries were discussed toward future burning plasma experiments.

International Advisory Committee

H. Berk (University of Texas, Austin, USA)
D. Borba (EFDA, Culham, UK)
D. Darrow (Princeton Plasma Physics Laboratory, USA)
L.G. Eriksson (CEA, Cadarache, France)
A. Fasoli (CRPP, Lausanne, Switzerland)
W. Heidbrink (University of California, Irvine, USA)
T. Hender (UKAEA, Culham, UK)
Y. Kolesnichenko (Institute for Nuclear Research, Kyiv, Ukraine)
M. Lisak (Chalmers University of Technology, Göteborg, Sweden)
R. Nazikian (Princeton Plasma Physics Laboratory, USA)
F. Porcelli (INFM and Politecnico di Torino, Italy)
S. Sharapov (UKAEA, Culham, UK)
K. Tobita (Japan Atomic Energy Agency, Naka, Japan)
K. Toi (Chairman, National Institute for Fusion Science, Toki, Japan)
F. Zonca (ENEA, Frascati, Italy)

Local Organizing Committee

M. Emoto
N. Hayashi
M. Isobe
R. Kumazawa
M. Nishiura
S. Ohdachi
M. Osakabe
Y. Todo
K. Toi (Chairman)

Scientific Secretary

A. Malaquias, International Atomic Energy Agency, Vienna, Austria

Preface

The 9th IAEA Technical Meeting on *Energetic Particles in Magnetic Confinement Systems* was held in Takayama, Japan from 9 November to11 November 2005, of which series of meeting was held at Kiev (1989), Aspenas (1991), Trieste (1993), Princeton (1995), JET/Abingdon (1997), Naka (1999), Göteborg (2001) and San Diego (2003). This meeting was organized by the National Institute for Fusion Science, Toki, Japan. Over 60 participants from 9 member states of IAEA attended this international meeting.

In this meeting, the present status of experimental and theoretical studies on energetic ions, alpha particles and runaway electrons in a wide variety of magnetic confinement geometries was discussed. The meeting focused on the following important topics: (A) Alpha particles physics, (B) Transport of energetic particles, (C) Effects of energetic particles in magnetic confinement fusion devices, (D) Collective phenomena: Alfvén eigenmodes, energetic particle modes and others, (E) Runaway electrons and disruptions, and (F) Diagnostics for energetic particles. 16 invited talks, 13 oral talks and 24 posters were presented. About half of presentations devoted themselves to discussing Alfvén eigenmodes and their effects on energetic ion transport in tokamaks, helical devices or stellarators, and spherical tori. About one third of them devoted themselves to discussing various diagnostics for energetic particle measurements. An invited talk discussed generation of energetic electrons during plasma disruption. This volume includes papers submitted for the proceedings. For the case that the authors did not submit their paper, this volume includes a submitted abstract. Most of invited talks will be published as a cluster paper in a special issue of *Nuclear Fusion* journal. In addition, files used for presentations of all talks and posters can be downloaded from the web site:
http://htpp.lhd.nifs.ac.jp/IAEATM-EP2005/index.html.

On behalf of the Local Organizing Committee (LOC), I would like to thank all participants for their contributions to this meeting. I also thank all members of the International Advisory Committee and IAEA for their support and cooperation. I'm grateful to Director General Prof. Motojima and staffs of the National Institute for Fusion Science for their support.

Kazuo TOI
Chair of LOC

Contents

List of Presentations

◆ **Invited Talks**

◆ **Oral Talks**

◆ **Poster Presentations**

9th IAEA Technical Meeting on Energetic Particles in Magnetic Confinement Systems, 9 to 11 Nov. 2005, Takayama, Japan

IT01

This paper will be published as a cluster paper in a special issue of Nuclear Fusion journal.

Alfvén cascades in JET discharges with NBI-heating

S.E. Sharapov[1], B.Alper[1], H.L. Berk[2], D.Borba[3], C.Boswell[4], B.N.Breizman[2], E.A.Evangelidis[5], S.Hacquin[3], V.G.Kiptily[1], S.D.Pinches[6], P.Sandquist[7], N.P.Young[8], and JET EFDA contributors*

[1]*Euratom/UKAEA Fusion Association, Culham Science Centre, Abingdon, Oxfordshire OX14 3DB, UK*
[2]*Institute for Fusion Studies, University of Texas at Austin, Austin, Texas, USA*
[3]*Euratom/IST Fusion Association, Centro de Fusao Nuclear, Lisboa, Portugal*
[4] *PSFC, Massachussets Institute of Technology, Cambridge, USA*
[5]*Euratom/Hellenic Fusion Assoc., Democritos University of Thrase, Xanthi, Greece*
[6]*Max-Plank Institute for Plasmaphysics, Euratom Association, Garching, Germany*
[7]*Euratom/VR Fusion Association, Chalmers Univ. of Technology, Goteborg, Sweden*
[8]*Department of Physics, University of Warwick, Coventry, UK*
**See the Appendix of J.Pamela et al., Fusion Energy 2004 (Proc. 20th Int. Conf. Vilamoura, 2004) IAEA, Vienna (2004)*

The recently developed interferometry diagnostics for detecting Alfvén eigenmodes on JET [1] reveals excitation of Alfvén cascades (ACs) in JET discharges with high-power NBI heating when the external Mirnov magnetic coils show almost no sign of ACs because of the high level of magnetic noise. With the use of interferometry, the ACs in NBI-heated plasmas are studied experimentally to assess their stability in burning plasma relevant high-density JET discharges and as a diagnostic tool. Theoretically, the particle-to-wave power transfer as a function of frequency and parallel wave-vector of ACs is analysed for the resonant interaction between ACs and NBI-produced passing ions and the conditions for the AC damping/drive due to such ions are obtained [2]. The experimentally observed excitation of ACs by sub-Alfvénic NBI-produced ions with parallel velocities as low as $V_{\|NBI} \approx 0.2 \cdot V_A$ on JET is analysed and the comparison of a DIII-D – JET experiment on NBI-driven ACs and their effect on the beam power deposition profile [3] is discussed. New opportunities for MHD spectroscopy, which are associated with the larger number of detected ACs and with the possibility to excite the modes by sub-Alfvénic ions are demonstrated including the use of grand-cascades as indicators of triggering events for internal transport barriers in NBI-heated discharges. MHD-spectroscopy based on the interferometry detection of ACs, when no mode number can be identified, is discussed and alternative ways to obtain the necessary information on the mode numbers from the Doppler-shift effect in toroidally rotating NBI-heated plasmas for ACs are described.

This work was funded partly by the UK EPSRC and by the European Communities under the contract of Association between EURATOM and UKAEA. The views and opinions expressed herein do not necessarily reflect those of the European Commission. This work was carried out within the EFDA framework.

[1] S.E. Sharapov et al., Phys. Rev. Lett. **93** 165001 (2004).
[2] E.Evangelidis et al., work in progress (2005).
[3] R.Nazikian et al., Fusion Energy 2004 (Proc. 20th Int. Conf. Vilamoura, 2004) (Vienna: IAEA), paper EX/5-1.

IT02

This paper will be published as a cluster paper in a special issue of Nuclear Fusion journal.

Alfven Eigenmode Observations on DIII-D*

M.A. Van Zeeland,[1] G.J. Kramer,[2] R Nazikian,[2] H.L. Berk,[3] T.N. Carlstrom, W.W. Heidbrink,[4] G.R. McKee,[5] W.A. Peebles,[6] T.L. Rhodes,[6] W.M. Solomon,[2] G. Wang,[6] L. Zeng[6]

General Atomics, P.O. Box 85608, San Diego, California 92186-5608 USA
[1]Oak Ridge Institute for Science Education, Oak Ridge, Tenessee, USA
[2]Princeton Plasma Physics Laboratory, Princeton, New Jersey, USA
[3]Institute for Fusion Studies at University of Texas at Austin.
[4]University of California, Irvine, California, USA
[5]University of Wisconsin, Madison, Wisconsin, USA
[6]University of California, Los Angeles, California, USA
Corresponding author: vanzeeland@fusion.gat.com; Phone: (858) 455-3315; Fax: (858) 455-4156

For next-step devices such as ITER, alpha particle driven Alfven eigenmode (AE) instabilities are predicted and there is a concern that substantial loss of hot fusion-born alpha particles will occur. Understanding the spatial structure and stability properties of such modes through modeling and direct experimental observation is essential in order to have confidence in our ability to predict Alfvenic activity and their nonlinear consequences in future devices. Recent upgrades to many of the diagnostic systems on DIII-D such as the CO_2 interferometer, FIR scattering, BES, and quadrature reflectometer have significantly extended their capabilities and made possible the experimental study of AEs. Measurements have revealed the presence of several different classes of AEs including both the TAE and reverse shear Alfven eigenmode (RSAE) in various DIII-D discharges. Due to the nature of these density fluctuation measurements, information about the AE internal mode structure beyond that obtainable with magnetic pick-up loops alone is demonstrated. Experimental data are compared with NOVA calculations of the linear TAE and RSAE spatial structure. Theoretical predictions of RSAEs show strong localization to regions of low shear near the minimum of the magnetic safety factor when there is an inverted shear profile, suggesting additional information can be obtained from these diagnostics about the q-profile itself.

*Work supported by the U.S. Department of Energy under DE-FC02-04ER54698, DE-AC05-76OR00033, DE-AC02-76CH03073, SC-G903402, DE-FG03-96ER54373, DE-FG03-01ER54615, DE-FG03-86ER53266.

IT03

This paper will be published as a cluster paper in a special issue of Nuclear Fusion journal.

Enhanced radial transport of Energetic Particles with Alfven Eigen mode on LHD

M.Osakabe, S.Yamamoto[*1], K.Toi, Y.Takeiri, S.Sakakibara, K.Tanaka, K.Narihara, and LHD-experimental Group

National Institute for Fusion Science, Toki 509-5292, Japan
[*1] *Graduate School of Enginnering, Osaka University, 2-1 Yamadaoka Suita, Japan*

Abstracts

The interaction of Alfvén Eigen (AE) modes on the transport of super Alfvénic energetic particle is one of the most important issues in fusion reactor research since the interaction with fusion produced alphas might cause serious problem on the performance of a fusion reactor. On LHD, energetic hydrogen neutral beam, up to 180 keV, are tangentially injected to plasmas and the operational magnetic fields are ranging from 0.4-3.0[T]. These conditions enable us to study the interaction with super Alfvénic particles on LHD.

During the high-beta experimental campaign on LHD, where the magnetic field strength is set around at 0.5[T], the fast change of energetic neutral particles being associated with toroidal-AE(TAE)-burst signals were observed on the tangential E//B-NPA[1,2]. The signals of neutral particles at high energy(typically ~130-keV) were increased with the bursts, while the signal increase of lower energy particles occurred after the increase of the high energy particles. From the analysis, it turned out that the signal increase at high energy region is the result of a formation of a “clump” with the enhanced transport of energetic particle by the TAE-bursts and that the increase at low energy is simply the result of the energy slowing-down of the “clump”. Recently, the creation of a “hole” and its slowing-down are also observed on LHD. Using the NPA data, the slowing-down time of both the clump and the hole are evaluated. With this slowing-down information being combined with the orbit analysis on the NPA sight line, the location of the clump and hole formations are identified and the enhanced transport of energetic particles with TAE-bursts are clearly observed by the experiments. Moreover, the enhancement of heat loads close to the diverter regions are also observed with these bursts by an infrared-camera. The heat loads are enhanced at the different regions from the diverter trace, and are considered to be the results of the loss of energetic particles. In the presentation, the analysis for these phenomena will be shown.

[1] M.Osakabe, *et al.*, Proc. 30th EPS Conf. (2002) P1-083
[2] M.Osakabe, *et al.*, Proc. EX-P4/44 20th IAEA Fusion Energy Conf. (2004)

IT04

This paper will be published as a cluster paper in a special issue of Nuclear Fusion journal.

Studies on fast ion transport induced by energetic particle modes using fast particle diagnostics with high time resolution in CHS

M. Isobe[1], K. Toi[1], H. Matsushita[2], M. Takeuchi[3], K. Nagaoka[1], Y. Yoshimura[1], C. Suzuki[1], T. Akiyama[1], T. Minami[1], M. Nishiura[1], K. Matsuoka[1], S. Okamura[1], D. S. Darrow[4], K. Shinohara[5], M. Sasao[6] and CHS group

[1]*National Institute for Fusion Science, Toki 509-5292 Japan*

[2]*The Graduate University for Advanced Studies, Toki 509-5292 Japan*

[3]*Nagoya University, Nagoya 464-8603 Japan*

[4]*Princeton Plasma Physics Laboratory, Princeton 08543 USA*

[5]*Japan Atomic Energy Research Institute, 311-0193 Naka Japan*

[6]*Tohoku University, 980-8579, Japan.*

Energetic particle modes (EPMs) are thought to be important in a burning plasma, similar to energetic-ion driven Alfvén eigenmodes. EPMs are often observed in CHS when high power neutral beam (NB) is tangentially co-injected into a relatively low density target plasma. This mode is characterized by periodic recurrence and fast frequency sweeping for each burst [1]. Currently, effects of EPMs on fast ion transport and resulting losses are investigated by use of neutral particle analyzer (NPA) and escaping fast ion probes [1] with high time resolution. Coinciding with appearance of EPM bursts, the NPA viewing co-going transit beam ions indicates that flux of high energy neutral particles whose energy is close to injection energy E_b of NB rapidly increases and subsequently decays with a time constant less than 1 ms. H_α light emissivity from only peripheral domain of large R (R : major radius) side also behaves like the NPA signals in the energy range of ~E_b. It should be noted that there is no significant change on neutral flux in somewhat lower energy range than E_b. These imply that beam ions only near E_b are lost toward large R side by excited EPMs. It is interesting to note that enhanced neutral flux correlated with EPM bursts appears in the range of higher energy than E_b. The clear evidence to prove the existence of beam ion losses induced by the EPM is a signal from scintillator- based escaping fast ion probe. The probe indicates that the beam ions whose energy is near E_b are dominantly lost and the losses to the probe begin just after the mode amplitude reaches the maximum. In addition to these observations, the relation between spatial structure of EPMs measured with soft X-ray detector's array and the mode-induced fast ion losses will be also presented.

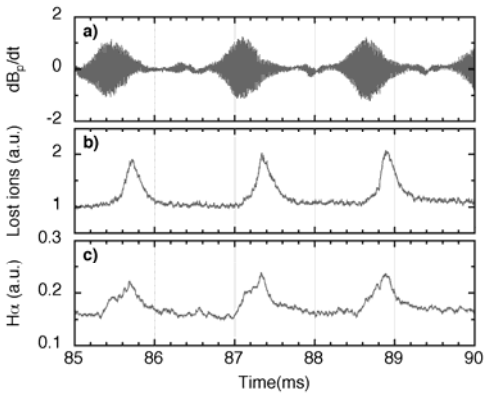

Fig.1 Time traces of a) magnetic probe, b) escaping fast ion probe signal, c) H_α light

[1] K. Toi *et al.*, Nuclear Fusion **40**(2000)1349

Observation of Confinement Degradation of Energetic Ion due to Alfvén Eigenmodes in weak shear plasmas onJT-60U

M. Ishikawa , M. Takechi, K. Shinohara, Y. Kusama, G. Matsunaga , V. A. Krasilnikov 1), Yu. Kashuck 1), M. Isobe 2), T. Nishitani, A. Morioka, M. Sasao 4), C. Z. Cheng 4), N. N. Gorelenkov 5), G. J. Kramer 5), R. Nazikian 5), and JT-60 team

Japan Atomic Energy Agency, Naka-Shi, Ibaraki 319-0193, Japan
1) Troitsk Institute of Innovating and Fusion Research, Troitsk, Moscow region 142092, Russia
2) National Institute for Fusion Science, Toki-Shi, Gifu 509-5292, Japan
3) Department of Engineering, Tohoku Univ., Sendai-Shi, Miyagi 980-8578, Japan
4) National Space Organization, Hsin Chu City 300, Taiwan
5) Princeton Plasma Physics Laboratory, Princeton University, Princeton, NJ 08543, USA

E-mail: ishikawm@fusion.naka.jaeri.go.jp

Abstract. Confinement degradation due to Alfvén Eigenmodes has been investigated with negative ion based injection at ~ 370 keV into weak shear plasmas on JT-60U. The AEs with a rapid frequency sweeping and then saturation as the minimum value of safety factor (q_{min}) decrease have been observed. These frequency behavior can be explained by reversed-shear induced AE (RSAE) and the transition from RSAE to TAE. Reduction rate of total neutron emission rate in the presence of AEs is evaluated by calculation with Orbit Following Monte-Carlo code taking into account changing in bulk plasmas. The changes in total neutron emission rate and CX-NP flux suggested energetic ion transport due to these AEs. The evolution indicates confinement of energetic ions is degraded due to AEs. In particular, it is found confinement degradation is maximum during transition from RSAE to TAE and the maximum reduction rate $(\Delta Sn/Sn)_{MAX}$ is estimated ~ 45 %..

1. Introduction

Burning plasmas are self-sustained by alpha-particle heating. However, high alpha particle pressure gradient can destabilize Magnetohydrodynamics (MHD) instabilities such as toroidicity-induced AEs (TAEs) [1] or Energetic particle modes (EPMs) [2]. These MHD instabilities can induce enhance transport of α-particles from a core region, which degrade the performance of burning plasmas. Further lost α-particles may also damage first walls. Thus, the understanding of α-particle transport due to these instabilities is one of the urgent research issues for ITER. So far, TAEs or EPMs have been studied theoretically and experimentally. Furthermore, effects of TAEs or EPMs on energetic ions have been studied in TFTR [3], DIII-D [4], and JT-60U [5, 6] and so on. In particular, it was found that bursting modes in the frequency range of TAE, which is called Abrupt Large-amplitude Events, expelled a significant energetic ion population from core region to outer region and induce redistribution and loss of energetic ions using neutron emission profile measurements [7] and charge-exchange (CX) neutral particle flux measurement [8] in JT-60U [9].

Recently, another type AEs, which have a rapid and large frequency sweeping as the minimum values of safety factor (q_{min}) changes, are extensively studied and experimentally observed in JET [10], CHS [11, 12] and JT-60U [13] in reversed shear (RS) plasmas. AEs with a strong frequency dependence on q_{min} in reversed shear plasmas were first explained by numerical studies using the Transport Analyzing System for Tokamak/Wave Multimode (TASK/WM) code[14], which is a full code

assuming that thermal particles follows their guiding center motion. Then, AEs with large frequency sweeping observed in JT-60U RS plasmas were identified as reversed-shear Alfven eigenmodes (RSAEs) [13]. On the other hand, the existence of observed large frequency sweeping modes, are called Alfvén cascades (ACs), by using the model of EPMs by Berk *et al.* [15]. However, it has not been reported how RSAEs or ACs affect energetic ions, so far.

In JT-60U weak shear (WS) plasmas, AEs with rapid frequency sweeping and then saturation of frequency as q_{min} decrease have been observed during Negative-ion-based Neutral Beam (NNB) injection [16]. The frequency evolution can be explained by RSAE and transition from RSAE to TAE. In the present work, we evaluate confinement degradation in the presence of RSAEs and TAEs in WS plasmas from the comparison between measured neutron and calculated neutron with Orbit Following Monte-Carlo (OFMC) code [17]. Further the energetic ion transport due to these modes is estimated using CX neutral particle flux measurement [8]. In this paper we present results of the experiment conducted in N-NB injected WS plasmas in order to investigate confinement degradation due to AEs. Section 2 describes diagnostics utilized to investigate energetic ion transports. The property of observed AEs in WS plasmas is described in Section 3 and the evolution of confinement degradation of energetic ions using OFMC code is given in Section 4. The summary is presented in Section 5.

2. Experimental

We performed AE experiments using N-NB in WS plasmas with the following parameters: I_P = 1.0 MA, B_T = 1.7 T, P_{NNB} ~ 3.9 MW, E_{NNB} ~ 370 keV, where P_{NNB} and E_{NNB} are the power and energy of N-NB, respectively. The slowing down time of energetic ions from NNB injection is calculated using OFMC code as ~ 500 ms. In order to measure ion temperature and safety factor, two units of positive-ion-based NB (PNB) were also injected, where both power and energy of PNBs are ~ 2.0 MW and ~ 80 keV respectively. In this discharge, $v_{b//} / v_A \sim 0.6$ and calculation with the OFMC code shows $<\beta_h> \sim 0.4$ %, where $v_{b//} / v_A$ is the ratio of the beam ion velocity and $<\beta_h>$ is the volume averaged classical energetic ion beta. Figure 1 shows the plasma configuration in this experiment and two NNB beam lines.

In order to investigate energetic ion behavior, we measure total neutron emission rate using Fission Chamber [18]. Because beam-thermal neutron, $Sn_{b\text{-}th}$,

$$Sn_{b\text{-}th} \propto \int n_b n_i <\sigma v> dv,$$

accounts for ~ 90 % of total neutron emission rate in such AE experiments, changes in neutron emission rate mean directly those in the energetic ion population if bulk plasma parameters don't change. Here, n_b and n_i are a density of beam ions and bulk ions, respectively, and $<\sigma v>$ is a fusion reactivity of beam-thermal reaction.The sampling late of the Fission Chamber is 1ms. The charge exchange (CX) neutral particle flux and spectrum are also measured by a NDD [9,19,20]. The NDD detects neutral particles whose pitch angles are almost the same as that of birth energetic ions produced by the NNB injection, since energetic ions are neutralized through charge exchange reactions with the neutral particles D^0 or the hydrogen-like carbon ions C^{5+} and are emitted from the plasma as neutral particles. Therefore we can investigate behavior of NNB ions. The sampling rate of the CX neutral particle measurement is 1 ms. Frequencies, amplitudes and mode numbers of the instabilities are measured by Mirnov coils located near the first wall.

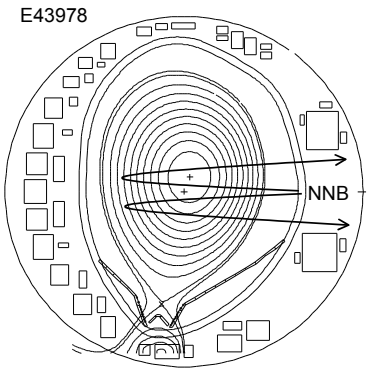

Fig.1 *plasma configuration, two beam lines of NNBs*

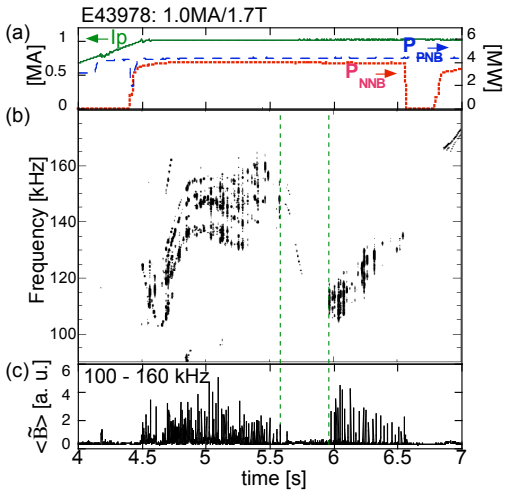

Fig.2 *Time traces of plasma parameters of E43978. (a): Plasma current, I_P, and beam injection power of N-NB and two units of P-NB for diagnostics of q-profile and ion temperature. The beam energy of N-NB and both P-NB is ~370 keV and and ~80keV, (b) Frequency spectrum of magnetic fluctuations. (c) Amplitude of magnetic fluctuations with frequency of 100-160 kHz.*

3. Property of Instabilities in NNB Injected Weak Shear Plasmas

Shown in Fig.2 are the waveforms of plasma parameters in the discharge described in Sec.2. Figure 2 (a) shows the time evolution of plasma current and injected NNB and PNB power. Figures 2 (b) and 2 (c) show the time traces of the frequency spectrum and mode amplitude with frequency of 100 - 160 kHz, respectively. An instability appears with a frequency of about 100 kHz at about 4.6 s and its frequency chirps up to about 150 kHz at about 4.8 s. After the saturation of the frequency sweeping from 4.8s to 5.5s, instabilities were almost stabilized for ~ 0.4 s from t ~ 5.5 s. Further another frequency sweeping started from t ~ 5.9 s. So far, such instabilities with frequency sweeping have been labeled as the slow Frequency Sweeping modes [16]. However, the cause of the mode has been not identified yet.

In order to understand the large and rapid frequency sweeping and its subsequent saturation in WS plasmas, we propose a model of RSAE and its transition to TAE as q_{min} decreases [14]. RSAE is a global AE near the zero shear region of the RS plasma. However, we consider RSAE can be applied to AEs with the large frequency sweeping in WS plasmas. Shown in Fig. 3 are the Alfvén continuum spectrum for n = 1 mode and the safety factor versus minor radius (r/a) at (a) t = 4.7s, (b) 5.3s and (c) 5.7s in the discharge shown in Fig. 2, respectively. Values of q_{min} in Fig. 3 are (a) 1.7, (b) 1.4 and (c) 1.2, respectively. Frequency gaps outside the region (r/a > ~ 0.7) are similar in all three figures. The gap structures around the q_{min} region, however, are entirely different even if change in q_{min} is small. Gaps shown in Fig. 3 (b) and (c) are the TAE gaps formed by toroidal coupling of the m = 2 and m = 1 harmonics around q = 1.5 locations. On the other hand, in Fig. 3 (a), there is no q = 1.5 and the continuum gap is formed due to the weak shear q-profile in center region. The lower continuum is due to the m = 2 harmonic and the upper continuum is due to m = 1. Around the upper and the lower boundary of this continuum around q_{min} (r/a ~ 0.0), AEs can be destabilized by large energetic ions pressure and its gradient as shown in Fig. 4. Shown in Fig. 4 is classical pressure profile of energetic ions calculated with

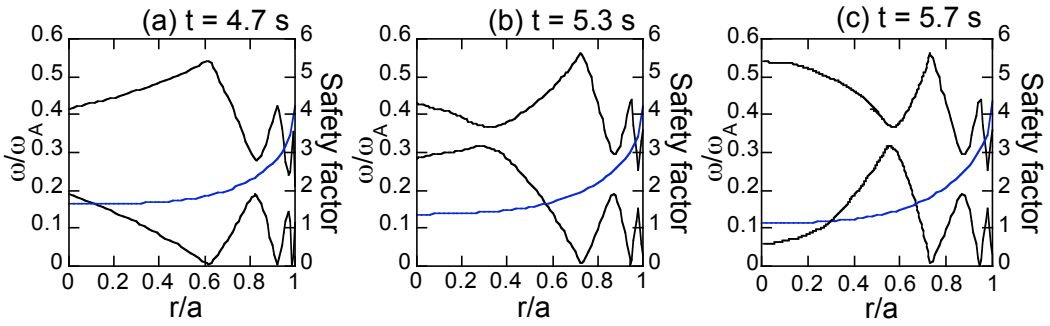

Fig.3 *Alfén continuum spectrum for n = 1 mode, safety factor profile at (a) 4.7s, (b) 5.3s and (c) 5.7s*

the OFMC code. A peaked pressure profile of NNB ions was produced with upper beam line shown in Fig.1. These modes can be called RSAE because the resonance condition for this mode is the same as for RSAE described in Ref.14. Therefore, the large and rapid frequency sweeping of AEs can be explained by RSAE and the subsequent frequency saturation by the evolution from RSAE to TAE. The AE frequencies are estimated as follows [14] :

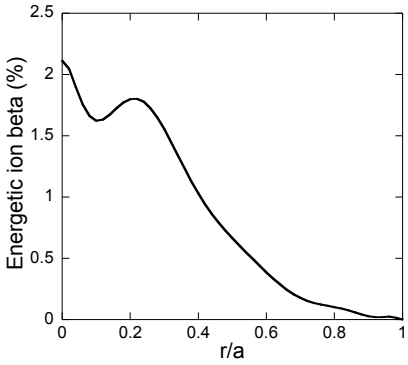

Fig.4 *Profile of classical energetic ion beta produced by NNB injection.*

(i) as q_{min} decreases in the range of

$$(m+1/2)/n + c < q_{min} < (m+1)/n,$$

there are two RSAEs: the frequency of the high frequency RSAE (HRSAE) decreases as

$$f_{HRSAE} \sim (n - m/q_{min})\ v_A/2\pi R, \quad (1)$$

and the frequency of the low frequency RSAE (LRSAE) increases as

$$f_{LRSAE} \sim ((m+1)/q_{min} - n)\ v_A/2\pi R, \quad (2)$$

(ii) for $m/n < q_{min} < (m+1/2)/n+c$, TAE gaps form and TAE frequency is approximately given by

$$f_{TAE} \sim v_A/4\pi q_{TAE} R, \quad (3)$$

where $c \sim r_{min}/nR$, R is the major radius, and $q_{TAE} = (m-1/2)/n$. Note that the toroidal effect causes the m and $m+1$ harmonics to couple in the range of $m/n < q_{min} < (m+1/2)/n + c$. Thus, AEs have changed from RSAEs to TAEs in this q_{min} range. Here, we estimate frequency of RSAE and TAE for the case of the instabilities shown in Fig.2 (b) using eqs. 1-3, where $R \sim 3.3$ (m) $n_i(q_{min}) \sim 1.2\times10^{19}$ (m^{-3}), $c \sim 0$, $B = 1.7$T. The broken lines in Fig. 2 denote the estimated frequency. As shown in Fig. 2 (b), the large and rapid frequency sweeping and its subsequent saturation can be explained by RSAE and its transition to the TAE. On the other hand, any AEs are not observed although there is the TAE gap in the case of Fig. 3 (c). This is considered to be due to small pressure of energetic ion and its gradient around TAE gap (r/a ~ 0.5) as shown in Fig. 4. Thus, we show the property of AEs in WS plasmas by the RSAE model.

4. Confinement Degradation of Energetic Ions by RSAE and TAE

Figure 5 shows time trace of the frequency spectrum of magnetic fluctuation, the total neutron emission rate, neutral particle flux in energy of 20 ~500 keV and line integrated electron density.

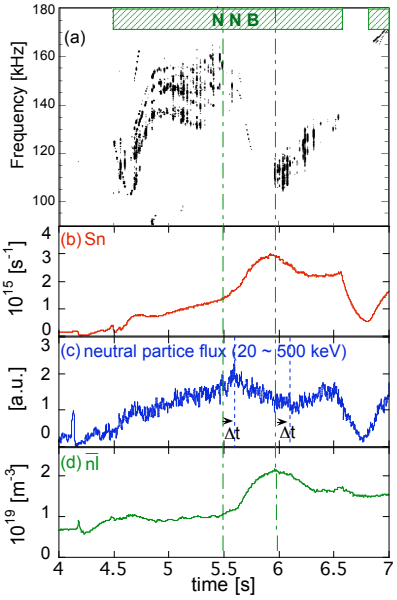

Fig.5 Time trace of (a) frequency spectrum of magnetic fluctuation (b) Total neutron emission (Sn) measured by Fission chamber. (c) charge exchange neutral particle flux of E ~ 20 - 500 keV. (d) Line averaged electron density (nl)

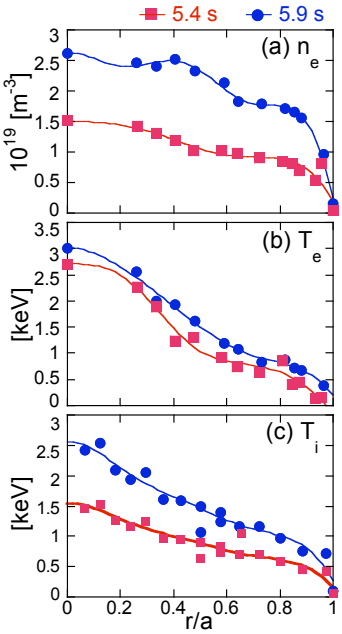

***Fig.6** Profiles of (a) electron density, (b) electron temperature and (c) ion temperature at 5.4 s (with AEs) and 5.9 s (without AEs)*

One can see that an increase of total neutron emission rate (Sn) seems to be suppressed in the presence of RSAE and TAE for t ~ 4.5 – 5.5 s. After TAE was stabilized at t ~ 5.5 s, the increasing rate of Sn is enhanced rapidly. However, Sn decrease after another RSAE appear after t ~ 5.9 s. On the other hand, CX neutral particle (CX-NP) flux increases for t ~ 4.5 – 5.5 s. Then, after ~ 100 ms from distablizing TAE, the CX-NP flux starts decreasing. Further the CX-NP flux increases again after ~ 100 ms from appearance of another RSAE. This time lag (Δt) the change in CX-NP flux for the change in Sn in Fig.5(c) can be explain by time scale of energetic ion transport due to AEs to outer region. Because the NDD detects energetic ions neutralized through charge exchange reactions with D^0 or C^{5+} in outer region of the plasma, Such changes in Sn and CX-NP flux suggest that energetic ions is transported due to these AEs. However, as can be seen in Fig. 5 (d), line averaged electron density changes in similar way as changes in Sn. Figure 6 shows radial profiles of (a) electron density, (b) electron temperature and (c) ion temperature with AEs (at t = 5.4 s) and without AEs (at t = 5.9 s), respectively. One can see that all parameters of bulk plasmas increase after AEs was stabilized. Because neutron emission rate depends on bulk plasma parameter, in particular is proportional to bulk ion density, the change in Sn might be dominantly due to changes in bulk plasma, not energetic ions.

Then, in order to evaluate how does confinement of energetic ions degrade, neutron emission rate is calculated with OFMC code, taking into account the changes in the bulk plasma. The calculation is performed assuming that the confinement of energetic ions is classical and the beam-target fusion reaction is dominant in total neutron emission rate. Actually, the beam-target neutrons account for ~ 90% of the total neutron emission in this discharge according to the calculation by TOPICS [21]. Shown in Fig. 7 (b) is measured total neutron emission rate (solid line) and calculated one with OFMC code (circle). Compared with both neutron emission rates, measured neutron emission rate is smaller than calculated one in the presence of RSAE and TAE. Whereas, after AEs are stabilized, measured neutron rate is close to calculated one, then consistent with that at t = 5.9 s. This result indicates confinement of

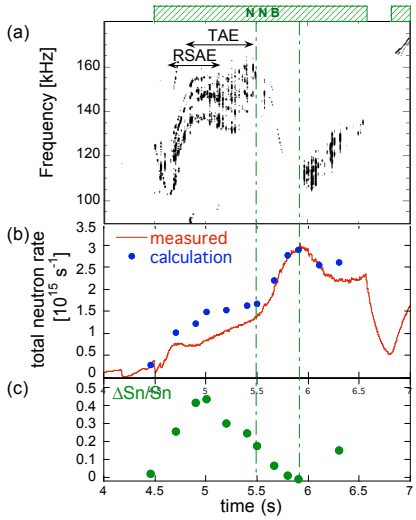

Fig.7 Time trace of (a) frequency spectrum of magnetic fluctuation, (b) measured neutron emission rate (solid line) and calculated one with OFMC code (circle) and (c) reduction rate of neutron emission rate (ΔSn/Sn).

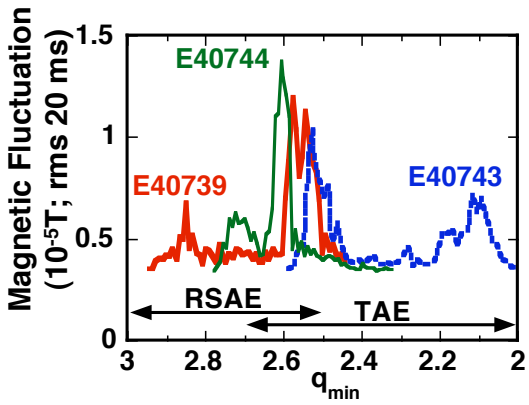

Fig.8 *Dependence of AE magnetic fluctuation amplitude on q_{min} in RS plasmas in three shots (E40739, E40743 and E40744). The n = 1 AE amplitude is enhanced in range of 2.4 < q_{min} < 2.7 (Ref. 13)*

energetic ions is degraded due to RSAE and TAE. Further, it is considered that the difference between the measured one and the calculation one decreased after AEs disappeared because the confinement of energetic ions is close to classical. Figure 7 (c) shows time trace of reduction rate of neutron emission rate. This reduction rate is estimated from the ratio of calculated neutron rate to measured one. The reduction rate is large in the transition phase from RSAE to TAE from ~ 4.8 s to ~ 5.2 s, Here the maximum reduction rate is estimated $(\Delta Sn/Sn)_{MAX}$ ~ 45 % at t ~ 5.0s.

In the previous studies in JT-60U RS plasmas, it was observed in experimentally and predicted by numerical studies using TASK/WM code in theoretically that AEs are most unstable in the transition phase from RSAEs to TAEs [13]. Figure 8 shows the results of AE experiments in RS plasmas (I_p = 1.3 MA, B_t = 3.73 T). In these experiments, in order to investigate the dependence of mode amplitude on the q-profile change, the time of NNB injection was changed in three shots, where the values of q_{min} at the time of the NNB injection are about 3.0, 2.8 and 2.6 for the shots of E40739, E40744 and E40743, respectively. For all cases the n = 1 modes was observed and the amplitude was largest in the range 2.4 < q_{min} < 2.7, whose range corresponded to the transition phase from RSAEs to TAEs, as shown in Fig.8. Thus understanding of the excitation mechanism of RSAE and its transition to TAE was progressed. However, effects of RSAE, TAE and the transition from RSAE to TAE on energetic ion confinement have been understood yet. In present study, confinement degradation of energetic ions in the presence of RSAE and TAE is evaluated for the first time.

5. Summary

In present work confinement degradation due to Alfvén Eigenmodes has been investigated with negative ion based injection WS plasmas on JT-60U. The AEs with a rapid frequency sweeping and then saturation as the minimum value of safety factor (q_{min}) decrease have been observed. These frequency behavior can be explained by RSAE and the transition from RSAE to TAE. The changes in total neutron emission rate and CX-NP flux suggested energetic ion transport due to these AEs. The

reduction rate of total neutron emission rate in the presence of AEs is evaluated by calculation with Orbit Following Monte-Carlo code taking into account changing in bulk plasmas. The result indicates confinement of energetic ions is degraded due to AEs. In particular, it is found confinement degradation is maximum during transition from RSAE to TAE and the maximum reduction rate $(\Delta Sn/Sn)_{MAX}$ is estimated ~ 45 %.

Acknowledgment

The authors would like to thank member of JAERI for their support and useful discussions. This work was partly supported by JSPS, Grant-in-Aid for Scientific Research (B) No.14208056. Work done by PPPL group is also supported by US DOE contract No. DE-AC02-CHO-3073.

Reference

[1] CHENG, C.Z., CHANCE, M.S., Phys. Fluids **29** (1986) 3695.
[2] CHEN, L., et al., Phys. of Plasmas **1** (1994) 1519.
[3] WONG, K.L., et al., Phys. Rev. Lett. **66** (1991) 1874.
[4] STRAIT, E.J., et al., Plasma Phys. Control. Fusion 36 (1994) 1211.
[5] SAIGUSA, M., et al.,Plasma Phys. Control. Fusion **37** (1995) 295.
[6] KUSAMA, Y., et al., Nucl Fusion **39** (1999) 1837.
[7] ISHIKAWA, M., et al., accepted for Nucl. Fusion, (2005)
[7] SHINOHARA, K., et al., Nucl. Fusion **41** (2001) 603.
[8] ISHIKAWA, M., et al., Rev. Sci. Instru.**73** (2002) 4236.
[9] ISHIKAWA, M., et al., Rev. Sci. Instru.**75** (2004) 3643.
[10] Sharapov, S., et al., Phys. Lett. A **289**, (2001) 127.
[11] TAKECHI, M. et al., Annual Report of National Institute for Fusion Science, April 1999–March 2000, pp. 268, ISSN 0917-1185 (2000) .
[12] TAKECHI, M. et al., J. Plasma Fusion Res. **12**, (2002) 1273 .
[13] TAKECHI, M. et al., Plasam of Phys. **12**(2005).82509
[14] FUKUYAMA A. et al., in 6TH IAEA Technical Committee Meeting on Energetic Particles in Magnetic Confinement Systems, 12-14, October, 1999, Naka (IAEA, Vienna, 1999).
[15] Berk, L., et al., Phys. Rev. Lett. **87** (2001)185002 .
[16] SHINOHARA, et al., Nucl. Fusion **42** (2001) 603
[17] TANI, K., et al., Phys. Soc. Jpn. **50** (1981) 1726
[18] NISHITANI, T., et al., Rev. Sci. Instru. **63** (1992) 5270.
[19] KRASILNIKOV, A.V., et al., IEEE trans. Nucl. Sci. **45** (1998) 385.
[20] KRASILNIKOV, A.V., et al., J. Plas. Fusion Res. **75** (1999) 967.
[21] SHIRAI, H., et al., J. Phys. Soc. Jpn. **64** (1995) 4209.

IT06

This paper will be published as a cluster paper in a special issue of Nuclear Fusion journal.

Observation and Modelling of Fast Ion Loss

S. D. Pinches[1], L.-G. Eriksson[2], H.-U. Fahrbach[1], M. García-Muñoz[1], V. G. Kiptily[3], S. E. Sharapov[3], the ASDEX Upgrade Team and JET-EFDA Contributors[*]

[1]*Max-Planck-Institut für Plasmaphysik, Euratom Association, D-85748 Garching, Germany*
[2]*Assocation EURATOM-CEA, CEA-Cadarache, F-13108 St. Paul lez Durance, France*
[3]*Euratom/UKAEA Fusion Association, Culham Science Centre, Abingdon, OX14 3DB, UK*

The confinement of fast particles is of crucial importance for future large fusion devices [1]. The ICRF heating systems on ASDEX Upgrade and JET are capable of accelerating minority ions up to energies in the MeV range. On JET, protons with energies exceeding 5 MeV have been detected using a gamma-ray spectrometer and a 19 channel array of 2D gamma-ray detectors to view the emissions from the inelastic scattering of such energetic protons with carbon, $^{12}C(p,p'\gamma)^{12}C$ [2]. Recent experiments on JET have shown a significant decrease in the gamma-ray emissivity from this process (by a factor of 2) during so-called tornado modes (TAE within the $q = 1$ surface) and standard TAE in sawtoothing plasmas. This is indicative of a loss or extensive re-distribution of these (> 5 MeV) particles from the plasma core [3].

In ASDEX Upgrade, a new fast ion loss detector has been mounted on the midplane manipulator [4]. Due to its high resolution in pitch angle, energy and time it has enabled the direct observation of fast ion losses during various MHD phenomena to be studied in detail. ELM induced fast ion losses have been directly observed for the first time in a fusion plasma device. The enhancement of fast ion losses has been observed from specific areas of phase-space in the presence of (3,2) and (2,1) NTMs. Measurements during TAE activity have revealed particle losses localized in velocity-space and with the same frequency as the mode ($f \sim 180$ kHz). This has been interpreted as clear evidence of a mode-particle resonance.

In this paper, simulations with the HAGIS code [5] are presented describing the interaction of the energetic particles present and the modes observed in JET and ASDEX Upgrade. In the latter case, the additional effects of toroidal field ripple are also included. The spectrum of modes used is calculated using a linear MHD stability analysis based upon reconstructions of the MHD equilibria from the experiments. In the JET case of simultaneous TAE and tornado mode activity, the calculations show that the combined eigenfunctions of all the modes present extend almost completely across the minor radius of the device allowing an extensive interaction with, and consequent expulsion of, the energetic ions.

This work has been conducted under the European Fusion Development Agreement.

[1] S. D. Pinches et al., Plasma Phys. Control. Fus. **46** (2004) B187
[2] V. G. Kiptily, Nuclear Fusion **42** (2002) 999
[3] S. E. Sharapov et al., Fusion Energy 2004 (Proc. 20th Int. Conf. Vilamoura, 2004) paper EX/5-2Ra
[4] M. García-Muñoz et al., 32nd EPS Plasma Physics Conference, Tarragona, Spain (2005) P5.085
[5] S. D. Pinches et al., Comput. Phys. Comm. **111** (1998) 131

[*]See the Appendix of J.Paméla et al., Fusion Energy 2004 (Proc. 20th Int. Conf. Vilamoura, 2004)

IT07

This paper will be published as a cluster paper in a special issue of Nuclear Fusion journal.

Axisymmetric Phase Space Structures Driven by Fast Ions in JET

H. L. Berk[1], C. J. Boswell[2], D. Borba[3,4], T. Johnson[5], M. F. F. Nave[3], S. D. Pinches[6], S. E. Sharapov[7], and JET EFDA contributors[*]

[1]*Institute for Fusion Studies, University of Texas at Austin, Austin Texas, USA*
[2]*Plasma Science and Fusion Center, MIT, Cambridge, Massachusetts, USA*
[3]*Centro de Fusão Nuclear, Associação EURATOM/IST, Instituto Superior Ténico, Av Rovisco Pais, 1049-001 Lisboa, Portugal*
[4]*EFDA Close Support Unit, Culham Science Centre, OX14 3DB, UK*
[5]*Alfvén Laboratory, KTH, Euratom-VR Association, Sweden*
[6]*Max-Planck Institute for Plasma Physics, EURATOM Association, Boltzmannstrasse 2, D-85748 Garching, Germany*
[7]*Euratom/UKAEA, Culham Science Centre, Culham, UK*
[*]*See the Appendix of J. Pamela et al., Fusion Energy 2004 (Proc. 20th Int. Conf. Vilamoura, 2004) IAEA, Vienna (2004)*

Theoretical analysis shows that frequency sweeping of kinetically driven instabilities, near marginal stability, may arise due to spontaneous formation of phase space structures [1]. The JET observation of axisymmetric (n=0) chirping modes induced by energetic particles (produced by high-field-side off-axis ICRH) is indicative of the formation of such structures. Both up and down frequency sweeping appear simultaneously in ~5 ms intervals with a ~40% upsweep and ~25% downsweep from the initial frequency. The puzzles in this data have been: (1) What causes the instability, as the typical instability drive, spatial gradients in the energetic particle distribution, requires that the perturbed modes be non-axisymmetric ($n\neq0$), (2) What basic plasma mode frequency is being excited at a frequency that is roughly one third of the TAE frequency? (3) What plasma-wave resonances allow the observed frequency sweeping? (4) Why should the modes disappear after neutral beam heating is turned on? (5) Why should the modes only be excited with high-field-side off-axis ICRH? A consistent explanation attributes the linear mode excitation to the geodesic acoustic mode which requires n=0 for mode existence. The SELFO Monte Carlo code [2] shows that a bump-on-tail fast ion distribution is established with high-field-side ICRH and that the trapped particle bounce frequencies are found to coincide with the range of the chirped frequency span. Additional ion heating by tangential neutral beams makes the energetic particle distribution more isotropic, weakening the instability drive and increasing the damping mechanisms, thereby causing a quench of the mode. The understanding of the linear and nonlinear characteristic of the axisymmetic phase space structures gives a good example of plasma-wave interactions.

[1] Berk H L *et al.* (1999) *Phys. Plasmas* **6** 3102
[2] Hedin J, Hellsten T and Carlsson J (1998) *Proc. Joint Varenna-Lausanne Workshop "Theory of Fusion Plasmas"* 467

Self-consistent Study of Fast Particle Redistribution by Alfvén Eigenmodes During Ion Cyclotron Resonance Heating

T. Bergkvist, T. Hellsten and T. Johnson
Alfvén Laboratory, Association Euratom-VR, Sweden

e-mail: tommy.bergkvist@alfvenlab.kth.se

Abstract. Alfvén eigenmodes (AEs) excited by fusion born α particles can degrade the heating efficiency of a burning plasma and throw out αs. To experimentally study the effects of excitation of AEs and the redistribution of the fast ions, ion cyclotron resonance heating (ICRH) is often used. The distribution function of thermonuclear αs in a reactor is expected to be isotropic and constantly renewed through DT reactions. The distribution function of cyclotron heated ions is strongly anisotropic, and the ICRH do not only renew the distribution function but also provide a strong decorrelation mechanism between the fast ions and the AE. Because of the sensitivity of the AE dynamics on the details of the distribution function, the location of the resonance surfaces in phase space and the extent of the overlapping resonant regions for different AEs, a self-consistent treatment of the AE excitation and the ICRH is necessary. Interactions of fast ions with AEs during ICRH has been implemented in the SELFO code. Simulations are in good agreement with the experimentally observer pitch-fork splitting and rapid damping of the AE as ICRH is turned off. The redistribution of fast ions have been studied in the presence of several driven AEs.

1. Introduction

Alfvén eigenmodes (AEs are used here as a common name for various types of Alfvén eigenmodes) are often seen in experiments during ion-cyclotron resonance heating (ICRH). The ICRH produces peaked density profiles of anisotropic high-energy ions with wide trapped or non-standard drift orbits which can resonate with AEs. The AEs redistribute the high-energy resonant particles and can affect the performance of ICRH. The resonance is defined by two-dimensional surfaces in the three dimensional phase space of drift orbit invariants. Interactions with AEs displace the particle along a one-dimensional characteristic in phase space. In absence of decorrelation of the phase between the particle and AEs, the particle will undergo a superadiabatic oscillation in phase space without a net exchange of energy with the mode. The decorrelation caused by Coulomb collisions will be weak for high-energy ions while ICRH provides a strong decorrelation mechanism for these particles. In some parts of phase space the distribution function of resonant ions is increasing with energy along the characteristics of an AE, and hence drive the mode while the distribution function is flattened in the resonant regions. In other parts of phase space the distribution function decreases with energy along the characteristics, which will damp the mode as the distribution function is flattened. In absence of mechanisms restoring the distribution function an unstable mode will grow while flattening the distribution function in the most unstable parts of phase space. As the mode grows and the unstable parts of the distribution function is flattened the stable parts in phase space will become more important and damp the mode.

Coulomb collisions and ICRH will displace ions in and out of the AE resonant region with an energy above or below the mean energy along the AE characteristic. An ion entering at the high-energy part of the characteristic will drive the mode while if it enters at the low-energy part it will damp the mode and vice versa for an ion leaving the resonant region. The effect of decorrelation by Coulomb collisions and ICRH is important since it leads to an effective broadening of the resonant regions in phase space, and hence increases the energy transport, the saturation level of the AE and the number of regions with overlapping modes.

In experiments it has been observed that when the ICRH is turned off the ICRH-excited AEs are damped much faster than the time scales of both slowing down and resistive damping by the background plasma [1]. Another observation is the pitch fork splitting, appearing as symmetric side bands centred at the mode frequency in the Fourier decomposed time evolution

of the measured magnetic signal [1, 2]. The splitting is interpreted as an oscillation of the mode amplitude [3, 4], and are related to an effective collision frequency [2]. The observed separation of the side bands is larger than can be explained by Coulomb collisions [2]. It has been proposed that the renewal of the distribution function by ICRH can explain this difference [1].

Interactions with several AEs lead to a decorrelation of the 1D superadiabatic oscillation resulting in a two dimensional redistribution. It also leads to several resonant regions and if these regions overlap in phase space the distribution function is flattened over a larger region.

The SELFO code [5] used for calculating the distribution functions and the fast magnetosonic wave field self-consistently during ICRH has been upgraded to include the effects of interactions with AEs [6]. The SELFO code consists of the FIDO code for calculating the distribution functions during ICRH, including effects of finite drift orbit widths, and the LION code for calculating the electric field.

Detailed studies of the dynamics of toroidicity-induced Alfvén eigenmode (TAE) excitation during ICRH is in good agreement with experiments on the separation of the side bands and the fast damping of the TAE when the ICRH is turned off [6]. The effects on the distribution function of a single unstable TAE is, in general, small, since the resonant regions in phase space are rather narrow. The effects of several modes significantly increases the transport of resonant particles in phase space. The change in energy of the particle distribution is still rather small, but the relatively large redistribution in space caused by the change in toroidal angular momentum can affect the heating profile. Whereas the redistribution in toroidal angular momentum takes place on a time scale of an orbit time, the effect of the redistribution on the fast particle energy content takes place on a slowing down time.

2. Theory

Three invariants of the equation of motion (E, P_ϕ, μ) are used to describe the guiding centre orbit of a charged particle. E is the energy, $P_\phi = mRv_\phi + eZ\Psi$ is the canonical toroidal angular momentum where Ψ is the poloidal flux and μ is the magnetic momentum. There is also a label, σ, to distinguish between different types of orbits with the same invariants, e.g. co- and counter-passing orbits. The change in invariants due to interactions with AEs are obtained by integrating the equation of motion along the drift orbit

$$dE/dt = eZ\mathbf{E}_1 \cdot \mathbf{v}_{d0} + \mu \partial B_{1\|}/\partial t \tag{1}$$

where index 0 indicates unperturbed quantities and 1 first order perturbations. The zeroth order drift velocity, $\mathbf{v}_{d0}$, is given by gradients and curvature of $\mathbf{B}_0$. The first order perturbed electric and magnetic field can be written on the form $\Phi(r,\theta)A(t)e^{i(n\phi-\omega t-\alpha(t))}$, where $\Phi(r,\theta)$ is the poloidal structure of the eigenmode, $A(t)$ is the mode amplitude, n is the toroidal mode number, ω is the mode frequency and α the phase of the mode. The resonance condition is given by

$$n\frac{\Delta\phi}{\tau_b} - \omega \pm j\frac{2\pi}{\tau_b} = 0 \tag{2}$$

where $\Delta\phi$ is the precessional drift during a bounce time τ_b, and j is an integer representing higher harmonics which lead to a set of resonance surfaces in phase space. In the space defined by (E, P_ϕ, μ) for an axisymmetric plasma, the superadiabatic oscillation of an orbit takes place near its resonance along a characteristic defined by $\Delta P_\phi = \frac{n}{\omega}\Delta E$ and $\Delta\mu = 0$ [7].

Phase decorrelations of the interaction between a particle and an AE occur due to changes in the invariants by collisions or interactions with other waves, such as the magnetosonic waves used for cyclotron heating. The changes in invariants due to these interactions move the particle to a neighbouring AE characteristic where the guiding centre orbit has a different orbit time.

As time passes, the phase between the particle and the AE starts to differ from what it would have had if it had not been subjected to ion-cyclotron interactions or Coulomb collisions. After several such interactions the phase between the guiding centre orbit and AE will change but the displacement from the original AE characteristic will be small due to the diffusive nature of the interactions. The decorrelation time is given by [6]

$$\tau_d^3 = \frac{3 \cdot 2\pi}{\dot{\sigma}_{IC}^{EE} G_{IC}^2 + \dot{\sigma}_C^{EE} G_E^2 + \dot{\sigma}_C^{\Lambda\Lambda} G_\Lambda^2} \tag{3}$$

where $\sigma_L^{I_i I_j}$ is the covariance of the invariants I_i and I_j, where $\Lambda = \mu B_0/E$, from the interaction with operator L, where C denotes collisions and IC ion-cyclotron interactions. The rate of change in phase of the particle along the invariant I is denoted by G_I, where the invariant direction IC denotes the characteristic of the ion-cyclotron interactions. By limiting the allowed deviation of phase between AE and particle to 2π during a decorrelation time, the resonance surfaces are expanded into volumes and the resonance condition can be written as

$$\left| n\frac{\Delta\phi}{\tau_b} - \omega \pm j\frac{2\pi}{\tau_b} \right| \tau_d \leq 2\pi \tag{4}$$

Outside the resonance region the phase between the particle and AE varies rapidly, giving only a small contribution, which has been neglected here.

AEs which overlap along a characteristic in phase space will increase the extent of the region in which the modes redistribute the ions. An unstable distribution function in such a continous region in phase space will be flattened over a larger region and thus decrease its energy more than if the resonant regions were barely overlapping. A distribution function which is unstable along some part of the characteristic will during mode excitation be flattened and possibly build up an unstable distribution function in a neighbouring overlapping AE region, which in its turn grows up and flattens the distribution function and further redistribute the ions, leading to a cascade of AEs.

The transport of resonant particles caused by AE interactions inside the resonant regions lead to an energy transfer, ΔE_{AE} , to the mode according to

$$\Delta E_{AE} = \int\int \Delta E_r \mathbf{\Gamma}_{AE} \cdot \mathbf{ds} dt \propto \int A^2 dt \tag{5}$$

where $\Delta E_r(E, P_\phi, \Lambda, \sigma)$ is the extension in energy of the resonant region along a characteristic, $\mathbf{\Gamma}_{AE}$ is the flux of particles inside the resonant region caused by AE interactions and A is the mode amplitude. Since the change in particle energy is related to a change in toroidal angular momentum according to $\Delta P_\phi = \frac{n}{\omega}\Delta E$ the change in mode energy is thus proportional to $\int\int \Delta P_\phi \mathbf{\Gamma}_{AE} \cdot \mathbf{ds} dt$. For trapped particles, which in general are those responsible for destabilization of AEs, the change in P_ϕ is related to a radial displacement of the turning points $\Delta r = (\partial\Psi/\partial r)^{-1}\Delta P_\phi/eZ$. The radial redistribution of trapped particles depends on the width of the resonant region, which in its turn depends on the phase decorrelation caused by ICRH and Coulomb collisions and the flux of particles across the resonant region, which depends on the renewal rate of the distribution function caused by ICRH. As a trapped ion heated by ICRH enters the resonant region of the AE with an energy higher than the mean energy of the resonant part of the AE characteristic it will transfer energy to the mode and at the same time be displaced outwards, where it will leave the AE resonant region by ion-cyclotron interactions.

The evolution of the distribution function is calculated with a Monte Carlo method. The diffusion coefficients of AE interaction is obtained by integrating Eq. (1) for a set of mode numbers during a decorrelation time assuming the phase to be randomly distributed in the interval $[0, 2\pi]$. The resonance condition, Eq. (4), yields a set of resonant regions in phase space in which the

variation of the changes in energy, ΔE, due to interactions with the AE have a rather complex structure. The structure of the diffusion coefficient is determined by the structure, $\Phi(r, \theta)$, of the eigenmode.

3. Results

In the first scenario the dynamics of an unstable TAE during ICRH is studied for a JET-like H-minority heating scenario with $5\,\mathrm{MW}$ of ICRH power at $51\,\mathrm{MHz}$ with $+90^0$ phasing between the currents in the antenna straps in a plasma with circular cross-section, $r_0 = 0.9\,\mathrm{m}$, $R_0 = 2.97\,\mathrm{m}$, $n_H/n_D = 0.04$, $n_D = 2 \times 10^{19}\,\mathrm{m}^{-3}$, $Z_{eff} = 2.2$, $T_e(0) = T_D(0) = 10\,\mathrm{keV}$, $B_0 = 3.45\,\mathrm{T}$ and $I_p = 2.6\,\mathrm{MA}$. The steady state distribution function of H ions in the absence of TAEs is first computed. The effect of the renewal of the distribution function on the evolution of the mode amplitude of an unstable TAE, which is described by a simplified model [3], is shown in Fig. 1 and a close up of the initial stage in Fig. 2. The effect of the renewal of the distribution function by collisions and ICRH have been studied for three cases: in the absence of collisions and ICRH; in the absence of ICRH and including collisions; and including collisions and ICRH. To isolate the effect of the renewal rate from the effect of the change of the width of the resonant regions, which is determined by the diffusive contribution from collisions and ICRH according to Eqs. (3) and (4), the decorrelation time is determined by both collisions and ICRH in all three cases. The initial growth rates for the three cases are almost identical with $\gamma/\omega = 2.6\,\%$ where the mode frequency is $\omega = 1.45 \times 10^6\,\mathrm{s}^{-1}$. When the mode grows the distribution function in the high-energy regions in phase space is flattened along the TAE characteristics and at the same time reducing the drive. The interactions in the regions in phase space where the resonant ions have lower energy then become more important. If the local distribution function decreases with energy along the TAE characteristics, these interactions will then damp the mode on longer time scales. Whereas the calculation of the linear growth rate is rather straightforward, the damping of the mode is more difficult to estimate since it is subjected to both fluctuations, caused by statistical noise and chaotic behaviour of the non-linearity of the system. The intrinsic damping rate coming from ion Landau damping, essentially of high-energy ions, in the absence of collisions and ion-cyclotron interactions is estimated to be $\gamma_d/\omega \approx 1\,\%$. In the absence of mechanisms restoring the distribution function, such as collisions or ion-cyclotron interactions, the intrinsic damping will damp out the mode even in the absence of a background damping. The Coulomb collisions will still cause a flow of particles through the resonant regions, as discussed earlier, giving rise to new bursts as the distribution function is partially restored. The simulations demonstrate that the renewal rate of the distribution function and the start of the new burst are strongly affected by ICRH, but the initial growth rate is not significantly affected by Coulomb collisions or by ion-cyclotron interactions. When collisions are included we estimate the damping rate to be $\gamma_d/\omega = 1.4\,\%$ while collisions and ion-cyclotron interactions together yield an estimate of $\gamma_d/\omega = 0.5\,\%$.

As the particles are heated by ICRH and enter the resonant region they are, in general, displaced outwards with respect to the minor radius while transferring energy to the mode. This may lead to an oscillation of the mode amplitude; or rather bursts of TAE activity, since the flattening and renewal of the distribution function take place on different time scales. The initial condition for starting the TAE simulation with a preheated distribution function affects essentially only the first TAE burst. In the following bursts the distribution function is partially restored by collisions and ion-cyclotron interactions. The fact that the growth and damping of the TAE take place on the same time scale suggests that the unstable TAE takes off when the linear growth rate just exceeds the damping as assumed in the model by Berk *et al* [3].

The frequent bursts give rise to a frequency splitting of the Fourier decomposed time-dependent wave field as illustrated in Fig. 3. In the absence of ion-cyclotron interactions the

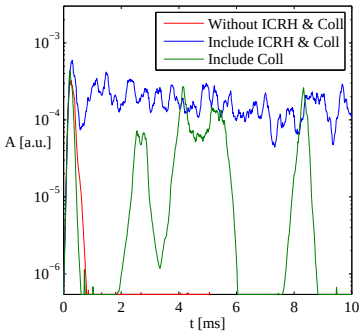

Fig. 1: *TAE amplitude with and without ICRH and collisional operators.*

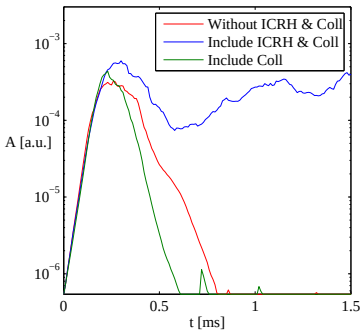

Fig. 2: *Initial stage of TAE amplitude with and without ICRH and collisional operators.*

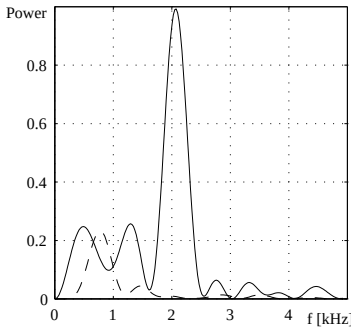

Fig. 3: *Fourier decomposition of mode amplitude. (—) ICRH and collisions, (- - -) collisions.*

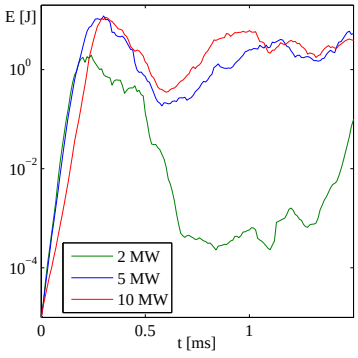

Fig. 4: *TAE amplitude for different ICRH powers.*

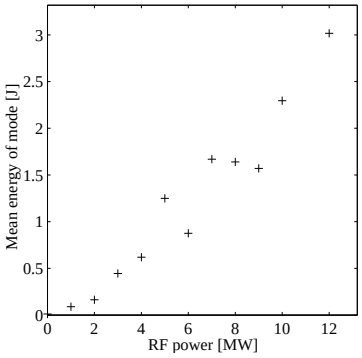

Fig. 5: *Time averaged mode energy versus ICRH power.*

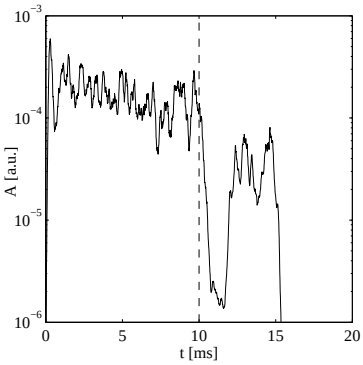

Fig. 6: *TAE amplitude when ICRH is turned off at* 10 ms.

typical period of the fluctuations of the mode amplitude is 1.5 ms, corresponding to $\Delta\omega = 2\pi \times 6.7 \times 10^2$ s^{-1}. When both ion-cyclotron interactions and Coulomb collisions are included the resulting period between the bursts decreases to 0.5 ms, corresponding to $\Delta\omega = 2\pi \times 2.0 \times 10^3$ s^{-1}.

The dynamics of the TAE activity is strongly affected by the strength of the ion-cyclotron interactions. This is clearly seen in Fig. 4, which illustrates the time variation of the mode amplitude for different ICRH powers. When the power rises from 2 to 5 MW there is a significant change in the repetition rate of the TAE bursts. As the power increases further from 5 to 10 MW it is not so much the frequency of the bursts that increases but rather the mode amplitude that stays at a higher level for a longer time.

To analyse how the spatial redistribution of the fast ions by a single TAE is affected by cyclotron interactions, we use the fact that the time-averaged redistribution of resonant ions by a TAE is in steady state related to the time-averaged mode energy, assuming that the damping of the mode by resonant ions and background damping is constant in time. To reduce the effect of the preheating and the associated growth of an initially unstable mode we average the mode energy from 1.5 to 10 ms. In Fig. 5 we have plotted the time-averaged mode energy versus ICRH power for simulations using the same initial distribution function obtained through 5 MW of heating.

To study the intrinsic damping by the resonant ions in the simulation with 5 MW of ICRH power the ICRH is turned off after 10 ms of TAE activity. The rapid decay of the mode amplitude is illustrated in Fig. 6 and the damping rate is estimated to $\gamma_d/\omega = 0.6$ %.

Interactions with several modes can be added straightforward in the Monte Carlo operators. However, analysis of the AE dynamics in presence of several modes become very difficult since the structure of the diffusion coefficient in phase space is very complicated and the location of

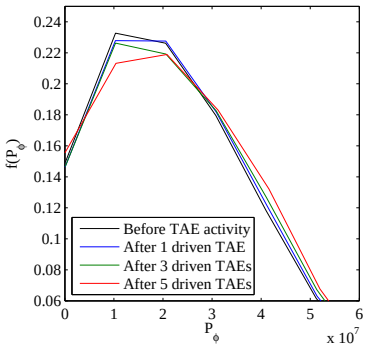

Fig. 7: *Change in P_ϕ-distribution of trapped particles above* 100 keV.

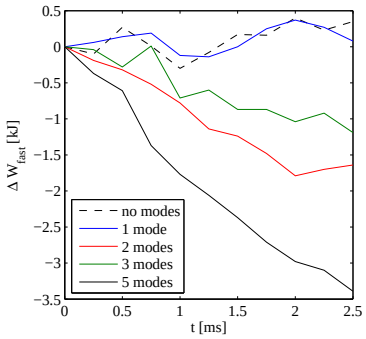

Fig. 8: *Change in fast particle energy content during TAE activity.*

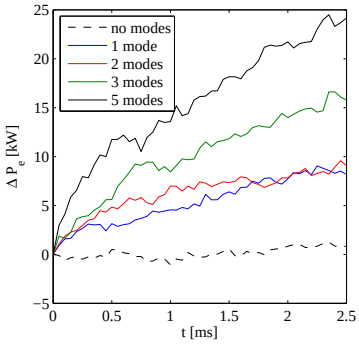

Fig. 9: *Change in power transer from ions to electrons during TAE activity.*

the resonant regions and their overlap is not known. To isolate the effect of the redistribution of resonant particles and how it effects the heating profiles the power transfer from ions to electrons has been studied using constant mode amplitudes. Several modes significantly increases the redistribution of fast particles towards higher P_ϕ. As P_ϕ increases the turning points of trapped particles are displaced outwards where the electron temperature is lower. The collision frequency, and hence the power transfer, between the high-energy ions and electrons depends on the electron temperature and density according to $\gamma_s \propto nT_e^{-3/2}$. The redistribution in P_ϕ of trapped particles above 100 keV is shown in Fig. 7 after 2.5 ms of mode activity with both one single mode, 3 modes and 5 modes. The change in fast particle energy content for different number of driven modes is shown in Fig. 8 and the case with no modes is simulated to determine noise level. As the orbits are displaced outwards by AE interactions the power transfer to the electrons increases as shown in Fig. 9. In the simulation with one single mode it is seen that even though the change in fast particle energy content and the redistribution in P_ϕ is small, the effect on the power transfer from ions to electrons is noticeable. As more modes are added it is clear that the effect on both fast particle energy content and redistribution in P_ϕ is increasing. In Fig. 10, the sum of the fraction of resonant particles in each separate mode and the total fraction of resonant particles is plotted. The fraction of particles resonating with more than one mode increases as more modes are added indicating an increased overlap in phase space.

From Fig. 9 it is not possible to determine if the increased power transfer is a sum of the contributions from each mode or if overlap between modes has a stronger effect. To study the effect of the increased overlap caused by an increase in ICRH power the case with three driven modes is studied. An increase in the overlapping regions can be seen in Fig. 11 where the fraction of particles resonating with more than one mode increases as the ICRH power is increased. In Fig. 12 it is shown how the power transfer from ions to electrons is altered by an increase in ICRH power. As the ICRH power is increased the overlap increases, the redistribution takes place over a larger region in phase space and the restoration of the distribution function is faster. With driven modes with constant amplitude it is seen in Fig. 12 that the redistribution of the distribution function reaches a steady state after about 3 ms and that the increased restoration rate has a stronger effect than the increased overlap and increased redistribution.

4. Conclusions

A model allowing self-consistent studies of the effects of decorrelations by ICRH and Coulomb collisions of ions interacting with AEs has been developed and implemented in the SELFO code taking into account the complex structure of the resonant regions in phase space [8]. The variation of the distribution function in phase space produces regions with destabilizing and

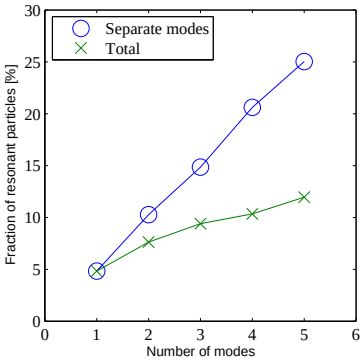

Fig. 10: *Fraction of resonant particles as a function of number of modes with 5MW ICRH power.*

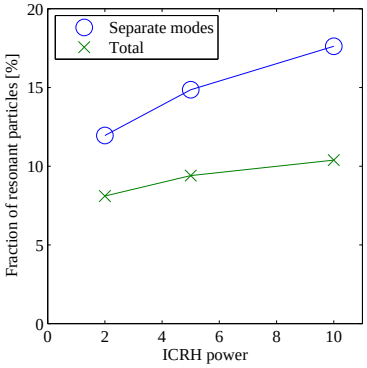

Fig. 11: *Fraction of resonant particles for 3 TAEs as a function of ICRH power.*

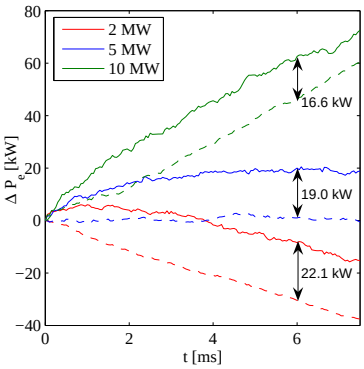

Fig. 12: *Change in power transer from ions to electrons. (—) with 3 TAEs, (- - -) without TAEs.*

stabilizing AEs. A typical intrinsic damping rate of about $1\ \mathrm{ms}$ is found, comparable with the damping by resistivity and ELD, and the growth rate of the AEs. The decorrelation of fast ions and the renewal of the distribution function by ion-cyclotron interactions have a strong effect on the dynamics of the modes and the redistribution of resonant ions. The typical oscillation period, which is of the order $1\ \mathrm{ms}$, of the mode amplitude is seen to decrease with increasing decorrelation by ion-cyclotron interactions, which is in agreement with experimental observations [2, 9, 10] and numerical simulations. The fast decay of the TAE-mode, which is observed in experiments when the ICRH is turned off, is also reproduced in the simulations.

One single driven TAE with constant amplitude have a small effect on the fast particle energy content and the redistribution in toroidal angular momentum. Several TAEs however have a significant effect on the radial redistribution and the associated loss in power from high-energy ions to electrons. There are three effects associated with an increased ICRH power: increase of resonant regions in phase space; increased overlap of resonant regions; faster restoration of the distribution function. Which of these effects is the dominant depends on where in phase space the resonant regions are located and the distribution function within these regions.

References

[1] WONG, K.L., et al., Phys. Plasmas **4** (1997) 393
[2] FASOLI, A., et al., Phys. Rev. Lett. **81** (1998) 5564
[3] BERK, H.L., BREIZMAN, B.N., PEKKER, M.S., Nucl. Fusion **35** (1995) 1713
[4] BERK, H.L., BREIZMAN, B.N., PEKKER, M.S., Phys. Rev. Lett. **76** (1996) 1256
[5] HEDIN, J., HELLSTEN, T., CARLSSON, J., Proc. Joint Varenna-Lausanne Workshup on Theory of Fusion Plasmas 1998 p467 ISBN 88-7794-146-7
[6] BERGKVIST, T., HELLSTEN, T., Nucl. Fusion **45** (2005) 485
[7] BERK, H.L., BREIZMAN, B.N., YE, H., Phys. Fluids B **5** (1993) 1506
[8] BERGKVIST, T., HELLSTEN, T., Proc. Joint Varenna-Lausanne Workshup on Theory of Fusion Plasmas 2004 p123 ISBN 88-7438-020-8
[9] FASOLI, A., et al., Plasma Phys. Control. Fusion **39** (1997) B287
[10] WONG, K., Plasma Phys. Control. Fusion **41** (1999) R1

Analysis of the supra-thermal electrons during disruption instability in the T-10 tokamak

P.V.Savrukhin, A.V.Sushkov

Russian Research Center ‘‘Kurchatov Institute,’’ 123182, Moscow, Russia

Generation of electron beams with nonthermal energies (E_γ *~100keV*) is one of the common feature of disruption instability in tokamaks [1,2]. Resent experiments in T-10 tokamak have indicated that the beams are often characterised by narrow localisation around magnetic surfaces with rational values of the safety factor (*q=1,2*). Such localisation of the beams can be connected with strong electric fields induced due to reconnection of the magnetic field lines during growth of the large-scale MHD perturbations (see [3]). Analysis [4] indicated, that while density of the nonthermal electrons induced during magnetic reconnection is two orders of magnitude smaller than the equilibrium plasma density, they can substitute considerable fraction of the plasma current around the rational *q* surfaces and can lead to growth of the runaway avalanches during major disruption. Present paper represents analysis of spatial localisation and temporal evolution of x-ray burst connected with the electron beams during density limit disruption and evaluate role of the primary electron beams in intensive hard x-ray spikes in post-disruptive plasma in the T-10 tokamak. The x-ray intensity is identified using standard *Si* detectors array and gas detectors with orthogonal view of the plasma column and in-vessel CdTe detectors with tangential view of the plasma column [5].

The x-ray bursts connected with the non-thermal electrons are observed most clearly in T-10 plasma, as well as in experiments in other tokamaks (see Ref. 1,2), during energy quench at the density limit disruption. Typical evolution of x-ray emissivity is shown in the case in Fig.1. Unstable plasma configuration with large-scale *m=1,n=1* and *m=2,n=1* modes is formed in the case after additional gas puffing at the quasi-stationary stage of the discharge (t>700ms). Energy quench observed at t=750.7ms (see Fig.1) is accompanied with intensive bursts of the x-ray emission. Energy quench leads to cooling down of the bulk plasma, increase of the total radiated power, and strong influx of impurities due to enhanced plasma-wall interaction. This follows by considerable increase of the loop voltage and production of beams of the runaway electrons, which eventually hit the plasma facing components (see “secondary” x-ray bursts at t=756ms in Fig.1).

Relatively small size of the bright spots observed at the initial stage of the disruption (see t=750.7ms in Fig.1) can indicate indirectly narrow localisation of the non-thermal electrons inside a specific area of the plasma cross section (see also [2]). The bright spots are typically observed when maximum x-ray perturbations (associated with position of the X-point of the m=2 magnetic island) are placed in field of view of the detectors. Appearance of the bursts at specific angular position of the MHD perturbations can indicate indirectly connection of the bursts with the m=2 magnetic island.

While typically observed at the initial stage of an energy quench, the x-ray bursts are also often observed prior to the disruption. The non-thermal x-ray bursts have maximum amplitude at the growing phase and at the top of the m=2,n=1 mode (see Fig.2). Amplitude of x-ray intensity during a single burst can be modulated in the case with repetition rate of order of 10-30 kHz (see [4]).

The burst are also observed in plasma after an energy quench at the density limit disruption. Time evolution of the plasma parameters is shown in the case in Fig. 3. Energy quench (appeared in the case in series of two minor disruptions at $t = 811.5$ *ms* and $t = 824.0$ *ms*) is followed by intensive x-ray spikes observed with the TX array (see, *txray2* at t>~ 824 *ms* in Fig. 3). The spikes are generally observed as non-regular perturbation of the x-ray emissivity, while sometimes oscillations with typical repetition rates of order of $\gamma \sim 0.2\ ms^{-1}$, $3\ ms^{-1}$, and $30 - 40\ ms^{-1}$ can be identified in the signals (see Fig. 3). The repetition rate is close to one of the bursts observed prior the disruption in similar plasma conditions. The spikes represented in Fig. 3 are generally not observed with the orthogonal view x-ray array (*xcdtea2*) and gas detector (*xwda35*). This can indicate, indirectly, that spikes can appear as a result of forward bremsstrahlung radiation produced by nonthermal electrons “in flight” interacting with the residual plasma. Limited observation of the x-ray radiation during the “internal” spikes is in sharp contrast with hard x-ray bursts due to loss of the runaway electrons onto the vessel wall observed with all x-ray detectors.

Possible connection of the x-ray bursts with the electron beams accelerated in longitudinal equilibrium electric field can be checked in experiments with additional current ramp up just prior a disruption at high density (see Fig. 4). Growth of the plasma current is accompanied in the case by considerable increase of the longitudinal electric field at the outer part of the plasma. (Loop voltage is increased from quasi-stationary value $U_l \sim 1.5\ V$ up to $U_l \sim 16\ V$ just prior the energy quench and further up to $U_l \sim 70\ V$ during disruption. It should be pointed out that power supply system used in T-10 for control of plasma current is capable to provide increase of the loop voltage even after the energy quench.) The process should be

accompanied by amplification of runaways electron beams with possible subsequent increase of the x-ray bursts amplitude. Growth of the x-ray intensity is in fact observed during secondary bursts after the energy quench in comparison with discharges with no current ramp-up [see *t > 822.6 ms*, in Fig. 4 and *t > 824 ms* in Fig. 3]. However, no considerable difference in amplitude of the x-ray perturbation prior the energy quench is observed in the experiments (see *t < 807.8 ms* in Fig. 4 and *t < 811.9 ms* in Fig. 3). While present experiments can not provide detailed information for qualitative comparison of the runaway electrons acceleration in both cases, it seems that increased loop voltage during current ramp-up (in the analysed U_l - range) does not change considerably initial stage of the disruption.

Further studies of the phenomena are planned in the T-10 tokamak using in-vessel array with adjustable field of view of the CdTe detectors.

The work is supported by Russian Fund for Basic Research (Grant 05-02-17294).

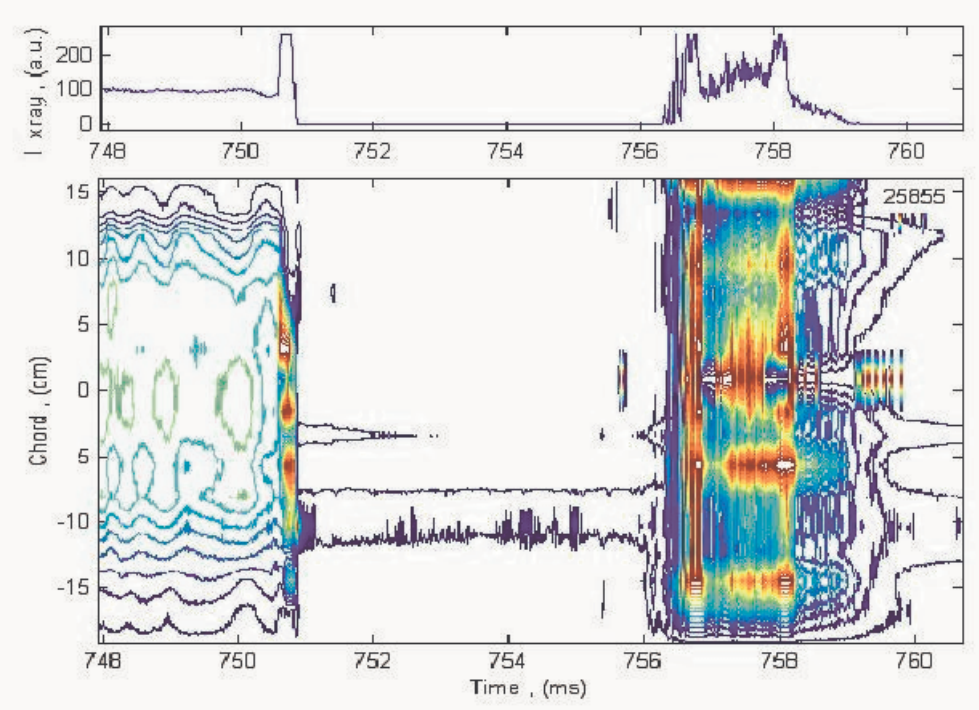

Fig.1. Time evolution of the x-ray intensity and x-ray contour plot measured during density limit disruption with the use of array of Si detectors with orthogonal view of the plasma column.

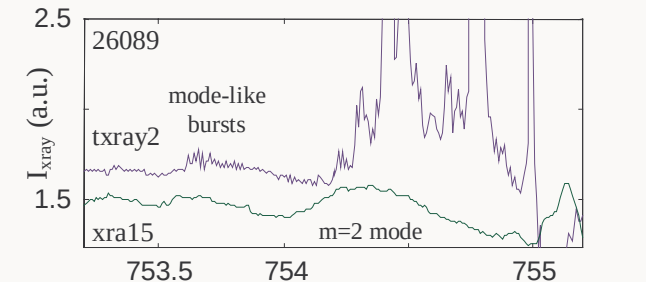

Fig.2. Time evolution of the x-ray intensity measured with the tangential (txray2) and orthogonal view (xra15) x-ray detectors just prior to the density limit disruption.

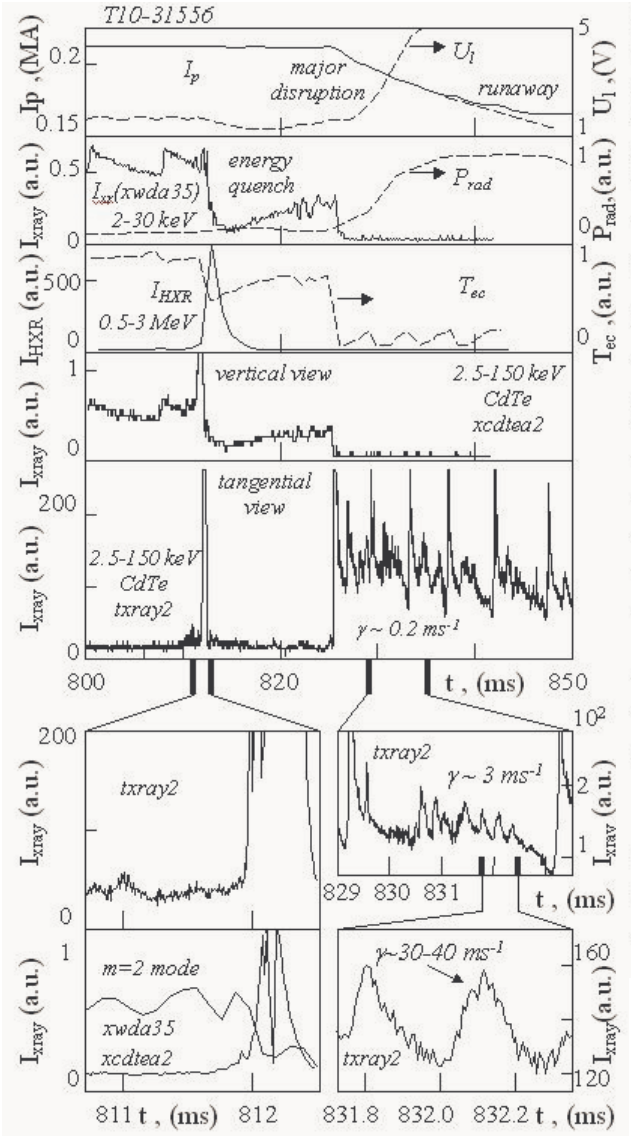

FIG. 3. Time evolution of plasma parameters after an energy quench during density limit disruption in ohmically heated plasma. Here, I_p is plasma current, U_l loop voltage, P_{rad} total radiated power, T_{ec} electron (ECE) temperature, I_{HXR} hard x-ray intensity, I_x(xwda35) x-ray intensity measured using XWDA gas detector. Also shown, intensity of the x-ray radiation measured using CdTe detectors with orthogonal (xcdtea2) and tangential (txray2) view of the plasma column.

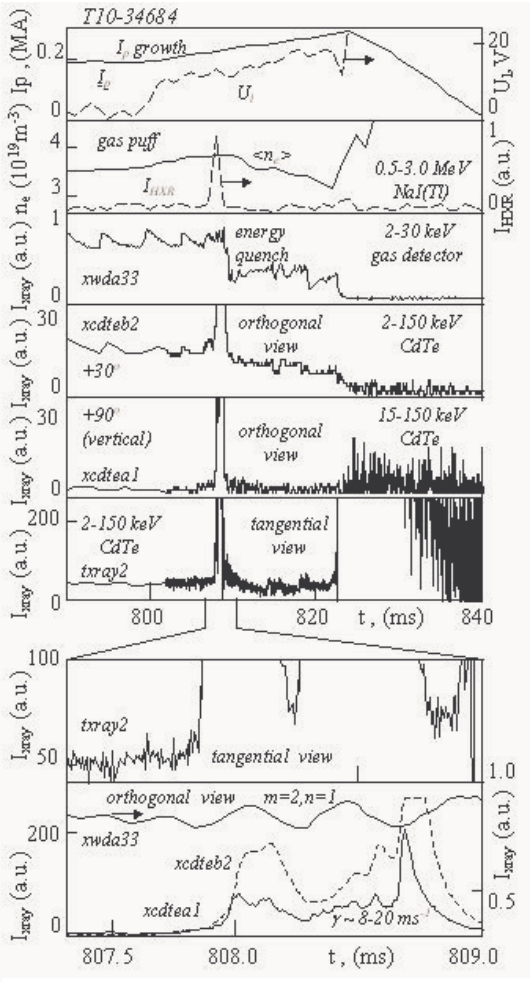

FIG. 4. Time evolution of plasma parameters in experiments with ramp-up of plasma current, I_p, just prior the density limit disruption. Here, U_l is loop voltage, $<n_e>$ line averaged electron density, I_{HXR} hard x-ray intensity, I_{xray}(xwda33) x-ray intensity measured using XWDA gas detector. Also shown, intensity of the x-ray radiation measured using CdTe detectors with orthogonal (xcdtea1, xcdteb2) and tangential (txray2) view of the plasma column.

[1] ITER Physics Expert Group on Disruptions, Plasma Control, and MHD, ITER Physics Basis Editors, Nucl. Fusion **39**, 2251 (1999).
[2] Gill, R. D., Alper, B., Edwards, A. W., *et al.*, Nucl. Fusion **40** (2000) 163.
[3] Frank, A. G., Plasma Phys. Controlled Fusion **41** (1999) A687.
[4] Savrukhin, P. V., Physics of Plasmas **9** (2002) 3421.
[5] Savrukhin, P. V., Rev. Sci. Instrum. **73** (2002) 4243.

IT10

This paper will be published as a cluster paper in a special issue of Nuclear Fusion journal.

On Ion Cyclotron Current Drive for Sawtooth control

L.-G. Eriksson[1], T. Johnson[2], M.L. Mayoral[2], R.J. Buttery[2], S. Coda[3], D. McDonald[2], T. Hellsten[4], M.J. Mantsinen[5], A. Mueck[6], J.-M. Noterdaeme[6,7], O. Sauter[3], P. de Vries[2], E. Westerhof[9] and JET-EFDA contributors*

[1]Association EURATOM-CEA, CEA/DSM/DRFC, CEA-Cadarache, F-13108 St. Paul lez Durance, France
[2]UKAEA/Euratom Fusion Association, Culham, Science Centre, Abingdon, United Kingdom
[3]EURATOM Confédération Suisse, CRPP-EPFL, Lausanne, Switzerland
[4]Euratom-VR Association, Stockholm, Sweden
[5]Helsinki University of Technology, Association Euratom-Tekes, Finland
[6]Max-Planck IPP-EURATOM Assoziation, Garching, Germany
[8]Gent University, Department EESA, Belgium
[9]FOM-Rijnhuizen, Ass. EURATOM-FOM, TEC, Nieuwegein, The Netherlands
* See the Appendix of J.Pamela et al., Fusion Energy 2004 (Proc. 20th Int. Conf. Vilamoura, 2004) IAEA, Vienna (2004)

In a reactor based on the tokamak concept, it could be important to have a capability to control the sawtooth activity. For instance, there is evidence that crashes of fast ion induced long sawteeth can trigger neoclassical tearing modes (NTMs). In view of the strong presence of fast alpha particles in a reactor, it is likely that they will influence the length of the sawtooth period, i.e. induce long sawtooth free periods. Consequently it is of interest to control the sawtooth behaviour and try to avoid long sawtooth free periods. One possibility is to perturb the current profile near the q = 1 surface. Several methods could be used for this purpose, e.g. Electron Cyclotron Current Drive (ECCD) and Ion Cyclotron Current Drive (ICCD). The principle behind ICCD is to use directed waves in the Ion Cyclotron Range of Frequencies (ICRF) and place a cyclotron resonance of an ion species (normally a minority species) near the q = 1 surface. The fast resonating ions will then drive a bi-polar current, which can increase the shear at the q = 1 surface and thereby shorten the sawtooth period. Experiments with ICCD on JET have, for the first time, demonstrated that fast ion induced long sawteeth can be shortened by the application of ICCD (previously only normal sawteeth had been influenced). In order to improve the understanding of the ICCD mechanism for sawtooth control, which could be relevant for ITER, a number of experiments were carried out at JET. These included a scan of the concentration of resonating minority ions and a change of the spectrum of the launched waves. Results of these experiments are presented together with a theoretical discussion of the main features observed.

IT11

This paper will be published as a cluster paper in a special issue of Nuclear Fusion journal.

Overview of fast ion driven MHD in NSTX

E.D. Fredrickson, D. Darrow, S. Medley, J. Menard, H. Park, L. Roquemore,
Princeton Plasma Physics Laboratory, Princeton, NJ
D. Stutman, K. Tritz, *Johns Hopkins University, MD,*
S. Kubota, *University of California, Los Angelos, CA.*
K.C. Lee, *University of California, Davis, CA*

A wide variety of fast ion driven instabilities are excited during neutral beam injection (NBI) in the National Spherical Torus Experiment (NSTX) by the large ratio of fast ion velocity to Alfvén velocity, $V_{fast}/V_{Alfvén}$, together with the relatively high fast ion beta. The modes can be divided into three categories; chirping Energetic Particle Modes (EPM) in the frequency range 0 to 120 kHz, the Toroidal Alfvén Eigenmodes (TAE) with a frequency range of 50 kHz to 200 kHz and the Compressional and Global Alfvén Eigenmodes (CAE and GAE, respectively) between 300 kHz and the ion cyclotron frequency. Calculated fast ion distributions find a bump-on-tail in the perpendicular energy direction that satisfies the Doppler-shifted ion cyclotron resonance believed to excite the CAE. The same resonance is believed to drive the GAE, and is found to support behavior similar to "hole-clump pairs" under special circumstances. The internal amplitude, and to a lesser extent the spatial structure, of the TAE, CAE, GAE and EPMs has been measured with Heterodyne reflectometry in L-mode plasmas. Soft x-ray cameras provide more detailed information on the structure of the lower frequency EPMs. The TAE bursts have internal amplitudes of up to $\tilde{n}/n \approx 1\%$ and toroidal mode numbers $2 \leq n \leq 6$. The EPMs are core localized, kink-like modes similar to the fishbones in conventional aspect ratio tokamaks. Unlike the fishbones, the EPMs can be present with $q(0) > 1$ and can have a toroidal mode number $n > 1$. The range of the frequency chirp can be quite large and the resonance can be through the fishbone-like precessional drift resonance, or through a bounce resonance. Fast ion driven modes are of particular interest because of their potential to cause substantial fast ion losses. In all regimes of NSTX NBI heated operation we see transient neutron rate drops, correlated with bursts of TAE or fishbone-like EPMs. The CAE and GAE may also affect fast ion confinement, but there is little direct evidence for direct fast ion losses caused by these instabilities. The fast ion loss events are predominantly correlated with the EPMs, although losses are also seen with bursts of multiple, large amplitude TAE. The latter is of particular significance, because the transport of fast ions from the expected resonance overlap in phase space will reveal a "sea of Alfvén modes" kind of physics similar to that expected in ITER.

*This work supported by U.S. DoE Contract DE-AC02-76CH03073.

IT12

This paper will be published as a cluster paper in a special issue of Nuclear Fusion journal.

Perturbative versus non-perturbative modes in Spherical Tokamaks

M.P. Gryaznevich[1], S.E. Sharapov[1], and the MAST Team[1],
H.L. Berk[2], S.D. Pinches[3], RG.L. Vann[4].
[1]*Euratom/UKAEA Fusion Association, Culham Science Centre, Abingdon, UK*
[2]*Institute for Fusion Studies, University of Texas at Austin, Austin, Texas, USA*
[3]*Max-Plank Institute for Plasmaphysics, Euratom Association, Garching, Germany*
[4]*Department of Physics, University of Warwick, Coventry,UK*

The physics of highly energetic ions in tokamaks and their associated instabilities is one of the most important issues for the fusion programme. Such instabilities are often excited by fast super-Alfvénic ions produced by neutral beam injection in plasmas of the spherical tokamaks START and MAST. These instabilities are seen as discrete weakly-damped toroidal and elliptical Alfvén eigenmodes (TAEs and EAEs) with frequencies tracing in time the Alfven scaling with the equilibrium magnetic field and density, or as energetic particle modes (EPMs) whose frequencies sweep down in time faster than the equilibrium parameters change. It is important to distinguish EPMs of two types: linear EPMs [1], the frequencies of which don't start from the TAE-frequency, and non-linear EPMs [2,3], the mode frequencies of which start from the TAE-frequency, but deviate significantly from the TAE-frequency during non-linear mode evolution, when BGK-type non-linear modes are formed.

Recent progress in the diagnosis of AE and EPM in tokamaks, including passive and active MHD spectroscopy, reflectometry and visualisation techniques have opened new opportunities for the detection of Alfvén instabilities. It is now very important to be able to classify them, in particular, to specify which modes could be potentially dangerous and important for plasma performance and tokamak operation in present and future devices.

Perturbative modes in STs have been studied intensively recently, both theoretically and experimentally [4]. These modes are widely used for diagnostics purposes and new diagnostics opportunities will be discussed. In some discharges, NBI excites modes that start from the TAE frequency range and sweep both up and down. These modes are interpreted as 'hole-clump' nonlinear fluctuations of the fast ion distribution function first found in [2]. Modelling of the up-down sweeping modes on MAST with the particle-following HAGIS code [3] is discussed.

Recent progress in the modelling allows detailed investigation of non-perturbative modes, which play an important role in plasma performance. We are now able to distinguish and classify these modes both from their starting frequency and frequency evolution. They are characterised by the linear sweep in frequency and may start outside the main TAE gap.

Analysis of the experimental data from MAST and START indicates that the Alfvén instabilities weaken in both the mode amplitude and in the number of unstable modes as the pressure of the thermal plasma increases. Interpretation of this data is given in terms of increased thermal ion Landau damping and the high-pressure effect on TAE existence. The effect of plasma pressure on AEs now found to play an important role on STs was considered for conventional aspect ratio tokamaks in [5], and observed on TFTR and JET [6].

This work was funded jointly by the UK EPSRC and by the European Communities under the contract of Association between EURATOM and UKAEA. The views and opinions expressed herein do not necessarily reflect those of the European Commission

[1] F Zonca, L Chen, Phys. Plasmas 3 (1996) 323;
[2] H.L.Berk, B.N.Breizman, N.V.Petviashvili, Phys. Lett. **A238** (1998) 408
[3] S.D.Pinches, H.L.Berk, M.P.Gryaznevich, S.E.Sharapov, PPCF **46** (2004) S47
[4] M.P.Gryaznevich and S.E.Sharapov, Nuclear Fusion **40** (2000) 907; M.P.Gryaznevich and S.E.Sharapov, Plasma Physics Controlled Fusion **46** (2004) S15
[5] L.Chen, in Theory of Fusion Plasmas (Proc. Joint Varenna-Lausanne Int. Workshop 1988), Editrice Compositori, Bologna (1988) 327
[6] G.Y.Fu, Phys. Plasmas, v.2 (1995) 1029; H.L.Berk et al., Phys. Plasmas, v.2 (1995) 3401; S.E.Sharapov et al., Nuclear Fusion, v.39 (1999) 373

IT13

This paper will be published as a cluster paper in a special issue of Nuclear Fusion journal.

Discrete Compressional Alfven Eigenmode Spectrum in tokamaks

N.N. Gorelenkov, E. Fredrickson, W.W. Heidbrink[♭]

Princeton Plasma Physics Laboratory

[♭]*University of California, Irvine, California and*

e-mail: ngorelen@pppl.gov

Sub-cyclotron frequency instabilities of Compressional Alfvén Eigenmodes (CAE) have been observed in the similarity experiments on National Spherical Torus (NSTX) and DIII-D [W.W. Heidbrink, et.al. submitted to Nuclear Fusion]. Theoretical analysis of these instabilities predicts their localization in poloidal (at the low field side) and radial (toward the plasma edge) directions [N.N. Gorelenkov, et.al., Nucl. Fusion, **42** 977 (2002)]. In this work we apply a numerical ideal MHD code NOVA to study CAE properties in similarity experiments on NSTX and DIII-D. NOVA is applied using the numerical equilibrium and is able to recover main properties of these modes predicted by the theory. Among those are the discrete spectrum of CAEs, which are characterized by three quantum numbers (M, n, s), where M, n, and s are poloidal, toroidal, and radial mode numbers, respectively. In the example shown in the figure for DIII-D shot $\#122806$, we present one CAE mode structure, its magnetic field in the poloidal cross section, and the discrete spectrum versus M, for two branches $(M, 0, 1/2)$ and $(M, 0, 1)$. For better numerical convergence and to avoid interaction with the continuum, only $n = 0$ modes were analyzed. In the analyzed case of DIII-D plasma it was found that the observed mode frequency splitting between s and $s + 1$ branches is similar to the one numerically obtained. Poloidal mode number splitting, i.e. between M and $M + 1$ modes, is larger by a factor of two, which is possibly due to neglecting the Hall term. Obtained modes are used for the numerical stability analysis with the NOVA-K kinetic code. CAE properties and their implications are discussed.

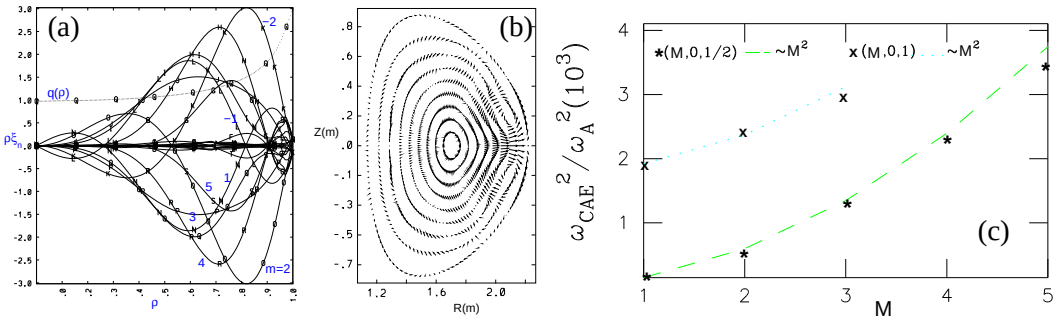

Figure 1: *Normal to the surface component of the plasma displacement of (4,0,1/2) CAE poloidal harmonics, m, is shown in Figure (a). Perpendicular magnetic field of CAE in the tokamak cross section is shown in Figure (b). CAEs discrete spectrum for (M,0,1/2) and (M,0,1) modes is shown versus the poloidal mode number. Here frequencies are normalized to $\omega_A = v_{A0}/Rq_{edge}$, so that $\omega_A/2\pi = 36.64kHz$.*

IT14

Gamma-Ray Measurements of Fast Alpha Particles

V. G. Kiptily and JET EFDA contributors *

Euratom/UKAEA Fusion Association, Culham Science Centre, Abingdon, Oxon, UK
vkip@jet.uk * *See the Appendix of J.Pamela et al., Fusion Energy 2004 (Proc. 20th Int. Conf. Vilamoura, 2004) IAEA, Vienna (2004)*

An overview of γ-ray diagnostic observations of fast α-particles and ^{4}He-ions in JET is presented and capabilities of this diagnostics in ITER are discussed. The talk will cover the following points: 1). An introduction to the physics of the used α-particle diagnosis, which based on measurements of the γ-ray emission from the ^{9}Be(α,nγ)^{12}C nuclear reaction. 2). A description of the experimental equipment used for the measurements, in particularly, γ-ray spectrometers and 2-D γ-cameras. 3). First measurements of γ-ray spectra from nuclear reactions between fusion-born α particles and Be impurities, which were done in JET D-majority plasmas just after short blips of T-NBI. In the performed experiments the time dependence of the measured spectra allowed the determination of the density evolution of alphas, and in this way a correlation between the γ-ray emission decay and plasma parameters in different plasma scenarios was established. 4). Results of the γ-ray measurements of fast ^{4}*He* and *D* -ions accelerated with 3^d-harmonic ion-cyclotron-resonance heating of ^{4}*He*-beam [2]. Gamma-ray images of fast ^{4}*He* and *D*-ions and evolution of the γ-ray emission were simultaneously recorded for the first time in JET experiments [3] dedicated to the investigation of burning-like plasmas with 3.5-MeV fusion α-particles. 5). An application of this technique for ITER. Simultaneous measurements of several fast-ion species are paramount for the burning plasma in ITER. At least two types of fast ions are expected in the ITER plasma: 1-MeV deuterons from NBI heating and fusion α-particles. A principal diagnostic problem in ITER will be discriminating the NBI deuterium from the fusion α-particles. The similar measurements with 2-D γ-cameras could be used in ITER, but the γ-ray detector array should be protected against severe neutron emission with special neutron filters [4]. Simultaneous measurements of the NBI power deposition and evolution of the α-particle density profiles are very important for optimisation of different plasma scenarios and understanding of the α-particle confinement effects.

[1] Kiptily *et al* 2004 *Phys. Rev. Lett.* **93** 115001; [2] Mantsinen *et al* 2002 *Phys. Rev. Lett.* **88** 105002;
[3] Kiptily *et al* 2005 *Nucl. Fusion* **45** L21; [4] Kiptily *et al* 1998 *Tech. Physics* **43** 471

This work was funded jointly by the UK EPSRC and by the European Communities under the contract of Association between EURATOM and UKAEA. The views and opinions expressed herein do not necessarily reflect those of the European Commission. This work was carried out within the EFDA framework.

D-Alpha Measurements of the Fast-ion Distribution Function in DIII-D*

W.W. Heidbrink (wwheidbr@uci.edu), Y. Luo,
University of California, Irvine
K.H. Burrell and the DIII-D Team
General Atomics

Hydrogenic fast-ion populations are common in toroidal magnetic fusion devices, especially in devices with neutral beam injection. As the fast ions orbit around the device and pass through a neutral beam, some fast ions neutralize and emit Balmer-alpha light. The intensity of this emission is weak compared to the signals from the injected neutrals, the warm (halo) neutrals, and the cold edge neutrals but, for a favorable viewing geometry, the emission is detectable. The intrinsic spatial resolution of the technique is ~5 cm for 40 keV/amu fast ions; the energy resolution is ~10 keV. In DIII-D experiments, we have measured the fast-ion velocity distribution and spatial profile under a wide variety of operating conditions. The technique is best suited for measurements of ~ 40 keV/amu hydrogenic fast ions but useful information on the confinement of 1000 keV deuterium beam ions in ITER may be obtainable.

Diagnosis of the fast-ion population is important because the fast ions are often a major source of energy, momentum, and particles for the plasma. Moreover, the fast-ion pressure and driven current can have a significant impact on macroscopic stability properties. Although dilute populations of fast ions often behave classically, intense populations can drive instabilities that redistribute or expel the fast ions from the plasma. This is often the case in experiments in the DIII-D tokamak, where anomalous fast-ion diffusion rates of approximately 0.5~m^2/s are commonly inferred during neutral beam injection [1]. In DIII-D, it is difficult or expensive to detect diffusion at this level using standard techniques [2].

Excited states of atomic hydrogen radiate the Lyman and Balmer series of spectral lines. The most familiar of these are the Lyman alpha line, which is a transition from the n=2 to n=1 energy level, and the Balmer alpha line, which is the 3→2 transition. Because Lyman alpha is in the ultraviolet, it is relatively difficult to measure but the Balmer-alpha transition emits a visible photon, which is easily measured with standard lenses, spectrometers, and cameras. Light from this transition is commonly called H-alpha or D-alpha.

Conceptually, the use of D-alpha light to diagnose a fast deuterium population is similar to the diagnosis of fast helium populations using charge exchange recombination spectroscopy [3]. Fast helium populations during ^{3}He neutral beam injection were measured on JET [4]. Alpha particles produced in deuterium-tritium reactions were measured on TFTR [5]. For spectroscopic measurements of either fast helium ions or fast hydrogenic ions, avoiding the bright emission from other sources is a major challenge. There are several populations of hydrogenic neutrals in a typical tokamak plasma: cold edge neutrals, injected neutrals, and thermal (halo) neutrals created when the injected neutrals undergo a charge-exchange reaction. Fortunately, for a judicious choice of viewing angle, the light from fast ions is Doppler shifted away from the bright light produced by the other neutral populations.

A paper that explains the diagnostic concept and presents the first observation of signals from fast ions was already published [6]. This paper also discusses several possible applications of the technique. After the first successful measurements using the existing charge-exchange recombination (CER) diagnostic, a dedicated instrument was assembled for this application;

* Supported by U.S. DOE subcontract SC-G903402 and DE-FC02-04ER54698.

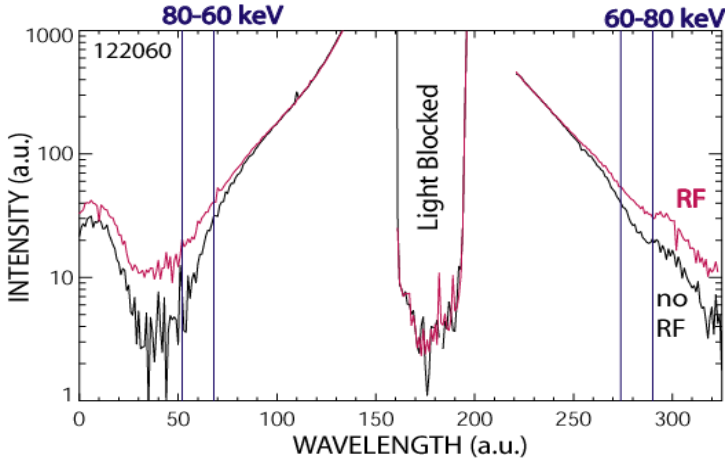

Figure 1. Spectra measured with and without 60 MHz, 4th harmonic ion cyclotron heating. Wavelengths that correspond to a perpendicular energy of 60 & 80 keV are marked.

an instruments paper [7] describes the design of this instrument. Data from this instrument and from spare CER channels were obtained during the 2005 experimental campaign. A wide variety of plasma conditions were diagnosed. Care is required to obtain fast-ion spectra that are free from pollution by halo neutrals, impurity line radiation, bremsstrahlung, and sudden changes in background light associated with ELMs. The data indicate that the achieved resolution was ~10 keV for energy, at least 10~cm spatially, and ~ 5 ms temporally. Figure 1 shows detection of fast ions that are accelerated above the injection energy (80 keV) during ion cyclotron heating experiments. Fast-wave heating at the fourth, fifth, and sixth harmonics accelerate fast ions above the injection energy; the profile data show that the acceleration is greatest near the cyclotron harmonic resonance layer. Pitch-angle scattering and slowing down of beam ions are studied by varying the injection energy, beam angle, plasma density, and electron temperature in MHD-quiescent plasmas. Comparison with neutral particle measurements indicate that neutral-particle diagnostics are much more sensitive to pitch-angle scattering than the D-alpha measurements. In plasmas with instabilities, the spatial profile is often flatter than classically predicted. The spatial profiles in plasmas with internal transport barriers, with helical magnetic perturbations from a nonaxisymmetric coil, and with cascade, toroidicity-induced, and compressional Alfven eigenmode activity are also measured. The 2005 physics results will be published in papers by Luo and Heidbrink.

References

[1] HEIDBRINK, W.W., et al., Nucl. Fusion **42** (2002) 972.
[2] HEIDBRINK, W.W., et al., Rev. Sci. Instrum. **74** (2003) 1743.
[3] POST, D.E., et al., J. Fusion Energy **1** (1981) 129.
[4] VON HELLERMANN, M.G., et al., Plasma Phys. Cont. Fusion **35** (1993) 799; GERSTEL, U., et al., Plasma Phys. Cont. Fusion **39** (1997) 737.
[5] MCKEE, G., et al., Phys. Rev. Lett. **75** (1995) 649.
[6] HEIDBRINK, W.W., et al., Plasma Phys. Cont. Fusion **46** (2004) 1855.
[7] LUO, Y., et al., Rev. Sci. Instrum. **75** (2004) 3468.

IT16

9th IAEA Technical Meeting on
Energetic Particles in Magnetic Confinement Systems
November 9–11, 2005, Takayama, Japan

Integrated Analysis of Alfvén Eigenmode in Toroidal Plasmas

A. Fukuyama and A. Sonoda
Department of Nuclear Engineering, Kyoto University, Kyoto 606-8501, Japan
fukuyama@nucleng.kyoto-u.ac.jp

The linear stability of Alfvén eigenmodes (AE) is numerically studied for various configurations in toroidal plasmas. We use the three-dimension full wave code (TASK/WM) which solves Maxwell's equation with a kinetic dielectric tensor in a magnetic flux coordinates as a boundary value problem and obtain the spatial structure of an Alfvén eigenmode with a complex eigen frequency. The TASK/WM code is now included as a module in the integrated simulation code system, TASK. We may employ spatial profiles predicted by the transport module or obtained from the ITPA profile database. We may also make use of the velocity distribution function of energetic ions computed by the three-dimensional bounce-averaged Fokker-Planck module. The distribution function is numerically integrated to give the kinetic dielectric tensor.

We consider three cases: (1) $Q = 10$ standard operation on ITER, (2) advanced operation with negative magnetic shear on ITER, (3) helical configuration on compact helical system (CHS). In the case of ITER standard operation, the profiles of density, temperature and safety factor are computed by the transport module with the CDBM turbulent transport model. The dependence of the AE stability on the energy distribution function of alpha particles is examined by varying the external heating profile. In the case of ITER advanced operation, systematic study on the negative magnetic shear and the internal transport barrier of density is carried out. In the case of CHS plasma, three-dimensional magnetic configuration calculated by the MHD equilibrium code, VMEC, is employed. The linear stabilities of global, toroidal and helical AEs are examined and the results are compared with experimental observations.

Formulation for the integro-differential analysis including the effects of finite particle orbit size will be also discussed.

Nonlinearly Driven Second Harmonics of Alfvén Cascades

H. Smith[1], B. N. Breizman[2], M. Lisak[1], D. Anderson[1]
[1] *Dept. of Radio and Space Science, Chalmers University of Technology, SE-41296 Göteborg, Sweden*
[2]*Institute for Fusion Studies, The University of Texas at Austin, Texas 78712, USA*

In recent experiments on Alcator C-Mod [1], measurements of density fluctuations with Phase Contrast Imaging through the plasma core show a second harmonic of the basic Alfvén Cascade (AC) signal. The present work describes the perturbation at the second harmonic as a nonlinear sideband produced by the Alfvén Cascade eigenmode via quadratic terms in the MHD equations.

1. Introduction

Alfvén Cascades have been observed in reversed shear operation of JT-60U [2], JET [3], and TFTR [4], and they are interpreted theoretically as shear Alfvén eigenmodes localized around the minimum q surface [5][6], where $q = q_\star$. The eigenmode frequency ω is slightly higher than the local maximum of the Alfvén continuum, $\omega_{\mathrm{A}m,n} = k_\parallel v_\mathrm{A} = (m - nq_\star)v_\mathrm{A}/Rq_\star$. In recent experiments on Alcator C-Mod, [1], measurements of density fluctuations with Phase Contrast Imaging through the plasma core show a second harmonic of the fundamental AC perturbation. The aim of the present work is to evaluate the second harmonic density perturbation produced by a given AC eigenmode via nonlinear terms in the momentum balance and continuity equations. For the sake of simplicity, the analysis will be limited to the case of a plasma with low-pressure ($\beta = 0$) and large aspect ratio ($\epsilon \ll 1$), for eigenmodes with large poloidal mode number ($m \gg 1$).

To be able to interpret the laser interferometric measurements conclusively, one has to consider the specific laser path and estimate the nonlinearities introduced by the measurement. These measurement-specific aspects require additional investigation, and will be addressed in a future publication.

The second harmonic perturbation at 2ω is nearly resonant with the $2m, 2n$ branch of the Alfvén continuum $\omega_{\mathrm{A}2m,2n}$. The resulting enhancement of the second harmonic is counteracted by the relatively weak non-linearity of the shear Alfvén wave. For shear Alfvén perturbations in a uniform equilibrium magnetic field, the quadratic terms $[4\pi\rho(\mathbf{v}\cdot\nabla)\mathbf{v}$ and $(\mathbf{B}\cdot\nabla)\mathbf{B}]$ tend to cancel in the momentum balance equation . For this reason, extreme care is needed to properly include magnetic curvature effects and to evaluate the coupling between shear Alfvén perturbations and compressional perturbations.

2. The Structure of the Problem

The AC mode is dominated by a single poloidal component in the Fourier representation of the perturbation. This part of the mode structure is known from linear theory (see Refs. [5] and [6]), and is assumed to be given. The main part of the plasma displacement in an AC mode is incompressible, which points to the need to keep track of small compressional displacements in both linear and nonlinear calculations of the perturbed density. Coupling between different plasma displacement components (or equivalently, plasma velocity components) is determined by the momentum balance equation. Once all relevant perturbed velocities are derived for both the first and second harmonics, the density perturbation can be calculated via the continuity equation.

Let all quantities X (which can stand for magnetic field $\mathbf{B}$, velocity $\mathbf{v}$, density ρ, etc.) be represented as

$$X = X_0 + \sum_{l=1}^{\infty} X_l + \text{c.c.}, \tag{1}$$

where X_0 is the equilibrium part, and $X_l \propto \exp(-li\omega t)$ are the perturbed parts. We assume that $X_0 \gg X_1 \gg X_l$ for $l \neq 1$, which prevents any nonlinear feedback from the 2ω perturbation to the fundamental mode at the basic frequency ω.

The plasma velocity has three degrees of freedom, which can be represented by three scalar functions ξ, Φ, and Ψ through

$$\mathbf{v} \equiv \dot{\xi}\mathbf{b}_0 + \frac{\mathbf{b}_0}{B_0} \times \nabla\dot{\Phi} + \frac{1}{B_0}\nabla_\perp\dot{\Psi}, \tag{2}$$

where B_0 is the magnitude and $\mathbf{b}_0$ the direction of the equilibrium magnetic field, and an overhead dot denotes a partial time derivative. Through this representation, one can distinguish between the acoustic (ξ), shear (Φ), and compressional (Ψ) velocity perturbations. Generally, in a first-order perturbation analysis of a uniform plasma with straight magnetic field lines, Φ corresponds to the scalar potential and Ψ is related to the perpendicular component of the vector potential, provided that a suitable gauge is chosen. In a curved magnetic field with second-order perturbations taken into account, this physical interpretation of the potentials is no longer valid; nevertheless, it is still possible to use the velocity representation of Eq. (2).

It should be pointed out that plasma pressure effects on Alfvén Cascades are limited to the lowest frequencies of their sweeping interval [7]. The AC is virtually insensitive to plasma pressure in the rest of its frequency interval, which allows us to treat that part in the zero-pressure limit neglecting the plasma pressure in the perturbed momentum balance equation. It is convenient to apply the time derivative operator to the momentum balance equation, after which the first and second harmonic components of the momentum balance equations become

$$4\pi\rho_0\ddot{\mathbf{v}}_1 - (\nabla \times \mathbf{B}_0) \times \nabla \times [\mathbf{v}_1 \times \mathbf{B}_0] - (\nabla \times \nabla \times [\mathbf{v}_1 \times \mathbf{B}_0]) \times \mathbf{B}_0 = 0, \tag{3}$$

$$\begin{aligned} &4\pi\rho_0\ddot{\mathbf{v}}_2 - (\nabla \times \mathbf{B}_0) \times \nabla \times [\mathbf{v}_2 \times \mathbf{B}_0] - (\nabla \times \nabla \times [\mathbf{v}_2 \times \mathbf{B}_0]) \times \mathbf{B}_0 = \\ &= (\nabla \times \mathbf{B}_0) \times \nabla \times [\mathbf{v}_1 \times \mathbf{B}_1] + (\nabla \times \nabla \times [\mathbf{v}_1 \times \mathbf{B}_1]) \times \mathbf{B}_0 + \\ &+ \frac{\partial}{\partial t}\left\{-4\pi\rho_0(\mathbf{v}_1 \cdot \nabla)\mathbf{v}_1 + (\mathbf{B}_1 \cdot \nabla)\mathbf{B}_1 - 4\pi\rho_1\dot{\mathbf{v}}_1 - \frac{1}{2}\nabla(\mathbf{B}_1 \cdot \mathbf{B}_1)\right\}, \end{aligned} \tag{4}$$

where $\dot{\mathbf{B}}_1 = \nabla \times [\mathbf{v}_1 \times \mathbf{B}_0]$. The right-hand side of Eq. (4) contains all quadratic terms in $\mathbf{v}_1$, which represent a driving force determining the second harmonic velocity $\mathbf{v}_2$ through the linear operator on the left-hand side.

The vector equations (3) and (4) can each be split up into three scalar equations by applying the three operations

$$\begin{aligned} &\mathbf{b}_0 \cdot \{\text{Eq. 3 or 4}\}, \\ &\nabla \cdot (\mathbf{b}_0/B_0 \times \{\text{Eq. 3 or 4}\}), \\ &\nabla \cdot (1/B_0\,\{\text{Eq. 3 or 4}\}_\perp). \end{aligned} \tag{5}$$

which produce the acoustic, vorticity, and compressional equations, respectively. This transforms Eqs. (3) and (4) into six equations, which can be written symbolically as

$$\text{Eq. (3)} \quad \Leftrightarrow \quad L^{1\alpha} = 0, \tag{6}$$

$$\text{Eq. (4)} \quad \Leftrightarrow \quad L^{2\alpha} = S^{\alpha}, \tag{7}$$

where the superscript α = a, v, and c indicates the acoustic, vorticity, and compressional equations, respectively. Equations (6) and (7) can be written as sums over contributions from the different velocity components,

$$L^{1\alpha} \equiv \sum_{i=\Phi_1,\Psi_1,\xi_1} L_i^{1\alpha}, \qquad L^{2\alpha} \equiv \sum_{i=\Phi_2,\Psi_2,\xi_2} L_i^{2\alpha}, \qquad S^{\alpha} \equiv \sum_{i,j=\Phi_1,\Psi_1,\xi_1} S_{ij}^{\alpha}. \tag{8}$$

For example, $S^{\rm a}_{\Phi_1\Psi_1}$ represents the parallel projection (i.e., acoustic component) of the terms on the right-hand side of Eq. (4) that are bilinear in Φ_1 and Ψ_1. We do not distinguish between different orders of the two indices i and j (e.g. $S^{\rm a}_{\Phi_1\Psi_1} = S^{\rm a}_{\Psi_1\Phi_1}$). Equations (6) and (7) will be examined in detail in the following Sections, and the dominating contributions to the second harmonic density perturbation ρ_2 will be identified.

The density perturbation is related to $\mathbf{v}_1$ and $\mathbf{v}_2$ by the first and second harmonic components of the continuity equation

$$\dot{\rho}_1 = -\nabla\cdot(\rho_0\mathbf{v}_1), \tag{9}$$

$$\dot{\rho}_2 = -\nabla\cdot(\rho_1\mathbf{v}_1) - \nabla\cdot(\rho_0\mathbf{v}_2). \tag{10}$$

The first term on the right-hand side of Eq. (10) is generated by the nonlinearity of the continuity equation, while the second term is generated by nonlinearities in the momentum balance equation (4). The density ρ_2 can also be written in terms of the partial contributions from ξ_1, Φ_1, Ψ_1, ξ_2, Φ_2, and Ψ_2 as

$$\rho_2 = \rho_{\Phi_1^2} + \rho_{\Psi_1^2} + \rho_{\xi_1^2} + \rho_{\Phi_1\Psi_1} + \rho_{\Phi_1\xi_1} + \rho_{\Psi_1\xi_1} + \rho_{\xi_2} + \rho_{\Phi_2} + \rho_{\Psi_2}. \tag{11}$$

The first six of these contributions to the density perturbation come from the first term in Eq. (10), and the last three contributions come from the second term.

3. First Harmonic Velocity Perturbation

The first harmonic equations are

$$L^{\rm 1a} = L^{\rm 1a}_{\xi_1} = -4\pi\rho_0\omega^2\xi_1 = 0, \tag{12}$$

$$L^{\rm 1c} = L^{\rm 1c}_{\Psi_1} + L^{\rm 1c}_{\Phi_1} = $$

$$= -\nabla\cdot\frac{1}{B_0}\left(\nabla\nabla\cdot(B_0\nabla\Psi_1) + [(\nabla F_1\cdot\nabla)\mathbf{B}_0 - (\mathbf{B}_0\cdot\nabla)\nabla F_1]\times\mathbf{B}_0\right) = 0, \tag{13}$$

$$L^{\rm 1v} = L^{\rm 1v}_{\Phi_1} = \nabla\cdot\left(\frac{\omega^2}{v_{\rm A}^2}\nabla_\perp\Phi_1\right) + (\mathbf{B}_0\cdot\nabla)\frac{1}{B_0^2}\nabla\cdot(B_0^2\nabla_\perp F_1) - \nabla^2\mathbf{B}_0\cdot\nabla F_1 = 0, \tag{14}$$

where $F_1 \equiv \mathbf{b}_0/B_0\cdot\nabla\Phi_1$. Because of the $\beta = 0$ assumption, Eq. (12) immediately yields $\xi_1 = 0$, which implies that $\rho_{\xi_1^2} = \rho_{\Psi_1\xi_1} = \rho_{\Phi_1\xi_1} = 0$. Furthermore, Eq. (13) can be used together with $(\mathbf{B}_0\cdot\nabla) \sim k_\parallel \sim 1/(Rq)$, to obtain the estimate

$$\Psi_1 \sim \frac{\epsilon^2}{m^2q^2}\Phi_1, \tag{15}$$

which yields

$$\rho_{\Phi_1\Psi_1} \sim \frac{m^2}{r^2R^2q^2}\frac{\rho_0}{B_0^2}\Phi_1^2, \quad \rho_{\Psi_1^2} \sim \frac{1}{R^4q^4}\frac{\rho_0}{B_0^2}\Phi_1^2. \tag{16}$$

Let us now review the eigenmode analysis for Alfvén Cascades to establish the radial profile $\tilde{\Phi}_1$ of the shear perturbation $\Phi_1 \equiv \tilde{\Phi}_1(r)e^{i(n\varphi - m\theta - \omega t)}$ where $d\tilde{\Phi}_1/dr \sim m/r$. The eigenmode equation for $\tilde{\Phi}_1(r)$ follows from Eq. (14) and takes the form

$$\frac{1}{r}\frac{d}{dr}\left(rD\frac{d\tilde{\Phi}_1}{dr}\right) - \frac{m^2}{r^2}\tilde{\Phi}_1 D = 0, \tag{17}$$

where $D \equiv \omega^2/\bar{v}_{\rm A} - \bar{k}_\parallel^2$, and a bar denotes a flux surface average.

Equation (17) is oversimplified because it does not include the hot ion contribution and higher-order toroidal corrections. The reason why these additional terms are essential is that they shift the eigenmode from the Alfvén continuum. In what follows, we add these terms to Eq. (17), taking their explicit form from Ref. [6]. We also introduce a normalized coordinate $x \equiv (r - r_0)m/r_0$ and Taylor expand $\bar{k}_\parallel$ around the zero shear point $r = r_\star$ where the AC is located. After these steps, we find the amended Eq. (17) to be

$$\frac{d}{dx}(S + x^2)\frac{d\tilde{\Phi}_1}{dx} - (S + x^2)\tilde{\Phi}_1 + Q_1\tilde{\Phi}_1 = 0, \tag{18}$$

where

$$S \equiv \frac{2(\omega - \omega_{\rm A})\omega_{\rm A}}{\overline{v}_{\rm A}^2}\frac{mq_\star}{r_\star^2 q_\star''}\frac{\bar{R}^2 q_\star^2}{m - nq_\star}, \tag{19}$$

and the coefficient Q_1 describes the effects of hot ions and toroidicity in the same way as in Ref. [6], i.e.,

$$Q_1 = Q_{\rm hot} + Q_{\rm tor} \equiv \omega_{\rm A}^2\frac{q_\star^2\bar{R}^2}{\overline{v}_{\rm A}^2(m - nq_\star)}\frac{q_\star}{r_\star^2 q_\star''}\left(\frac{\omega_{\rm ch}}{\omega_{\rm A}}\left(-\frac{r}{\rho}\frac{d\bar{\rho}_{\rm hot}}{dr}\right)_{r=r_\star} + \frac{2m\epsilon_\star(\epsilon_\star + 2\Delta_\star')}{1 - 4(m - nq_\star)^2}\right). \tag{20}$$

In this expression, $\rho_{\rm hot}$ is the hot ion density and Δ is the Shafranov shift. As shown in Refs. [5] and [6], Q_1 has to be greater than 1/4 for an eigenmode to exist. By introducing a new unknown function $G_1(x) = \tilde{\Phi}_1(x)\sqrt{S + x^2}$, and using a variational approach with the ansatz $G_1 = A\exp(-x^2/(2a^2))$, we obtain for $Q_1 = 1$ the following approximate solution: $a = 1.247$ and $S = 0.0983$. This result agrees with the lowest order radial eigenmode found in Ref. [5].

Now we are in a position to estimate the Φ_1 contribution to ρ_2 through the quadratic nonlinearity in the continuity equation,

$$\rho_{\Phi_1^2} \simeq \left(\left[\frac{\mathbf{b}_0}{B_0}\times\nabla\Phi_1\right]\cdot\nabla\right)\left[\rho_0\nabla\Phi_1\cdot\left(\nabla\times\frac{\mathbf{b}_0}{B_0}\right)\right] \sim \frac{m^2}{r^3 R}\frac{\rho_0}{B_0^2}\Phi_1^2. \tag{21}$$

The estimates in Eqs. (16) and (21) show that $\rho_{\Phi_1^2} \gg \rho_{\Psi_1^2},\ \rho_{\Phi_1\Psi_1}$.

4. Second Harmonic Velocity Perturbation

The acoustic equation $L_{\xi_2}^{\rm 2a} = S_{\Phi_1^2}^{\rm a} + S_{\Phi_1\Psi_1}^{\rm a}$ has the form

$$\frac{(2\omega)^2}{v_{\rm A}^2}\xi_2 = \frac{1}{2B_0^2}\left(\mathbf{b}_0\cdot\nabla\right)\left[B_0^2\nabla F_1\cdot\nabla F_1\right] - \mathbf{b}_0\cdot\left(\nabla_\perp\frac{\nabla\cdot(B_0\nabla\Psi_1)}{B_0^2}\times\nabla F_1\right). \tag{22}$$

The low β assumption does not allow us to discard ξ_2 immediately (as we did with ξ_1), since second harmonic parallel velocity perturbations can arise from the nonlinear ponderomotive

force (not associated with plasma pressure). Straightforward estimates of the two terms on the right-hand side of Eq. (22) give

$$\xi_2 \sim \frac{m^2}{r^2 R q}\frac{\Phi_1^2}{B_0^2} \;\Rightarrow\; \rho_{\xi_2} \sim \frac{m^2}{r^2 R^2 q^2}\frac{\rho_0}{B_0^2}\Phi_1^2 \ll \rho_{\Phi_1^2}. \tag{23}$$

These estimates show that ξ_2 can safely be neglected in calculating the perturbed density.

The second harmonic compressional Alfvén wave equation reduces to $L^{2c}_{\Psi_2} + L^{2c}_{\Phi_2} = S^{c}_{\Phi_1^2} + S^{c}_{\Phi_1\Psi_1}$. If we make an assumption that $L^{2c}_{\Psi_2} \sim L^{2c}_{\Phi_2}$ we find $\Psi_2 \sim \epsilon^2/(m^2q^2)\Phi_2$ (which is similar to what follows from Eq. (13)), and the resulting density perturbation is relatively small ($\rho_{\Psi_2} \ll \rho_{\Phi_2}$). Alternatively, we can estimate Ψ_2 by assuming that $L^{2c}_{\Psi_2} = S^{c}_{\Phi_1^2} + S^{c}_{\Phi_1\Psi_1}$ or equivalently,

$$-\nabla\cdot(B_0\nabla\Psi_2) = -\frac{1}{2}B_0^2\left(\nabla F_1\cdot\nabla F_1\right) + \frac{1}{2}\mathbf{B}_0\cdot\left(\nabla\frac{\nabla\cdot(B_0\nabla\Psi_1)}{B_0^2}\times\nabla_\perp\Phi_1\right). \tag{24}$$

The nonlinear terms on the right-hand side of this equation can be estimated as $S^{c}_{\Phi_1^2} + S^{c}_{\Phi_1\Psi_1} \sim m^4/(r^4R^2q^2)\Phi_1^2$, so that

$$\Psi_2 \sim \frac{\Phi_1^2}{B_0R^2q^2} \;\Rightarrow\; \rho_{\Psi_2} \sim \frac{m^2}{r^2R^2q^2}\frac{\rho_0}{B_0^2}\Phi_1^2 \ll \rho_{\Phi_1^2}. \tag{25}$$

Based on the above estimates, we neglect the Ψ_2 contribution to the perturbed density. As a result, Eq. (11) for the second harmonic density perturbation simplifies to $\rho_2 = \rho_{\Phi_2} + \rho_{\Phi_1^2}$.

In order to calculate ρ_{Φ_2}, we need to determine Φ_2 from the second harmonic vorticity equation $L^{2v} = S^{v}$. When dealing with the source term $S^{v}_{\Phi_1^2}$, we must pay special attention to the cancellation of the $-4\pi\rho_0(\mathbf{v}_1\cdot\nabla)\mathbf{v}_1$ and $(\mathbf{B}_1\cdot\nabla)\mathbf{B}_1$ terms in a homogeneous plasma with straight magnetic field lines. The resulting second-harmonic vorticity equation has the form

$$\begin{aligned} &4\frac{1}{r}\frac{d}{dr}\left(rD\frac{d\tilde\Phi_2}{dr}\right) - 16\frac{m^2}{r^2}\tilde\Phi_2 D = \\ &= \frac{m}{r\bar B_0}\left[2\frac{dD}{dr}\left(\left(\frac{d\tilde\Phi_1}{dr}\right)^2 - \frac{m^2}{r^2}\tilde\Phi_1^2\right) + D\left(\frac{d\tilde\Phi_1}{dr}\frac{d^2\tilde\Phi_1}{dr^2} - \tilde\Phi_1\frac{d^3\tilde\Phi_1}{dr^3}\right) - \bar k_\parallel\frac{d^2\bar k_\parallel}{dr^2}\frac{d\tilde\Phi_1^2}{dr}\right], \end{aligned} \tag{26}$$

where $\Phi_2 = \tilde\Phi_2(r)e^{2i(n\varphi - m\theta - \omega t) - i\pi/2}$. In deriving Eq. (26), flux surface averaging has been performed to eliminate the poloidal sidebands in S^{v} that are proportional to $\sin\theta$ or $\cos\theta$. These off-resonant sidebands produce only a small $2m \pm 1$ correction to the dominant second harmonic response.

Taylor expanding the coefficients in Eq. (26) around the zero shear point $r = r_\star$ enables us to transform Eq. (26) to

$$\begin{aligned} &4\frac{d}{dx}(S+x^2)\frac{d\tilde\Phi_2}{dx} - 16(S+x^2)\tilde\Phi_2 + 4Q_2\tilde\Phi_2 = \\ &= \;4x\left(\left(\frac{dT}{dx}\right)^2 - T^2\right) + (S+x^2)\left(\frac{dT}{dx}\frac{d^2T}{dx^2} - T\frac{d^3T}{dx^3}\right) + \frac{d(T^2)}{dx}, \end{aligned} \tag{27}$$

where $T(x) \equiv m\tilde\Phi_1/(r_\star\sqrt{\bar B_0})$, S is the eigenvalue of the AC eigenmode equation (18), and the effects of hot ions and toroidicity have been added through the parameter Q_2.

To illustrate the second harmonic response, we choose a special case in which $Q_{\rm hot} \gg Q_{\rm tor}$. This assumption makes Q independent of the mode numbers and, consequently, we have $Q_1 = Q_2 = Q$. Fig. 1 shows numerical solutions to Eq. (27) in the above limit for two different values of Q. It is essential that the values of the constant S in Eq. (27) are different from the eigenvalues of the linear operator on the left-hand side for both values of Q, insuring uniqueness of the solutions. These solutions give $\Phi_2 \sim T^2 \sim m^2\Phi_1^2/(r^2 B_0)$ when $Q \simeq 0.65$. They also indicate that Φ_2 decreases with increasing Q.

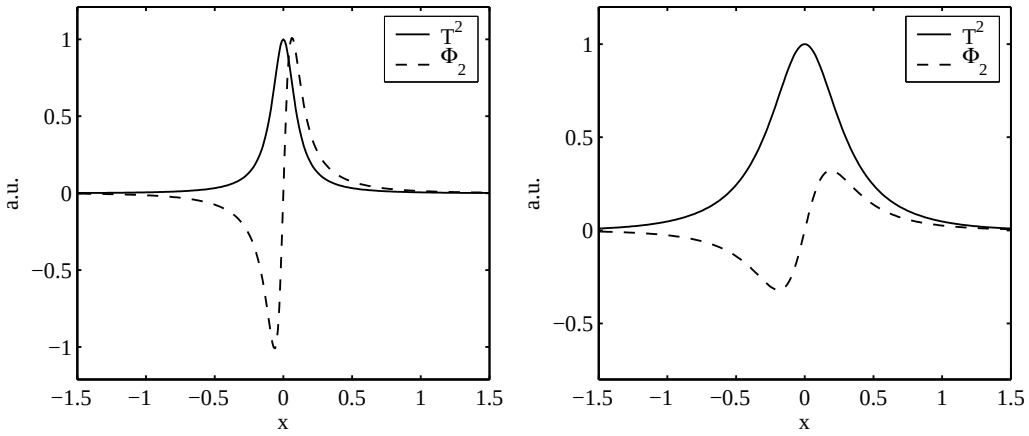

Figure 1: *Solution to Eq. (27) for $Q = 0.65$, $S = 0.011$ (left) and $Q = 1$, $S = 0.10$ (right). Note that the amplitude of Φ_2 decreases with increasing Q, and that $\tilde{\Phi}_2(x)$ is an odd function of x whereas $\tilde{\Phi}_1(x)$ is an even function of x.*

5. Second Harmonic Density Perturbation

The second harmonic density perturbation generated by Φ_2 can be estimated as

$$\rho_{\Phi_2} = -\rho\nabla\Phi_2 \cdot \left(\nabla \times \frac{\mathbf{b}_0}{B_0}\right) - \left(\frac{\mathbf{b}_0}{B_0} \times \nabla\Phi_2\right) \cdot \nabla\rho_0 \sim \left(\frac{1}{R} + (\ln\rho_0)'\right) \frac{m^3}{r^3} \frac{\rho_0 \Phi_1^2}{B_0^2}, \qquad (28)$$

which shows that ρ_{Φ_2} is larger than $\rho_{\Phi_1^2}$ in Eq. (21) by a factor $m \gg 1$. However, the resonant enhancement becomes less efficient when Q increases because of the increasing frequency shift $\Delta\omega$ away from the Alfvén continuum and the concomitant widening of the first harmonic radial profile. It is evident from the numerical solution shown in Fig. 1 that the amplitude of Φ_2 decreases with increasing Q. For $Q = 1$, the amplitude of Φ_2 is already lower than T^2 by roughly a factor of 3. For larger values of Q this numerical factor may exceed the mode number m, making $\rho_{\Phi_1^2}$ comparable to or greater than ρ_{Φ_2} for high Q.

To compare ρ_2 with ρ_1 we need an estimate for the first harmonic density perturbation, which can be obtained from Eq. (9),

$$\rho_1 = -\rho\nabla\Phi_1 \cdot \left(\nabla \times \frac{\mathbf{b}_0}{B_0}\right) - \left(\frac{\mathbf{b}_0}{B_0} \times \nabla\Phi_1\right) \cdot \nabla\rho \sim \left(\frac{1}{R} + (\ln\rho_0)'\right) \frac{m}{r} \frac{\rho_0 \Phi_1}{B_0}. \qquad (29)$$

For moderately large values of Q, the ratio ρ_2/ρ_1 is approximately of order

$$\frac{\rho_2}{\rho_1} \sim \frac{\rho_{\Phi_2}}{\rho_1} \sim \frac{m^2}{r^2} \frac{\Phi_1}{B_0} \sim \frac{mq}{\epsilon} \frac{|\mathbf{B}_{\Phi_1}|}{B_0}. \qquad (30)$$

This rough estimate only refers to the maximum values of ρ_1 and ρ_2, whereas locally the ratio of ρ_2 to ρ_1 can differ significantly from Eq. (30) as these two quantities have different radial and poloidal dependences.

6. Summary

The main results of this work are: (1) that the shear Alfvén perturbation is the dominant contributor to the second harmonic density fluctuations produced by Alfvén cascades, and (2) that one can calculate the second harmonic density perturbation from Eqs. (21) and (28) by first solving Eq. (27), in which the radial profile of the AC eigenmode is known from Eq. (18). For moderate values of Q, the nonlinearity of the momentum balance equation is more important than the nonlinearity of the continuity equation and the resulting second harmonic density is given by Eq. (28).

This analysis, together with experimental measurements, can potentially be used to determine the AC amplitude at the mode center, rather than just at the edge as with magnetic probes.

7. Acknowledgments

We are grateful to Andrew Cole and James Van Dam for stylistic comments. This work was supported by the European Community under an association contract between Euratom and Sweden, and by the U.S. Department of Energy Contract No. DE-FG03-96ER-54346.

References

[1] Snipes, J. A. , *et al.*, Phys. Plasmas **12**, 056102 (2005).

[2] Kimura, H., *et al.*, Nucl. Fusion **38**, 1303 (1998).

[3] Sharapov, S. E., *et al.*, Phys. Lett. A **289**, 127 (2001).

[4] Nazikian, R., Kramer, G. J., Cheng, C. Z., Gorelenkov, N. N., Berk, H. L., and Sharapov, S. E., Phys. Rev. Lett. **91**, 125003 (2003).

[5] Berk, H. L., Borba, D. N., Breizman, B. N., Pinches, S. D., Sharapov, S. E., Phys. Rev. Lett. **87**, 185002-1 (2001).

[6] Breizman, B. N., Berk, H. L., Pekker, M. S., Pinches, S. D., Sharapov, S. E., Phys. Plasmas **10**, 3649 (2003).

[7] Breizman, B. N., Pekker, M. S., Sharapov, S. E., Phys. Plasmas **12**, 112506 (2005).

OT02

Modelling nonperturbative frequency sweeping

R. G. L. Vann[1,2], R. O. Dendy[3,2], M. P. Gryaznevich[3], S. E. Sharapov[3]
[1]*Department of Physics, University of York, Heslington, York YO10 5DD, U.K.*
[2]*Department of Physics and Centre for Scientific Computing, University of Warwick, Coventry CV4 7AL, U.K.*
[3]*Euratom/UKAEA Fusion Association, Culham Science Centre, Abingdon, Oxfordshire OX14 3DB, U.K.*

High frequency magnetohydrodynamic (MHD) activity in tokamak plasmas may be driven by energetic ion populations. The time evolution of this MHD behaviour, notably frequency sweeping, provides insights into the changing properties of both the energetic particle population and the ambient plasma. To extract this information, it is necessary to model the self-consistent nonlinear interaction of the energetic particles with the MHD modes, incorporating energetic particle resonance and background damping; this is done by applying a fully nonlinear self-consistent numerical implementation [2] of the Berk-Breizman augmentation of the Vlasov-Maxwell system (hereafter "VM(BB)"). Perturbative frequency sweeping observations [3,4] have already been successfully modelled using the VM(BB) system. In this paper we report new results on modelling nonperturbative frequency sweeping.

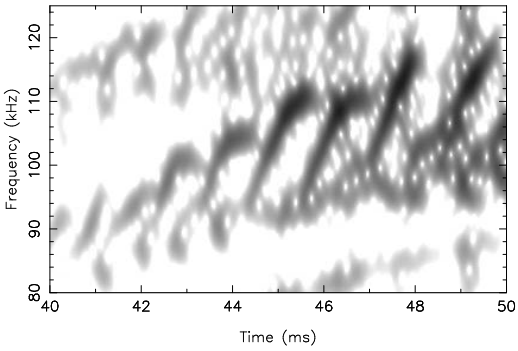

Figure 1: MAST shot 11005

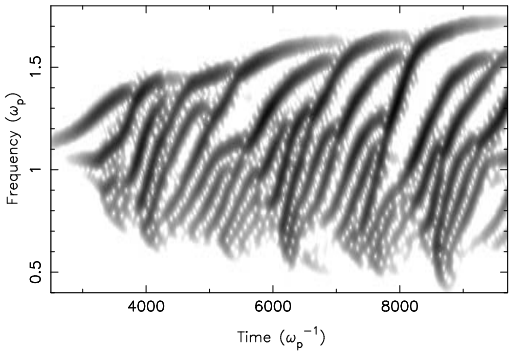

Figure 2: VM(BB) simulation

Plasma waves driven by energetic particles are said to be nonperturbative if their dispersion properties are modified significantly by the energetic particle population [1]. Figure 1 shows data from the Mega-Amp Spherical Tokamak that is believed to reflect this effect. In this paper we present self-consistent nonlinear modelling of nonperturbative frequency sweeping using VM(BB) (Fig. 2). In both Fig. 1 and Fig. 2 we note that: the sweeping rate is approximately constant until it begins to die; modes are born at different frequencies; the sweeping is predominantly in one direction only. The nonperturbative frequency sweeping shown in Fig. 2 occurs for fixed model parameters, suggesting that Fig. 1 need not imply evolving plasma properties. In this respect it resembles recent modelling [4] of perturbative frequency sweeping.

[1] F. Zonca and L. Chen, *Phys. Plasmas* **3**, 323 (1996)
[2] R. G. L. Vann *et al.*, *Phys. Plasmas* **10**, 623 (2003)
[3] S. D. Pinches *et al.*, *Plasma Phys. Control. Fusion* **46**, S47 (2004)
[4] R. G. L. Vann, R. O. Dendy, and M. P. Gryaznevich, *Phys. Plasmas* **12**(3) (2005)

This work was funded in part by Euratom and the UK EPSRC.

Damping of Kinetic Alfvén Eigenmodes in Tokamak Plasmas

Ph. Lauber*, S. Günter*, S.D. Pinches*, A. Könies*

*Max-Planck-Institut für Plasmaphysik, EURATOM-Association, Garching, Germany
*Max-Planck Institut für Plasmaphysik, EURATOM-Association, Greifswald, Germany

Email: pwl@ipp.mpg.de

1 Abstract

The ability to predict the stability of fast-particle-driven Alfvén eigenmodes in burning fusion plasmas requires a detailed understanding of the dissipative mechanisms that damp these modes. In order to address this question, the linear gyro-kinetic, electromagnetic code LIGKA [1] is employed to investigate their behaviour in realistic tokamak geometry. LIGKA is based on an eigenvalue formulation and self-consistently calculates the coupling of large-scale MHD modes to gyro-radius scale length kinetic Alfvén waves. It uses the drift-kinetic HAGIS code [2],[3] to accurately describe the unperturbed particle orbits in general geometry. In addition, a newly developed antenna-like version of LIGKA allows for a frequency scan, analogous to an external antenna.
With these tools the properties of the kinetically modified TAE in or near the gap (KTAE, radiative damping or 'tunnelling') and its coupling to the continuum close to the edge are numerically analysed. The results are compared with previous calculations based on fluid and other gyro-kinetic models. Also first linear calculations on cascade modes are presented.

2 Introduction

The stability properties of the toroidal Alfvén eigenmode (TAE) [4],[5] in magnetically confined fusion plasmas are of great interest because TAEs can be driven unstable by fusion-born α-particles with dangerous consequences for the overall plasma stability and confinement [6]. In order to make predictions for an ignited plasma like ITER, the background damping mechanisms of TAEs have to be investigated carefully. These mechanisms are electron and ion Landau damping, continuum damping, collisional damping and radiative damping. The latter mechanism requires a non-perturbative description, since the MHD properties of the mode structure are modified by coupling to the kinetic Alfvén wave (KAW) [7].
In this paper numerical calculations on the kinetic properties, especially damping rates of TAEs and KTAEs using the gyro-kinetic, linear eigenvalue code LIGKA [1] are carried out. LIGKA covers all the damping mechanisms mentioned above, except collisional damping, which is assumed to be small compared to the other types of damping.
The underlying equations of LIGKA can be simplified to the 'reduced kinetic model' as used in [8] and [9] proofing their validity in the regime under investigation.

3 Basics, Equations and Numerical Model

The inclusion of non-ideal effects, namely parallel electric fields and finite ion gyro-radii, leads to significant changes of the TAE modes and generates a new set of modes, the kinetic TAEs (KTAEs) and a new type of damping, called radiative damping or 'tunnelling' [7, 8]. They are quantified by the non-ideal parameter

$$\lambda = \frac{4ms\varrho_i}{r_m \hat{\epsilon}^{3/2}} \sqrt{\frac{3}{4} + \frac{T_e}{T_i}} \tag{1}$$

with $\varrho_i = v_{thi}/\omega_{ci}$ being the ion gyro-radius, $v_{th} = \sqrt{T/m}$ the particles' thermal velocity, ω_c the cyclotron frequency and $\hat{\epsilon}^{3/2} = 5r_m/2R$.
In the framework of the 'reduced kinetic model', the following basic equation is found as the relevant one for non-ideal shear Alfvén modes:

$$\nabla_\perp \cdot \frac{\omega^2}{v_A^2} \nabla_\perp \phi + \frac{\partial}{\partial s} \nabla_\perp^2 \frac{\partial \phi}{\partial s} = \delta_s^2 \frac{\omega}{c} \nabla_\perp^4 \frac{\partial A_\parallel}{\partial s} - \frac{3}{4} \frac{\omega^2}{v_A^2} \varrho_i^2 \nabla_\perp^4 \frac{\partial A_\parallel}{\partial s} \tag{2}$$

It is derived from the vorticity equation with finite Larmor radius (FLR) corrections and Ohm's law as given in Ref. [10, 11]. Here, ϕ is the electrostatic potential, $A_\parallel \mathbf{b}$ the magnetic vector potential, r the radial coordinate and s the coordinate along the field line. δ_s is the skin depth $\delta_s = c^2\epsilon_0/\omega\sigma$ with σ being the parallel complex electrical conductivity, which was chosen to be $\sigma/\epsilon_0 = i\omega_{pe}^2/(\omega + i\nu_{eff} - k_\parallel^2 v_{the}^2/\omega)$. ω_{pe} and ν_{eff} are the electron plasma frequency and the effective electron collision frequency respectively.
Near the singular layer of the ideal MHD equation (left hand side of Eq. 2), the right hand side becomes most important and it can be simplified by the substitutions $i\omega A_\parallel/c \to \partial\phi/\partial s$, $\partial/\partial s \to ik_\parallel \equiv i\big(n - m/q(r)\big)/R$, $\omega^2/\omega_A^2 \equiv \Omega^2 = \Omega_m^2 \equiv 1/4q_m^2$ to yield a coupled system of fourth-order differential equations with the right hand side reducing to

$$-r_{LT}^2 \Omega_m^2 \frac{\partial^4 \phi_m}{\partial r^4} \tag{3}$$

with

$$r_{LT}^2 = \frac{3}{4}\varrho_i^2 + \varrho_s^2 = \varrho_i^2 \left\{ \frac{3}{4} + \frac{T_e}{T_i} \Big[1 + \frac{v_A^2}{v_{the}^2} (1 + \frac{\nu_{eff}}{|k_\parallel| v_A}) \Big] \right\}. \tag{4}$$

The underlying equations of LIGKA (derived in [12, 13]) consist of the quasi-neutrality equation

$$\sum_a \Big[\int d^2\mathbf{v} J_0 f_a + \frac{e_a}{m_a} \nabla_\perp \frac{n_{a0}}{B^2} \nabla_\perp \phi(\mathbf{x}) + \frac{3e_a v_{th,a}^2 n_{a0}}{4 m_a \Omega_a^4} \nabla_\perp^4 \phi(\mathbf{x}) \Big] = 0 \tag{5}$$

and the gyro-kinetic moment equation:

$$\begin{aligned} - & \frac{\partial}{\partial t} \frac{e}{m} \nabla_\perp \frac{n_0}{B^2} \nabla_\perp \phi + \nabla A_\parallel \times \mathbf{b} \cdot \nabla (\frac{\nabla \times \mathbf{B}}{B}) + (\mathbf{B} \cdot \nabla) \frac{(\nabla \times \nabla \times \mathbf{A}) \cdot \mathbf{B}}{B^2} \\ = & -\sum_a e_a \int \mathbf{v}_d \cdot \nabla J_0 f_a d^3\mathbf{v} + \frac{c}{v_{A0}^2} \frac{3 v_{th,a}^2}{4\Omega_a^2} \nabla_\perp^4 \frac{\partial \phi(\mathbf{x})}{\partial t} + \\ & \mathbf{B} \cdot \nabla \Big(\frac{4\pi e_a^2 n_{a0} v_{th,a}^2}{2 B m_a c^2 \Omega_a^2} \nabla_\perp^2 A_\parallel \Big) + \mathbf{b} \times \nabla (\frac{2\pi e_a n_{0a} v_{th,a}^2}{B\Omega_a}) \cdot \nabla \nabla^2 \phi \end{aligned} \tag{6}$$

Here, $\sum_a$ indicates the sum over different particle species with the perturbed distribution function f_a, mass m_a, charge e_a, unperturbed density n_{a0}, thermal velocity $v_{th,a} = \sqrt{T_a/m_a}$ and cyclotron frequency Ω_a. In the same simple limit as described above, carrying out the velocity space integrals and using $A_\parallel = c(\nabla\psi)_\parallel/i\omega$, these equations can be reduced to:

$$\phi - \psi = \hat{r}_{LT}^2 \nabla_\perp^2 \phi \tag{7}$$

and

$$\nabla_\perp \cdot \frac{\omega^2}{v_A^2} \nabla_\perp \phi + \frac{\partial}{\partial s} \nabla_\perp^2 \frac{\partial \psi}{\partial s} = 0 \tag{8}$$

leading, by elimination of ψ, to exactly the same fourth order equation as given above in equations (2) and (3). It should be noted however, that $\hat{r}_{LT}$ is not the same as r_{LT}: the physics connected with parallel electric fields and collisions (Landau damping, finite banana orbit effects) would appear on the left hand side of Eq. (7) resp. right hand side of Eq. (8) originating from the exact kinetic integrals over the velocity space.

The basic version of LIGKA [1] solves equations (5), (6) and the linear gyro-kinetic equation for the perturbed distribution function f up to 2nd order in $k_\perp \varrho_i$. Straight field line coordinates for the background quantities given by the equilibrium code HELENA [14] are chosen. LIGKA has been extended to calculate correctly the residual part of the Landau-type integrals for the case of negative growth rates, i.e. damped modes. It uses a rational interpolation scheme for the resonance denominator which allows for accurate and fast evaluation of the pole contributions without employing derivatives. Grid refinement techniques are also applied for the velocity space integration. When examining the rich spectrum around a gap, many closely spaced modes are expected. Using a Nyquist solver is cumbersome under these conditions because many poles require a high number of sample points along the integration contour. Thus an antenna-like version of LIGKA was developed: A drive vector is added to the right hand side of the homogeneous equation:

$$M(\omega) \begin{pmatrix} \phi \\ \psi \end{pmatrix} = \mathbf{d} \tag{9}$$

where $\mathbf{d}$ is only nonzero for the last finite element at the plasma edge, prescribing a small perturbation from the outside. The eigenfunctions are found by inverting $M(\omega)$ resulting in:

$$\mathbf{I} \begin{pmatrix} \phi \\ \psi \end{pmatrix} = M(\omega)^{-1} \mathbf{d}, \tag{10}$$

and the plasma response is 'measured' by an integral over the eigenfunction:

$$\mathcal{R} = \sum_m \int_0^a \phi_m \phi_m^* dr \tag{11}$$

4 Benchmarks and Results on TAEs

In this section benchmarks for the three main damping mechanisms are given:
Fig. 1 shows a benchmark with the drift kinetic perturbative CAS3D-K [15] in the Tokamak limit. Based on a real JET equilibrium case (#42979, [16]) the isotope mass of the

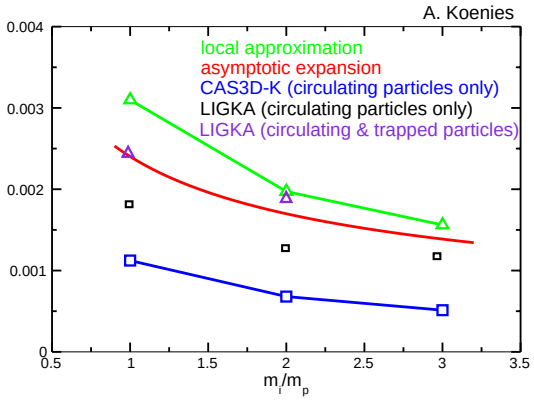

Figure 1: Damping rates for a TAE in an open gap dependent on the background isotope mass

background plasma is varied, resulting in a decreasing damping rate as the isotope mass increases. Without all the gyro-kinetic contributions, electron Landau damping is the most important damping mechanism. Agreement within a factor of 2 between the analytical calculation [17], CAS3D-K and LIGKA in the drift kinetic limit is found. However, the differences between CAS3D-K and LIGKA can be attributed to additional $E_{\|}$-effects included in LIGKA that cannot be turned off easily.

For the radiative damping, a benchmark with a code based on the reduced kinetic model[9] was carried out. For a circular equilibrium based on JET shot #38573@5.0s(details in Ref. [9]) the temperature and thus also the gyro-radius of the background ions is varied: with growing gyro-radius the non-ideal parameter λ grows, resulting in an increasing damping rate. Fig. 2 shows very good agreement between the two codes. The remaining differences may be attributed to collisional damping effects that are missing in LIGKA, but are taken into account in G. Fu's code.

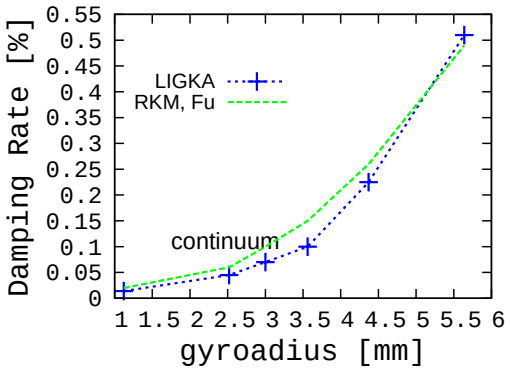

Figure 2: Dependence of the radiative damping on the gyro-radius

Figs. 3 and 4 show how the KAW 'tunnels' on top of the TAE mode: for a small gyro-radius no change in the global TAE mode structure can be seen whereas for the case corresponding to the experimental values (Fig. 3, middle) and a slightly larger gyro-radius (left) changes

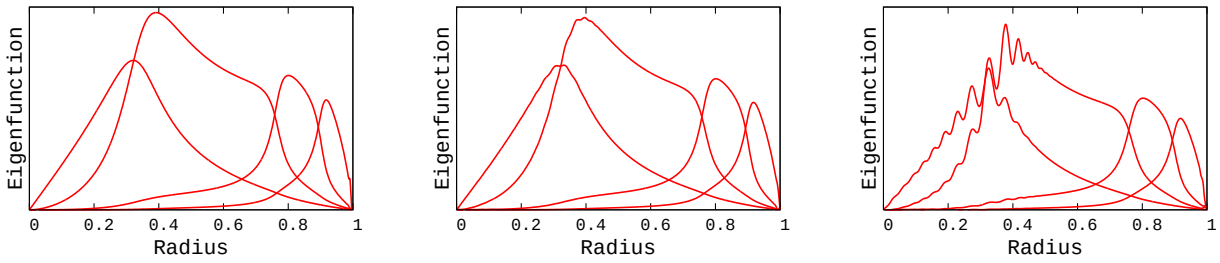

Figure 3: Eigenfunction for kinetic TAE for $\varrho_i = 1$mm (left), $\varrho_i = 3$mm (middle) and $\varrho_i = 5.5$mm (right)

in the eigenfunction can be seen. This fact confirms that a non-perturbative treatment is necessary.

The third damping mechanism, the continuum damping can be explored when the TAE gap is closed at the edge due to a small, near-zero edge density. In this case an additional KAW is excited at the modes' intersection with the Alfvén continuum as can be seen on the right in Fig. 4 at the radial position $s = 0.97$. The damping rate (LIGKA) increases to from 0.10% to 0.69%. This is relatively close to Fu's result 0.5%. Thus continuum damping at the edge is found to be the dominant damping mechanism for TAEs in a closed gap.
The calculated damping rates for an open gap are typically about a factor of 10 too small compared to experimental measurement [18][19] and other gyro-kinetic calculations [18] by PENN, [21] where mode conversion in the plasma centre was found to be the dominant damping mechanism. LIGKA finds only negligible mode conversion in the centre. However, in the closed gap case LIGKA's results become comparable to the experimental value.

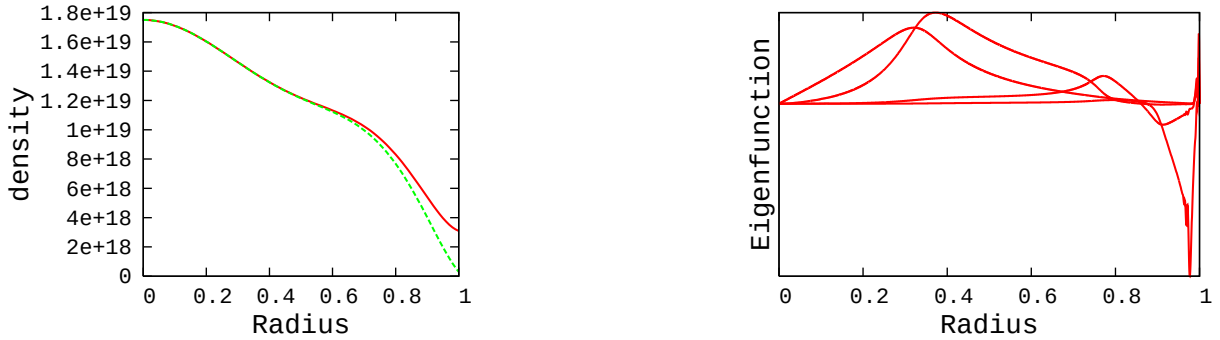

Figure 4: Density profiles for an open and closed gap case (left) and the eigenfunction for the kinetic TAE for a closed gap with $\varrho_i = 3$mm (right)

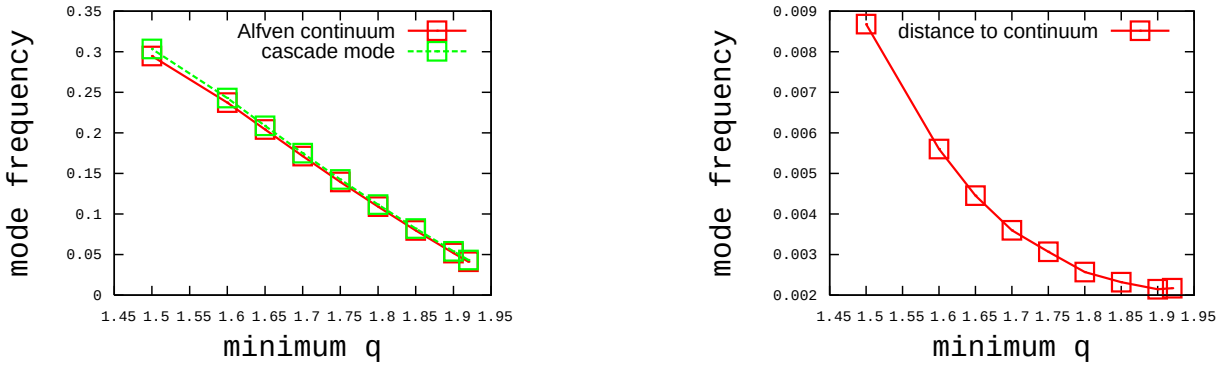

Figure 5: $q_{\min}$-dependence of the cascade mode frequency (left) and its distance to the Alfvén continuum (right)

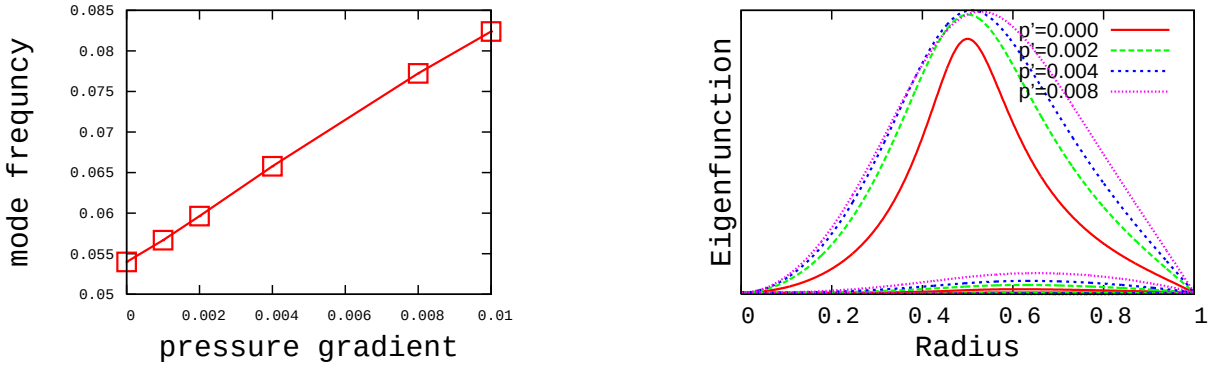

Figure 6: Dependence of the cascade mode frequency on the pressure gradient (left) and corresponding eigenfunctions (right)

5 Cascade Modes

In plasmas with a reversed q-profile global shear Alfvén modes can exist because of the lack of continuum damping near the flat shear region. There have been many experimental observations [22],[23] and also analytical analysis [24], [25]. In the latter references conditions on the existence of the mode dependent on the q-profile and mode numbers and the hot particle drive have been derived. For a shifted circle equilibrium part of these results are reproduced with LIGKA: using a parabolic q-profile with $q = q_0 + 0.5q''(s-0.5)^2$ and 'sweeping' $q_{\min}$ from $m/n = 2/1$ to $m - 0.5/n$, the mode is shifted away form the continuum [25] as shown in Fig. 5 It is also of interest how finite- β-effects modify these criteria. Numerical calculations with NOVA-K [26], CASTOR or also LIGKA in similar geometry based on numerical equilibria found that increasing the pressure gradient helps the mode to exist. A version of LIGKA for analytical equilibria in shifted circle flux geometry also confirms the numerical calculations (Fig 6). Analytical work is in progress to explain these results.
Also the non-ideal effects as continuum damping and radiative damping will be investigated.

References

[1] Ph. Lauber, 'Linear Gyrokinetic Description of Fast Particle Effects on the MHD Stability in Tokamaks', Ph.D. Thesis, TU München, (2003)

[2] S. D. Pinches, 'Nonlinear Interaction of Fast Particles with Alfvén Waves in Tokamaks', Ph.D. Thesis, The University of Nottingham (1996)

[3] S. D. Pinches, L.C. Appel, J. Candy *et al.*, CPC **111**, 131 (1998)

[4] C.Z. Cheng, L. Chen, M.S. Chance, Annals of Physics **161**, 21 (1985)

[5] C.Z. Cheng, M.S. Chance, Phys. Fluids **29**, 11 (1986)

[6] G.Y. Fu, J.W. VanDam, Phys. Fluids **1**, 1949 (1989)

[7] R.R. Mett, S.M. Mahajan, Phys. Fluids B **4**, 2885 (1992)

[8] H.L Berk, R.R. Mett, and D.M. Lindberg, Phys. Fluids B **5**, 3969 (1993)

[9] G.Y. Fu, H. L. Berk, A. Pletzer, Phys. Plasmas **12**, 082505 (2005)

[10] A. Hasegawa, L. Chen, Phys. Rev. Lett. **35**, 370 (1975)

[11] A. Hasegawa, L. Chen, Phys. Fluids **19**, 1924 (1976)

[12] H. Qin, 'Gyrokinetic Theory and Computational Methods for Electromagnetic Perturbations in Tokamaks', Ph.D. Thesis, Princeton University (1998)

[13] H. Qin,W.M. Tang, G.Rewoldt, Phys. Plasmas **5**, 1035 (1998)

[14] G.T.A. Huysmans. J.P. Goedbloed, W. Kerner, Proc. CP90 Conf. on Comp Phys.Proc., World Scientific Publ.Co., p. 371 (1991)

[15] A. Könies, Joint Varenna-Lausanne Int. Workshop on 'Theory of Fusion Plasmas', (2004)

[16] A. Jaun, private communication (2004)

[17] G.Y. Fu, J.W. Van Dam , Phys. Fluids B **1** 2404 (1989)

[18] A. Fasoli, A. Jaun, D. Testa, Phys. Lett. A **265**, 288 (2000)

[19] D. Testa, G.Y. Fu, A. Jaun, A. Fasoli, O. Sauter and JET-EFDA contributors, Nucl. Fusion **43**, 479 (2003)

[20] D. Borba, H.L. Berk, B.N. Breizman, A. Fasoli, F. Nabais, S.D. Pinches, S.E. Sharapov, D. Testa and JET-EFDA contributors, Nucl. Fusion **42**, 1029 (2002)

[21] A. Jaun, K. Appert, J. Vaclavik and L. Villard, CPC **92**, 153 (1995)

[22] H. Kimura *et al* , Nucl. Fusion **38**, 1303 (1998)

[23] S.E. Sharapov *et al* , Phys. Plasmas **9**, 2027 (2002)

[24] H.L.Berk, D.N. Borba, B.N. Breizman, S.D. Pinches, S.E.Sharapov, Phys. Rev. Lett. **87**, 185002 (2001)

[25] B.N. Breizman, H.L Berk, and M.S. Pekker, Phys. Plasmas **10**, 3649 (2003)

[26] G.Y. Fu, private communication, (2005)

Alfvén Eigenmode Spectroscopy by Application of External Magnetic-Field Perturbations in the Compact Helical System

G. Matsunaga, K. Toi[a], C. Suzuki[a], A. Shimizu[a], M. Takechi,
N. Nakajima[a], A. Fukuyama[b] and CHS Group[a]

Japan Atomic Energy Agency, Naka 311-0193, Japan
[a]*National Institute for Fusion Science, Toki 509-5292, Japan*
[b]*Dept. of Nuclear Engineering, Kyoto University, Kyoto 606-8501, Japan*

Abstract
In many tokamaks and helical devices, Alfvén eigenmodes (AEs) driven by energetic ions are intensively studied because of the importance in a fusion reactor. In particular, much attention is paid to the damping rates of AEs. In order to evaluate the damping rate of AEs, AE spectroscopy system was constructed in the CHS. In the system, alternating currents are induced along the magnetic field line using two inserted electrodes. This system was applied to low temperature plasmas produced with 2.45GHz microwaves, for a basic study of damping mechanisms of AEs. The damping rate and AE frequency were derived from an analysis of frequency dependence of a transfer function measured by this system. In low temperature plasma produced at very low toroidal field $B_\mathrm{t} < 0.1\,\mathrm{T}$, fairly large damping rates of about $5 \sim 20\%$ were obtained. The AE spectroscopy experiments in low temperature plasmas were carried also for helium and neon gasses by changing electron density and B_t, to study characteristics of the damping rates in the wide range of the ratio of electron thermal velocity to the Alfvén one.

1. Introduction

In a future fusion reactor, energetic alpha particles could destabilize Alfvén eigenmodes (AEs) and in turn AEs would enhance a loss of alpha particles and lead to quench of DT ignition. The stability of energetic-ion driven AEs is determined through competition between the energetic ion drive and various damping mechanisms, such as ion and electron Landau damping, radiative, continuum and collisional damping and so on. These damping mechanisms have been theoretically investigated and several models have been suggested. However, it is difficult to experimentally confirm these models, because the damping rate of AE cannot be estimated in a plasma with fast ions. To obtain pure damping rates of AEs experimentally, it is necessary that stable AEs are excited using external perturbations, and plasma response as transfer function, which includes eigen-frequency and damping rate, are measured, that is the so-called 'Alfvén Eigenmodes Spectroscopy'. This experimental method was applied for the first time to a JET using saddle coils [1]. In helical device, we constructed AE spectroscopy system in the Compact Helical System (CHS), and then, carried out experiments in a low temperature plasma produced with 2.45GHz microwaves [2]. In our system, external magnetic perturbations can be generated by two electrodes inserted into a plasma. Furthermore, magnetic probe array was also inserted into a plasma to obtain a radial profile of transfer function. Since the plasma produced with 2.45GHz microwaves has very low electron and ion beta, that is $\beta_\mathrm{e} \ll 1$, $\beta_\mathrm{i} \ll 1$, neither electron nor ion Landau damping of background plasma can be effective. Besides, collisional damping with neutrals is also negligibly small because of highly ionized plasma. Therfore, continuum and radiative damping are expected to be dominant in this

type of plasma. In this paper, we will report the experimental results and compare them with theoretical results.

2. Experimental Setup

Alfvén eigenmodes spectroscopy system was constructed in the CHS with poloidal and toroidal field period numbers $l = 2$ and $N = 8$, of which major and averaged minor radii are $R \simeq 1\,\mathrm{m}$ and $\langle a \rangle \simeq 0.2\,\mathrm{m}$, respectively [3]. The magnetic configuration of a low beta plasma is determined mostly by external coils (helical and vertical coils), so that the safety factor q profile is well known. This is one of advantages for Alfvén eigenmodes study. In CHS, external coils make a strong magnetic shear $|s| > 1$ at the plasma edge compared with a tokamak device, $s\,(= (r/q)\mathrm{d}q/\mathrm{d}r)$, where q is the safety factor and r is the minor radius. Strong continuum damping is expected in CHS plasmas.

The schematic drawing of the newly developed AE spectroscopy in CHS is shown in Fig. 1. This system is composed of two insertable electrodes that are arranged apart from 180 degrees in the toroidal direction to specify the toroidal mode number, that is, even mode such as $n = 2$. An oscillatory voltage in the range of $1 \sim 300\,\mathrm{kHz}$ is applied between each electrode and the vacuum vessel wall, the oscillatory current is induced along a specified magnetic field line as an electron or ion saturation current, depending on the polarity of the applied voltage. That is, each electrode acts as a single Langmuir probe. The peak voltage applied to each electrode is $\pm 75\,\mathrm{V}$, and the electron saturation current reaches in the order of $1 \sim 4\,\mathrm{A}$. The electrode has a metallic plate of $30\,\mathrm{mm} \times 10\,\mathrm{mm}$ size perpendicular to the magnetic field line. One side of the metallic plate is insulated with a block of boron-nitride to specify the path of oscillatory current in the one toroidal direction. The most significant point of this system is that magnetic perturbations induced by the oscillatory current are perpendicular to the equilibrium magnetic field, and would generate shear Alfvén waves very effectively. Moreover, these electrodes can be inserted into a plasma core region up to the normalized radial position $\rho\,(= r/\langle a \rangle) \simeq 0.7$. In addition, detailed internal information of AE fluctuations can easily be obtained by insertion of a magnetic probe array and Langmuir probes.

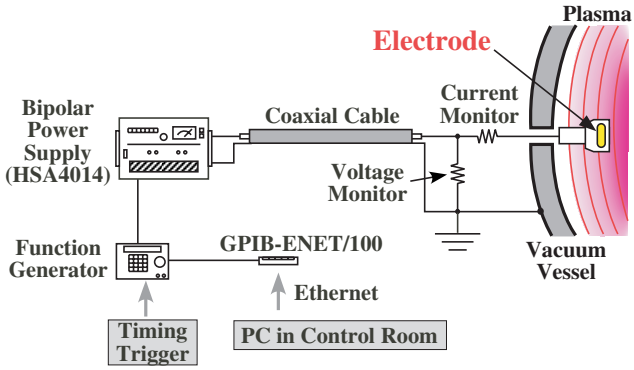

Fig. 1: Schematic drawing of AE spectroscopy system in CHS. An oscillatory voltage is applied between each electrode and the vacuum vessel wall

3. Experimental Results

3.1 Experiment in Low-β Plasma

We have carried out AE experiments in a very low-β plasma produced with 2.45GHz microwaves at very low toroidal field $B_\mathrm{t} < 0.1\,\mathrm{T}$. The line averaged electron density

and electron temperature at the plasma edge are in the range of $\bar{n_e} \sim 3 \times 10^{17}\,\mathrm{m}^{-3}$ and $T_e \leq 10\,\mathrm{eV}$, as shown in Fig. 2(b). These are measured by 2mm interferometer and Langmuir probe, respectively.

To investigate the dependence of the AE frequency on Alfvén velocity v_A, the line averaged electron density $\bar{n_e}$ was stepped up three times in one shot by the step-up of microwave power. In this experiment, the electrodes were inserted inside beyond the last closed flux surface (LCFS) up to $\rho \simeq 0.7$ in a low density and low temperature helium plasma. In this plasma an oscillatory voltage is applied in the frequency range 1 $\sim$ 300 kHz between each electrode and the vacuum vessel wall, since the expected TAE gap frequency is in the range of 50 kHz to 300 kHz. The oscillatory current is dominantly electron saturation current as expected, as shown in Fig. 2(e). This current is stepping up with increasing the electron density.

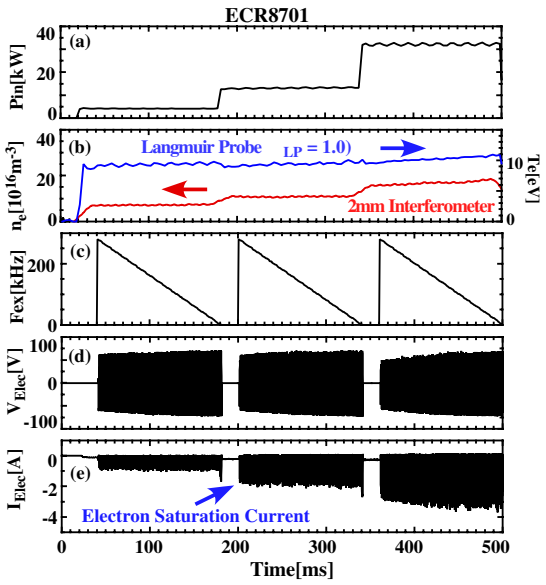

Fig. 2: Typical discharge waveform in the AE spectroscopy experiment. (a) Input microwave power, (b) electron temperature and density, (c) excitation frequency, (d) voltage and (e) current of electrode.

3.2 Transfer Function

We measured the radial profile of magnetic perturbations using magnetic probe array inserted into plasma. Therefore, plasma response with respect to the externally applied field can be obtained as complex function of excitation frequency f_{ex} and radial position r. Now, plasma response is deduced as a transfer function,

$$G_\theta(f_{ex}, r) = \frac{\dot{b}_\theta(f_{ex}, r)}{I_{Elec}(f_{ex})}\,[\mathrm{T}/(\mathrm{A}\cdot\mathrm{s})],$$

where $\dot{b}_\theta$ is the poloidal component of magnetic probe signal and I_{Elec} is the electrode current. In Fig. 3, the real part $\mathrm{Re}[G_\theta]$ and imaginary one $\mathrm{Im}[G_\theta]$ and the absolute value $|G_\theta|$

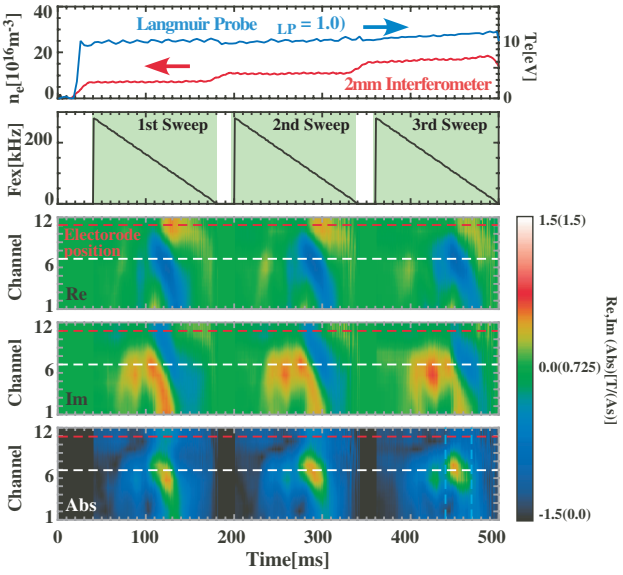

Fig. 3: Real part, imaginary part and absolute value of a transfer function with electron temperature, density and excitation frequency. Electrode position (red dash) and resonance position (white dash) are also shown.

are shown. Note that channel $1 \sim 12$ are corresponding to $r/a = 0.15 \sim 0.75$. When the excitation frequency $f_{\rm ex}$ is swept around 100 kHz, the transfer function $G_\theta(f_{\rm ex}, r)$ at ch.7 ($r/a \simeq 0.5$) would exhibit a character of resonance behavior related to $f_{\rm TAE}$.

3.3 Eigenfunction

In order to determine the location of the excited mode, eigen-function was roughly estimated from ideal MHD equations. The magnetic perturbation vector $\boldsymbol{b}$ will be related to the plasma displacement vector $\boldsymbol{\xi}$ through $\boldsymbol{b} = \nabla \times (\boldsymbol{\xi} \times \boldsymbol{B_0})$, where $\boldsymbol{B_0}$ is the vector of the equilibrium magnetic field. If a cylindrical configuration is assumed for simplicity, the radial displacement ξ_r is evaluated as

$$\begin{aligned} \xi_r(r) &\simeq -\frac{1}{B_\theta(r)} \int_0^r b_\theta(r') \mathrm{d}r' \\ &\propto \frac{1}{B_\theta(r)} \int_0^r G_\theta(r') \mathrm{d}r', \end{aligned}$$

where B_θ is the poloidal magnetic field. In this calculation, the magnitude and phase of G_θ are taken into account. The spatial integration of G_θ is shown in Fig. 4. This indicates that the eigenmode has a peak in the radial location of $\rho \simeq 0.4 - 0.6$.

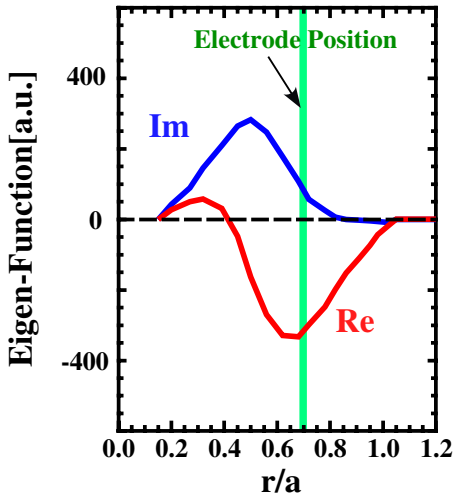

Fig. 4: Roughly estimated eigen-function at the resonance. Integration of real part and imaginary part of the transfer function.

3.4 Eigen-frequency and Damping Rate

In a low-β plasma without fast ions, the effective damping rate $\gamma_{\rm eff}\,(= \gamma_{\rm d} - \gamma_{\rm f})$ is equivalent to the damping rate $\gamma_{\rm d}$ because the fast ion drive $\gamma_{\rm f}$ is zero. Therefore, the damping can be derived from the shape of the transfer function $|G_\theta|$ at frequency $f_{\rm obs}$ where the absolute value of G_θ has a resonance peak. That is, $\gamma_{\rm d}^{\rm exp}/\omega_0 \propto \Delta f / f_{\rm obs}$, where Δf is the full width at the half maximum of the resonance peak and $\omega_0 = 2\pi f_{\rm obs}$. Plasma parameters related to the Alfvén velocity, that is, the toroidal field $B_{\rm t}$, the electron density $n_{\rm e}$ and the mass of the fuel ion $A_{\rm i}$ are varied in order to confirm that this resonance is related to AEs. Dependence of the observed resonance frequency $f_{\rm obs}$ on $v_{\rm A}$ and the estimated damping of excited modes are shown in Fig. 5. This

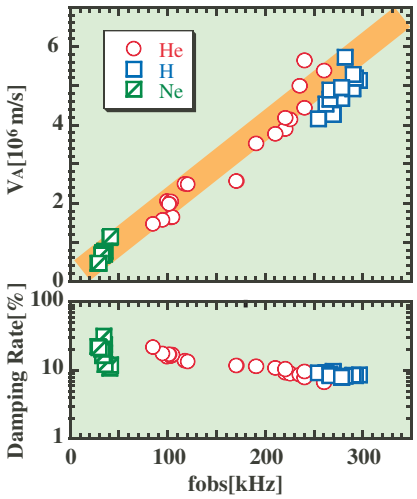

Fig. 5: Dependence of observed resonance frequency on $v_{\rm A}$ and damping rate of excited modes.

figure clearly indicates that the resonance is related to AEs and the damping is fairly large up to $\sim 20\%$.

3.5 Discussion

As mentioned above, electron and ion Landau damping of background plasma are negligibly small in the present plasma condition. Besides, collisional damping with neutrals is also negligible because the ionization degree is not fairly low [5]. Since CHS has a large magnetic shear near the plasma edge, continuum damping, which occurs as the resonant power absorption at the intersection of the eigenfrequency with a shear Alfvén continuum, is expected to be large. Here, the profiles of rotational transform $= 1/q$ and magnetic shear s in CHS are shown in Fig. 6(a). The magnetic shear is high, that is, $|s| > 1$ in the region of $\rho > 0.7$. The continuum damping is estimated by the equation in Ref.[4], as shown in Fig. 6(b). As shown in Fig. 4, the eigenfunction estimated from the experimental data seems to be broadened and then interact with Alfvén continuum near the edge. This eigenmode would suffer from large continuum.

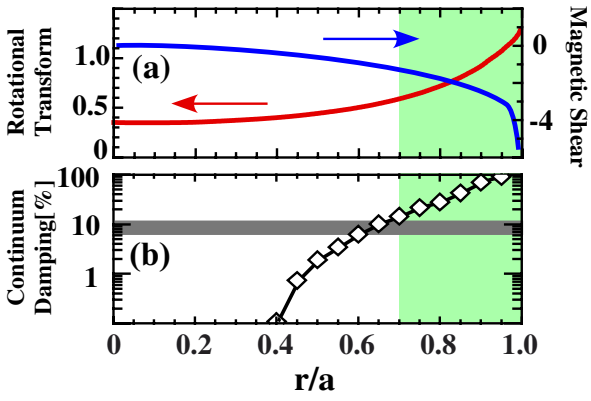

Fig. 6: Profile of (a) rotational transform ($= 1/q$), magnetic shear and (b) continuum damping rate calculated from Ref.[4].

Another important damping mechanism is radiative damping in this experimental condition. Radiative damping takes place within the gap region through mode coupling between AE and kinetic Alfvén wave (KAW) under $v_e > v_A$, where v_e is the electron thermal velocity. KAW transfers the wave energy of AE to the plasma core region from the gap region[6, 7]. Note that the radiative damping is effective under $k_\perp \rho_s \geq 1$, where $k_\perp$ and ρ_s are the wave number perpendicular to the magnetic field and the ion Larmor radius evaluated with the electron temperature. It expected that the radiative damping can be effective with the increase in ρ_s. Here, a dependence of the estimated damping rate on the ratio between electron thermal v_e and Alfvén velocity v_A is shown in Fig. 7. As shown in Fig. 7, the damping rates become larger in the range of $v_e > v_A$. It is qualitatively consistent with the radiative damping. The radiative damping is estimated by the equation

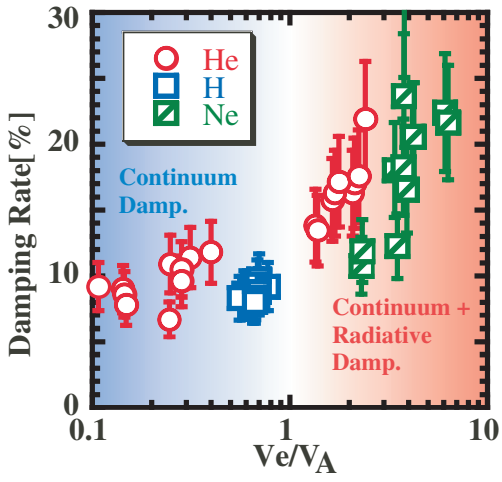

Fig. 7: The estimated damping rate versus the ratio between electron thermal v_e and Alfvén velocity v_A.

in Ref.[6], that is,

$$\frac{\gamma_{\rm k}}{\omega} = 3\left\{\frac{m(m+1)}{2m+1}\left(\frac{s}{\sqrt{2}}\right)\frac{\rho_{\rm s}}{r}\right\}^{2/3}.$$

In the rang of $v_{\rm e} \simeq v_{\rm A}$, $\rho_{\rm s}$ and the radiative damping is about 1 cm and $5 \sim 20\%$, respectively.

In addition, other damping mechanisms are still possible candidates. This plasma is more resistive compare with those of large tokamaks. Alfvén wave can be damped by the resistivity having a functional dependence of $T_{\rm e}^{-3/2}$. However, the damping rates would be very large and the mode becomes purely damped wave without an oscillatory character, if resistive damping is dominant. At the moment, it is thought that continuum and radiative damping are dominant in this plasma condition.

4. Summary

In conclusion, AE spectroscopy using electrodes was successfully carried out in a low temperature plasma produced by 2.45GHz ECH on CHS. In this experiment, the eigen-frequency and damping rate of AEs were successfully derived from the resonant character of the transfer function G_θ. Transfer functions show that the eigenmode which agrees well with AE gap frequency is located around $r/a \sim 0.5$. The derived damping rate of $\sim (5-20)\%$ is thought to be dominated by continuum damping. Moreover, in the regime of $v_{\rm A} \leq v_{\rm e}$, the damping rates are enhanced. Radiative damping may be responsible for the enhanced damping.

Application of this newly developed electrode technique to a low temperature and low density plasma will make the detailed investigation of the excitation and damping of AEs easier in three-dimensional magnetic configuration such as various types of stellarators or helical devices.

Acknowledgments

This work was supported in part by the Grand-in-Aid for Scientific Research from MEXT, No. 16082209 and from JSPS, No. 15206107.

References

[1] A. Fasoli et al., Phys. Rev. Lett. **75**, 645 (1995).

[2] G. Matsunaga et al., Phys. Rev. Lett. **94**, 225005 (2005).

[3] K. Matsuoka et al., in *Plasma Physics and Controlled Nuclear Fusion Research 1988: Proceedings of the 12th IAEA Conference Nice, 1988* (IAEA, Vienna, 1989), vol. 2, p. 411.

[4] M. N. Rosenbluth et al., Phys. Rev. Lett. **68**, 596 (1992).

[5] Y. Amagishi and A. Tsushima, Plasma Phys. & Controlled Fusion **26**, 1489 (1984).

[6] R. R. Mett and S. M. Mahajan, Phys. Fluids B: Plasma Phys. **4**, 2885 (1992).

[7] A. Jaun et al., Phys. Plasmas **5**, 2952 (1998).

Stability boundaries for fast particle driven TAE in stellarators

Axel Könies

Max-Planck-Institut für Plasmaphysik, Teilinstitut Greifswald,
EURATOM-Association, D-17491 Greifswald, Wendelsteinstr. 1
axel.koenies@ipp.mpg.de

Abstract

The influence of fast particles on TAE modes in stellarators is investigated in the framework of a kinetic MHD approach. The theoretical model couples ideal MHD with a drift kinetic equation allowing the perturbative calculation of growth and damping rates due the several particle species. Here, the code considers passing particles only. Comparison is made between the numerical results and a local theory where the latter turned out to be a useful first guess approximation. While the fast particle drive is, as in tokamaks, mainly due to the coupling with the toroidal components of the modulus of the magnetic field, the ion contributions to the damping stem from the coupling with the helical components.

1. Introduction

Meanwhile, several experimental investigations of fast particle effects in stellarators as eg., in W7-AS [1, 2], have been made. Recently, the parameter space for the exitation of toroidal Alfvén eigen modes (TAE's) and energetic particle modes (EPM's) has been explored at LHD [3]. Regarding this progress in the quantitative assessment, it is desirable to develop according theoretical tools.
We will show that the theory can predict stability limits for Alfvén eigenmodes in three-dimensional equilibria from both the analytical and the numerical point of view.
A drift-kinetic extension [5] of the ideal magneto-hydrodynamic (MHD) stability code CAS3D [7] is applied to shot No. 39042 of W7-AS [1] and a W7-X equilibrium. The equilibrium for W7-X is a high-β ($\beta = 4.2\%$) practically island free equilibrium which has been obtained from a PIES calculation [4].

2. Theory

We start from a three- dimensional MHD description of plasma stability and use the CAS3D stability code [7]. It has been shown that a kinetic energy principle can be derived which couples the drift kinetic particle species (electron, ions, and a fast ion component) to the MHD stability equations via an expression for the pressure in the force balance equation [5].
To avoid following 3D particle orbits explicitly, a technique invented by Rewoldt et al. [9] which is being used in numerous 2D codes [10, 11] has been adopted. The particles move

along field lines feeling a bounce or transit averaged drift only. The radial extension of the particle orbits is not taken into consideration.
The particle-wave energy exchange by resonant interaction is given by

$$\begin{aligned}\delta W_{\rm s} &= \frac{\pi}{M^2}\left\{\begin{matrix}\sum\\ \sigma\end{matrix}\right\}\int ds\int d\varphi\int d\mu\, d\epsilon\left(-\int\frac{d\vartheta}{|v_{||}|}\sqrt{g}B\right)\\ &\times\sum_{\substack{n,m\\ n',m'}}\sum_{p=-\infty}^{\infty} e^{-i\frac{2\pi}{N_p}(n'-n)\varphi}\\ &\times\left(\frac{\partial F}{\partial\epsilon}\right)_\mu\frac{\omega-2\pi(\frac{n}{N_p}J-mI)\omega^*}{m\left\langle\omega_d^\vartheta\right\rangle+\frac{n}{N_p}\left\langle\omega_d^\varphi\right\rangle+\left\{\begin{matrix}\sigma(p+nq)\\ p\end{matrix}\right\}\omega_{\left\{\begin{matrix}t\\ b\end{matrix}\right\}}-\omega}\\ &\times L^{(1)*}_{m'n'}\mathcal{M}^{m'n'*}_{pn}\,L^{(1)}_{mn}\mathcal{M}^{mn}_{pn}\end{aligned}\tag{1}$$

with the following definitions of $\mathcal{M}^{m'n'}_{pn}$:
for passing particles

$$\mathcal{M}^{m'n'}_{pn}=\left\langle e^{i[2\pi(m'+n'q)\vartheta''-(p+nq)\omega_t t'']}\right\rangle_{\vartheta''}\tag{2}$$

and for reflected particles

$$\mathcal{M}^{m'n'}_{pn}=\left\langle e^{2\pi i(m'+n'q)\vartheta''}[\cos^2(\frac{\pi}{2}p)\cos(p\omega_b t'')-i\sin^2(\frac{\pi}{2}p)\sin(p\omega_b t'')]\right\rangle_{\vartheta''}.\tag{3}$$

The perturbed particle Lagrangian is given by

$$L^{(1)}=-(Mv_\parallel^2-\mu B)\vec{\xi}_\perp\cdot\vec{\kappa}+\mu B\vec{\nabla}\cdot\vec{\xi}_\perp\,.$$

Here, $\langle\ldots\rangle$ denotes the transit or bounce average ($t''=t''(\vartheta'')$)
The complete energy integral can be written as

$$\omega^2\delta W_{\rm kin}=\delta W_{\rm mag}+\sum_{\rm s=i,e,hot}\delta W_{\rm s}(\omega)\tag{4}$$

and constitutes a nonlinear eigenvalue problem for the mode frequency ω. In this paper, we will restrict to passing particles and a perturbative approach, i.e. we assume that $\delta W_{\rm s}\ll\delta W_{\rm mag}$, where $\delta W_{\rm kin}$ and $\delta W_{\rm mag}$ are the constituents of the ideal MHD energy principle with vanishing pressure contribution ($\gamma_a\approx 0$).
In this linear model, each species contributes separately to the growth or damping rate of the mode which can be calculated perturbatively according to:

$$\Delta\omega_s+i\gamma_s\approx\frac{1}{2}\frac{\delta W_{\rm s}(\omega_0)}{\delta W_{\rm mag}}\omega_0\tag{5}$$

using the MHD eigenfunctions and the MHD frequency ω_0 of the CAS3D result on the right hand side.
Obviously, the mode is unstable if the growth rate γ is larger than zero:

$$\gamma=\gamma_{\rm hot}+\gamma_{\rm i}+\gamma_{\rm e}>0\,.\tag{6}$$

This condition allows the derivation of stability boundaries (i.e. a critical $\beta_{\rm fast}$) with respect to different parameters.

3. Local limit and resonance condition for fast particles

In the limit of localized modes, i.e. very large aspect ratio the expression for the passing particle fraction in Eq. (5) corresponds to the local theory developed in [8]. Additionally, we allow for a temperature gradient of thermal electrons and ions and arbitrary couplings between the mode and the Fourier components of the equilibrium magnetic field but neglect the suggested reflected particle correction. Furthermore we correct a numerical error in the application of the local theory in an earlier publication [6].

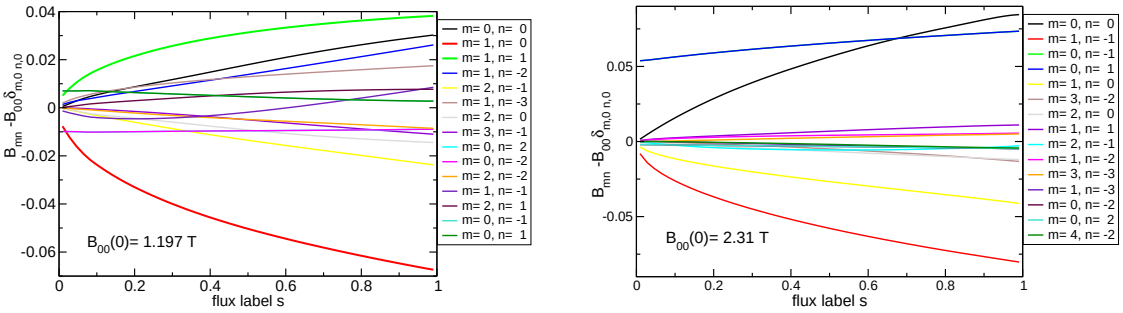

Figure 1: *Fourier components of the modulus of the magnetic field for W7-AS(#39042) (left) and W7-X (right)*

In the large aspect ratio limit the resonance condition is

$$v^{\mathrm{res}}_{m'n'} = v_A \left| 1 \pm \frac{m'\iota^* + n' N_p}{m\iota^* + n} \right|^{-1} \tag{7}$$

where N_p is the number of periods, ι^* labels the local value of the rotational transform where the Alfvén branches cross, m, n are the mode numbers of the Alfvén wave and m', n' label the component $B_{m'n'}$ to which the mode couples. For the local calculations, we consider the two main components of B_{mn} (see Fig. 1) only.

4. Results

We chose a W7-AS shot (No. 39042) which has already been discussed in the literature [1, 6]. Although, in this case, the fast ion drive is relatively small, the mode numbers and

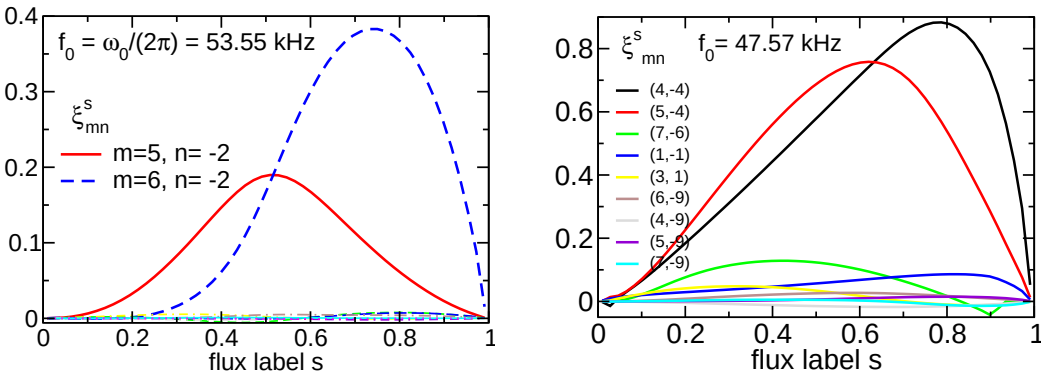

Figure 2: *mode structures of the W7-AS case (left) and the W7-X case (right)*

the mode structure were identified experimentally to be a toroidal Alfvén eigen mode (TAE) with its main Fourier components being $m = 5, n = -2$ and $m = 6, n = -2$. The calculations have been performed resembling the experimental conditions as close as possible taking a slowing down distribution for the fast ions from the neutral beam injection. Additionally, the energy of the bulk and beam ions will be varied to distinguish different contributions to the growth rate and to calculate stability diagrams.

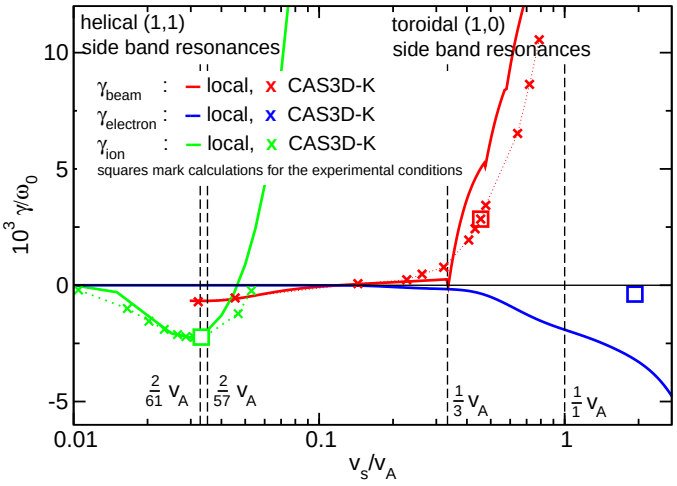

Figure 3: *Growth or damping rates, resp. of electrons, ions and beam ions vs. the ratio of velocity of the species to the Alfvén velocity. The lines of the major side band resonances have been indicated by dashed lines. Note, that* β_{fast} *was kept constant during the variation, while* $\sqrt{\beta_i} = v_{th,i}/v_A$*. The calculations for the experimental conditions have been marked with a square.* $v_A(s_0) = 4.65 \cdot 10^6\,\text{ms}^{-1}$

The growth or damping rates for bulk and fast ions, both being deuterons, are shown in Fig. 3. In general the agreement between both approaches is remarkably good considering the simplicity of the local approach.

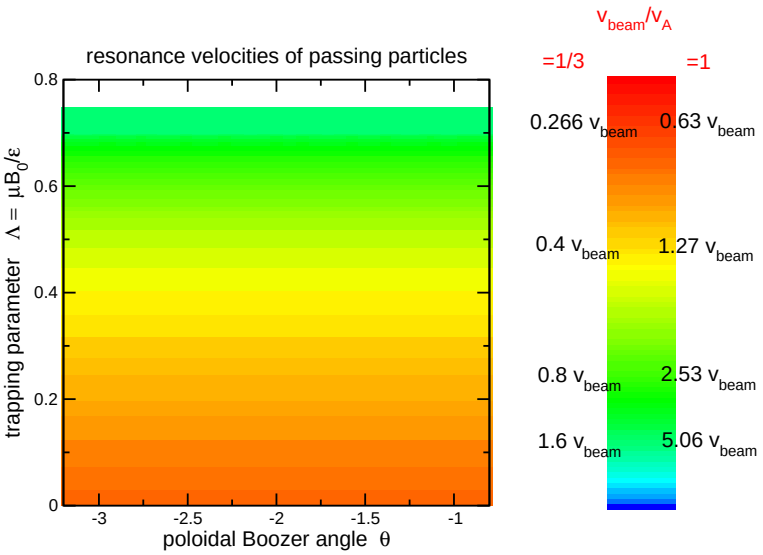

Figure 4: *Shown is the field line average of the transit frequency* $< \omega_t >$ *from Eq. (1), but normalized to the toroidal resonance velocities in units of* v_{beam}/v_A*.* v_{beam} *denotes the maximum beam velocity here. Therefore only those particles with* $v_t|_r < 1.0 v_{beam}$ *can contribute. Note, that the angle* θ *serves here as a field line label.*

We see that the main contributions to both, ion damping and fast ion growth rate, are connected with the resonance velocities due the coupling of the mode with the equilibrium magnetic field. For the hot particles, the growth rate increases rapidly when the maximum beam velocity exeeds the resonance velocity of $1/3 v_A$. The electron damping is weak ($\gamma_e = -3.82 \cdot 10^{-4}$) because the electron thermal velocity at the location of the mode ($\approx 1.933\, v_A(s_0)$) is beyond the important resonances.
To understand how the resonance condition looks like in the complex numerical model we look at the variation of the field line averaged transit frequency (Fig. 4): The

variation of this quantity with the field line label is so small that it is not resolved in the figure. It does mainly depend on the trapping parameter. In this sense, the picture shows a tokamak-like behaviour. On the other hand, we see that those particles which have a large $v_{||}$ (small Λ) can resonate with the side bands and contribute to the growth rate. This fits to the assumptions of the local theory and may partly explain its relative success. Another reason is presumably the relatively low shear of both equilibria. From eq. (7) we see that the smaller the change in ι the smaller is the radial variation of the resonance condition. The comparison of the stability diagrams (see Fig.5) with the

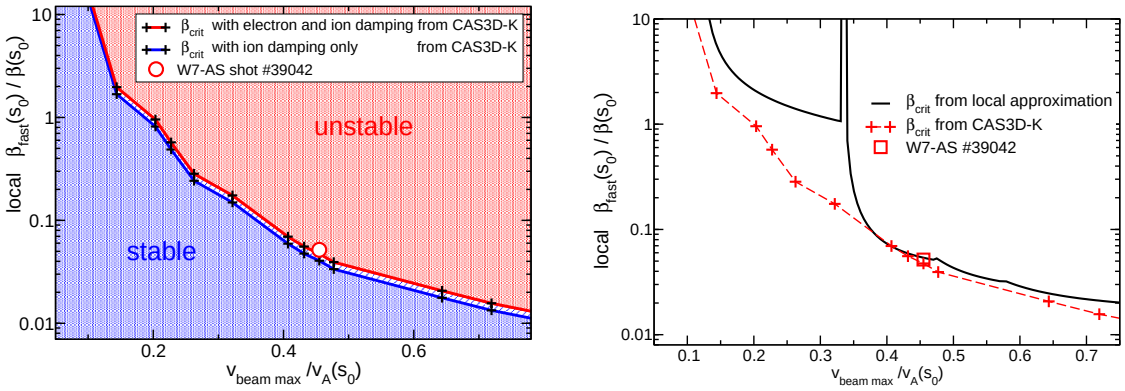

Figure 5: *The critical $\beta_{\rm fast}/\beta$ vs. the ratio of maximum beam velocity to Alfvén velocity which constitutes a stability limit. The local approach following [8] is compared with the results from CAS3D-K.*

beam velocity shows differences for small beam velocities. The global code predicts a weak instability of $1.1\beta_{\rm fast\,crit}$, being in good agreement with the local result. The same is true for the approximate threshold value in $v_{\rm beam\ max}/v_A \approx 0.1$

For the W7-X mode, the agreement between local and global results is still better than a factor of two. Nevertheless, the numerical model again predicts the mode to be less stable. However, for the high β_i case considered here, the low energy part of the fast particle distribution function is expected to deviate from the simple slowing down model for envisaged neutral beam injection scenarios [12]. Therefore, to predict NBI stability, a refined model of the distribution function will be included in CAS3D-K.

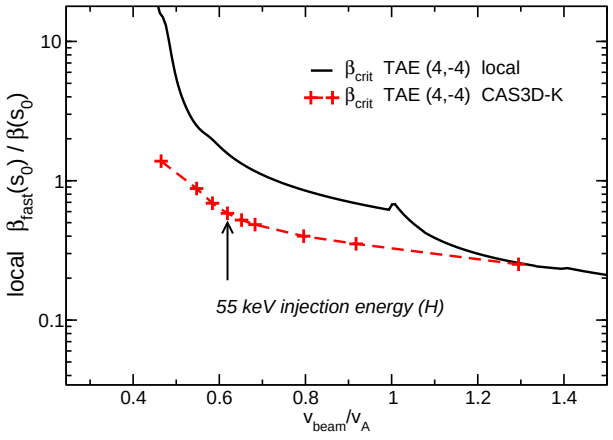

Figure 6: *The critical $\beta_{\rm fast}/\beta$ vs. the ratio of maximum beam velocity to Alfvén velocity. As for the W7-AS case, the injection energy has been varied.*

5. Contribution of thermal ions

In this type of theory (kinetic MHD), it is possible that modes are destabilized by the temperature gradients of the thermal ions. This is illustrated in Fig. 7.

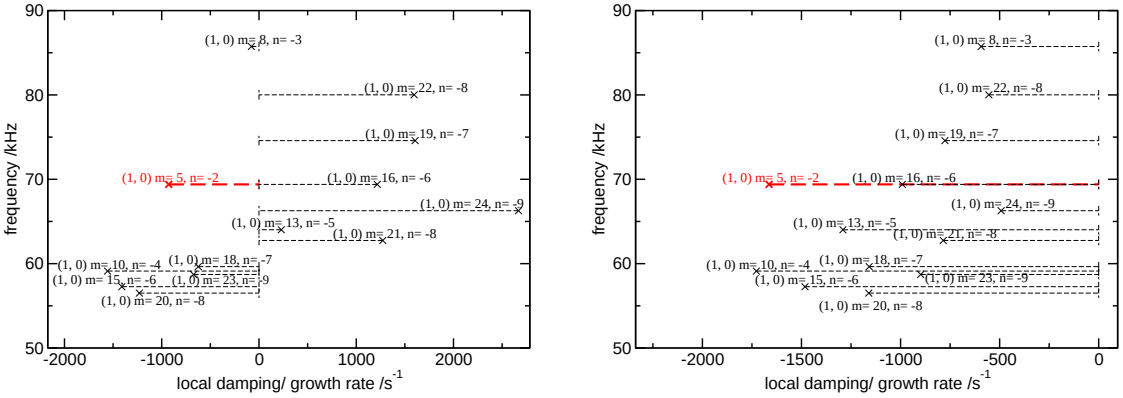

Figure 7: *local approach to ion damping rate with (left) and without (right) temperature gradient considered for several TAE modes for the W7-AS case*

It is an interesting question in how far this MHD model of kinetic growth and damping rates reflects the real behavior of the plasma. However, a decisive answer is not yet known, not even for tokamaks but can be expected from gyrokinetic codes as e.g. [11, 13, 15] see also [14]. In this paper we only took a closer look on modes which are stable also with an ion temperature gradient The extension of the model to include non-ideal

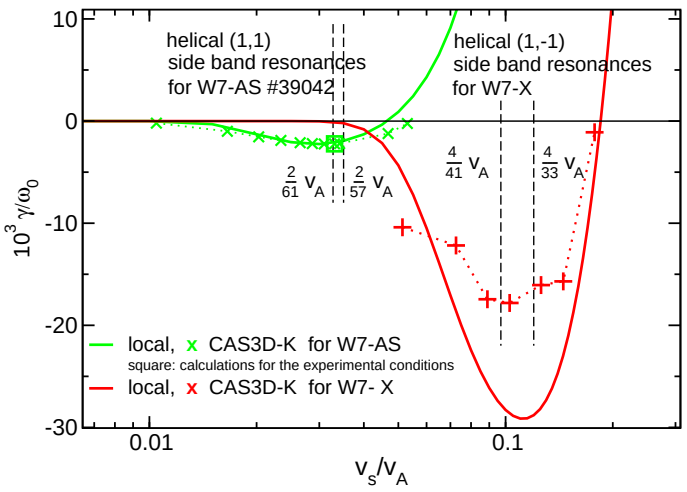

Figure 8: *Comparison of the ion damping for the W7-AS and the W7-X case. The main contributions come from the coupling to the helical components of B. Note, that the peak damping rate for W7-AS corresponds to $T_i = 400eV$, while the ion temperature for the W7X-case is $T_i = 3.8keV$. The higher ι of the W7-X equilibrium mainly accounts for the difference in the resonance conditions*

(i.e. finite gyro radius and finite $E_{\|}|$ effects) at least on the fluid side (for the equations see e.g. [16]) is underway and will allow access to cases where the gaps are closed.

6. Conclusion

The drift kinetic MHD growth and damping rates of a fast particle driven TAE mode have been calculated for realistic 3D conditions (W7-AS shot No. 39042).
Varying parameters as ion temperature and maximum beam velocity, stability diagrams have been calculated. The results indicate that this particular shot is close to marginality. These theoretical stability diagrams open up a possibility for more comparisons with the experimental exploration of the parameter space.

The results for the chosen W7-X equilibrium show that the local theory is a reasonable approximation but may deviate quantitatively, especially for small injection energies. The good agreement may be due to the small shear of the considered equilibria.
It is shown that resonances stemming from the coupling to the helical side bands contribute mainly to the ion damping for both equilibria. This constitutes a genuine effect of three dimensional equilibria.
The fast particle drive, on the other hand, comes mainly from the well known toroidal side band resonances at $1/3v_A$ and $1/1v_A$. The electron contribution to the damping is small because the electron velocity is larger than the Alfvén velocity.

Acknowledgment

The author wants to thank S. Zegenhagen for the good collaboration and many discussions, also J. Nührenberg, C. Nührenberg, R. Kleiber and M. Drevlak for valuable comments, A. Werner, H. Massberg and A. Weller for stimulating helpful discussions and informations on the experimental conditions.

References

[1] A. Weller et al., Phys. Plasmas, **8**, 931 (2001).

[2] A. Weller et al.,Plasma Phys. Control. Fusion, **45**, A285 (2003).

[3] K. Toi et al., Nucl. Fusion **44** 217 (2004).

[4] M. Drevlak, D. Monticello, and A. Reiman, Nucl. Fusion **45** 731 (2005)

[5] A. Könies, Phys. Plasmas **7**, 1139 (2000).

[6] A. Könies, in "Theory of Fusion Plasmas", Eds. J. W. Connor et al., Bologna 2004, p. 297.

[7] C. Nührenberg, Phys. Plasmas **6**, 137 (1998), C. Nührenberg, Plasma Phys. Control. Fusion **41**. 1055 (1999)

[8] Ya. I. Kolesnichenko, V. V. Lutsenko, H. Wobig, Yu. V. Yakovenko, Phys. Plasmas **9**, 517 (2002).
Ya. I. Kolesnichenko, et al. Phys. Plasmas, **11** 158 (2004).

[9] R. Marchand, W.M. Tang, and G. Rewoldt, Phys. Fluids **23** 1164 (1980)

[10] C. Z. Cheng, Phys. Rep. **211**, 1 (1992).

[11] H. Qin, W. M. Tang, and G. Rewoldt, Phys. Plasmas **6**, 2544 (1999)

[12] S. Zegenhagen, private communication.

[13] P. Lauber, Diss. TU München (2003).

[14] P. Lauber et al., this conference

[15] A. Jaun, Nuclear Fusion, **40**, 1343 (2000).

[16] J. Candy, M. N. Rosenbluth, Plasma Phys. Control. Fusion **35**, 957 (1993).

Simulation Study of Energetic Ion Distribution during Combined NBI and ICRF Heating in LHD

S. Murakami[1], A. Fukuyama[1], V. Kasilov[2], T. Mutoh[3], R. Kumazawa[3], T. Seki[3], K. Saito[3], T. Watari[3], M. Isobe[3], M. Nishiura[3], T. Ozaki[3], M. Osakabe[3], M. Sasao[4], and LHD Experimental Group

[1]Department of Nuclear Engineering, Kyoto University, Kyoto 606-8501, Japan
[2]Institute of Plasma Physics, National Science Center, KIPT, Kharkov, Ukraine
[3]National Institute for Fusion Science, Oroshi, Toki, Gifu 509-5292, Japan
[4]Graduate School of Engineering, Tohoku University, Sendai 980-8579, Japan

e-mail contact of main author: murakami@nucleng.kyoto-u.ac.jp

1. Introduction

In the LHD, significant performances of ICRF heating (fundamental, minority heating regime) have been demonstrated[1-4] and up to 500keV of energetic tail ions have been observed by fast neutral particle analysis (NPA)[5-7]. These measured results indicate a good property of energetic ion confinement in helical systems. From the 9th campaign of LHD experiment (FY2005) a new perpendicular NBI heating system (P<3MW) has been installed and an effective heating of perpendicularly injected beam ions by the higher harmonics ICRF heating is expected.

ICRF heating generates highly energetic tail ions, which drift around the torus for a long time (typically on a collisional time scale). Thus, the behavior of these energetic ions is strongly affected by the characteristics of the drift motions, which depend on the magnetic field configuration. In particular, in a three-dimensional (3D) magnetic configuration, complicated drift motions of trapped particles would play an important role in the confinement of the energetic ions and the ICRF heating process. Therefore a global simulation of ICRF heating is necessary for the accurate modeling of the plasma heating process in a 3D magnetic configuration.

In this paper we study the energetic ion distribution during combined NBI and 2nd harmonics ICRF heating in LHD using two global simulation codes: a full wave field solver TASK/WM[8] and a drift kinetic equation solver GNET[9-11]. GNET solves a linearized drift kinetic equation for energetic ions including complicated behavior of trapped particles in 5-D phase space. TASK/WM solves Maxwell's equation for RF wave electric field with complex frequency as a boundary value problem in the 3D magnetic configuration.

2. Simulation Model

In order to study the ICRF heating in a 3D magnetic field configuration we have been developing two global simulation codes; GNET and TASK/WM. GNET solves a linearized drift kinetic equation for energetic ions including complicated behavior of trapped particles in 5-D phase space

$$\frac{\partial f_{beam}}{\partial t} + (\mathbf{v}_{//} + \mathbf{v}_D)\cdot\nabla f_{beam} + \mathbf{a}\cdot\nabla_{\mathbf{v}} f_{beam} \; - C(f_{beam}) - Q_{ICRF}(f_{beam}) - L_{particle} = S_{beam}\,, \quad (1)$$

where $C(f)$ and Q_{ICRF} are the linear Coulomb Collision operator and the ICRF heating term. S_{beam} is the particle source term by NBI heating. The $S_{particle}$ is evaluated by NBI heating analysis code, HFREYA.

The particle sink (loss) term, $L_{particle}$, consists of two parts. One is the loss by the charge exchange loss. In the simulation we assume the same neutral particle profile as the source term calculation. The other is the loss by the orbit loss escaping to outside of the simulation region. In this simulation we assume the outermost flux surface as the boundary of simulation region.

The Q_{ICRF} term is modeled by the Monte Carlo method. When the test particle pass through the resonance layer where $\omega - k_{//}v_{//} = n\omega_c$, the perpendicular velocity of this particle, $\mathrm{v}_{\perp 0}$, is changed by the following amount

$$\begin{aligned}\Delta \mathrm{v}_\perp &= \sqrt{\left(\mathrm{v}_{\perp 0} + \frac{q}{2m} I|E_+| J_{n-1}(k_\perp\rho)\,\cos\phi_r\right)^2 + \frac{q^2}{4m^2}\left\{I|E_+| J_{n-1}(k_\perp\rho)\right\}^2\,\sin^2\phi_r} - \mathrm{v}_{\perp 0} \\ &\approx \frac{q}{2m} I|E_+| J_{n-1}(k_\perp\rho)\,\cos\phi_r + \frac{q^2}{8m^2\mathrm{v}_{\perp 0}}\left\{I|E_+| J_{n-1}(k_\perp\rho)\right\}^2\,\sin^2\phi_r\end{aligned} \quad (5)$$

where E_+ and ϕ_r are the RF wave electric fields and random phase, respectively. Also, q, m, ρ, J_n are the charge, mass and the Larmor radius of the particle, and n-th Bessel function, respectively. The time duration passing through the resonance layer, I, is given by the minimum value as, $I = \min(\sqrt{2\pi/n\dot{\omega}}\,,\, 2\pi(n\dot{\omega}/2)^{-1/3}Ai(0))$, which corresponds to two cases; the simply passing of the resonance layer and the passing near the turning point of a trapped motion (banana tip).

The spatial profile of RF wave electric field is necessary for the accurate calculation of the ICRF heating. The profile of RF wave field is an important factor on the ICRF heating and this profile affects the particle orbit. We evaluate the RF wave field by the TASK/WM code. TASK/WM solves Maxwell's equation for RF wave electric field, $\mathbf{E}_{RF}$, with complex frequency, ω, as a boundary value problem in the 3D magnetic configuration.

$$\nabla\times\nabla\times\mathbf{E}_{RF} = \frac{\omega^2}{c^2}\vec{\varepsilon}\cdot\mathbf{E}_{RF} + i\omega\mu_0\mathbf{j}_{ext}, \quad (8)$$

Here, the external current, $\mathbf{j}_{\mathrm{ext}}$, denotes the antenna current in ICRF heating. The response of the plasma is described by a dielectric tensor including kinetic effects in a local normalized orthogonal coordinates.

3. Simulation Results

We consider a LHD configuration (R_{ax} = 3.6m; the in-ward shifted configuration) to investigate the energetic ion distribution during combined heating of perpendicular NBI and ICRF heating. The LHD configuration of R_{ax} = 3.6m conforms the σ-optimized configuration and shows relatively good trapped particle orbit. Most of ICRF heating experiments have been performed in this configuration because of the relatively good performances of this configuration.

We, first, solve the drift kinetic equation for the beam ions without ICRF heating using GNET. Figure 1 shows the iso-surface plot of the steady state distribution of beam ions without ICRF heating. We plot the flux surface averaged tail ion distribution in the three dimensional space (r/a, E, θ_p), where a/r, E and θ_p are the normalized averaged minor radius, the total energy and the pitch angle, respectively. The plasma temperature and density are assumed as $T_s=(T_{s0}-T_{sw})(1-(r/a)^2)+T_{sw}$ with $T_{e0}=T_{i0}$=1.6keV and $n_e=(n_{e0}-n_{ew})(1-(r/a)^8)+n_{sw}$ with n_{e0}=1.0x10^{19}m^{-3}. The injection perpendicular beam ion energy, E_b, is 40keV.

The high distribution regions can be seen near the beam sources: the pitch angle is about π/2 (almost perpendicular) and the three energy components (E_b, $E_b/2$, $E_b/3$). The beam ion distribution shows slowing down and pitch angle diffusion in velocity space.

Next we study the energetic ion distribution during combining heating of perpendicular NBI and 2nd harmonics ICRF. Based on the wave field profile by TASK/WM code, a simple RF wave electric fields profile; $E_+= E_{+0}\tanh((1-r/a)/l)\cos\theta$ with l=0.2 is assumed as a first step in the GNET simulation. The other wave field parameters are set as k_{perp}=62.8m^{-1} and $k_{//}$=0. The amplitude of the wave field, E_{+0}, is changed in the range 0.5kV/m through 1.5kV/m to obtain the dependency on the heating power.

Figure 2 shows the iso-surface plot of the steady state distribution of the beam ions with 2nd harmonics ICRF heating obtained by GNET. The RF wave accelerates beam ions perpendicularly in the velocity space and we can see perpendicularly elongated beam ion distributions by 2nd-harmonics ICRF heating. We find a peaked energetic tail ion distribution near r/a~0.5. The elongation of the distribution is larger than that of the fundamental heating case[11].

We next evaluate the beam ion pressure (a energy weighted population of energetic ions) in the real space. We plot the one of ten helical pitches and the right (left) side is the outside (inside) of torus. We can see the clear difference between two heating cases. The high-pressure regions are localized along the helical ripples where the magnetic field is weak in the case without the ICRF heating. On the other hand the high-pressure region is strongly localized near the resonance surface along the helical ripples in the case with the ICRF heating.

We have simulated the NDD-NPA[7] using the GNET simulation results. It is found that the tail ion energy is enhanced to MeV order and a larger tail formation can be seen than that of the fundamental harmonic heating case.

5. Conclusions

We have been developing an ICRF heating simulation code in toroidal plasmas using two global simulation codes; GNET and TASK/WM. The GNET code solves a linearized drift kinetic equation for energetic ions including complicated behavior of trapped particles in 5-D phase space and the TASK/WM code solves Maxwell's equation for RF wave electric field with complex frequency as a boundary value problem in the 3D magnetic configuration. The complete combining of these two codes is being developed and we perform a simulation using the tentative version.

The developed code has been applied to investigate energetic ion distribution during combining heating of the perpendicular NBI and 2nd harmonics ICRF heating in the LHD. A steady state distribution of energetic tail ion has been obtained and the characteristics of distribution in the phase space are clarified. The GNET simulation results have shown an effective energetic particle generation in the 2nd harmonics ICRF heating in LHD.

Acknowledgments
This work was supported by Grant-in-Aid from the Japanese Ministry of Education, Culture, Sports, Science and Technology. Also this work is performed with the support and under the auspices of the NIFS Collaborative Research Program.

References

[1] MUTOH, T., et al, Phys. Rev. Lett. **85** (2000) 4530.
[2] KUMAZAEA, R., et al., Phys. Plasmas **8** (2001) 2139.
[3] WATARI, T., et al. Nucl. Fusion **41** (2001) 325.
[4] MUTOH, T., et al., Fusion Sci. Technol. **46** (2004) 175.
[5] KRASHILNIKOV, A.V., et al., Nucl. Fusion 42 (2002) 759.
[6] SAIDA, T., et al., Nuclear Fusion **44** (2004) 488.
[7] ISOBE, M., et al., Rev. Sci. Instrum. **72** (2001) 611.
[8] FUKUYAMA, A., YOKOTA, E., AKUTSU, T., Proc. 18th IAEA Conf. on Fusion Energy (Sorrento, Italy, 2000) **THP2-26**.
[9] MURAKAMI, S., et al., Nuclear Fusion **40** (2000) 693.
[10] MURAKAMI, S., et al., Fusion Sci. Technol. **46** (2004) 241.
[11] MURAKAMI, S., et al., *in Proc.* 20th IAEA Fusion Energy Conf. 2004, Vilamoura, Portugal, IAEA, 2005, **TH/P4-30**.

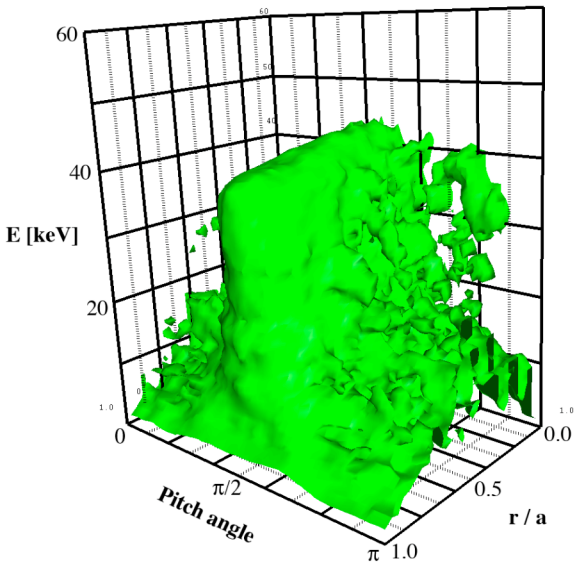

FIG. 1 *Steady state distribution of beam ions in the (r/a, E, pitch angle) space without ICRF heating.*

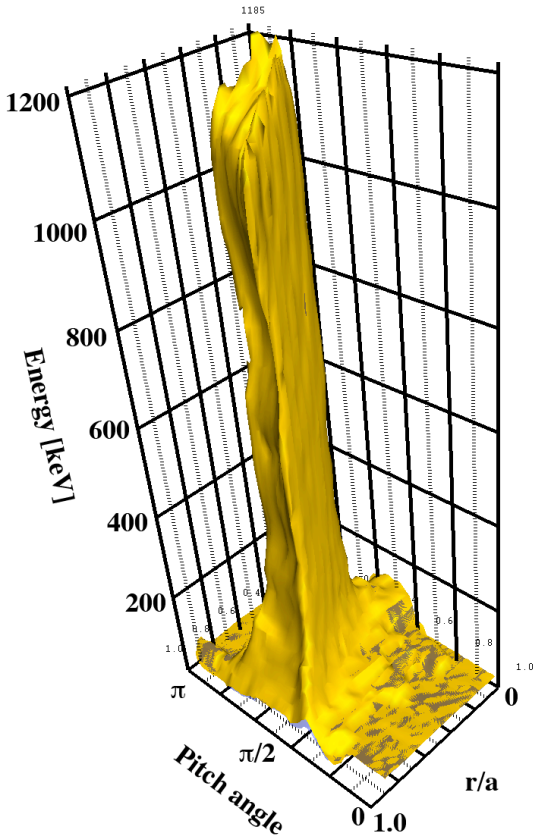

FIG. 2 *Steady state distribution of beam ions in the (r/a, E, pitch angle) space with 2nd harmonics ICRF heating.*

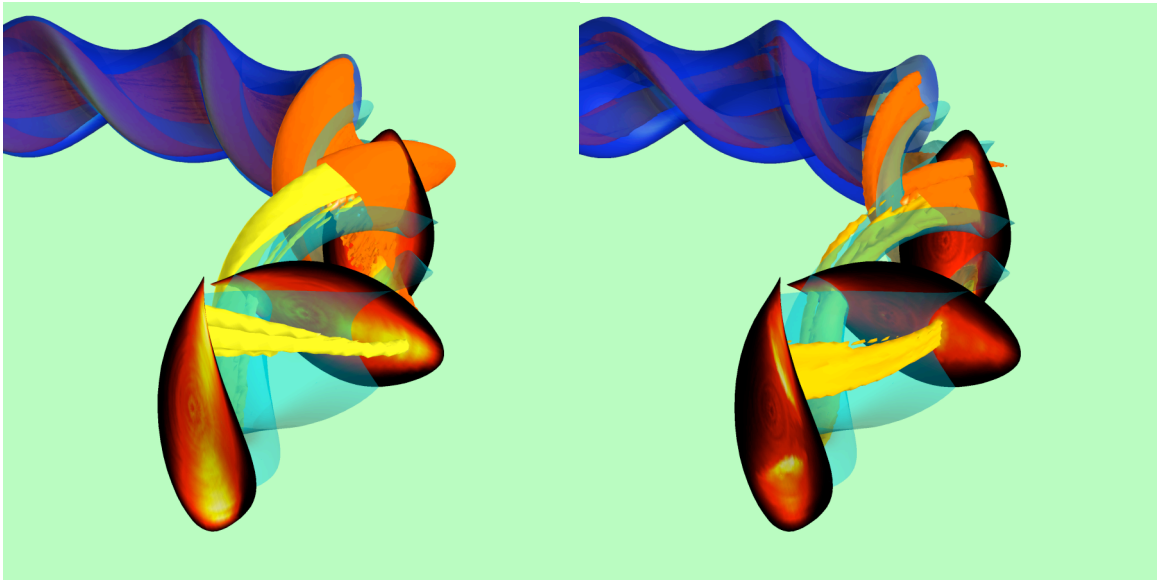

FIG. 3: *3D plots of the beam ion pressure without ICRF heating (left) and with the 2nd harmonics ICRF heating (right).*

Fishbones Activity in JET Low Density Plasmas

F. Nabais 1), D. Borba 1), M. Mantsinen 2), S. Sharapov 3) and JET-EFDA contributors[1]

1) Association EURATOM/IST, Av. Rovisco Pais, 1049-001 Lisboa, Portugal
2) Association EURATOM/TEKES, Helsinki University of Technology, Espoo, Finland
3) EURATOM/UKAEA Fusion Association, Culham Science Centre, Abingdon, OX14 3DB, U.K.

e-mail contact of the main author: fnabais@cfn.ist.utl.pt

Abstract. Fishbone activity with frequencies around the precessional drift frequency of the fast ions and the diamagnetic frequency of the bulk ions have been observed in several tokamaks. In the first case, fishbone bursts occur when the precessional fishbone branch of the internal kink mode becomes unstable, while in the second case fishbone bursts are caused by the ion branch, which corresponds to a different solution of the same dispersion relation. JET discharges carried out with low density plasmas and high ICRH power provided a scenario where the precessional fishbone branch and the ion branch coalesced. In this case, two new fishbones regimes were observed: a regime where fishbone bursts covered both ranges of frequencies showing hybrid characteristics, and a regime where low amplitude bursts of both types of fishbones occurred simultaneously. These coalescent regimes may also be reached if the radius of the q=1 surface is large, as it is predicted to be in ITER. Fishbone activity is analysed by means of a variational formalism that allows the calculation of the regions of stability for each branch in the space of parameters upon which the fishbone stability depends. This allows not only the analysis of experimental results but also the prediction of how fishbone stability would evolve in different circumstances, depending on the evolution of the relevant parameters.

1. Introduction

Fishbone activity [1] with frequencies around the precessional drift frequency of the fast ions $\omega \sim \omega_{DH}$ [2] are commonly observed in many tokamaks when the fast ions beta β_h (kinetic pressure / magnetic pressure) is sufficiently high. These fishbones, which in this paper will be referred to as precessional fishbones, are caused by the fishbone branch of the internal kink mode. The fishbone branch is not a "normal solution" of the MHD dispersion relation, it only appears as solution of the dispersion relation when the fast ions energy functional δW_{HOT} is included. Thus, its existence is dependent on the presence in the plasma of a fast ions population. The growth rate of this mode goes to $-\infty$ ($\gamma \to -\infty$) as $\beta_h \to 0$, but it increases when increasing β_h and the mode becomes unstable for values of β_h above a critical value, causing precessional fishbone bursts to occur. Fishbone bursts can also be observed at low values of β_h, but in this case, fishbones appear at frequencies around the diamagnetic frequencies of the bulk ions $\omega \sim \omega_{*i}$ [3]. Fishbones of this type, which in this paper will be referred to as diamagnetic fishbones, are caused by the ion branch of the internal kink mode. The ion branch appears as solution of the dispersion relation when diamagnetic effects are introduced and it can become unstable if the diamagnetic frequency sufficiently high. However, to turn the mode unstable it is also needed the presence in the plasma of fast ions to tap the source of energy for the instability, which is related to the pressure gradient of the plasma bulk. Thus, two different types of fishbone bursts have been usually observed, being caused by two different branches of the internal kink mode: the fishbone branch, which is associated with fast ion effects and that becomes unstable when the critical parameter β_h is sufficiently high, and the ion branch, which is associated with diamagnetic effects and that requires ω_{*i} to be sufficiently high for instability to be possible. Usually, the precessional fishbones regime is observed for high values of β_h while the diamagnetic fishbones regime is observed for low

[1] See appendix of J. Pamela et al., "Overview of JET Results" OV/1-2, Fusion Energy 2004, IAEA, (2004)

values of β_h, being both regimes separated by a stable window. When the diamagnetic frequency of bulk ions is significantly lower than the precessional drift frequency of the fast ions, $\omega_{*i} << \omega_{DH}$, it is also possible classify the fishbones regimes as high frequency fishbones and low frequency fishbones. Aside from the fishbone branch and the ion branch, the internal kink mode dispersion relation has the "normal MHD" solution, the kink branch. The kink branch becomes unstable when the ideal growth rate γ_I is sufficiently high, causing sawteeth to occur (γ_I is defined as $\gamma_I \equiv -\omega_A \delta W_{MHD}$, where ω_A is the Alfven frequency and δW_{MHD} is the usual minimized variational energy for the internal kink mode [4]).

In JET experiments with low density plasmas and where the only auxiliary heating used was ICRH (Ion Cyclotron Resonance Heating), aside from high and low frequency fishbones, two new fishbones regimes were observed: a regime of fishbones covering both high and low frequencies and a regime where high and low frequency fishbones occur simultaneously. These experimental results are presented in Sec. II. In Sec. III, the regions of stability for each branch of the internal kink mode in the space of parameters ($\beta_h, \omega_{*i}, \gamma_I$) are presented. In Sec. IV the changes in the regions of stability and the evolution of the parameters (β_h, ω_{*i}, γ_I) are determined, allowing a theoretical explanation for the appearance of the two new fishbone regimes. In Sec. V the dependence on frequency of the resonant exchange of energy and the types of orbits of the resonant particles are shown. Finally, in Sec. VI, conclusions are drawn.

2. New experimental results

Recent JET experiments carried out with low density plasmas and high power of ICRH provided a scenario where fishbone behaviour was observed to change during the period of a monster sawtooth. Sawtooth stability was also observed to change during the discharges, being related to the plasma density. In fact, there was a threshold in density above which sawtooth was stable and below which was unstable [5]. When unstable, sawteeth were observed along with precessional fishbones. After sawteeth being stabilized (following an increase in the plasma density), fishbones behaviour was observed to change gradually from high frequency fishbones to low frequency fishbones. In intermediate stages, two new fishbones regimes were observed: a regime of fishbones covering both ranges of frequencies and a regime where both types of fishbones occur simultaneously (see fig.1).

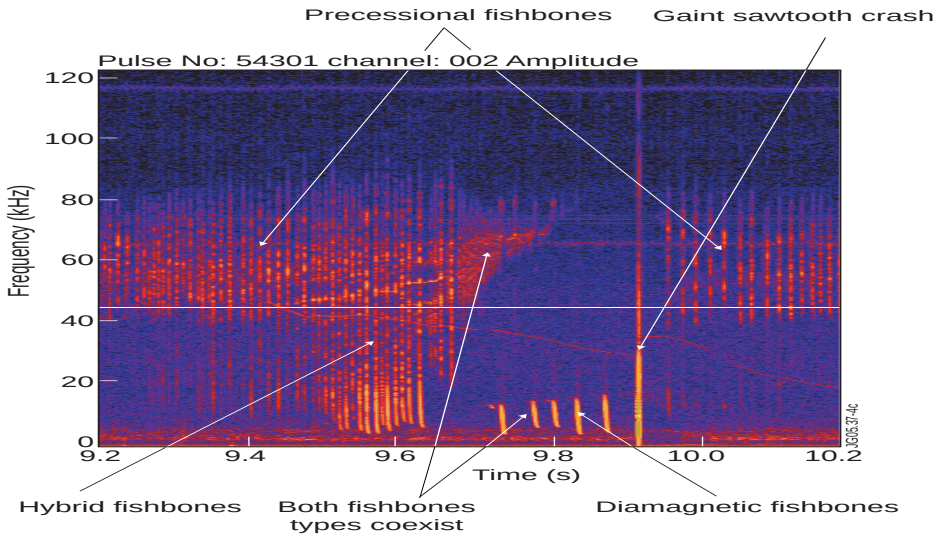

Figure 1: Spectrogram showing the evolution of fishbones behaviour along a monster sawteeth.

After a sawtooth crash it is always observed the regime of precessional fishbones. This regime evolves to a regime of fishbones covering both high and low frequencies (around t= 9.5 s). This new type of fishbones were designated as hybrid fishbones [6] since they have characteristics of both precessional and diamagnetic fishbones. The hybrid fishbones evolve then to a regime where both types of fishbones (precessional and diamagnetic) are observed simultaneously (around t= 9.75 s). However, when this occurs, both types of fishbones reach only small amplitudes. Gradually the high frequency fishbones disappear and only the low frequency fishbones remain, while its amplitude increases. The regime of diamagnetic fishbones is then reached. Finally, a sawtooth crash occurs and the precessional fishbones regime is restored.

3. Regions of stability

To analyse the fishbones behaviour it is used a qualitative approach based on a variational method. The first step consists in determine the regions of stability for each branch of the internal kink mode in the space of the relevant parameters ($\beta_h, \omega_{*i}, \gamma_I$).The second step will consist in to determine how these parameters evolve during a monster sawtooth and the third to evaluate how this affect fishbones behaviour. The dispersion relation for the internal kink mode including fast ion, resistive and diamagnetic effects in the large aspect ratio circular cross-section approximation is given by [7-9],

$$\delta W_{MHD} + \delta W_{HOT} - \frac{8i\Gamma\left[\left(\Lambda^{3/2}+5\right)/4\right]\left[\omega\left(\omega-\omega_{*i}\right)\right]^{1/2}}{\Lambda^{9/4}\Gamma\left[\left(\Lambda^{3/2}-1\right)/4\right]\omega_A} = 0 \qquad (1)$$

where, $\Lambda = -i\left[\omega\left(\omega-\hat{\omega}_{*e}\right)\left(\omega-\omega_{*i}\right)\right]^{1/3}/\gamma_R$, $\gamma_R = S^{-1/3}\omega_A$ is the resistive growth rate, S is the magnetic Reynolds number, ω_A is the Alfven frequency, ω_{*e} is the electron diamagnetic frequency $\omega_{*e} = \left(en_eBr\right)^{-1} dP_e/dr$, P_e and n_e are the electron pressure and density respectively and $\hat{\omega}_{*e} = \omega_{*e} + 0.71\left(eBr\right)^{-1} dT_e/dr$. The Euler gamma functions in equation (1) come from the inertial layer and are evaluated at the q=1 surface. To establish the regions of stability for each branch it is only necessary to determine when the stability of the mode changes, i.e, when the imaginary part of the complex frequency is zero. To proceed, the ideal limit is assumed. Considering an ICRH driven fast ions population characterized by a single normalized magnetic momentum $\lambda \equiv \mu B_0/E = 1$ (on-axis heating) and a Maxwellian distribution in energy, the threshold condition $\mathrm{Im}(\omega) = 0$ is given by,

$$\gamma_I = \frac{3}{4}\left[\frac{\omega}{\langle\omega_D\rangle}\left(\frac{\omega}{\langle\omega_D\rangle}-\frac{\omega_{*i}}{\langle\omega_D\rangle}\right)\right]^{\frac{1}{2}}\left(\frac{\omega}{\langle\omega_D\rangle}\right)^{-\frac{3}{2}}\left[\frac{1}{2}+\frac{\omega}{\langle\omega_D\rangle}+\left(\frac{\omega}{\langle\omega_D\rangle}\right)^{\frac{3}{2}}\mathrm{Re}\,Z\left[\left(\frac{\omega}{\langle\omega_D\rangle}\right)^{\frac{1}{2}}\right]\right], \qquad (2)$$

with the corresponding value of β_h given by,

$$\beta_h = \frac{3}{4}\frac{\varepsilon\omega_A}{\pi^{1/2}\langle\omega_D\rangle}\left[\frac{\omega}{\langle\omega_D\rangle}\left(\frac{\omega}{\langle\omega_D\rangle}-\frac{\omega_{*i}}{\langle\omega_D\rangle}\right)\right]^{\frac{1}{2}} e^{\omega/\omega_D}\left(\frac{\omega}{\langle\omega_D\rangle}\right)^{-\frac{5}{2}}. \qquad (3)$$

When ω_{*i} and $\langle\omega_D\rangle$ are of the same order of magnitude, β_h is a monotonic function of ω and equation (2) has two solutions provided that $\gamma_I < \gamma_M$, where γ_M is the maximum possible value for the right hand side of equation (2). These two solutions can be drawn in the plan

(β_h, γ_I), where they make approximately a triangle with the line $\gamma_I = 0$. The diamagnetic frequency ω_{*i} plays the role of a parameter determining the location of the top of the triangle.

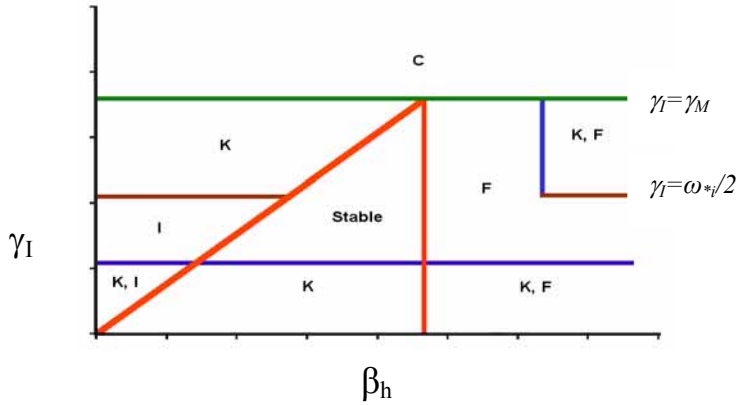

Figure 2: Regions of stability for the different branches in the space of parameters. In the regions labelled with K, I and F, the kink, ion and fishbone branches respectively are unstable. In the region labelled with C, the high and low frequency modes coalesce.

The two solutions of equation (2), represented by red lines in figure 2, correspond to the values of β_h above which the high frequency branch (the fishbone branch) is unstable and below which one of the low frequency branches is unstable. If $\gamma_I > \omega_{*i}/2$ the unstable branch is the kink branch, while if $\gamma_I < \omega_{*i}/2$ the unstable branch is the ion branch. For $\gamma_I > \gamma_M$ the high frequency branch and low frequency branches coalesce and the stable window in β_h vanishes. To complete the diagram, a blue horizontal line was included in order to traduce the resistive effects that were dropped during the calculations and that may turn the kink branch unstable if γ_I is small. The location of this line depends on the magnetic Reynolds number. A blue vertical line was also added in order to traduce finite orbit width effects, which are not included in equation (2). When the fast ions temperature is high enough, the orbits of the fast ions become large and sawtooth stabilisation by fast ions lose its efficiency, so, for high values of β_h sawtooth may become unstable again.

4. Evolution of fishbones behaviour

Having established the regions of stability for each of the branches as function of the relevant parameters (β_h, ω_{*i}, γ_I), the next step consists in evaluate how these parameters evolve during the period of a monster sawtooth. The ideal growth rate γ_I is expected to increase, since γ_I scales with r_1^3 [10], where r_1 is the radius of the q=1 surface, and the q=1 surface expands between sawtooth crashes as consequence of magnetic diffusion. This is confirmed by experimental observations, comparing the inversion radius of monster sawteeth with the inversion radius of the precedent small period sawtooth: The inversion radius is much smaller in the case of the small period sawtooth, which strongly suggests that the q=1 radius has a significant increase during the period of the monster sawtooth. The diamagnetic frequency also increases significantly between sawtooth crashes. $f_{*i} = \omega_{*i}/2\pi$ was previously estimated to be below 3 kHz after sawtooth crashes [5] (regime of short sawteeth). This frequency reaches above 10 kHz when diamagnetic fishbones are first observed and around 20 kHz before the monster crash. These values can be observed directly from the spectrogram since the initial frequency of the diamagnetic fishbones is around f_{*i}. Diagnostics corroborate that ω_{*i}

increases, showing that both the density and temperature profiles of the bulk ions peak during a monster sawtooth. Finally, for β_h, it is assumed that it increases slowly between fishbones bursts and that it decreases abruptly during a fishbone burst as the fast ions are expelled from the plasma centre. This behaviour is well established in fishbones theory [2, 3].

The third step consists now in determine how the evolution of the parameters ($\beta_h, \omega_{*i}, \gamma_I$) affect fishbones behaviour. In the beginning of the monster sawtooth period the plasma is in a state (blue cross in fig. 3) that corresponds to the region of the stability diagram where the fishbone branch is unstable, i.e., with β_h above both solutions of the marginal equation. As a precessional burst is initiated, β_h decreases and the fishbone branch will eventually become stable (see figure 3, left). When this happens, the mode amplitude starts decreasing until the fishbone burst ends. β_h will then increase slowly until a new fishbone burst be triggered.

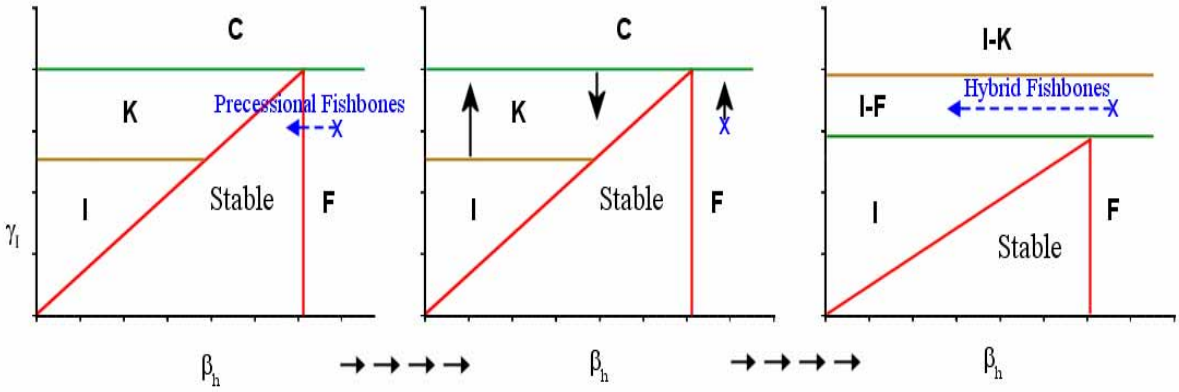

Figure 3: Evolution of the regions of stability during the sawtooth free period.

As γ_I increases, the cross representing the state of the plasma moves upward in the plan (β_h, γ_I), while the increase in ω_{*i} causes the borders of the regions of stability to change: the brown line corresponding to $\gamma_I = \omega_{*i}/2$ moves upward and the green line corresponding to $\gamma_I = \gamma_M(\omega_{*i})$ moves downward (see figure 3, middle). Thus, the increases in γ_I and ω_{*i} will cause the coalescence region to be reached. The unstable branch is now the coalescent ion-fishbone branch, which is unstable for all values of β_h and behaves like the fishbone branch at high β_h and like the ion branch at low β_h (these values depend on ω_{*i}). When a fishbone burst is initiated at high β_h it starts as a "precessional burst", since at high β_h the coalescent ion-fishbone mode behaves like the fishbone mode. However, the decrease in β_h during the burst no longer causes the stable region to be accessed. Instead, the coalescent ion-fishbone mode remains unstable as β_h decreases while its behaviour changes to a "diamagnetic behaviour" and the burst that started as a "precessional" gradually becomes "diamagnetic". This mechanism causes hybrid fishbones to occur. As ω_{*i} continues to increase during the sawtooth free period, the coalescent ion-fishbone mode behaviour becomes "more diamagnetic" and reaches a state where the "precessional behaviour" is no longer dominant over the "diamagnetic behaviour". At this point, small amplitude bursts of both types are triggered independently and can occur simultaneously. Finally, the diamagnetic behaviour becomes dominant and the coalescent mode behaves just like the ion mode producing diamagnetic bursts.

5. Numerical results

The interaction between a mode with an internal kink structure and populations of ICRH driven fast ions was also investigated numerically with the CASTOR-K code [11], which uses the eigenmode calculated by the MISHKA code [12]. A more accurate eigenmode and mode growth rates can be calculated with the NOVA-K code [13]. The CASTOR-K calculates the resonant transference of energy δW_{HOT} between the fast particles population and the mode, which is presented in figure 4 for different values of T_{HOT} as function of the mode frequency.

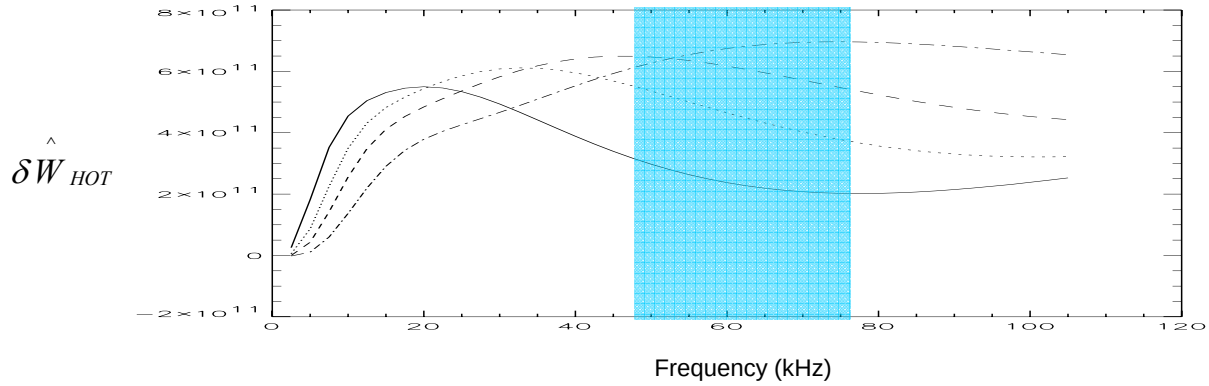

Figure 4: Resonant transference of energy between the internal kink mode and an ICRH driven fast ions population with temperatures of 500 keV (solid line), 750 keV (dotted), 1 MeV (dashed) and 1.5 MeV (dashed/dotted). The observed frequency of precessional fishbones is shadowed.

Figure 4 shows that the best fit between experimental and numerical results is for a fast ions temperature T_{HOT} between 1 MeV and 1.5 MeV, while the value of T_{HOT} estimated for these experiments was around 1 MeV. It can also be seen that the mode expected frequency increases rapidly as the fast ions temperature increases.

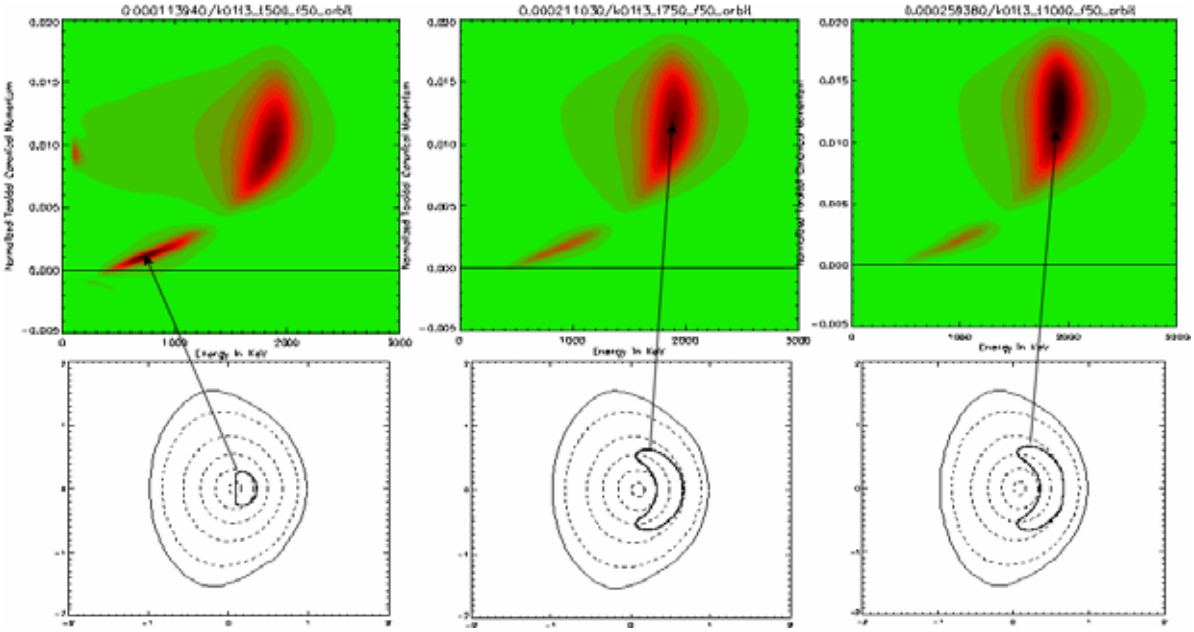

Figure 5: Upper line - Resonant transference of energy between the internal kink mode (f=50 kHz) and an ICRH driven fast ions population as function of the energy and the toroidal canonical moment for three different fast ions temperatures: 500 keV (left), 750 keV (middle) and 1000 keV (right). Lower line: Orbits of the particles with a stronger interaction with the node, for each case.

Figure 5 (upper half) shows the resonant transference of energy between the internal kink mode (f=50 kHz) and three ICRH driven fast ion populations characterized by different temperatures (500, 750 and 1000 keV). The orbits of the particles in stronger resonance with the mode are also represented in figure 5 (lower half). It can be seen that there are two main resonances, one corresponding to particles nearer the magnetic axis centred around 900 keV and the other corresponding to particles farer from the plasma axis centred around 1.8 MeV. This second resonance becomes dominant when the fast ions temperature increases (it is already dominant for T_{HOT}=750 keV). The change in the type of orbits of the particles strongly interacting with the mode may contribute to explain the high frequency of the precessional fishbones observed experimentally.

6. Summary and conclusions

In JET experiments with low density plasmas, when sawtooth are stable, the absence of crashes allows the bulk ions pressure profile to peak. This causes a significant increase in the diamagnetic frequency and under these circumstances the high frequency branch solution of the internal kink dispersion relation coalesces with the low frequency branch. The coalescent ion-fishbone mode is always unstable and behaves like the ion mode for low values of β_h and like the fishbone mode for high values of β_h. Two new fishbone regimes were observed: a regime of hybrid fishbones is observed when the ion-fishbone mode is unstable with dominant precessional behaviour and a regime where small amplitude precessional and diamagnetic bursts occur simultaneously is observed when the ion-fishbone mode is unstable but none of the behaviours is dominant. It was also found that the particles in resonance with the internal kink high frequency branch can have two types of orbits. The main resonance in the space (E, P_φ) changes when increasing the fast ions temperature, which may cause a considerable increase in the mode frequency.

Aknowledgments
This work, supported by the European Communities and "Instituto Superior Técnico" under the Contract of Association between EURATOM and IST, has been carried out within the framework of the European Fusion Development Agreement. Financial support was also received from "Fundação para a Ciência e Tecnologia" in the frame of the Contract of Associated Laboratory. The views and opinions expressed herein do not necessarily reflect those of the European Commission, IST and FCT.

References

[1] – K. McGuire *et al*. Phys. Rev. Lett. **50** 891 (1983)
[2] – L. Chen, R. White and M. Rosenbluth, Phys. Rev. Lett. **52** 1122 (1984)
[3] – B. Coppi and F. Porcelli, Phys. Rev. Lett. **57**, 2272 (1986)
[4] – M. Bussac *et al*. Phys. Rev. Lett. **35**, 1638 (1975)
[5] – M. Mantsinen *et al*. Plasma Phys. Control. Fusion **42**, 1291, (2000)
[6] – F. Nabais *et al*. Phys. Plasmas 12, 102509 (2005)
[7] – R. White, L.Chen, F. Romanelli and R. Hay, Phys. Fluids **28**, 278 (1985)
[8] – R. White, M. Bussac and F. Romanelli, Phys. Rev. Lett. **62**, 539 (1989)
[9] – R. White, F. Romanelli and M. Bussac, Phys. Fluids B **2**, 745 (1990)
[10] – C. K. Phillips *et al*. Phys. Fluids B **4** (7), 2155 (1995)
[11] – D. Borba and W. Kerner, J. Computational Physics **153**, 101 (1999)
[12] – A. B. Mikhailovskii *et al*. Plasma Physics Reports **10**, 844 (1997)
[13] – N. N. Gorelenkov, C. Cheng, V. Kiptily, M. Mantsinen and S. E. Sharapov, Proc. 20th IAEA Fusion Energy Conference 2004, (Vilamoura, 2004) (Vienna: IAEA), paper TH/5-2 Rb

Non-Conventional Fishbone Instabilities Driven by Circulating Energetic Ions

V.S. Marchenko[1], Ya.I. Kolesnichenko[1], R.B. White[2]
[1] *Institute for Nuclear Research, National Academy of Sciences of Ukraine, Kyiv, 03680, Ukraine*
[2] *Princeton Plasma Physics Laboratory, P.O. Box 451, Princeton, New Jersey, 08543, USA*
march@kinr.kiev.ua

A new kind of fishbone instability associated with circulating energetic ions is predicted. The considered instability is essentially the energetic particle mode and arises in plasmas with on-axis safety factor q_0 close to unity and extended shear-free central core, separated from the wall by a region with finite shear. The frequency of this "quasi-interchange" fishbone mode is $\omega \sim k_{0\|} v_\alpha$ with $k_{0\|}$ the parallel wave number in the shear-free core and v_α the injection velocity of energetic ions. "Infernal" fishbone modes with the same properties, but $m/n > 1$ with $m(n)$ the poloidal (toroidal) mode number, are investigated. A possibility to explain recent experimental observations of the $m=2$ fishbone oscillations accompanied by strong changes of the neutron emission during tangential neutral beam injection in the National Spherical Torus Experiment is shown.

1. Introduction

Some tokamak discharges are characterized by safety factor q close to unity in a wide region in the plasma core, which is separated from the wall by the edge region with large magnetic shear. This is the case for the "hybrid" regime, which is considered as a third operational scenario for ITER [1]. Furthermore, q-profiles with extended flat region and q_0 close to low-order rational are typical for high beta discharges in spherical tokamaks [2]. Since all mentioned discharges are accompanied by strong neutral beam injection (NBI), the problem of kinetic stability of such low-shear configurations in the presence of energetic ions represents considerable interest, which motivated present work.

In the framework of ideal MHD stability theory equilibrium with this type of q-profile is susceptible to a pressure-driven "infernal" modes [3,4]. A particular case of these instabilities is the quasi-interchange (QI) mode with poloidal and toroidal mode numbers $m=n=1$ [5-7]. The eigenfunction of this instability is of convective, or "cellular" character, in contrast with rigid kink displacement in the finite shear case. In the present work we show that this property, combined with finite orbit width of energetic ions, leads to the new kind of the fishbone mode with characteristic frequency of the Cherenkov resonance in the shear-free core, $\omega \sim k_{0\|} v_\alpha$ with $k_{0\|}=(m-nq_0)/q_0R$ and v_α injection velocity.

The purpose of the present work is to extend the ideal MHD theory of the QI mode in toroidal plasmas, developed in [6,7], to equilibrium with minor population of energetic ions. In the next section dispersion relation for the QI fishbone is derived and analyzed. The case of arbitrary (m, n) is considered in Sec.3. Section 4 is a short summary.

2. Dispersion Relation for the QI Fishbone Mode

The eigenmode equations for the QI fishbone can be obtained from the minimization of the total energy of the perturbation

$$E = \frac{R_0}{\pi^2 B_0^2}(\delta W_{MHD} + \delta W_k) - \frac{\omega^2}{\omega_A^2} N, \tag{1}$$

where δW_{MHD} is the ideal MHD potential energy [6,7], $\omega_A = V_A/R_0$ with $V_A(r) \approx$ const the Alfven speed and R_0 the major radius of the torus,

$$N = \frac{1}{2\pi^2 R_0} \int d^3 r \, | \vec{\xi}_\perp |^2 \tag{2}$$

with $\vec{\xi}_\perp$ the transverse displacement, and δW_k is the kinetic part of the potential energy, which encapsulates information regarding resonant energy exchange between energetic ions and fishbone mode [8]

$$\delta W_k = \frac{1}{2} \int d^3 r \vec{\xi}_\perp^* \bullet \nabla \Pi_\alpha^k = -\frac{\pi^2 m_\alpha}{\omega_{c\alpha}} \sum_o \int v^3 dv \int dP_\varphi \int d\Lambda \, \tau_b \frac{\partial F_\alpha}{\partial \mathrm{E}} \frac{\omega - \omega_{*\alpha}}{\omega - k_\parallel v_\parallel} \left| \left\langle \left(\frac{v_\perp^2}{2} + v_\parallel^2 \right) \vec{\xi}_\perp \bullet \vec{\kappa} \times \exp[i(\omega - k_\parallel v_\parallel)t] \right\rangle \right|^2 ,$$

where $\delta \Pi_\alpha^k = \delta p_{\perp\alpha}^k \hat{I} + (\delta p_{\parallel\alpha}^k - \delta p_{\perp\alpha}^k) \vec{b}\vec{b}$ is the pressure tensor with $\delta p_{\parallel,\perp\alpha}^k$ the parallel and perpendicular pressure perturbations associated with non-adiabatic response of the energetic ions, $\sigma = v_\parallel / | v_\parallel |$, $\Lambda = \mu_g B_0 / \mathrm{E}$ with $\mathrm{E}(\mu_g)$ the particle energy (magnetic moment), τ_b is the particle transit time, $\omega_{*\alpha} = (\partial F_\alpha / \partial \mathrm{P}_\varphi)(\partial F_\alpha / \partial \mathrm{E})^{-1}$, $\vec{\kappa}$ is magnetic field curvature, and $\langle ... \rangle$ denotes orbit averaging.

Below we assume that the energetic-ion population consists of well-circulating particles with the equilibrium distribution function given by

$$F_\alpha = \frac{\sqrt{2} m_\alpha^{3/2}}{\pi \mathrm{E}_\alpha} p_\alpha(\bar{r}) H(\mathrm{E}_\alpha - \mathrm{E}) \mathrm{E}^{-3/2} \delta(\Lambda) \quad , \tag{3}$$

where $p_\alpha(\bar{r})$ is the beam particle pressure and *H(x)* is the unit step function. Furthermore, it is assumed that energetic ions are deposited in the shear-free core, that is $p_\alpha(\bar{r} > r_0) \approx 0$, where r_0 is the radius at the interface between shear-free and finite shear regions.

Omitting term odd in θ in $\vec{\xi}_\perp \bullet \vec{\kappa}$, which does not contribute to δW_k, we obtain

$$\vec{\xi}_\perp \bullet \vec{\kappa} = -\frac{1}{R_0} \xi_1 \{r[\theta(t)]\} \cos[\theta(t)] \exp\{i[\theta(t) - \varphi(t) - \omega t]\} \quad , \tag{4}$$

where ξ_1 is the amplitude of the *m=1* radial displacement,

$$r[\theta(t)] = \bar{r} - \Delta_\alpha \cos[\theta(t)] \, , \; \Delta_\alpha = \frac{q(\bar{r})}{v_\parallel \omega_{c\alpha}} \left(\frac{v_\perp^2}{2} + v_\parallel^2 \right) , \; \theta(t) = \frac{v_\parallel}{q(\bar{r}) R_0} t \, , \; \varphi(t) = \frac{v_\parallel}{R_0} t \quad .$$

We now assume $\Delta_\alpha << \bar{r}$ and Taylor expand $\xi_1[r(\theta)]$ in Eq.(4). Substituting result to expression for δW_k together with Eq.(3), taking orbit average and velocity space integration, one can obtain

$$\frac{R_0}{\pi^2 B_0^2} \delta W_k = -\frac{2}{\pi^2} \rho_\alpha^3 R_0 F \left(\frac{\omega}{k_{0\parallel} v_\alpha} \right) \left| \frac{d\xi_1}{dr} \right|^2 \frac{d\beta_\alpha}{dr} \quad , \tag{5}$$

where $\rho_\alpha = v_\alpha / \omega_{c\alpha}$,

$$F(\Omega) \equiv \frac{1}{5} + \frac{\Omega}{4} + \frac{\Omega^2}{3} + \frac{\Omega^3}{2} + \Omega^4 + \Omega^5 \ln\left(1 - \frac{1}{\Omega}\right) \quad , \tag{6}$$

and $\omega << \omega_{*\alpha}$ has been assumed. Note that it is the quasi-interchange character of the mode ($d\xi_1/dr \neq 0$ in the shear-free core), which allows for efficient power transfer at the Cherenkov resonance in this case. This is in contrast with rigid internal kink, when only particles crossing *q=1* surface in the course of their drift motion contribute to the non-adiabatic response [9].

For simplicity below we take radial fast ion distribution in the form $\beta_\alpha = \beta_{\alpha 0}[1-(r/r_0)^4]$. Rescaling the variable *r/a*→*r* with *a* the plasma radius, one can obtain from minimization of energy in Eq.(1) the following Euler equations in the shear-free core:

$$\frac{d}{dr}\left\{\varepsilon^{-2}\left[(\mu-1)^2 + l_\alpha(\omega,r) - \frac{\omega^2}{\omega_A^2}\right] r^3 \frac{d\xi_1}{dr}\right\} - 4\left(\frac{r}{4}\beta_p' + \beta_p\right)^2 r^3 \xi_1 = \left(\frac{r}{4}\beta_p' + \beta_p\right)\frac{d}{dr}(r^3 \hat{\xi}_2) \quad , \tag{7}$$

$$\frac{d}{dr}\left(r^3 \frac{d\hat{\xi}_2}{dr}\right) - 3r\hat{\xi}_2 = -4r^3 \frac{d}{dr}\left[\left(\frac{r}{4}\beta_p' + \beta_p\right)\xi_1\right] \quad , \tag{8}$$

where μ=1/q with |μ-1| ~ ε in the shear-free core, $\xi_2 \equiv \varepsilon \hat{\xi}_2$ with ξ_2 the amplitude of the *m=2* radial displacement and $\varepsilon \equiv a/R_0$, $\beta_p(r) = -(8\pi R_0^2 / r^4 B_0^2)\int_0^r \hat{r}^2 (dp_c/d\hat{r}) d\hat{r}$ with p_c the background plasma pressure, and

$$l_\alpha(\omega,r) \equiv \frac{8}{\pi^2}\frac{\rho_\alpha^3 R_0}{r_0^4}\beta_{\alpha 0} F\left(\frac{\omega}{k_{0\|} v_\alpha}\right) H(r_0 - r) \quad . \tag{9}$$

The general solution of Eq.(8), which is regular on axis, has the form

$$\hat{\xi}_2 = r^{-3}\int_0^r \hat{r}^4 \beta_p(\hat{r}) \frac{d\xi_1}{d\hat{r}} d\hat{r} + [e - \beta_p(r)\xi_1(r)]r \quad , \tag{10}$$

where *e* is an integration constant. Substituting Eq.(10) into Eq.(7) and integrating, one can obtain

$$\frac{d\xi_1}{dr} = \frac{\varepsilon^2 e r \beta_p}{(\mu-1)^2 + l_\alpha(\omega,r) - \omega^2/\omega_A^2} \quad . \tag{11}$$

Dispersion relation can be obtained by matching the solution in the inner (shear-free) to the solution in the outer (sheared) region. In the latter region toroidal coupling in equation for ξ_2 can be neglected, since |μ-1| ~ 1 and therefore $\xi_1 \sim \varepsilon^2$ [see Eq.(11)]. Equation for ξ_2 in the sheared region then takes the form

$$\frac{d}{dr}\left[\left(\mu - \frac{1}{2}\right)^2 r^3 \frac{d\hat{\xi}_2}{dr}\right] - 3\left(\mu - \frac{1}{2}\right)^2 r\hat{\xi}_2 = 0 \quad , \tag{12}$$

which has the asymptotic solution in the shear-free region

$$\hat{\xi}_2 \propto \frac{r}{r_2} + \sigma\left(\frac{r}{r_2}\right)^{-3} \quad , \tag{13}$$

where $\mu(r_2)=1/2$ and constant σ should be determined numerically by integrating Eq.(12) through the outer region. Matching Eq.(13) with asymptotic form of Eq.(10) in the outer region, we obtain dispersion relation

$$\sigma = \left(\frac{r_2}{a}\right)^2 \int_0^a \frac{[\varepsilon \beta_p(r)]^2}{(\mu-1)^2 + l_\alpha(\omega,r) - \omega^2/\omega_A^2} \left(\frac{r}{r_2}\right)^5 \frac{dr}{r_2} \quad , \tag{14}$$

where dimensions have been restored. Note that the integrand in Eq.(14) has the pole at the Alfven resonance in the outer region. The residue at this pole represents continuum damping of the fishbone mode. Away from the resonance the integrand becomes negligible in the sheared region. Thus, we can rewrite Eq.(14) in the form

$$\sigma = \left(\frac{r_2}{a}\right)^2 \frac{\varepsilon^2}{(\mu_0-1)^2 + l_\alpha(\omega) - \omega^2/\omega_A^2} \int_0^{r_0} \beta_p^2(r) \left(\frac{r}{r_2}\right)^5 \frac{dr}{r_2} + \sigma_{res}(\omega) \quad , \tag{15}$$

where

$$\sigma_{es}(\omega) = \left(\frac{r}{r_2}\right)^2 \varepsilon^2 \beta_p^2(r_A) \left(\frac{r_A}{r_2}\right)^5 \lim_{\eta\to 0} \int_{r_A-0}^{r_A+0} \frac{1}{(\mu-1)^2 - (\omega+i\eta)^2/\omega_A^2} \frac{dr}{r_2} =$$

$$i\pi \left(\frac{r_2}{a}\right)^2 [\varepsilon \beta_p(r_A)]^2 \frac{(r_A/r_2)^5}{r_2 \,|\, \partial/\partial r (\mu-1)^2 \,|_{r=r_A}|} \equiv i\sigma_1(\omega) \quad , \tag{16}$$

and $|\mu(r_A)-1| = \omega/\omega_A$. Equations (15,16) can be used to determine critical fast ion pressure and mode frequency at the onset of the fishbone mode for any particular profiles of the rotational transform and background plasma pressure.

3. Infernal Fishbone Modes with Arbitrary Mode Numbers

In the present section we generalize results of the previous section to arbitrary mode numbers. In the shear-free core with $m - nq_0 \sim \varepsilon$ the mode equations for general *m, n* are

$$\frac{d}{dr}\left\{\left[\left(\frac{\mu}{n}-\frac{1}{m}\right)^2 + \frac{l_\alpha}{(mn)^2} - \left(\frac{\omega}{\omega_A mn}\right)^2\right] r^3 \frac{d\xi_m}{dr}\right\} - (m^2-1)\left[\left(\frac{\mu}{n}-\frac{1}{m}\right)^2 - \left(\frac{\omega}{\omega_A mn}\right)^2\right] r\xi_m -$$

$$\frac{\varepsilon^2}{m^2}\left[\frac{1}{2}(r\beta_p{}' + 4\beta_p)^2 + \left(1-\frac{n^2}{m^2}\right)(r\beta_p{}' + 4\beta_p)\right] r^3 \xi_m = \tag{17}$$

$$\frac{\varepsilon^2 n}{2m^2(m+1)} r^{1+m} (r\beta_p{}' + 4\beta_p) \frac{d}{dr}(r^{2+m}\hat{\xi}_{m+1}) \quad ,$$

$$\frac{d}{dr}\left(r^3 \frac{d\hat{\xi}_{m+1}}{dr}\right) - [(m+1)^2 - 1] r\hat{\xi}_{m+1} = -\frac{m+1}{2n} r^{2+m} \frac{d}{dr}[(r\beta_p{}' + 4\beta_p) r^{1+m} \xi_m] \quad , \tag{18}$$

where again $\xi_{m+1} \equiv \varepsilon \hat{\xi}_{m+1}$. The general solution of Eq.(18), which is regular on magnetic axis, takes the form

$$n\hat{\xi}_{m+1} = -\frac{1}{2}(1+m) r^{-(2+m)} \int_0^r d\hat{r} (\hat{r}\beta_p{}' + 4\beta_p) \hat{r}^{2+m} \xi_m + e r^m \quad . \tag{19}$$

Substituting Eq.(19) into Eq.(17), one can obtain

$$\frac{d}{dr}\left\{\left[\left(\frac{\mu}{n}-\frac{1}{m}\right)^2+\frac{l_\alpha}{(mn)^2}-\left(\frac{\omega}{\omega_A mn}\right)^2\right]r^3\frac{d\xi_m}{dr}\right\}-(m^2-1)\left[\left(\frac{\mu}{n}-\frac{1}{m}\right)^2-\left(\frac{\omega}{\omega_A mn}\right)^2\right]r\xi_m - \frac{\varepsilon^2}{m^2}\left(1-\frac{n^2}{m^2}\right)\frac{d}{dr}(r^4\beta_p)\xi_m=\frac{\varepsilon^2}{m^2}e\frac{d}{dr}(r^4\beta_p)r^{m-1} \quad . \tag{20}$$

With pressure profile given by $p_c = p_0[1-(r/a)^{2\nu}]$ we have $\beta_p = \hat{\beta}_p r^{2\nu-2}$. Thus one can see that, for $|m-nq_0|\sim\varepsilon$, the ratio of the last term on the left-hand side of Eq.(20), which represents stabilizing effect of the average magnetic well, to the second term on the LHS of this equation is of the order of $(r_0/a)^{2\nu} << 1$, where r_0 is again the radius at the transition between shear-free and sheared regions, which is assumed to be sufficiently abrupt to allow for asymptotic matching of the in these regions. Neglecting the last term on the LHS, Eq.(20) can be easily integrated. Imposing boundary condition $\xi_m(1)=0$, one finds

$$\xi_m=\frac{2\varepsilon^2 e\hat{\beta}_p(\nu+1)(r^{2\nu}-1)r^{m-1}}{[(2\nu+m)^2-1]l_\alpha(\omega,r)/n^2+4\nu(\nu+m)[(m/nq-1)^2-(\omega/\omega_A n)^2]} \quad . \tag{21}$$

Note that ξ_m is again negligible in the sheared region, except in the vicinity of the Alfven resonance. The dispersion relation again can be obtained by matching the asymptotic form of the solution Eq.(19) with ξ_m given by Eq.(21) in the sheared region, to the shear-free limit of the outer Eq.(18) (with the right-hand side neglected):

$$\hat{\xi}_{m+1}\propto\left(\frac{r}{r_{m+1}}\right)^m+\sigma_m\left(\frac{r}{r_{m+1}}\right)^{-(2+m)} \quad , \tag{22}$$

where $\mu(r_{m+1})=n/(m+1)$. We find

$$\sigma_m=\frac{1+m}{n(\nu+m)}\left(\frac{r_{m+1}}{a}\right)^{-2(m+1)}\left(\frac{r_0}{a}\right)^{2(\nu+m)}\times \frac{\varepsilon^2\hat{\beta}_p^2(\nu+1)^2}{[(2\nu+m)^2-1]l_\alpha(\omega)/n^2+4\nu(\nu+m)[(m/nq_0-1)^2-(\omega/\omega_A n)^2]}+\sigma_{res} \quad , \tag{23}$$

where we have restored radius dimension. For the μ-profile given by

$$\mu=\frac{n}{m+1}+\left(\mu_0-\frac{n}{m+1}\right)\left[1-\left(\frac{r}{r_{m+1}}\right)^{2\lambda}\right]$$

with $\lambda\geq m+2$, we have [6]

$$\sigma_m\approx\frac{m}{m+2}\left(1-\frac{m+1}{\lambda}\right) \quad , \tag{24}$$

and expression for σ_{res} takes the form

$$\sigma_{res}=i\pi\frac{(m+1)^3}{8\lambda n}\frac{\varepsilon^2\hat{\beta}_p^2(\nu+1)^2}{\nu(\nu+m)}\left(\frac{r_{m+1}}{a}\right)^{2(\nu-1)}\left[\frac{(m+1)\omega}{n\omega_A}\right]^{\frac{\nu+m}{\lambda}-2}\equiv i\sigma_{1m} \quad . \tag{25}$$

To make contact with NSTX experiment [10], we take $v_\alpha/V_A=2$, $m=2$, $n=1$, $q_0=1.7$, $R_0/a=1.5$, and choose $\nu=6$, $\lambda=4$, so that $\sigma_2=1/8$, $\sigma_{12}(\omega)=\text{const}$, $r_3/a \approx 0.8$, $r_0/a \approx r_2/a \approx 0.6$. Considering plasma at the margin of the MHD stability in the absence of fast ions [taking $l_\alpha = \omega = 0$ in Eq.(23)], and taking into account that $\hat{\beta}_p = (\beta_o/\varepsilon^2)(m/n)^2[\nu/(\nu+1)]$, we obtain $\beta_0^{marg}=0.35$, and Eq.(25) yields $\sigma_{res} \approx 0.55$. Equation (23) then yields at the margin of the fishbone stability ($Im\omega=0$)

$$\hat{\beta}_\alpha^{crit} = \frac{192}{195}\frac{4\Omega^2(2\mu_0-1)^2}{\mathrm{Re}\,F(\Omega)+(\sigma_{12}/\sigma_2)\,\mathrm{Im}\,F(\Omega)} \quad , \tag{26}$$

$$\mathrm{Im}\,F(\Omega)\left[4\Omega^2\left(\frac{\sigma_{12}}{\sigma_2}+\frac{\sigma_2}{\sigma_{12}}\right)-\frac{\sigma_{12}}{\sigma_2}\right] = \mathrm{Re}\,F(\Omega) \quad , \tag{27}$$

where $\hat{\beta}_\alpha \equiv (8/\pi^2)(\rho_\alpha^3 R_0/r_0^4)\beta_{\alpha 0}$. Solution of Eqs.(26),(27) yields $\Omega \approx 0.6$, $\hat{\beta}_\alpha^{crit} \approx 2.5\times10^{-2}$. Taking into account that in NSTX $r_0 \approx 0.6a \approx 40cm$, $R_0 \approx 100\ cm$, $\rho_\alpha \approx 20\ cm$, we obtain $\beta_{\alpha 0}^{crit} \approx 0.1$. For the chosen fast ion pressure profile this corresponds to the volume averaged fast ion beta $\langle\beta_\alpha\rangle = (2/3)(r_0/a)^2\beta_{\alpha 0} \approx 2.4\times10^{-2}$. Taking into account that energetic ions are deutrons with injection energy $80\ keV$, we obtain $f = 0.6(2\mu_0-1)v_\alpha/2\pi R_0 \approx 46kHz$. Both these values are in reasonable agreement with observed initial fishbone frequency in the plasma frame $f \approx 45\ kHz$ and volume averaged beam ion beta $\langle\beta_\alpha\rangle \approx 2\ \%$.

4. Summary

We have shown that in low-shear tokamaks fishbone modes with arbitrary mode numbers can be destabilized by the interaction with energetic circulating ions at the Cherenkov resonance. In contrast to the conventional $m=n=1$ circulating-ion-driven fishbone instability, the considered instability is caused mainly by particles with orbits inside the flux surface with the radius r_0 separating regions with low and finite magnetic shear. The efficient energy exchange between these particles and the perturbation takes place due to finite orbit width of the energetic ions and a radial gradient of the mode poloidal electric field. Both the mode frequency and critical fast ion pressure are in reasonable agreement with experimental observations of bursting $m=2$ fishbone oscillations accompanied by strong changes of the neutron yield in the NSTX spherical torus.

References

[1] LITAUDON, X., et al., Plasma Phys. Control. Fusion **46** (2004) A19.
[2] MENARD, J.E., et al., Nucl. Fusion **43** (2003) 330.
[3] MANICKAM, J., POMPHREY, N., TODD, A.M.M., Nucl. Fusion **27** (1987) 1461.
[4] CHARLTON, L.A., CARRERAS, B.A., LYNCH, V.E., Phys. Fluids **B2** (1990) 1574.
[5] WESSON, J.A., Plasma Phys. Control. Fusion **28** (1986) 243.
[6] WAELBROECK, F.L., HAZELTINE, R.D., Phys. Fluids **31** (1988) 1217.
[7] HASTIE, R.J., HENDER, T.C., Nucl. Fusion **28** (1988) 585.
[8] PORCELLI, F., STANKIEWICZ, R., KERNER, W., BERK, H.L., Phys. Plasmas **1** (1994) 470.
[9] BETTI, R., FREIDBERG, J.P., Phys. Rev. Lett. **70** (1993) 3428.
[10] FREDRICSON, E., CHEN, L., WHITE, R., Nucl. Fusion **43** (2003) 1258.

Nonlinear MHD Effects on the Alfvén Eigenmode Evolution

Y. Todo 1), H. L. Berk 2), B. N. Breizman 2)
1) National Institute for Fusion Science, Toki, Japan
2) Institute for Fusion Studies, University of Texas at Austin, Austin, United States

e-mail contact of main author: todo@nifs.ac.jp

Abstract. Two types of hybrid simulations of MHD fluid and energetic particles were carried out to investigate MHD nonlinear effects on Alfvén eigenmode evolution. The first type contains fully nonlinear effects of both the MHD fluid and the energetic particles. The second type of the simulation is similar to the first type but different in that the MHD equations are linearized. Comparison between the results of the two types of simulations clarifies the MHD nonlinear effects. A tokamak plasma, where a toroidal Alfvén eigenmode (TAE) with toroidal mode number n=4 is the most unstable, was investigated. When the saturation level is $\delta B/B \sim 2\times10^{-2}$ in the linear MHD simulation results, we found that the saturation level is $\delta B/B \sim 8\times10^{-3}$ in the nonlinear MHD simulation results. The MHD nonlinear effects suppress the saturation level of the TAE. Detailed analyses indicate that the suppression effect arises from the change in n=0 harmonics of the magnetic field that is generated by the nonlinear electric field $-\mathbf{v}_{TAE}\times\delta\mathbf{B}_{TAE}$, a product of the velocity field and the magnetic field of the TAE. Axisymmetric velocity fields are also generated in the nonlinear run, although the change in the n=0 magnetic field plays the dominant role in the suppression of TAE.

1. Introduction

For time evolution of Alfvén eigenmodes, an important nonlinearity arises from the dynamics of energetic particles that destabilize the Alfvén eigenmodes. It was demonstrated by computer simulations that the particle trapping cause the saturation of toroidal Alfvén eigenmodes (TAE) [1-4]. This enables reduced simulations of TAE, where spatial profiles and damping rates of TAEs are assumed to be independent of mode amplitude. TAE bursts at a Tokamak Fusion Test Reactor experiment were reproduced by a reduced simulation [5]. Many aspects of the TAE bursts were well reproduced, while only the saturation amplitude was $\delta B/B \sim 2\times10^{-2}$ which is higher than the value $\delta B/B \sim 10^{-3}$ inferred from the experimental plasma displacement [5,6]. In another simulation run of TAE bursts, where the MHD nonlinear effects are taken account, the saturation level is lower than $\delta B/B \sim 10^{-2}$ [7]. These simulation results motivate us to investigate the MHD nonlinear effects.

Two types of hybrid simulations of MHD fluid and energetic particles were carried out to investigate MHD nonlinear effects on Alfvén eigenmode evolution using MEGA code [8,9] and a linearized version of MEGA code. Fully nonlinear effects of both the MHD fluid and the energetic particles are contained in MEGA code. In the linearized version of MEGA code, the MHD equations are linearized while the nonlinear particle dynamics are followed. In this paper, simulation results of the two types of simulations are presented and compared. It is demonstrated that the MHD nonlinear effects suppress the saturation level of the TAE. Detailed analyses indicate that the suppression effect arises from the change in n=0 harmonics of the magnetic field that is generated by the nonlinear electric field $-\mathbf{v}_{TAE}\times\delta\mathbf{B}_{TAE}$, a product of the velocity field and the magnetic field of the TAE.

2. Simulation Model

The hybrid simulation model for MHD and energetic particles [2,8-10] is employed in MEGA code. Plasma is divided into bulk plasma and energetic ions. The bulk plasma is described by the nonlinear full MHD equations. The electromagnetic field is given by the MHD description.

This approximation is reasonable under the condition that the energetic ion density is much less than the bulk plasma density. The MHD equations with energetic ion effects are,

$$\frac{\partial \rho}{\partial t} = -\nabla \cdot (\rho \mathbf{v}) \tag{1}$$

$$\rho \frac{\partial}{\partial t}\mathbf{v} = -\rho\vec{\omega} \times \mathbf{v} - \rho\nabla(\frac{v^2}{2}) - \nabla p + (\mathbf{j} - \mathbf{j}_h') \times \mathbf{B} + \nu\rho[\frac{4}{3}\nabla(\nabla \cdot \mathbf{v}) - \nabla \times \vec{\omega}] \tag{2}$$

$$\frac{\partial \mathbf{B}}{\partial t} = -\nabla \times \mathbf{E} \tag{3}$$

$$\frac{\partial p}{\partial t} = -\nabla \cdot (p\mathbf{v}) - (\gamma - 1)p\nabla \cdot \mathbf{v} + (\gamma - 1)[\nu\rho\omega^2 + \frac{4}{3}\nu\rho(\nabla \cdot \mathbf{v})^2 + \eta\mathbf{j} \cdot (\mathbf{j} - \mathbf{j}_{eq})] \tag{4}$$

$$\mathbf{E} = -\mathbf{v} \times \mathbf{B} + \eta(\mathbf{j} - \mathbf{j}_{eq}) \tag{5}$$

$$\mathbf{j} = \frac{1}{\mu_0}\nabla \times \mathbf{B} \tag{6}$$

$$\vec{\omega} = \nabla \times \mathbf{v} \tag{7}$$

where μ_0 is the vacuum magnetic permeability, γ is the adiabatic constant, ν is an artificial viscosity coefficient chosen to maintain numerical stability and all the other quantities are conventional. Here, $\mathbf{j}_h'$ is the energetic ion current density without $\mathbf{E} \times \mathbf{B}$ drift. The effect of the energetic ions on the MHD fluid is taken into account in the MHD momentum equation [Eq. (2)] through the energetic ion current. The MHD equations are solved using a finite difference scheme of fourth order accuracy in space and time.

In the linear MHD simulation, the following equations are solved:

$$\frac{\partial \rho}{\partial t} = -\nabla \cdot (\rho_{eq}\mathbf{v}) \tag{8}$$

$$\rho_{eq}\frac{\partial}{\partial t}\mathbf{v} = -\nabla p_{eq} + (\mathbf{j}_{eq} - \mathbf{j}_{h\,eq}') \times \delta\mathbf{B} + (\delta\mathbf{j} - \delta\mathbf{j}_h') \times \mathbf{B}_{eq} + \nu\rho[\frac{4}{3}\nabla(\nabla \cdot \mathbf{v}) - \nabla \times \vec{\omega}] \tag{9}$$

$$\frac{\partial \mathbf{B}}{\partial t} = -\nabla \times \mathbf{E} \tag{10}$$

$$\frac{\partial p}{\partial t} = -\nabla \cdot (p_{eq}\mathbf{v}) - (\gamma - 1)p_{eq}\nabla \cdot \mathbf{v} \tag{11}$$

$$\mathbf{E} = -\mathbf{v} \times \mathbf{B}_{eq} + \eta(\mathbf{j} - \mathbf{j}_{eq}) \tag{12}$$

$$\mathbf{j} = \frac{1}{\mu_0}\nabla \times \mathbf{B} \tag{13}$$

$$\vec{\omega} = \nabla \times \mathbf{v} \tag{14}$$

The drift-kinetic description is employed for the energetic ions. The energetic ion current density without $\mathbf{E} \times \mathbf{B}$ drift in Eq. (2) includes the contributions from parallel velocity, curvature and gradient drifts, and magnetization current. The $\mathbf{E} \times \mathbf{B}$ drift disappears in $\mathbf{j}_h'$ due to quasi-neutrality [8].

It is important to start the simulations from MHD equilibria consistent with energetic ion distributions. When the energetic ion pressure is isotropic in the velocity space, the energetic ion contribution in Eq. (2) is just a scalar pressure gradient in the same form as the bulk pressure gradient [8]. Then, the equilibrium can be obtained from the Grad-Shafranov equation neglecting the energetic ion orbit width. However, if the energetic ion pressure is anisotropic in the velocity space and/or the energetic ion orbit width is not negligibly small,

the Grad-Shafranov equation should be extended. We solve an extended Grad-Shafranov equation developed in Ref. [11] in the cylindrical coordinates (R, φ, z) where R is the major radius coordinate, φ is the toroidal angle coordinate, and z is the vertical coordinate. Details of the kinetic equilibrium construction is reported in Ref. 9.

3. Simulation Results

A tokamak plasma with aspect ratio of 3.2 was investigated. The spatial profiles of safety factor and beam ion beta are shown in Fig.1. The maximum velocity of beam ions is $1.2v_A$. Here, v_A denotes Alfvén velocity at the plasma center. The ratio of the beam ion parallel Larmor radius to the minor radius is 0.09 for beam ion velocity equal to the Alfvén velocity. The magnetic moment is assumed to be zero to for simplicity. The number of grid points are 101×100×101 for the cylindrical coordinates (R, φ, z). The viscosity and resistivity are chosen $\nu = 10^{-6} v_A R_0$ and $\eta = 10^{-6} \mu_0 v_A R_0$, respectively.

For the equilibrium condition mentioned above, we found that the toroidal Alfvén eigenmodes (TAE) with toroidal mode numbers n=3-5 are linearly unstable. The spatial profile of the most unstable TAE with n=4 is shown in Fig. 2. The frequency of the TAE with n=4 is located inside the gap of the Alfvén continuous spectra, as shown in Fig. 3.

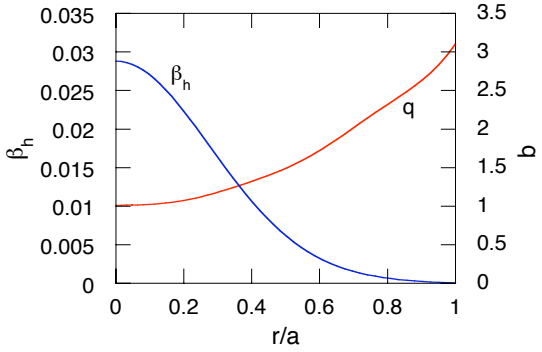

Fig.1 Spatial profiles of beam ion beta and safety factor.

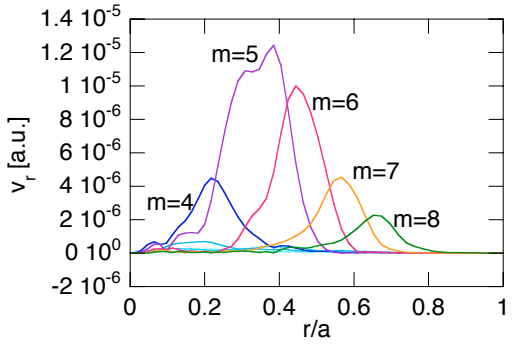

Fig.2 Spatial profile of each poloidal harmonic of the toroidal Alfvén eigenmode with toroidal mode number n=4.

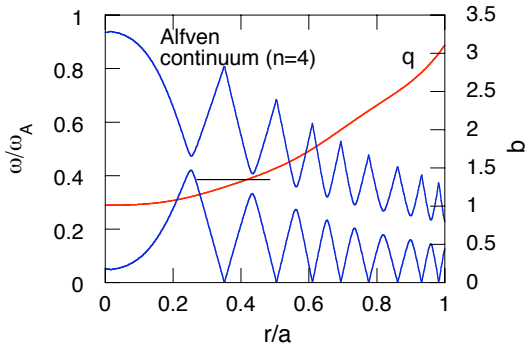

Fig.3 Frequency and location of the toroidal Alfvén eigenmode with toroidal mode number n=4. Alfvén continuous spectra are represented by blue curves. The safety factor profile is represented by red curve.

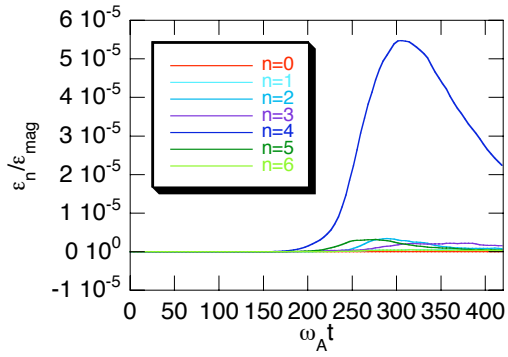

Fig.4 Time evolution of energy for each toroidal mode number in the linear MHD run.

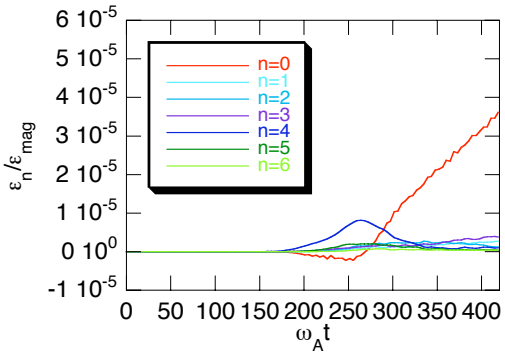

Fig.5 Time evolution of energy for each toroidal mode number in the standard nonlinear MHD run.

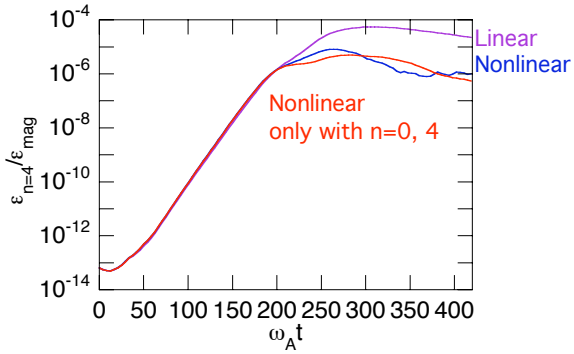

Fig.6 Comparison of energy evolution of toroidal mode number n=4 between the standard nonlinear MHD run (blue curve), the linear MHD run (violet curve), and the nonlinear MHD run where only n=0, 4 modes are retained (red curve).

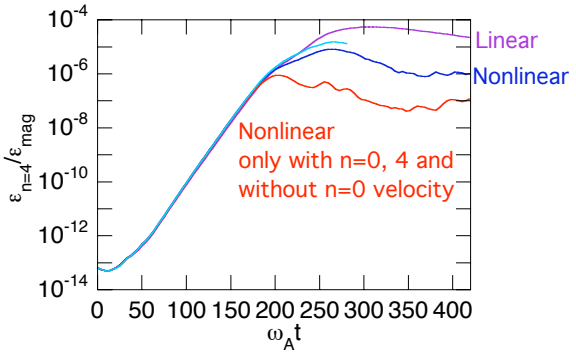

Fig.7 Comparison of energy evolution of toroidal mode number n=4 between the standard nonlinear MHD run (blue curve), the linear MHD run (violet curve), and the nonlinear MHD run where only n=0, 4 modes are retained and the n=0 velocity field is removed (red curve). Light blue curve represents a run where only n=0, 4 modes are retained and the n=0 magnetic field is removed.

A linear MHD simulation and a nonlinear MHD simulation were carried out. The evolution of energy for each toroidal mode number is shown in Fig. 4 for the linear run and in Fig. 5 for the nonlinear run. The n=4 TAE is the most unstable and is saturated at $\omega_A t = 300$ in Fig. 4 and at $\omega_A t = 260$ in Fig. 5. Comparing Figs. 4 and 5, the saturation level of the n=4 mode energy in the nonlinear MHD run is 15% of that in the linear MHD run. The saturation amplitude of the n=4 TAE is $\delta B / B \sim 2 \times 10^{-2}$ in the linear MHD run, and $\delta B / B \sim 8 \times 10^{-3}$ in the nonlinear MHD run. MHD nonlinear effects suppress the TAE saturation level. We see in Fig. 5 that the n=0 mode energy continuously grows until the end of the simulation after the saturation of the n=4 mode energy. This suggests that the beam ions continue to drive TAEs while some nonlinear mechanism stabilizes them converting the TAE energy into the n=0 mode energy.

We carried out another nonlinear MHD run where toroidal mode numbers only n=0 and 4 are retained. The time evolution of energy for toroidal mode number n=4 is shown in Fig. 6 with those of the standard nonlinear run shown in Fig. 5 and the linear run shown in Fig. 4. The saturation level in the run with the selected modes is similar to the standard nonlinear run. This indicates that the TAE saturation level is suppressed by the n=0 harmonics rather than the harmonics with higher toroidal mode numbers. We carried out other two runs where only n=0 and 4 harmonics are retained and the n=0 velocity field or the n=0 magnetic field is removed. The results are compared in Fig. 7. We see that the saturation level is the lowest when the n=0 velocity field is removed. These results indicate that the suppression effect arises from the change in n=0 harmonics of the magnetic field ($\delta\mathbf{B}_{n=0}$). Since there is no n=0 velocity field in this run, $\delta\mathbf{B}_{n=0}$ is generated by a nonlinear electric field $\mathbf{E}_{n=0} = -\mathbf{v}_{n=4} \times \delta\mathbf{B}_{n=4}$, which is the nonlinear electric field of the TAE. The lowest saturation level without the n=0 velocity field implies that the n=0 velocity field relaxes $\delta\mathbf{B}_{n=0}$ and its suppression effect.

It is not clear why $\delta\mathbf{B}_{n=0}$ suppresses the TAE saturation level. We show in Fig. 8 the Alfvén continuous spectra and the safety factor profile at $\omega_A t = 280$ in the standard nonlinear MHD run. In Fig. 5 the growth of the n=4 mode energy is saturated just before this time. We see that the safety factor profile is steepened near the n=4 TAE spatial peak at $r/a \sim 0.4$. The n=0 poloidal velocity field at the same time in the standard nonlinear MHD run is shown in Fig. 9. The poloidal harmonics m=0 and 1 are dominant in the n=0 poloidal velocity field. The poloidal velocity field sharply peaks near the n=4 TAE spatial peak.

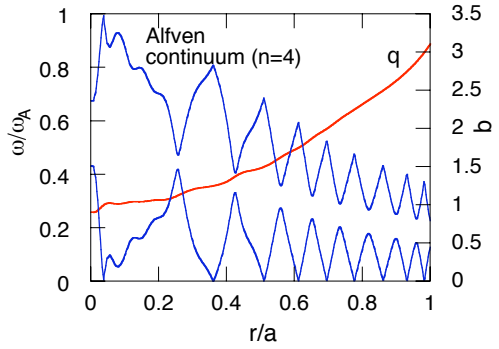

Fig.8 Alfvén continuous spectra with the toroidal mode number n=4 and the safety factor profile at $\omega_A t = 280$ *in the standard nonlinear run.*

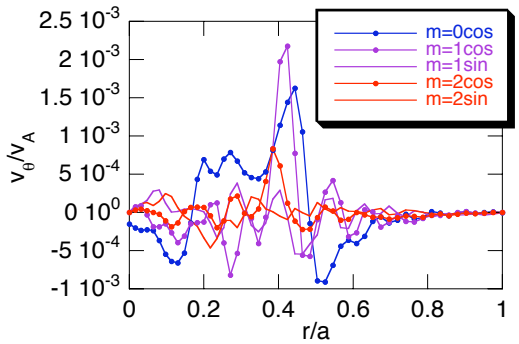

Fig.9 Poloidal velocity field with the toroidal mode number n=0 at $\omega_A t = 280$ *in the standard nonlinear run.*

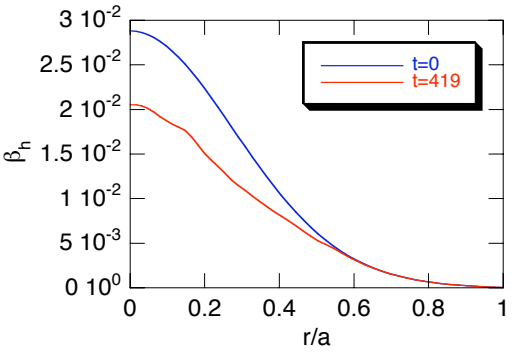

Fig.10 Initial and final beam ion beta profile in the linear MHD run.

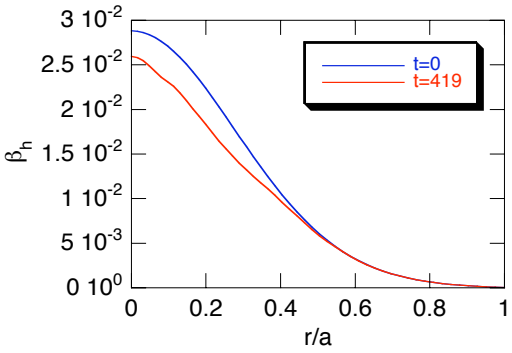

Fig.11 Initial and final beam ion beta profile in the standard nonlinear MHD run.

Initial and final beam ion beta profiles are compared in Fig. 10 for the linear MHD run and in Fig. 11 for the standard nonlinear MHD run. We see that the beam ion transport is also suppressed by the MHD nonlinear effects.

4. Discussion and Summary

Saturation of TAE instability due to MHD nonlinear effects was theoretically investigated in Ref. 12. Comparison between the present simulation results and the theory in Ref. 12 is needed. The change in safety factor profile and the generation of $\mathbf{E}\times\mathbf{B}$ flow were found in a computer simulation where energetic particles are approximated by the Landau Fluid model [13]. In Ref. 13, it is reported that the $\mathbf{E}\times\mathbf{B}$ flow has the dominant effects on the saturation of the TAE instability. On the other hand, in the present simulation results, it was found that the change in the n=0 magnetic field suppresses the saturation level of the TAE.

In this paper, the two types of simulation results were presented and compared. In the first type of the simulation the fully nonlinear MHD equations are solved, while linearized MHD equations are employed in the second type. A tokamak plasma, where a toroidal Alfvén eigenmode (TAE) with toroidal mode number n=4 is the most unstable, was investigated. Comparison between the results of the two types of simulations clarified the MHD nonlinear effects. We found that the saturation level is $\delta B/B \sim 8\times10^{-3}$ in the nonlinear MHD simulation results when the saturation level is $\delta B/B \sim 2\times10^{-2}$ in the linear MHD simulation results. The MHD nonlinear effects suppress the saturation level of the TAE. Detailed analyses indicate that the suppression effect arises from the change in n=0 harmonics of the magnetic field that is generated by the nonlinear electric field $-\mathbf{v}_{TAE}\times\delta\mathbf{B}_{TAE}$, a product of the velocity field and the magnetic field of the TAE. Axisymmetric velocity fields are also generated in the nonlinear run, although the change in the n=0 magnetic field plays the dominant role in the suppression of TAE.

We have demonstrated that the MHD nonlinear effects suppress the TAE saturation level. It was also demonstrated by a computer simulation that the synchronized bursts of multiple TAEs take place with the MHD nonlinearity [7]. Thus, we can expect a simulation which reproduces the TAE bursts with saturation amplitude closer to that inferred from the experimental plasma displacement. On the other hand, as has been shown in this paper, energetic ion transport is also suppressed by the MHD nonlinearity. These results indicate that we need to focus on the feedback of the MHD fluid for the saturation level as well as beam ion transport in phase space when we try to simulate the TAE bursts.

References

[1] G. Y. Fu and W. Park, Phys. Rev. Lett. **74**, 1594 (1995).
[2] Y. Todo, T. Sato, K. Watanabe, T. H. Watanabe, and R. Horiuchi, Phys. Plasmas **2**, 2711 (1995).
[3] Y. Wu, R. B. White, Y. Chen, and M. N. Rosenbluth, Phys. Plasmas **2**, 4555 (1995).
[4] S. Briguglio, F. Zonca, and G. Vlad, Phys. Plasmas **5**, 3287 (1998).
[5] Y. Todo, H. L. Berk, and B. N. Breizman, Phys. Plasmas **10**, 2888 (2003).
[6] R. D. Durst, R. J. Fonck, K. L. Wong, C. Z. Cheng, E. D. Fredrickson, and S. F. Paul, Phys. Fluids B **4**, 3707 (1992).
[7] Y. Todo, T.-H. Watanabe, Hyoung-Bin Park, and T. Sato, Nuclear Fusion **41**, 1153 (2001).
[8] Y. Todo and T. Sato, Phys. Plasmas **5**, 1321 (1998).
[9] Y. Todo, K. Shinohara, M. Takechi, and M. Ishikawa, Phys. Plasmas **12**, 012503 (2005).
[10] W. Park et al., Phys. Fluids B **4**, 2033 (1992).
[11] E. V. Belova, N. N. Gorelenkov, and C. Z. Cheng, Phys. Plasmas **10**, 3240 (2003).
[12] F. Zonca, F. Romanelli, G. Vlad, and C. Kar, Phys. Rev. Lett. **74**, 698 (1995).
[13] D. A. Spong, B. A. Carreras, and C. L. Hedrick, Phys. Plasmas **1**, 1503 (1994).

Effects on Ion Cyclotron Emission of the Orbit Topology Changes from the Wave-Particle Interactions

T. Hellsten, K. Holmström, T. Johnson, T. Bergkvist, and M. Laxåback

Alfvén Laboratory, Association VR-Euratom, Sweden
Email: torbjorn.hellsten@alfvenlab.kth.se

Abstract. It is known that non-relaxed distribution functions can give rise to excitation of magnetosonic waves by ion cyclotron interactions when the distribution function increases with respect to the perpendicular velocity. We have found that in a toroidal plasma also collisional relaxed distribution functions of central peaked high-energy ions can destabilise magnetosonic eigenmodes by ion cyclotron interactions, due to the change in localisation of the orbits establishing inverted distribution functions with respect to energy along the characteristics describing the cyclotron interactions. This can take place by interactions with barely co-passing and marginally trapped high-energy ions at the plasma boundary. The interactions are enhanced by tangential interactions, which can also prevent the interactions to reach the stable part of the characteristics where they interact with more deeply trapped orbits.

1. Introduction

Emission of waves in the ion cyclotron range of frequencies has received considerable attention because of the possibility to yield information on fast particle distributions, in particular on thermonuclear alpha particles. The emission spectra are characterised by series of narrow peaks corresponding to multiple harmonics of the cyclotron frequencies of suprathermal ions at the low field side of the plasma edge. In JET, emission related to fusion products has been found to correlate with the fusion reactivity over six orders in magnitude; in high current sawtoothing discharges (6MA discharges) the emission displayed inverted sawteeth [1], and vanished after large ELMs, but was less affected by small ELMs. This behaviour is consistent with excitation of waves at the outer part of the plasma by high-energy ions [2]. In plasmas heated with ion cyclotron resonance heating emission peaks appear when the power exceeds a threshold, and is delayed with a slowing down time after the application of RF power [3]. In TFTR supershot experiments with NBI a sudden change of the spectrum occurred during the discharge. In the early part of the heating phase, high amplitude peaks were seen corresponding to unshifted ion cyclotron resonances located just outside the plasma. At a later time the amplitude of the peaks were lower and the frequency higher, the corresponding cyclotron resonances were located just inside the plasma [2].

The high intensity of the emission is consistent with magnetosonic ion cyclotron instabilities driven by suprathermal high-energy ions, originating either from thermonuclear reactions, neutral beam- or ion cyclotron heating. Such instabilities can occur when the distribution function is inverted along the characteristics of the quasi-linear diffusion operator describing ion cyclotron interactions. It has been suggested that the anisotropy caused by high-energy ions with trapped drift orbits extending out to the plasma edge on the low-field side gives rise to magnetosonic instabilities causing the emission [4, 5]. Analysis by Dendy *et al* [4], in a uniform approximation of the plasma with a mono energetic distribution function, showed that the magnetosonic wave could be destabilised by obliquely propagating waves avoiding interactions with the thermal part due to the finite Doppler shift. A comprehensive analysis of the emission taking into account the two dimensional structure of the magnetsonic eigenmode and the finite banana width effects was made by Gorelenkov *et al* [6]; for instability it was necessary to have a collisional un-relaxed energy distribution. Such distribution function could exist provided the fast ions are lost before they are slowed

down. However, emission during ICRH appears only after times comparable to a slowing down time, when collisonal relaxed, steady state distribution functions, with sufficiently many high-energy ions have been established; such distribution functions would not satisfy the above mentioned condition for instability.

2. Wave-particle interactions in a toroidal geometry.

Whether an ion takes or delivers energy to the wave depends, for ion cyclotron interactions, on the difference between the phase of the wave oscillation and the gyro phase of the ion. On averaged, ions will give energy to the wave when the distribution function increases in energy along the characteristics for the cyclotron interactions. The variation of the distribution function along the characteristics depends on how the orbit changes as the invariants vary due to the interactions, in particular the innermost and the outermost positions of the orbit. The characteristics can be obtained by calculating the changes in the orbit invariants due to ion cyclotron interactions by integrating the equation of motion along the orbit. Here we use the orbit invariants W, P_ϕ and Λ in a toroidal geometry, where W is the energy, P_ϕ the canonical momentum and Λ an adiabatic invariant; defined by $P_\phi = mR\upsilon_\phi + eZ\Psi$ and $\Lambda = \mu B_0/W$, where $2\pi\Psi$ is the poloidal magnetic flux, μ is the magnetic moment and B_0 the magnetic field on the magnetic axis. The change in energy, ΔW, is given by

$$\Delta W = eZ\int_0^{\tau_B} \underline{\upsilon}\cdot\underline{E}\exp(-i\vartheta)dt \tag{1}$$

where ϑ is the phase difference between the wave oscillation and the gyro phase of the ion defined by

$$\vartheta = \int_0^t (\omega - n\omega_c - \underline{k}\cdot\underline{\upsilon})dt\,. \tag{2}$$

In general, the invariants of motion in a toroidal geometry, where the cyclotron frequency varies along the orbit, experience significant net changes only near the Doppler shifted cyclotron resonances, $\omega - n\omega_c - \underline{k}\cdot\underline{\upsilon} = 0$, due to the rapid variation of ϑ. Using the stationary phase method to integrate Eq. (1) one obtains

$$\Delta W = eZ\upsilon_\perp^{res}\,\mathrm{Re}\left\{\left(e^{-i\zeta}E_+\,\mathrm{J}_{n-1}(k_\perp\rho) + e^{i\zeta}E_-\,\mathrm{J}_{n+1}(k_\perp\rho)\right)\sqrt{\frac{i\pi}{\ddot{\vartheta}}}\exp i\vartheta_0\right\}, \tag{3}$$

where ζ defines the direction of the wave through $k_y/k_x = \tan\zeta$ in a local (x, y)-coordinate system with the x–direction perpendicular to the magnetic flux surface and the y–direction parallel to the magnetic flux surface and perpendicular to the magnetic field. ϑ_0 is the phase difference at the resonance, *i.e.* where the phase is stationary, ρ is the gyro radius, $k_\perp$ the perpendicular wave number. E_+ and E_-, given by $E_\pm = \frac{1}{2}(E_x \pm iE_y)$, are the perpendicular electric field components rotating in the direction of the ions (+) and counter to them (–).

Considerable enhancement of the wave-particle interactions takes place at tangential resonances where $\ddot{\vartheta}\to 0$ because $\ddot{\vartheta}\propto\sin\theta$. In this case a more accurate expression is required than that given by Eq. (3), which can be obtained by expanding the change in gyro phase around the Doppler shifted resonance yielding [7-9]

$$\Delta W = eZ\upsilon_\perp^{res}\,\mathrm{Re}\left\{\left(e^{-i\varsigma}E_+J_{n-1} + e^{i\varsigma}E_-J_{n+1}e^{i\Psi_R}\right)2\pi\left(\frac{2}{\ddot{\vartheta}}\right)^{1/3}\mathrm{Ai}\left[-\frac{1}{2^{2/3}}\frac{\dddot{\vartheta}^2}{\ddot{\vartheta}^{4/3}}\right]\right\}, \tag{4}$$

where Ai is the Airy function. The above expression defines the change in energy when two resonances are close together, merge into a tangential one and afterwards when they just

disappear. In the latter case the argument in the Airy function becomes imaginary, with Ai decreasing exponentially.

The changes in P_ϕ and $\Lambda = \mu B_0/W$ are given by:

$$\Delta P_\phi = \frac{n_\phi}{\omega}\Delta W \qquad \Delta\Lambda = \left(\Lambda_r - \Lambda\right)\frac{\Delta W}{W}, \tag{5}$$

where $\Lambda_r = n\omega_{c0}/\omega$, ω_{c0} is the cyclotron frequency at the magnetic axis and n the harmonics of the cyclotron frequency. In absence of decorrelation of the wave-particle interactions, a superadiabatic oscillation of the orbit invariants along the characteristics takes place. Decorrelated interactions with a single mode near one harmonic will describe a 1D-diffusion process of the orbit invariants along the characteristics [10, 11].

When an ion gains energy from the wave, the major radius of the Doppler shifted resonance increases and vice versa when it loses energy [11]. The energy an ion can reach due to the cyclotron interactions alone is limited either by the ion orbit intersecting the wall or by the Doppler shifted resonances merging into a tangential one at the low-field side for a passing orbit or at the low-field side of the inner or the outer leg for a trapped orbit [9, 11]. If the Doppler shifted resonances merge into a tangential one at the high-field side of the orbit, the minimum energy the ion can reach becomes also limited. In general, the distribution function increases only in a finite interval along the characteristics, the tangential resonances can prevent the interactions to continue into an upper stable part of the characteristics and at the same time enhance the interactions at the most unstable part by suitable choice of the frequency.

Unstable interactions appear when barely co-passing ions interact near the plasma boundary with co- or counter-propagating waves, for which the distribution function will be decreasing in energy below the trapped-passing boundary; fusion reactions and cyclotron heating produce only few high-energy co-passing ions there. Fig.1 illustrates the de-trapping of an orbit into a co-passing one as the wave takes energy from the ion. In the case the unshifted cyclotron resonance is located outside on the low-field side of the orbit the upper energy limit prevents interaction with the stable part of the distribution function consisting of deeply trapped ions.

For instability, the sum of the background damping and the interactions with all resonant ions has to result in a net increase of the mode energy. This can be achieved, if the interactions with the most unstable part of the distribution function takes place at tangential resonances and the mode is sufficiently localised at the plasma edge [5].

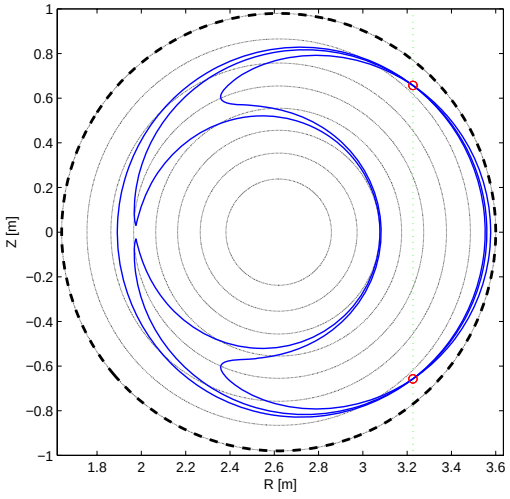

Fig. 1. Detrapping of a trapped orbit into a co-passing orbit as the energy is reduced due to cyclotron interaction, W = 1.0MeV, Λ= 0.9, (deeply trapped) W = 0.69MeV, Λ= 0.75 (marginal trapped) and W = 0.48MeV, Λ= 0.55 (co-passing) for n_ϕ= 0. The Cyclotron resonance is located at R=3.2m.

3. Numerical simulation.

The power absorbed in a volume element centred at (r, θ) is given by

$$P = \mathrm{Re}\left\{\frac{-i\omega}{8\pi}\iint \underline{E}^{*}\,\underline{\underline{\chi}}^{A}\,\underline{E}\; r dr d\theta\right\} \tag{6}$$

with

$$\underline{\underline{\chi}}^{A} = \frac{\omega_p^2}{\omega\omega_c}\int_0^{\infty} 2\pi v_\perp dv_\perp \int dv_{//}\,\frac{\omega_c}{\omega - \underline{k}\cdot\underline{v} - n\omega_c}\,\underline{\underline{S}}_n\,. \tag{7}$$

When neglecting the parallel electric field component $\underline{\underline{S}}_n$ becomes

$$\underline{\underline{S}}_n = v_\perp \begin{pmatrix} \left(\frac{n\omega_c J_n}{k_\perp v_\perp}\right)^2 & \frac{in\omega_c J_n J'_n}{k_\perp v_\perp} \\ -\frac{in\omega_c J_n J'_n}{k_\perp v_\perp} & \left(J'_n\right)^2 \end{pmatrix} \left\{\frac{\partial f}{\partial v_\perp}\left(1 - \frac{k_{//}v_{//}}{\omega}\right) + \frac{k_{//}v_\perp}{\omega}\frac{\partial f}{\partial v_{//}}\right\}. \tag{8}$$

Assuming the magnetic field to vary according to the toroidal equilibrium, expanding the nominator, $\omega - n\omega_c - \underline{k}\cdot\underline{v}$, around the resonance and integrating with respect to θ we obtain after some algebra

$$P \approx \frac{\omega}{4}\int r dr \int_{-\infty}^{\infty} dv_{//}\,\frac{\omega_p^2}{\omega\omega_c}\int_0^{\infty} 2\pi v_\perp dv_\perp \,\frac{\omega_c v_{//}}{|\ddot{\vartheta}| qR}\,\underline{E}^{*}\,\underline{\underline{S}}_n\,\underline{E}\;\Big|_{\theta 0} \tag{9}$$

When applying the quasi-homogenous dielectric tensor to a toroidal geometry there is no enhancement of the anti-Hermitian part with a factor $1/|\sin\theta|$ due to tangential interactions as $\ddot{\vartheta} \to 0$. The enhancement instead appears as an increase of the volume elements, where the anti-Herimtian part is significant, with the same factor. The integration in velocity space in Eq. (9) should only include particles that are resonant in the considered volume element. The ions give on averaged energy to the wave when

$$\frac{\partial f}{\partial v_\perp}\left(1 - \frac{k_{//}v_{//}}{\omega}\right) + \frac{k_{//}v_\perp}{\omega}\frac{\partial f}{\partial v_{//}} = \frac{n\omega_c}{\omega}\frac{\partial f}{\partial v_\perp} + \frac{k_{//}v_\perp}{\omega}\frac{\partial f}{\partial v_{//}} < 0 \tag{10}$$

To illustrate how thermonuclear alpha-particles can destabilize edge localised modes we calculate the susceptibility tensor with the SELFO code [12, 13] for a steady state alpha-particle distribution function, arising from slowing down of thermonuclear particles including finite orbit width effects in a circular tokamak with parameters similar to those of TFTR: R_0 =2.52m, a =0.9m, I_p =1.6MA, n_T =2.5 $\times 10^{19}$m^{-3}, n_D =2.5 $\times 10^{19}$m^{-3}, n_C =2.0 $\times 10^{18}$ m^{-3}, T_e =5keV , T_i =20keV, B_0 =5.0T, $n(r)=n_0(1-0.99(r/a)^2)^{0.2}$ and $T(r)= T_0(1-0.2(r/a)^2)^{10}$. For simplicity we have assumed that the resonances are located where $k_{||} = n_\phi/R$. Because of the relatively small value of $v_\perp k_\perp/\omega_c$ the anti-Hermitian part of the susceptibility tensor elements χ_{xx}, χ_{xy} and χ_{yy} are nearly similar. Some differences occur because the largest contribution to the susceptibility comes from the high-energy ions, for which ($n\omega_c J_n/ k_\perp v_\perp$) and J'_n starts to deviate. The anti-Hermitian part of the susceptibility tensor elements χ_{xy}, which in general has the largest negative anti-Hermitian part, is shown in Fig. 2 for some frequencies around $\omega \approx 4\omega_{c\alpha}$ at the low-field side edge, for waves with n_ϕ = 25 and n_ϕ = –25. Large regions with positive values of the anti-Herimitian part of the susceptibility tensor

elements χ_{xy} can be seen in the central region giving rise to damping; because of the weaker spatial gradients of the alpha particle density, the distribution function is decreasing in energy along the characteristics. For n_ϕ = 25 with f = 110MHz, Fig. 2f, when the 4th harmonic resonance is just outside the plasma at the low field side a large negative region at the low-field side appears corresponding to interactions with co-current passing ions and with marginally trapped ions at the outer leg. The unstable contributions from trapped and co-passing orbits were confirmed by separating the anti-Hermitian part of the susceptibility element into contributions from co-, counter-passing and trapped alpha particles. As the frequency is increased and the 4th harmonic resonance is displaced into the plasma at the low-field side, as for f = 116MHz shown in Fig. 2f, the unstable region is shifted into the plasma followed by a stable region. The stable region consists of deeply trapped high-energy ions and lower energy ions. This is consistent with as one follows the characteristics in the region of trapped orbits towards higher energy, the Doppler shifted resonances are shifted closer to the unshifted resonance as the orbits become more deeply trapped. Since the number of ions become fewer as they become more deeply trapped, the distribution function will decrease with energy along these parts of the characteristics, giving rise to a stable region. As the 4th harmonic resonance moves into the plasma on the low-field side also a large stable region caused by interactions with counter-passing ions at the high-field side at the low-field side of the 2nd harmonic resonance that will damp edge localised magnetosonic waves propagating poloidaly around the magnetic axis at the plasma edge.

Regions with negative anti-Hermitian part of the susceptibility element χ_{xy} appear also for waves propagating counter to the plasma current as for n_ϕ = 25 at f = 124MHz, Fig. 2d. An unstable region similar to that in Fig. 2g appears at the low-field side edge, but on the low-field side of the 4th harmonic resonance, which in this case also corresponds to interactions with co-current passing ions and with trapped ions on the outer leg. However, as the energy increases due to cyclotron interactions and the trapped orbits become more deeply trapped the Doppler shifted resonances are shifted towards the unshifted resonance thus into the plasma resulting in a stable region close to the unshifted resonance, which also include interactions with less energetic ions for which the distribution function is not inverted with respect to energy. Because of the presence of this stable region close to the unstable region unstable excitation of edge localised modes requires stronger localisation of the mode to the edge, which may be difficult to achieve.

By performing a frequency scan to identify the range, in which the instability at the edge, illustrated in Fig. 2f, can appear, we find it to be limited within the range of 104MHz to 113MHz, thus less than 10% of the frequency.

The behaviour of the anti-Hermitian part of the susceptibility tensor is similar at higher frequencies when the mode numbers are scaled up accordingly, but the regions, where the anti-Hermitian part of the susceptibility tensor are significant, start to overlap.

In most of the plasma the anti-Hermitian parts of the susceptibility tensor components are positive, in particular, near the centre, where they are large and will damp the waves. Thus only waves propagating near the plasma edge avoiding the stable regions can become unstable [5]. The typical width of edge localised modes, Δr, varies between 0.12 and 0.18r_0, when m_θ varies between 50 and 25, using the formula in Ref. [14]. Thus the width of the edge localised mode is conceivable with unstable excitation of a mode corresponding to the case outlined in Fig. 2f.

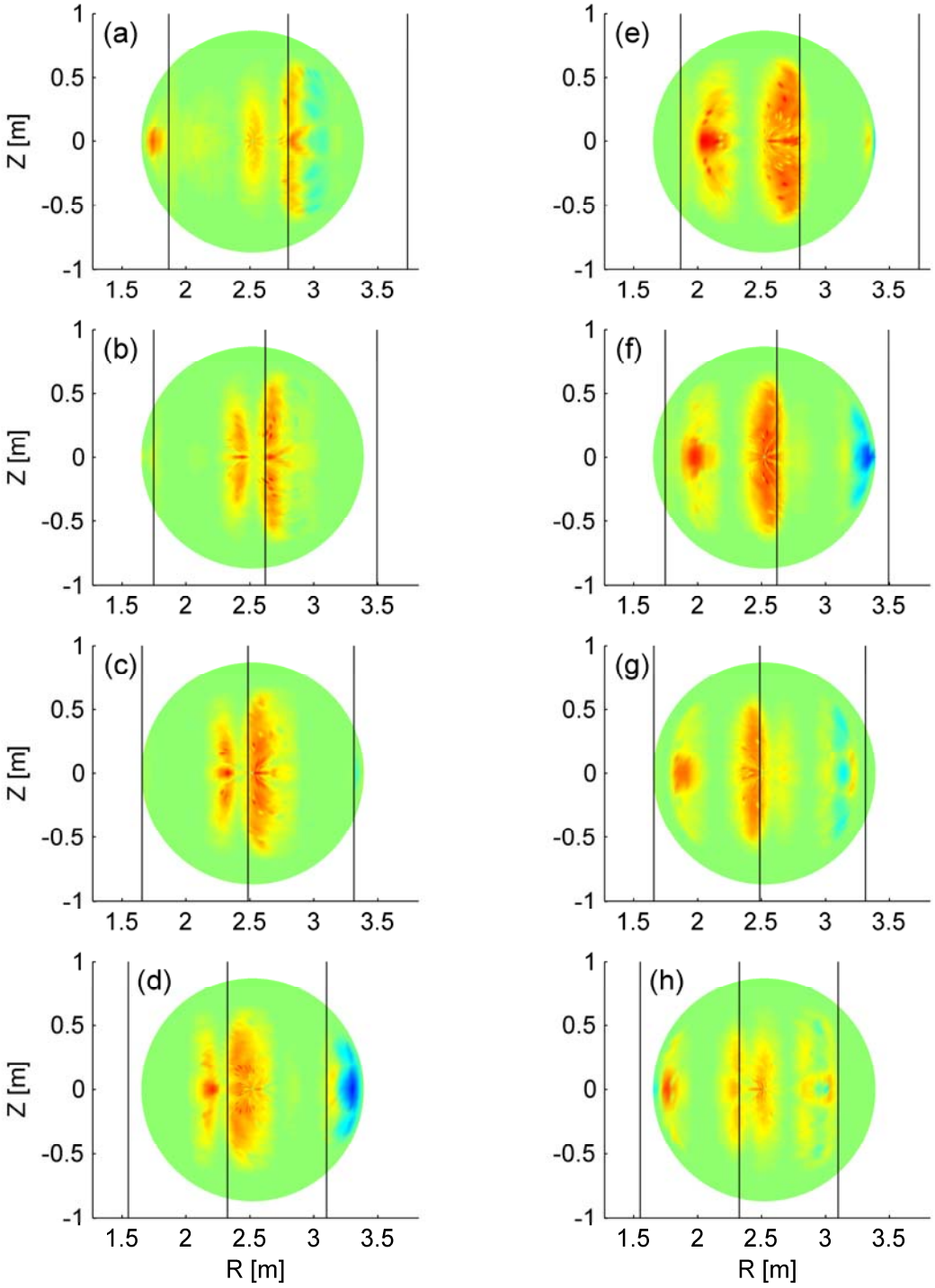

Fig. 2. The anti-Hermitian susceptibility tensor element χ_{xy} for alpha particles (blue is negative, green zero and yellow-red positive values) a-d) $n_\phi = -25$ a) f = 103MHz, b) f = 110MHz, c) f = 115MHz, d) f = 124MHz, e-h) $n_\phi = 25$, e) f = 103MHz f) f = 110MHz, g) f = 116MHz, h) f = 124MHz. The vertical lines indicates the harmonic cyclotron resonances $\omega = n\omega_c$ for n = 2, 3, 4.

4. Conclusions and Discussions

We have found that in a toroidal plasma, with a centrally peaked, collisional relaxed, steady state distribution function inverted distribution functions along the characteristics describing the quasi-linear diffusion by ion cyclotron interactions can be obtained because of the toroidal geometry. Interactions with marginally trapped and barely co-passing ions with co- and counter propagating waves are possible. Interactions at or near tangential resonances in the outer midplane can enhance the drive by the unstable part of the distribution function and limit it from interacting with the stable part.

The pattern with positive and negative regions of the anti-Hermitian part of the susceptibility tensor of a steady state thermonuclear alpha-particle distribution function is conceivable with excitation of edge localised magnetosonic waves with $m_\theta \approx -n_\phi$; even though the edge localised magnetosonic eigenmodes are not localised in major radius and that the distribution function has reached steady state by collisions.

The emission spectrum at the early phase in the TFTR supershots with emission peaks corresponding to harmonic cyclotron resonances just outside the plasma at the low-field side [2] is in good agreement with the case illustrated in Fig. 2f. The change in the spectrum at a later time in presence of NBI can be caused with the same mechanism, but since the ions have less energy the unshifted resonance has to be displaced closer or into the plasma.

5. References

[1] COTRELL, G. A., *et al*., Nucl. Fusion **33** (1993)1365
[2] CAUFFMAN, S., *et al.* Nucl. Fusion **35** (1995) 1597
[3] COTTRELL, G. A. Phys Rev. Lett **84** (2000) 2397
[4] DENDY, R.O., *et al.* Phys. Fluids **B5** (1993)1937
[5] COPPI, B. Physics Letters **A172** (1993)439
[6] GORELENKOV, N.N. and CHENG, C. Z. Nuclear Fusion **35** (1995)1743
[7] KERBEL, G. D. and McCOY, M. G. Phys Fluids **28** (1985) 3629
[8] LAMALLE, P.U. Plasma Physics and Controlled Fusion **39** (1997)1409
[9] JOHNSON, T., *et al*., submitted to Nuclear Fusion
[10] ERIKSSON, L.-G. and HELANDER, P. Physics of Plasmas **6** (1999)513.
[11] HELLSTEN, T. *et al.* Nucl. Fusion **44** (2004)892
[12] HEDIN, J. *et al* Proc. Joint Varenna-Lausanne Workshop "Theory of Fusion Plasmas" (Varenna) p 467, ISBN 88-7794-167-7 (1998)
[13] LAXÅBACK, M., *et al*. submitted to Nuclear Fusion.
[14] HELLSTEN, T. and LAXÅBACK, M., Phys. of Plasmas **10** (2003)4371

Integration of Lost Alpha-Particle Diagnostic Systems on ITER

M. Sasao, M. Isobe [A], M. Nishiura [A], B. J. Peterson [A], C. Walker [B], R. Barnsley [B], N. Kubo, H. Nishimura, T. Hirouchi, H. Utoh, K. Okada, M. Okamoto, K. Shinto, S. Kitajima, and S.V. Konovalov [C]

Tohoku University, 6-6 Aoba, Aramaki, Aoba, Sendai 980-8579, Japan

[A] National Institute for Fusion Science (NIFS), 332-6 Oroshi, Toki, Gifu 509-5292, Japan

[B] ITER International Team, Max-Planck-Institut Plasmaphysik, 85748 Garching, Germany

[C] Institute of Nuclear Fusion of RRC "Kurchatov Institute", Moscow , Russi

Abstract

Time-resolved measurement of lost alpha particles on the first wall is demanded on ITER, because it is anticipated that various kinds of collective instability are driven by alpha particles. Moreover, localization of alpha-particle loss on the first wall is one of the problems for the safe operation of ITER. However, the severe thermal/radiation environment of measurement location and the difficulties on the access and installation, limit the application of conventional measurement tools.

The ITER integration are studied for some candidates of lost alpha-particle measurement, such as the camera imaging of scintillators on the first wall, a scintillator probe, a Faraday-cup, and an imaging bolometer. An orbit calculation of escaping alpha particles is inevitable, and the orbit characteristics are considered in the conceptual design of these systems.

1. Introduction

The self-heating of a DT plasma by fusion-produced alpha particles is the key to the realization of self-sustainable ignition of a thermonuclear plasma for fusion reactors. The loss of alpha particles means the deterioration of the heating input power. Moreover, the localization of alpha particle bombardment on the first wall surface might induce a serious damage. Confinement of alpha particles is one of the key issues on ITER. Even before the real DT experiments lot of studies have been performed experimentally and theoretically, in these two decades, by using energetic beam particles for heating and fusion produced energetic ions from DD and D^3He reactions. As a result of the accumulation of these researches, it has been understood that the confinement of fast ions is governed by a number of processes, not only the magnetic structure, q-profiles and the energy and pitch angle diffusion originated in Coulomb collisions, but interaction with instabilities driven by themselves, and the other stochastic processes [1]. Especially some MHD events can transport alpha particles to the outer region of the plasma, and cause giant losses spiky in time and localized in space. Studies that combine alpha particles losses and characteristics of MHD activities are needed to identify the mechanisms responsible for alpha particle transport and loss.

In consideration of such a background, the diagnostic systems for the lost alpha particles prepared for ITER can be categorized into two groups. One is the energy and

pitch-angle resolved probes for the study of characterization of lost alpha particles, and the other one is the loss imaging on the surface of the first wall. Good time resolution is needed for systems of both groups.

However, the severe thermal/radiation environment of measurement location and the difficulties of access and installation, limit the application of conventional measurement tools. The typical neutron and γ flux on the first wall are 3 $x10^{18}$ n/m^2 /s, and $2x10^3$ Gr/s, respectively, at the maximum fusion power operation.

This paper describes the anticipated features of escaping alpha particle orbits, loss location (section 2), integration of several candidate systems of lost alpha-particle measurement (section 3), development and test of new type ceramic scintillator materials (section 4), and issues to be worked in future.

2. Features of alpha particle loss on ITER

The major origin of alpha particle loss is that of locally trapped in ripples, and banana particle loss. The former depends mostly on the ripple structure and is not so substantial in ITER, while the loss fraction of the latter is substantial and strongly depends on tokamak operation scenarios, the birth profile and the diffusion rate, as well as the ripple structure and strength. The poloidal distribution of the loss is ranging in 200 to 250 degree in angle from the inner mid-plane [2]. The typical heat load due to the alpha particle loss is expected in few kW/m^2 to several hundreds kW/m^2. The typical distribution under the standard operation is shown in Fig. 1. Under the operation of the reversed shear mode, it is anticipated that the loss might increase substantially. The MHD activities might also increase the loss.

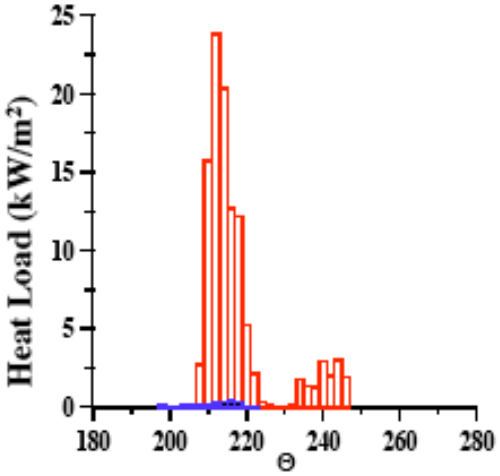

Fig. 1 Poloidal distribution of the heat load in the standard operation. Red histogram corresponds to banana particle loss and blue one shows locally trapped α loss [2].

The head load shown in Fig. 1 is smaller than the average 14 MeV neutron wall loading of 0.57 MW/m^2. But the effect of alpha bombardment on the first wall is severe because the energy deposit concentrates in a thin surface layer of the alpha particle range (in the range of few micro meters), while the neutron wall loading is received by the whole blanket materials.

3. ITER integration

Candidate methods of loss imaging are the IR camera imaging, camera imaging of scintillators fixed at various locations on the FW (scintillator imaging) [3, 4], and gamma ray imaging using $^{10}B(\alpha,p\gamma)^{13}C$ reaction [5]. Candidate methods of point measurement with energy and pitch-angle resolutions are faraday-cup detectors, Scintillator probes, and bolometric imaging [6]. In this paper, the ITER integration of scintillator imaging and the integration of various lost alpha probes are studied.

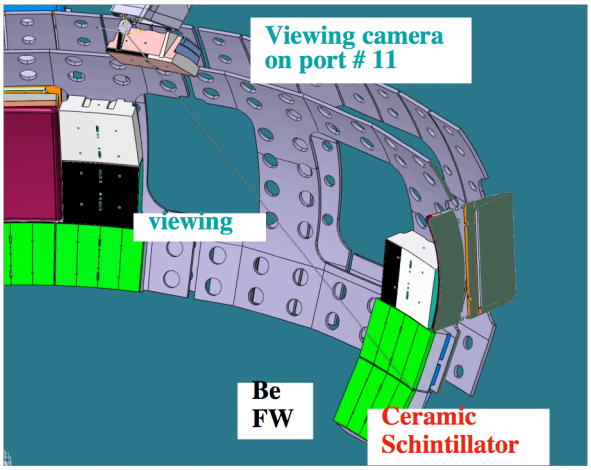

Fig. 2 Integration of the scintillator imaging system on a CAD drawing. The upper port 11 is used for the viewing camera, and the ceramic scintillators are fixed behind the edge of FW of BM #16, and #17 (Detector poison A).

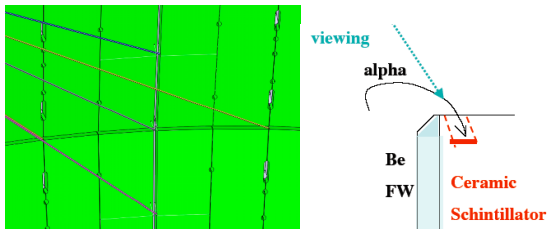

(a) (b)

Fig. 3 (a) The area viewed by the camera at the upper port 11. Extra holes on the slit of the first wall panels will be used for installation of various lost alpha probes.
Fig. 3 (b) A conceptual image of the scintillator imaging system.

Fig. 2 shows the geometry of the scintillator imaging system on a CAD drawing of ITER. Ceramic schintillators are fixed in holes on the edges of first wall (Cu backing) of the blanket module #16 and #17, and viewed by a camera with filters in the upper port. Fig. 3 shows the area view by the camera (a) and the conceptual image of the system.

Drift orbit calculations for escaping alpha particles have been performed starting from the detector position on the upper edge of the blanket module #17 (Fig. 4) with the time inverse. Only orbits with the pitch angle from $-\pi/2$ to 0 are shown because those with 0 to $\pi/2$ do not go back to the plasma. These drift orbits have turning points only in the peripheral region in the plasma, and they are not the best to monitor particles resonating with MHD excited in the inner region. Moreover, the drift orbits are too close wall surface as shown in the Fig. 4b. The straight lines in the Fig. 4b are connecting the outmost corners of the blanket module. The actual shape the corner is rounded and the module itself is curved poloidally and toroidally. It is necessary to carry out the full gyro-orbit calculation including the actual shape of the modules, in order to judge whether orbits starting from the detection

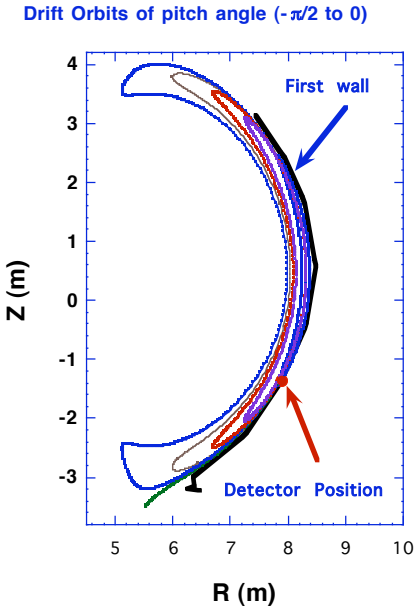

(a)

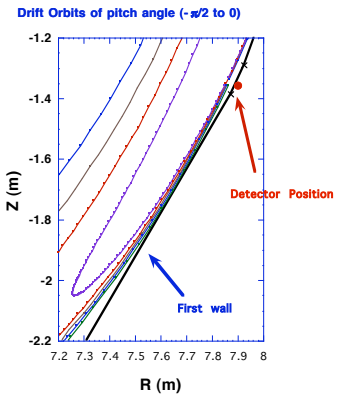

(b)

Fig. 4 (a) Drift orbits of escaping alpha particles calculated from the detector position on the upper edge of the blanket module #17 with the time inverse. (b) The closed up view of (a).

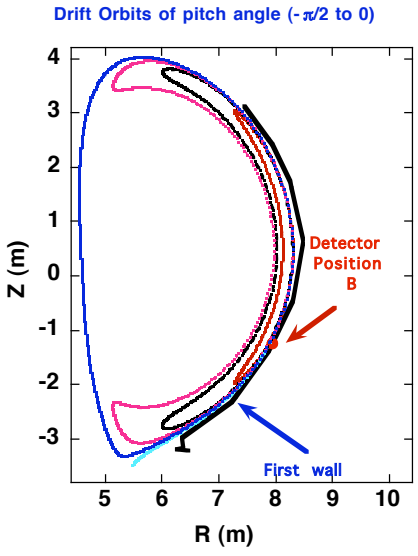

(a)

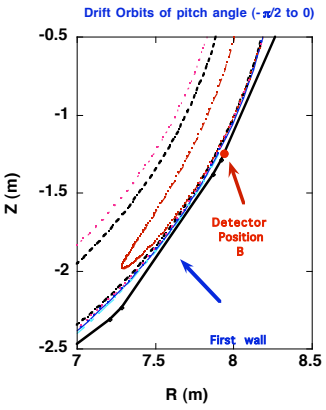

(b)

Fig. 5 (a) Drift orbits of escaping alpha particles calculated from the detector position on the slit of front panels of the blanket module #16 with the time inverse. (b) The closed up view of (a).

position really go back to plasma or not. Fig. 5 shows the drift orbit starting from the upper detection position, on the slit of front panels of the blanket module #16. These drift orbits have turning points in a wider region in the plasma, and include passing orbits. This detection

position is better to monitor particles resonating with MHD excited in the inner region, and is considered to be used for point measurement probes with energy and pitch-angle resolutions, such as faraday-cup detectors, scintillator probes, and bolometric imaging probes. Signals from these probes are transferred electrically (faraday cups) or optically (scintillators and bolometers).

4. Development and test of new type ceramic scintillator

New types of ceramic scintillator which are usable for lost alpha measurement under severe environment of high temperature have been developed [7]. It has been known that most of ceramic scintillator show thermal quench of luminescence at the temperature higher than 100 C. New ceramic plates were manufactured from inorganic ceramic compounds and various kinds of scintillation material. The ceramic scintillators thus made were bombarded by a 7 keV He^+ beam, extracted from a bucket-type source, and the scintillation spectra were measured with the PMA-11, changing the scintillator temperature with a sheath heater. Among four kinds of scintillation material tested, ZnS(Ag), ZnO(Zn), $Y_3Al_5O_{12}$(Ce), and $Y_3Al_5O_{12}$(Cr), the ceramics made from $Y_3Al_5O_{12}$(Cr) emit luminescence of the longest wave length. Considering the transmission degradation due to the neutron irradiation, the luminescence in the region of larger wave length is preferable.

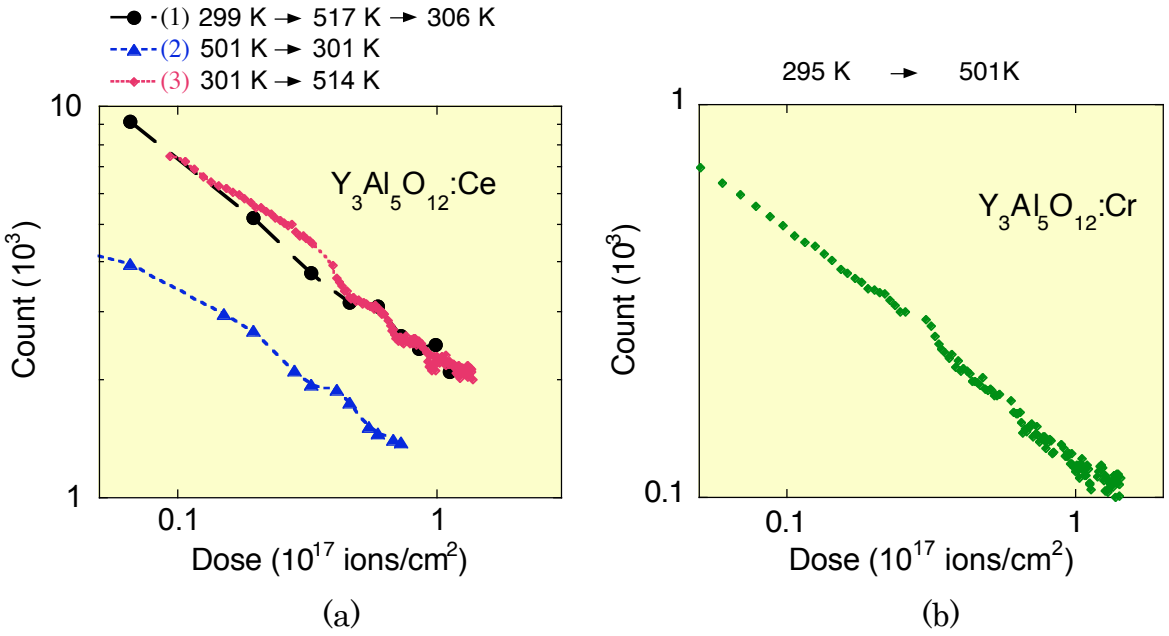

Fig. 6 Changes in scintillation efficiency of $Y_3Al_5O_{12}$(Ce) (a) and $Y_3Al_5O_{12}$(Cr) (b) with dose by 7 keV He^+ beam bombardment.

Figure 6 shows the changes in the scintillation efficiency of $Y_3Al_5O_{12}$(Ce) (a) and $Y_3Al_5O_{12}$(Cr) (b) during continuous bombardment by a 7 keV He^+ beam as a function of

with dose. The three results shown in the figure (a) are those of different thermal history. In case (1) , the bombardment and the measurement was started when the heater was turned on to increase the temperature, and the heater was turned off at T = 517 K. In case (2), the a new scintillator sample was preheated up to T = 501 K and then ion beam bombardment and measurement were started during the cooling down. The decay curves in figure 3(a) indicate that the change in scintillation efficiency during measurement is not due to the temperature. Moreover, the exponential decay indicates that the scintillation centers are destroyed by the incidence of the ion beam.

5. Conclusion and Issues to be worked in future

The integration of some candidate measurement tools of lost alpha-particles on ITER, such as the camera imaging of scintillators on the first wall, a scintillator probe, a Faraday-cup, and an imaging bolometer, have been studied, while the severe thermal/radiation environment of measurement location and the difficulties on the access and installation, limit the application of conventional measurement tools. The distribution of the loss is ranging in 200 to 250 degree in poloidal angle. It is proposed to fix ceramic scintillators in holes on the edges of first wall (Cu backing) of the blanket module #16 and #17, and viewed by a camera with filters in the upper port 11. The drift orbit calculation shows that detection position of the gap between the blanket module #16 and #17 catches some banana orbits but turning points are in the peripheral of the plasma. Upper positions on the gaps and slits of the blanket module #16 catch some passing particles and banana particles which have turning points are in the inner part of the plasma. Full-gyro orbit calculations including realistic detector designs and detailed 3D first wall shapes, are needed, and now under preparation**.** Here, we consider only detection of typical and standard escaping particles. The interaction with MHD has possibility to eject specific orbits, such as resonating passing particles. More studied focused on this aspect is waited.

New type of ceramic scintillators have been developed and tested at a temperature of T = 514 K. They had high scintillation efficiency and could potentially be used at ITER. The changes in scintillation efficiency due to continuous bombardment were studied, showing the exponential decay, and indicating that the scintillation centers are destroyed by the incidence of the ion beam. Further developments and experiments are planned, including the testing of new scintillation materials, and bombardment with 1–3 MeV alpha particles.

References

[1] W. W. HEIDBRINK and G.J. SADLER, NUCLEAR FUSION, Vo1.34, No.4 (1994), 535-615

[2] S.V. Konovalov, *“SUBTASK REPORT ON RIPPLE AMPLITUDE AND ALPHA*

PARTICLE RIPPLE LOSS IN ITER FEAT" (January 31, 2000, *RRC Kurchatov Institute)*

[3] M. Sasao, et al., Plasma Phys. Control. Fusion 46 (2004) S107-S118

[4] T. Saida, et al., Advanced Diagnostics for Magnetic and Inertial Fusion, Edited by Stott et al., (Kluwer Academic/Plenum Press, New York, 2002), 133-136

[5] V. Kipty et al., invited talk on this conference.

[6] B. J. Peterson et al, presented in this conference.

[7] M. Sasao, N. Kubo, M. Nishiura, M.Isobe, M. Shikama, Y. Tanaka, K. Shinto, S.Kitajima, "Development of ceramic scintillators for lost alpha measurement on ITER", Proceedings of The 32nd EPS Conference on Plasma Physics (2005, Tarragona), P4.089

OT12

Extended MHD Simulations of Internal Kink and Alfvén Waves in ITER*

G.Y. Fu

Princeton Plasma Physics Laboratory, Princeton, NJ

The n=1 internal kink mode and fishbone instability are investigated using the multi-level 3D extended MHD code M3D[1]. The M3D contains multi-levels of physics including ideal MHD, resistive MHD, two fluids, and particle-closure for both thermal ion and energetic particle stress tensor. Our models include the physics of alpha particle stabilization of internal kink mode, alpha particle's resonant destabiliztion of fishbone instability and Alfvén Eigenmodes, the effects of diamagnetic drift of thermal ions and the stabilizing effects of trapped thermal ions. Extensive simulations have been carried out for ITER parameters and profiles. It is found that the elongation of the ITER cross-section reduces the alpha particle stabilization significantly. The fishbone mode is found to be stable at the nominal ITER alpha beta. The effects of thermal ion's non-adiabatic response is strongly stabilizing for internal kink mode. The thermal ion's diamagnetic drift is expected to have a stabilizing effect on the kink mode. Details of these results and nonlinear simulations will be presented.

References

[1] W. Park, E.V. Belova, G.Y. Fu et al., Phys. Plasmas **6** 1796 (1999)

*Supported by DOE DE-AC02-76-CHO-3073.

#

Energetic Particle Transport and Alfvén Instabilities in Compact Stellarators

D. A. Spong (spongda@ornl.gov)
Oak Ridge National Laboratory, P. O. Box 2008, Oak Ridge, TN 37831-6169

Stellarator design tools have evolved in recent years to allow the development of a number of new compact stellarator configurations (QPS, NCSX) that maintain good plasma neoclassical confinement while improving on various shortfalls of the tokamak (e.g., absence of disruptions, stability to neoclassical tearing instabilities, lowered poloidal flow damping). These improvements have resulted from the development of rapidly evaluated optimization targets for thermal plasma stability and transport. In the case of energetic particle confinement and stability, efficiently evaluated target functions remain to be developed and, as a result, energetic particle physics issues must be evaluated a posteriori. Significant issues include: classical confinement of energetic ions during slowing-down, Alfvén gap modes, interaction of fast ions with plasma MHD modes, and impact of energetic ions on core transport properties (i.e., parallel viscosity, bootstrap current). We have developed tools to address a number of these issues. These include a parallel/vectorized fast particle Monte Carlo code (DELTA5D) and an Alfvén gap stability code (STELLGAP). These codes have been applied both to compact stellarators (QPS, NCSX) and to a variety of existing experiments (CHS, LHD, W7-AS, TJ-II, HSX). This analysis can lead to the development of optimization target functions that can be useful in flexibility studies and in the design of future devices. A moments method analysis has also been developed for analyzing both the E x B shearing rates driven by ambient flows (diamagnetic and E x B) and modifications due to beam momentum sources.

I. Introduction

Low aspect ratio stellarators potentially offer a lower cost development path to fusion, as well as near-term experimental concepts that provide large confined plasma volumes at moderate cost. These devices have been designed in recent years using optimization methods that target a variety of physics and engineering targets. A central theme of these efforts has been the improvement of confinement since traditional (un-optimized) stellarators have unattractively high levels of thermal and energetic particle loss. Confinement improvement has been achieved through measures such as the targeting of lowered effective ripple, alignment of collisionless drift surfaces with magnetic flux surfaces and lowered collisional transport coefficients. This has lead to configurations that are nearly quasi-symmetric; exact quasi-symmetry would provide a conserved canonical momentum invariant in the symmetry direction and zero bounce-averaged deviation of drift surfaces from flux surfaces. Two forms of quasi-symmetry have so far been found to be compatible with low aspect ratio: quasi-poloidal symmetry and quasi-toroidal symmetry. This has resulted in the QPS[1] and NCSX[2] designs, respectively. Configurations have not been found in either case (and may not be possible) that provide exact quasi-symmetry. The more realistic goal has been to lower neoclassical transport to a level where it is negligible in comparison to expected levels of anomalous transport. This can be achieved, but leaves open the question of confinement of the energetic, more collisionless particle populations used for heating. Energetic particle confinement has been analyzed using particle following calculations for these devices and is adequate for the purposes of the proposed experiments. Also, alpha particle confinement in reactor extrapolations of the QPS and NCSX configurations is adequate for power balance and ignition (based on thermal plasma confinement enhancement factors in the range 2 - 3), but may require further optimization to avoid unacceptably high heat loads on the first wall.

In this paper two specific issues related to the confinement of energetic particle and their effects in compact stellarator systems will be analyzed. These are the confinement of fast ions in the presence of instabilities and the impact of fast ion momentum sources on the ambipolar electric field and associated E x B velocity shearing rates.

II. Energetic particle confinement studies

The classical slowing-down and confinement of energetic particle populations in compact stellarator systems has been simulated both for versions of QPS and NCSX scaled to reactor size (R_0 = 10m, B = 5T), as well as for versions scaled to the size of the proposed experimental devices. Here only results for alpha particle slowing-down in a reactor scale QPS device will be discussed. As with thermal plasma transport, the actual levels of confinement will be influenced by fluctuation and turbulence that may be present in the plasma. Energetic particle confinement can especially be degraded by instabilities such as fishbones and Alfvén modes that involve resonant wave-particle interactions.

In order to analyze such effects, we have developed a Monte Carlo code (DELTA5D) that solves the following guiding center equations, which include a perturbed field component[3]:

$$\frac{d\theta}{dt} = \left[\left(\mu + \frac{mv_{\|}^2}{B}\right)\frac{\partial B}{\partial \psi} + e\frac{\partial \Phi}{\partial \psi}\right]\frac{\partial \psi}{\partial P_\theta} + eBv_{\|}\frac{\partial \rho_{\|}}{\partial P_\theta} + ev_{\|}B\frac{\partial \alpha}{\partial \psi}\frac{\partial \psi}{\partial P_\theta}$$

$$\frac{d\psi}{dt} = \frac{\dot{P}_\theta g - \dot{P}_\zeta I}{D}$$

$$\frac{d\zeta}{dt} = \left[\left(\mu + \frac{mv_{\|}^2}{B}\right)\frac{\partial B}{\partial \psi} + e\frac{\partial \Phi}{\partial \psi}\right]\frac{\partial \psi}{\partial P_\zeta} + eBv_{\|}\frac{\partial \rho_{\|}}{\partial P_\zeta} + ev_{\|}B\frac{\partial \alpha}{\partial \psi}\frac{\partial \psi}{\partial P_\zeta}$$

$$\frac{d\rho_{\|}}{dt} = \frac{\iota - \left(\rho_{\|} + \alpha\right)g'}{D}\dot{P}_\theta + \frac{\left(\rho_{\|} + \alpha\right)I'}{D}\dot{P}_\zeta + \frac{d\alpha}{dt}$$

These are solved in the presence of collisions, modeled using a Langevin[4] stochastic collision term. This is based on a collision operator that includes pitch angle and energy scattering, using the velocity-dependent potential coefficients. For the current calculations, Boozer magnetic coordinates (ψ, θ, ζ) are used.[5] The following form for the perturbed field function, α, is used:

$$\delta\vec{B} = \vec{\nabla} \times \left(\alpha\vec{B}\right) \qquad \alpha = \sum \alpha_{0mn}\left(n - im\right)\, e^{-(\psi-\psi_{mn})^2/\Delta_{mn}^2} e^{-i\left(\omega_r t + n\zeta - m\theta\right)}$$

A study has been made of the effect of several different forms of perturbed field. These include: (1) a collection of single mode number pairs with tearing parity displacement functions localized about their associated rational surfaces (referred to here as resonant MHD – characteristic of resistive tearing or ballooning modes), and (2) a dominant mode pair with coupled sidebands in which toroidal (TAE), mirror (MAE), and helical (HAE) couplings have been considered. Results for losses of slowing-down alpha particles in a reactor-sized QPS device are shown in Figure 1(a). This is based on an equilibrium at $<\beta>$ = 6%; the rotational

transform profile had relatively weak shear, varying from 0.44 at the magnetic axis to 0.48 at the edge as shown in Figure 1(b).

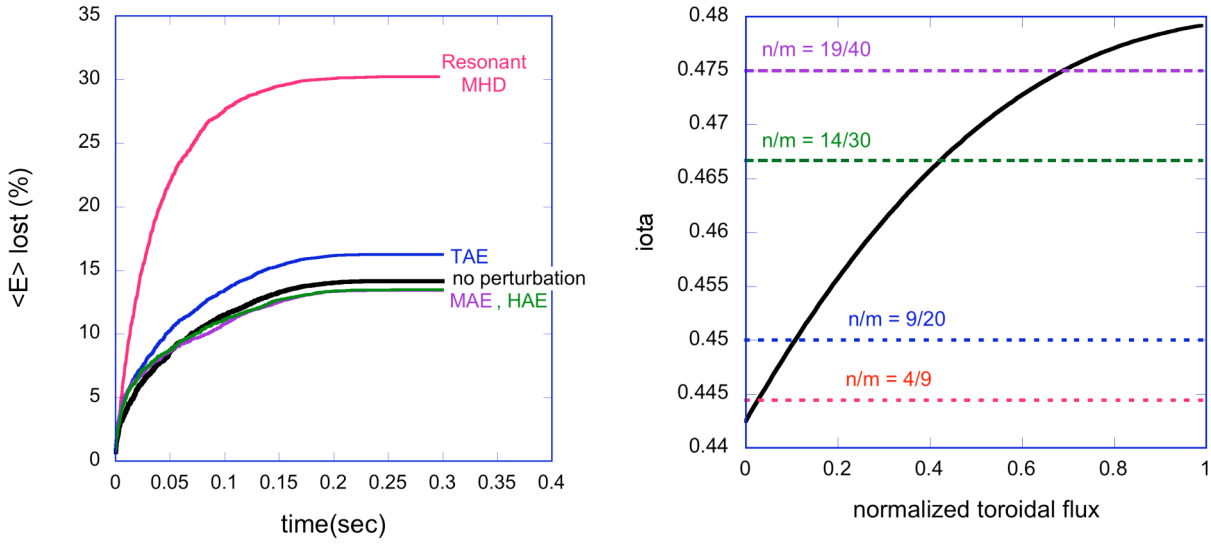

Figure 1 – (a) Alpha particle losses vs. time for various perturbed field models in a QPS configuration, (b) rotational transform profile with resonant surfaces indicated.

In this case, the resonant MHD perturbation included equal size terms for n/m = 9/20, 14/30, and 19/40. The TAE/MAE/HAE perturbations included a central n/m = 14/30 mode with coupled sidebands at n/m = 14/29, 14/31 (TAE), n/m = 15/30, 13/30 (MAE), and n/m = 15/31, 15/29 (HAE). For the AE cases, the sideband amplitudes were 0.4 times that of the central mode. In all cases a fixed frequency of $\omega_{real} = 10^6$ sec^{-1} was assumed. Fig. 1(b) indicates the location of the various rational surfaces in the rotational transform profile. As Fig. 1(a) shows, the resonant MHD perturbation model lead to the largest enhancement of losses. This is likely due to the fact that all three modes had the same amplitude and their resonant surfaces covered a range of radii in the plasma. The TAE perturbed field model resulted in increased losses while the MAE and HAE models actually decreased losses slightly. This effect of the MAE/HAE models is possibly due the instability causing an increased effective collisionality for the slowing-down alphas. Since the alphas are deeply in the $1/\nu$ transport regime, increased collisionality can improve their confinement. This effect has recently been proposed and analyzed for thermal stellarator plasmas[6] in the presence of electrostatic fluctuations.

III. Ambient and beam-driven E x B velocity shear

Plasma flow velocity characteristics are of importance in understanding and controlling the performance of toroidal plasmas for a number of reasons. First, there is much evidence both from simulations and experimental measurements that sheared flows can suppress turbulence and lead to enhanced confinement regimes. Next, it is expected that plasma flows can influence the formation and growth of magnetic islands.[7] Finally, plasma flow characteristics are closely coupled to understanding impurity transport in toroidal devices. Stellarators offer a range of different preferred plasma flow damping characteristics, depending on what form of quasi-symmetry they have.[8] Also, energetic particle populations, such as neutral beams and RF heating that act as momentum sources for the thermal plasma, will influence the ambipolar electric field and thus the plasma sheared flow properties.

In order to quantitatively analyze such effects in compact stellarators, a computational model has been developed,[9] based on a moments method analysis for stellarators.[10] This model calculates the plasma viscous stress tensor, and then uses the parallel momentum balance coupled with the ambipolar condition to solve for the self-consistent plasma flows and electric field. From this, flux surface average E x B velocity shearing rates can be calculated as shown in Figure 2.

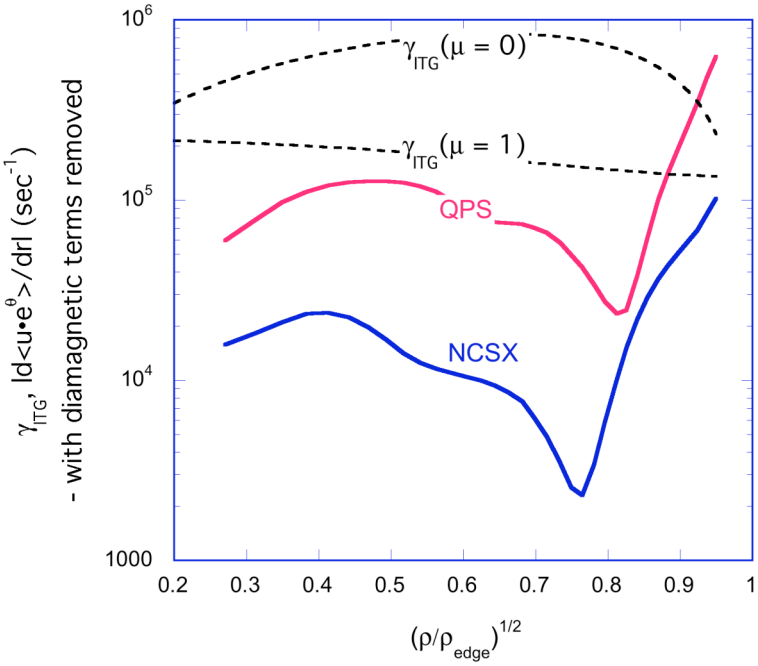

Figure 2 – Ambient E x B velocity shearing rates and ITG growth rate estimates vs. flux surface location.

These calculations are based on central temperatures and densities of $T_{ion}(0)$ = 0.3 keV, $T_{electron}(0)$ = 0.5 keV and n(0) = 8 x 10^{19} m^{-3}. As can be seen, QPS has the largest shearing rates due to its lowered level of poloidal viscosity and the stronger variation of its E x B velocity within flux surfaces (a consequence of its lower aspect ratio = 2.7). These shearing rates are compared with tokamak based estimates of ITG mode growth rates,[11] indicating that shearing rates can exceed growth rates near the plasma edge regions. More recent ITG/DTEM linear stability analysis,[12] based on fully 3D stellarator equlibria, for these two devices has indicated growth rates in the range of 0.2 to 1.6 x 10^5 sec^{-1}. The above shearing rates would easily exceed these growth rates for either device.

These shearing rates are based on the electric fields and flows that result from what are termed ambient conditions, i.e., only the diamagnetic drifts and electric fields resulting from neoclassical transport are taken into account. When momentum sources, such as neutral beams are included in the parallel force balance, these will perturb the ambipolar condition and can lead to either smaller or larger electric fields and E x B shearing rates. A beam induced momentum source has been introduced into this analysis, leading to the electric field variations shown in Figure 3(a) and 3(b).

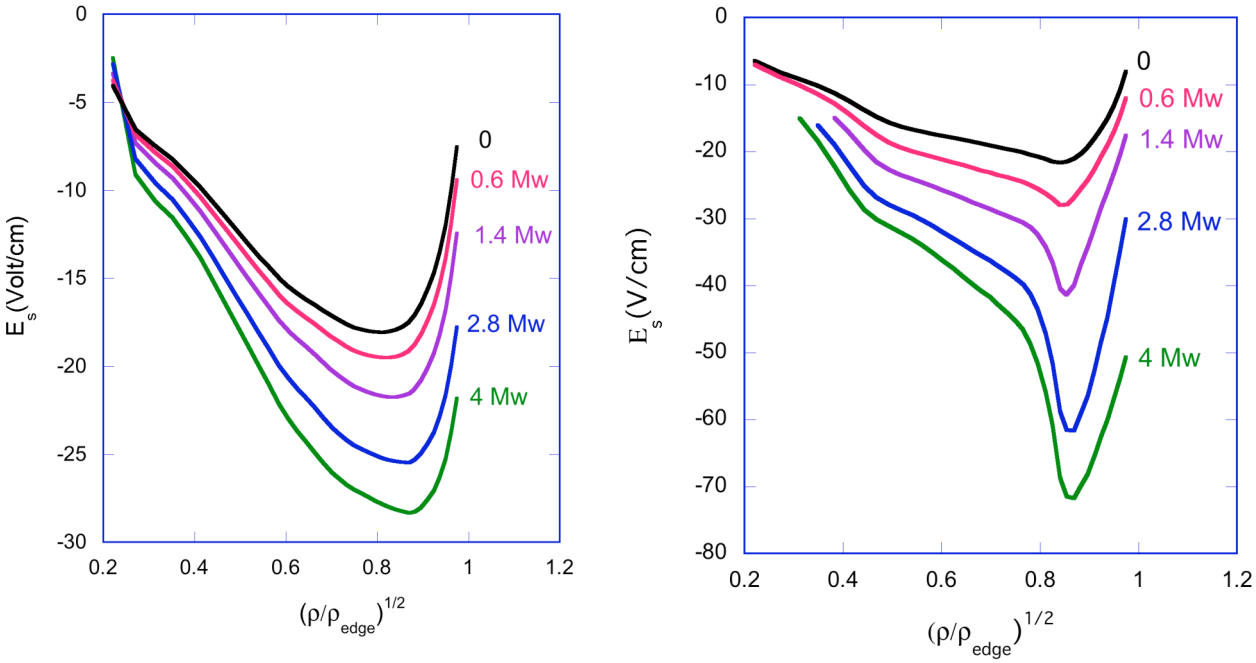

Figure 3 – Impact of a beam momentum source on the radial electric field levels in (a) QPS and (b) NCSX configurations.

In these calculations, various levels of momentum source were introduced into the ion and electron parallel force balance relations. The power levels indicated on Figure 3 are obtained by assuming that these momentum values come from a 40keV beam component injected parallel to field lines. As can be seen, the electric fields and thus E x B shearing rates in NCSX are more sensitive to the beam momentum source than for QPS. This is a consequence of the different magnetic symmetries. It would be expected that different beam injection angles than parallel may result in stronger sensitivities for the electric fields in QPS and devices with other forms of non-toroidal symmetry.

IV. Conclusions

Compact stellarators will provide a variety of energetic particle physics issues that differ from those of tokamaks. Two have been analyzed here: the effect of fluctuations on energetic particle confinement and the influence of beam momentum sources on electric field generation. In the case of particle confinement, a regime has been identified where fluctuations seem to slightly lower loss rates. In the case of beam induced changes in the electric field, the variation of this effect with different magnetic symmetries (quasi-poloidal and quasi-toroidal) has been studied. Besides these two areas, there are many other energetic particle issues such as Alfvén instabilities, fishbones, etc. that will need to be addressed in greater depth in the future for compact stellarator systems.

Acknowledgements – Useful discussions with Jeff Harris, Andrew Ware, Steve Hirshman, Hideo Sugama, Shin Nishimura, Wayne Houlberg, Mike Zarnstorff, David Mikkelson and Ben Carreras are acknowledged in the development of this model. Research sponsored by the U.S. Department of Energy under Contract DE-AC05-00OR22725 with UT-Battelle, LLC.

References:

[1] D. A. Spong, S. P. Hirshman, L. A. Berry, Nuclear Fusion **41** (711) 2001.
[2] M. C. Zarnstorff, L. A. Berry, A. Brooks, Plasma Physics and Controlled Fusion **43** (A237) 2001.
[3] R. B. White, *Theory of Tokamak Plasmas* (North-Holland, New York, 1989).
[4] A. H. Boozer, G. Kuo-Petravic, Phys. Fluids **24**, 851 (1981).
[5] A. H. Boozer, Phys. Fluids, 24, 1999 (1981)
[6] H. Mynick, A. H. Boozer, Phys. of Plasmas **12** (062513-1) 2005.
[7] A. Reiman, M. Zarnstorff, et al., Nuclear Fusion **45** (360) 2005.
[8] D. A. Spong, submitted to Fusion Technology (2005).
[9] D. A. Spong, Phys. of Plasmas **12** (056114-1) 2005.
[10] H. Sugama, S. Nishimura, Phys. of Plasmas **9** (4637) 2002.
[11] J. W. Connor, et al., Nuclear Fusion 44 (2004) R1
[12] G. Rewoldt, L.-P. Ku, W. M. Tang, PPPL-4082, June, 2005.

Fast Ion Transport Studies in the Large Plasma Device

Y. Zhang, H. Boehmer, W. Heidbrink (wwheidbr@uci.edu), R. McWilliams, L. Zhao
University of California, Irvine
B. Brugman, T. Carter, D. Leneman, S. Vincena
University of California, Los Angeles

The LArge Plasma Device (LAPD) at UCLA is an 18-m long linear device that produces highly reproducible ~10-ms duration plasmas with $n_e>10^{12}$ cm^{-3}, $T_e>1$ eV, and B~1 kG every second. Its large size and excellent diagnostic access accommodate detailed studies of fast-ion physics at reduced parameters. The first fast-ion experiments were conducted with a modified 100-1000 eV argon processing source that was inserted into the plasma. Measurements of energy deceleration and cross-field transport in the quiet "afterglow" plasma are in good agreement with classical Coulomb scattering theory. Recent experiments employ a 200-3000 eV lithium source. Deflection of the beam by shear Alfven waves is observed.

The LArge Plasma Device (LAPD) is a user facility for basic plasma physics research [1]. Computerized probe scans accommodate accurate measurements of fast ions and of wave fields, so the device is well suited for detailed studies of fast-ion physics. The first fast-ion experiments were conducted with a modified 100-1000 eV argon processing source that was inserted into the plasma [2]. It was found that the "spot" size of the beam is smallest when the gyro-angle of the helical fast-ion trajectory is an integer multiple of 2π [2]. This source was used to measure the fast-ion transport of a ~300 eV ribbon beam in the quiet afterglow plasma [3]. The parallel energy of the beam was measured by a two-grid energy analyzer at two axial locations (z = 0.32 m and z =6.4 m) from the ion gun. The calculated ion beam slowing-down time is consistent to within 10% with the prediction of classical Coulomb collision theory. To measure cross-field transport, the beam was launched at 15^o with respect to the magnetic field and radial beam profile measurements were performed at different axial locations. The measured cross-field transport is in agreement to within 15% with analytical classical collision theory and the solution to the Fokker-Planck kinetic equation. Collisions with neutrals have a negligible effect on the beam transport but do attenuate the beam current.

The study of shear Alfven waves is a specialty of the LAPD research program [4]. To produce super-Alfvenic beam ions, a new fast-ion source that uses a solid thermionic lithium emitter has been developed (Fig. 1). The lithium source emits ~1 mA of Li^+ ions at energies of <3000 eV. With this source, the speed of the fast ions can match the parallel phase speed of the ~10 G Alfven waves that are launched by loop antennas; the $\omega - k_z v_z = \Omega$ cyclotron resonance is also accessible. In recent experiments, deflections of the beam by ~1 G shear Alfven waves were detected when the fast ions satisfied the cyclotron resonance condition.

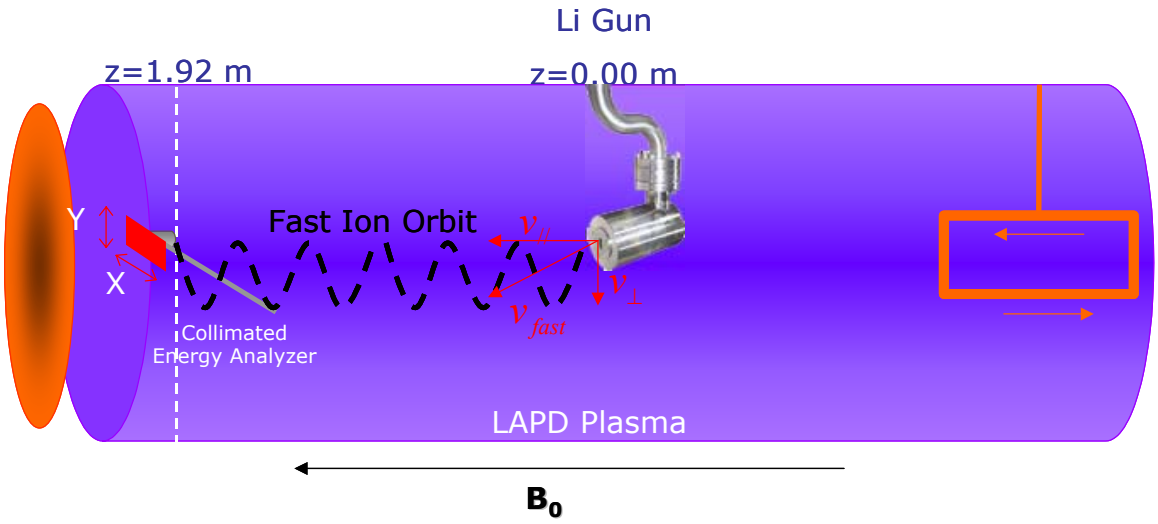

Figure 1. Apparatus for the measurement of resonant interaction of fast ions with Alfven waves. A "picture-frame" antenna launches shear Alfven waves in a helium plasma. A lithium source launches fast ions in the plasma. A collimated energy analyzer measures the response of the fast ions to the waves.

References

[1] *http://plasma.physics.ucla.edu/lapd*
[2] BOEHMER, H., et al., Rev. Sci. Instrum. **75** (2004) 1013.
[3] ZHAO, L., et al., Phys. Plasmas **12** (2005) 052108.
[4] e.g., GEKELMAN, W., et al., J. Geophys. Res. **102** (1997) 7225.

Radio-Frequency Heating of Sloshing Ions in a Straight Field Line Mirror

V.E.Moiseenko[1] and O. Ågren

Division of Electricity and Lightning Research, Ångström Laboratory, Uppsala University, Box 534, SE-751 21 Uppsala, Sweden

Abstract. Sloshing ions, the energetic ions with a velocity distribution concentrated to a certain pitch-angle, play an important role in plasma confinement in mirrors. They are normally produced in mirror traps with neutral beam injection. They also could be generated by ion-cyclotron heating. In the present report two radio-frequency heating scenarios to sustain a sloshing ion population in a newly proposed mirror device, the straight field line mirror, are examined. The first one consists in the ion cyclotron heating in two-ion species plasma using longitudinal wave conversion and fundamental harmonic heating of deuterium ions in tritium plasma. This scheme provides efficient ion heating for high deuterium "minority" concentration without substantial power deposition to the electrons. The second scenario is based on second harmonic heating of deuterium ions. The study uses numerical 3D calculations for the time-harmonic boundary problem for Maxwell's equations. For the radio-frequency heating in both schemes, a simple strap antenna is used. Calculations show that it has low antenna Q and operates in the regime of global resonance overlapping. For fundamental harmonic heating scenario only a small portion of the wave energy transits through the cyclotron layer and penetrates to the central part of the trap. The power deposition is peaked at the plasma core. The calculations show that this scenario is prospective for practical implementation in large mirror devices. First results of numerical calculations for second harmonic heating are reported.

A straight field line mirror [1,2] is a prospective device for fusion applications. Some beneficial properties with such a device is the MHD (magnetohydrodynamic) stability provided by a minimum B field, the minimum flux tube ellipticity and the local omnigenious property, with zero banana orbit widths, to the first order in the plasma β [3].

With a sloshing ion population, the straight field line mirror may serve as fusion reactor with relatively high Q factor (energy gain factor) [4]. Sloshing ions are the energetic ions with a velocity distribution concentrated to a certain pitch-angle, and they "slosh" between the magnetic mirrors where their concentration increases. The established technique to produce sloshing ions in mirror traps is neutral beam injection (see e.g.[5]). An alternative approach, although not yet tested experimentally with sufficient heating power [6], would be to sustain sloshing ions by radio frequency heating.

1. Fast wave propagation in mirrors and fundamental harmonic heating

The character of the fast wave propagation in open trap plasma is that along x and y, the directions perpendicular to the magnetic field, a fast wave normally form a standing wave structure with a low number of nodes, while in the longitudinal direction the number of oscillations is quite high (see e.g. Ref. [7]). We assume that the perpendicular node structure of the wavefield remains as the wave propagates along the plasma column [8]. Under this condition, the major features of the fast wave propagation could, to a certain extent, be described by the dispersion relation

---

[1] Permanent address: Institute of Plasma Physics, National Science Center "Kharkov Institute of Physics and Technology", 61108 Kharkiv, Ukraine

$$k_{\|}^2 = k_0^2 \varepsilon_\perp - k_\perp^2 / 2 \pm \sqrt{k_\perp^4 / 4 + k_0^4 g^2} \qquad (1)$$

where $k_{\|}$ and $k_\perp$ are the parallel and perpendicular components of the wave vector, $k_0 = \omega / c$, $\varepsilon_\perp = \varepsilon_{11} = \varepsilon_{22}$, $g = -i\varepsilon_{12} = i\varepsilon_{21}$ and ε_{ik} is the cold plasma dielectric tensor. Following this formula, Fig.1 shows the dependence of the normalized parallel wavenumber $\bar{k}_{\|} = k_{\|} c / \omega_{pH}$ on the normalized magnetic field $\bar{B} = \omega_{cH} / \omega$ in a D-T (deuterium-tritium) plasma.

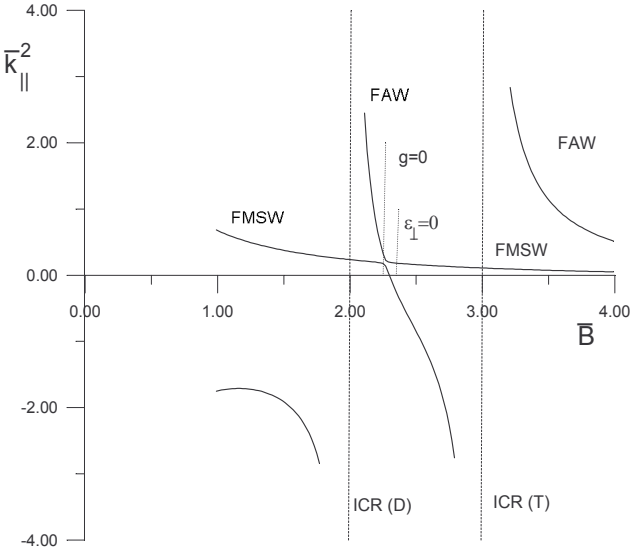

Figure 1 Normalized $\bar{k}_{\|}^2$ as a function of normalized magnetic field strength $\bar{B}$ for $\bar{k}_\perp = 0.3$.

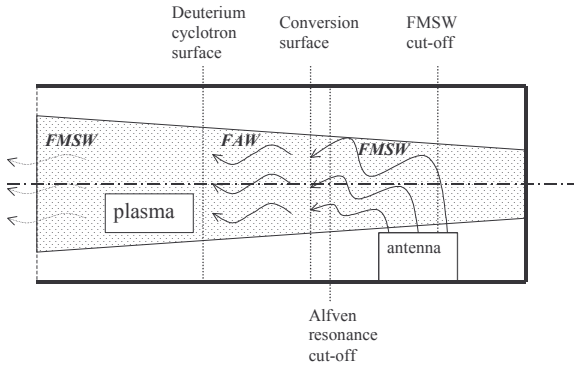

Figure 2 Sketch of rf heating scheme.

Based on (1), the following minority heating scenario is choosen: As sketched in Figure 2, a fast magnetosonic wave (FMSW) is excited by the antenna and launched towards lower magnetic field at a position where the magnetic field is lower than the resonant value for tritium ions and the real part of $\varepsilon_\perp$ is negative. This wave, traveling towards lower magnetic field, will convert to a fast Alfven wave (FAW). The FAW will reach the vicinity of the cyclotron zone for deuterium ions, where it will be damped by the cyclotron mechanism. As compared with the "magnetic beach" scheme, this approach has some advantages. The first is that it is easier to excite by the antenna the FMSW than the FAW, since there is less restriction for FMSW propagation in non-uniform plasma. Secondly, the antenna could be placed in the region where $\varepsilon_\perp < 0$, where it is easier to provide decoupling from the Alfvén resonances. It could be mentioned that the performance of this scheme could be decreased by reflections from the conversion zone and by over-barrier conversions. Numerical results for this fundamental frequency heating scheme are reported in Ref. [9].

The scenario for second harmonic heating is analogous. If $k_\perp$ is slowly varying along the mirror axis the effect of second harmonic cyclotron resonance could be modeled by the presence of minority with the half particle mass and the concntration $C_{\alpha 2} = 4 C_\alpha v_{T\alpha\perp}^2 / \omega_{H\alpha}^2$, where C_α is the concentration of the resonannt ion component. In such an approximation the second harmonic heating was studied in Ref. [7].

2. Numerical model

In the present study, electromagnetic calculations are used to analyze high-energy ion sustain in a reactor-scale straight field line mirror device. The magnetic field strength of that device is described by the following formula:

$$\vec{B} = B_0\left[\frac{\vec{e}_z}{1-z^2/c^2} - \vec{e}_x\frac{x}{c}\frac{1+z/c}{(1-z^2/c^2)^2} + \vec{e}_y\frac{y}{c}\frac{1-z/c}{(1-z^2/c^2)^2}\right], \qquad (2)$$

where c is the half-distance between the left and right poles of the trap. At the poles at $z=\pm c$, the magnetic field strength goes to infinity. We consider a reactor-scale device with $c=50\,\text{m}$, $a=150\,\text{cm}$ and $B_0=1.5\,\text{T}$. Here, a is the plasma radius at the central plane where the magnetic surfaces have a circular cross-section. The trap confines deuterium and tritium sloshing ions with the mirror point at $B_m=4B_0$ that corresponds to the coordinate $z/c=\sqrt{3}/2$. Following the scheme described above, the cyclotron resonance for deuterium should be located nearby this mirror point, and an estimate for the heating frequency is $\omega\approx 3\cdot 10^8\,\text{s}^{-1}$. The computation domain is $z\in(0.82c,0.9c)$, i.e. 41 m $<z<$ 45 m, which covers the deuterium cyclotron zone. Since the y component of magnetic field varies slowly, this variation may not seriously influence the rf heating and, we assume plasma and magnetic field uniformity along y.

To describe the transmission of rf power to sloshing ions, the boundary problem for Maxwell's equations

$$\nabla\times\nabla\times\left[\vec{E}-\vec{e}_{\|}(\vec{e}_{\|}\cdot\vec{E})\right]-k_0^2\hat{\varepsilon}\cdot\vec{E}=4\pi i\omega\mu_0\vec{j}_{ext} \qquad (3)$$

should be specified. Here $\vec{j}_{ext}$ is the external current, $\vec{e}_{\|}=\vec{B}/B$. The parallel electric field is neglected. The boundary condition at a metallic surface and at the left wall of the box at $z=41\,\text{m}$ are specified by $\vec{E}\times\vec{n}=0$, $\frac{\partial}{\partial z}(\vec{E}\times\vec{e}_z)+ik_w(\vec{E}\times\vec{e}_z)=0$, where $\vec{n}$ is the normal vector of the surface and k_w is a constant. The corrections caused by finite $k_{\|}$ are important only for the resonant part of the dielectric tensor $\hat{\varepsilon}$. This resonant component for ions is $\varepsilon_{++}=\vec{e}_+^{\,*}\cdot\hat{\varepsilon}\cdot\vec{e}_+$, where $\vec{e}_+=(\vec{e}_\tau-i\vec{e}_y)/\sqrt{2}$ and $\vec{e}_\tau=\vec{e}_y\times\vec{e}_{\|}$, and we use the following expression:

$$\varepsilon_{++}=1-\sum_\alpha\frac{\omega_{p\alpha}^2}{\omega\left|k_{\|}v_{T\alpha\|}\right|}\left[F(\beta_\alpha)-\frac{i\sqrt{\pi}}{2}\exp(-\beta_\alpha^2)\right] \qquad (4)$$

where $\beta_\alpha=\left(\omega-\omega_{c\alpha}\right)/\left|k_{\|}v_{T\alpha\|}\right|$ and F is the Dawson's integral.

For second harmonic heating, the resonant correction to the dielectric tensor also contributes to ε_{++}, and it is not a function in space, but the differential operator (see e.g. [7])

$$\delta\varepsilon_{++}E_+=\frac{\partial}{\partial r_+}\tilde{\varepsilon}_{2\alpha}\frac{\partial}{\partial r_-}E_+, \qquad (5)$$

where $r_{\pm} = \tilde{x} \pm iy$, $\tilde{x}$ is a local coordinate perpendicular to the magnetic field $\nabla\tilde{x} \approx \vec{e}_{\tau}$ and

$$\tilde{\varepsilon}_{2\alpha} = \sum_{\alpha} \frac{4\omega_{p\alpha}^2 v_{T\alpha\perp}^2}{\omega |k_{\parallel}| v_{T\alpha\parallel} \omega_{H\alpha}^2} \left[F(\beta_{2\alpha}) - \frac{i\sqrt{\pi}}{2} \exp(-\beta_{2\alpha}^2) \right] \left[1 + (1 - 2\omega_{H\alpha}/\omega)(v_{T\alpha\perp}^2 / v_{T\parallel}^2 - 1) \right] \qquad (6)$$

with $\beta_{2\alpha} = (\omega - 2\omega_{c\alpha}) / |k_{\parallel} v_{T\alpha\parallel}|$.

3. Results of calculations

We choose an antenna consisting of the strap elements oriented along the y axis. For good coupling to the plasma, the surface of the strap should be positioned as close as possible to the plasma surface. This determines the size of the strap in the x direction. As for the antenna positioning in the z direction, it would be better to place it near the wave cut-off where the wavefield comes out the plasma column to the maximum extent and where it is easier to couple it to the antenna. The antenna layout is shown in Figure 3.

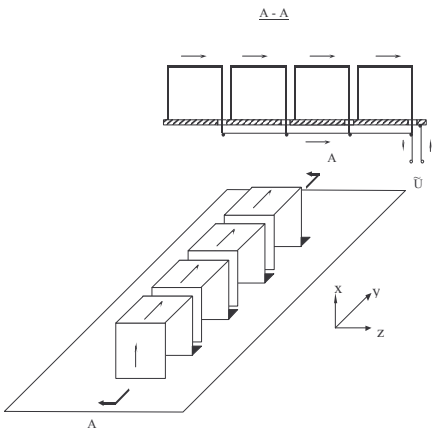

Figure 3 Strap antenna layout with the scheme of electric connection.

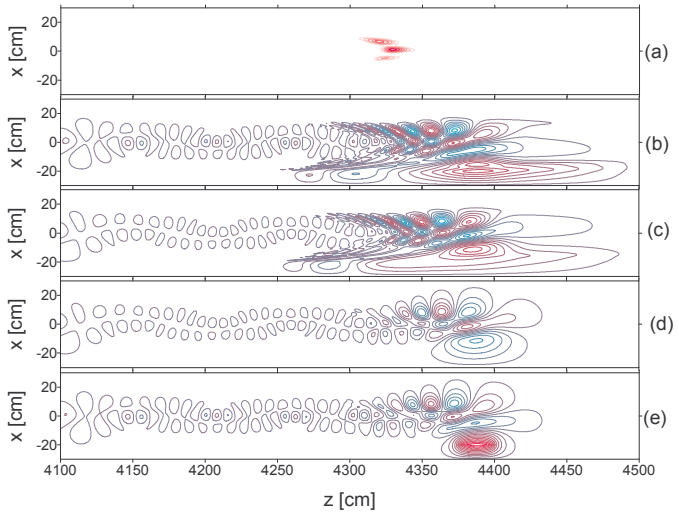

Figure 4 Contours of a) deposited power density b) $\mathrm{Re}\,E_{\tau}$, c) $\mathrm{Im}\,E_{\tau}$, d) $\mathrm{Re}\,E_{y}$ and e) $\mathrm{Im}\,E_{y}$ at the cross-section $y = 0$. Blue color corresponds to -0.5 V/cm and red is -0.5V/cm. Antenna current is 1A.

In the numerical calculations, the following set of parameters is chosen: Plasma density (in its maximum) is $n_{p0} = 5 \cdot 10^{14}\,\mathrm{cm}^{-3}$, heating frequency is $\omega = 2.5 \cdot 10^{8}\,\mathrm{s}^{-1}$, deuterium and tritium parallel thermal velocities at z-axis are $v_{TD\parallel} = v_{TT\parallel} = 5 \cdot 10^{5}$ m/s, the deuterium concentration is $C_D = 0.4$, $k_{\parallel} = 0.4\,\mathrm{cm}^{-1}$ and $k_w = 0.1$ cm^{-1}. For this set of parameters the electromagnetic field patterns are presented in Figure 4. In spite that the antenna currents are assumed real, both the real and the imaginary parts of the fields amplitude are of the same order. In accordance to the antenna current shape, the electromagnetic fields do not form an oscillational structure in the y direction. In the x direction, the wavefield has two nodes which indicates the dominance of the third radial mode. A FMSW wavefield near the antenna location ($z = 4350...4400$ cm) can be identified. As z decreases the amplitude of the E_y field component decreases having almost a FMSW structure while the E_{τ} component does not

decrease up to the zone of strong cyclotron damping. Its structure near the tritium cyclotron resonance could be qualified as a FAW structure. The front of the FAW is convex. This could be explained by the lower deuterium cyclotron zone width at the plasma edge where the FAW approaches closer to the ion cyclotron resonance surface. A slight excitation of Alfvén resonances is visible at the plasma periphery.

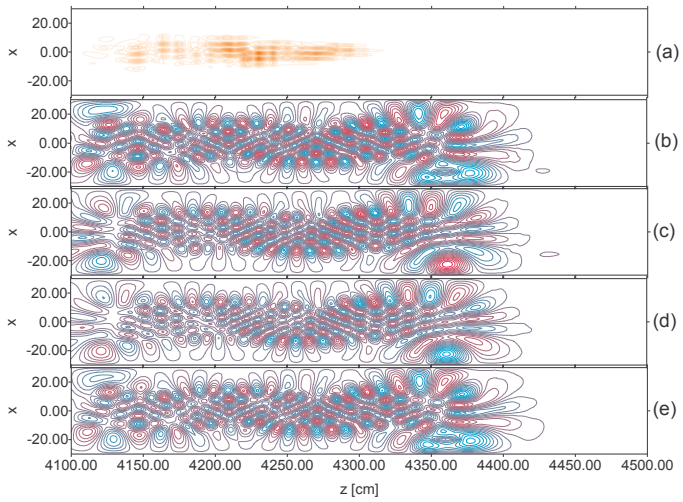

Figure 5 Contours of a) deposited power density, b) $\mathrm{Re}\,E_\tau$*, c)* $\mathrm{Im}\,E_\tau$*, d)* $\mathrm{Re}\,E_y$ *and e)* $\mathrm{Im}\,E_y$ *at the cross-section* $z = z_a$*. Blue color corresponds to -0.5 V/cm and red is 0.5 V/cm. Antenna current is 1A.*

For second harmonic tritium heating calculations, the parameters are the following: Plasma density (in its maximum) is $n_{p0} = 5 \cdot 10^{14}\ \mathrm{cm}^{-3}$, heating frequency is $\omega = 3.1 \cdot 10^8\ \mathrm{s}^{-1}$, deuterium and tritium thermal velocities at z-axis are $v_{TD\|} = v_{TT\|} = 5 \cdot 10^5$ m/s and $v_{TD\perp} = v_{TD\perp} = 1.5 \cdot 10^6$ m/s, the deuterium concentration is $C_D = 0.6$, $k_\| = 0.4\ \mathrm{cm}^{-1}$ and $k_w = 0.2\ \mathrm{cm}^{-1}$. The result of calculation is shown in Figure 5. In comparison with the minority heating, the power deposition zone is broader. For this specific calculation, cyclotron zone shine-through is about 18% in power, what is larger than for the minority heating, but within the range of acceptance.

ACKNOWLEDGEMENT

This study is financed in part by the Swedish Institute.

REFERENCES

[1] ÅGREN, O., SAVENKO, N., Phys. of Plasmas **11** (2004) 5041.
[2] ÅGREN, O. and SAVENKO, N., Phys. Plasmas **12** (2005) 042505.
[3] ÅGREN, O., MOISEENKO, V. AND SAVENKO, N., Phys. Rev. E **72** (2005) 026408.
[4] ÅGREN, O. and SAVENKO, N., Phys. Plasmas **12** (2005) 022506.
[5] SIMONEN, T. C., ALLEN, S. L., CASPER, T. A. et al, Phys.Rev. Lett. **50** (1983) 1668.
[6] ROSS, S., BREUN, R. A.,SANTARIUS, J. F. et al, Nucl. Fusion **28** (1988) 125.
[7] KASILOV, S.V., LEDOVSKOJ, YU.N., MOISEENKO, V.E., PILIPENKO, V.V. and STEPANOV, K.N., Physica Scripta **45** (1992) 373.
[8] WHITE, R.B.,YOSHIKAWA, S., OBERMAN, C., Phys. Fluids **25** (1982) 384.
[9] MOISEENKO, V. and ÅGREN, O., Phys. Plasmas **12** (2005) 015510.

Study of Tangentially Beam-injected Ion Behavior in LHD Using Natural Diamond Detectors

A.V.Krasilnikov[2], M.Isobe[1], T.Saida[1], S.Murakami[3], M.Sasao[4], H.Nishimura[4], M.Nishiura[1], M.Osakabe[1], Y.Takeiri[1], K.Toi[1], F.Watanabe[1], V.N.Amosov[2]

[1]National Institute for Fusion Science, 322-6 Oroshi-cho, Toki 509-5292, Japan
[2]Troitsk Institute for Innovating and Fusion Research, Troitsk, Moscow region, Russia
[3]Kyoto University, Kyoto, Japan
[4]Tohoku University, Sendai, Japan

E-mail: anatoli@triniti.ru

Abstract. Both energy spectra and dynamic of flux of fast ions originally tangentially injected into Large Helical Device plasma with energy 150 keV was studied using tangentially and perpendicular viewing charge exchange (CX) atom spectrometers based on natural diamond detectors. Measurements were performed in plasma configurations with magnetic axis at R_{ax} = 3.75 m, 3.6 and 3.53m for axial magnetic field .B_t = +2.5, -2.5, 1.5 and 0.75 T. The degradation of energy distribution and diminishing of decay times of fast CX atom flux were measured at B_t=0.75 T. Sharp increases of fast co-CX atom fluxes were measured in experiments with 200ms co-beam blip injection in R_{ax} = 3.53m and 3.6m configurations during the second part of the beam time when 50-60 kHz MHD instabilities appeared in plasma. Increase of fast co-moving ion transport from plasma center to periphery by 50-60 kHz energetic particle modes in R_{ax} = 3.53 and 3.6m configurations could be discussed as the reason of measured increase of fast CX atom flux.

1. Introduction

Fast ion behaviour in fusion reactor is of great importance for its design. Due to ripple structure, q profile and topology of fast ions trajectories the issue of fast ion confinement is more crucial in fusion reactor based on stellarator configuration. Experiments on Large Helical Device (LHD) [1] with neutral beam injection (NBI) are providing the possibility to study some aspects of fast ion behaviour in largest for today stellarator plasma configuration. Well developed diagnostic complex of LHD [2] is providing not only the data about spatial distributions of the number of LHD plasma characteristics important for this studies, but in particular the possibility to measure the evolution in time of the perpendicular and tangential confined fast ion energy distributions. The purpose of our work was to study experimentally the efficiency of confinement of fast tangential and perpendicular ions in relatively MHD-quiescent hydrogen plasma of LHD and under influence of some MHD instabilities.

2. Experimental Arrangement

The behavior of fast tangential and perpendicular protons confined in LHD plasma was studied using viewing tangentially to plasma at R = 3.65 m in equatorial plane and perpendicular vertically at R = 3.67 m [3] charge exchange (CX) atom spectrometers based on natural diamond detectors (NDD) [4]. The tangential and perpendicular NDDs integrate from their cones of view the CX atom fluxes created by fast ions having pitch angles of 140-180 (0-40 for counter-clockwise directed magnetic field) and 87-102 degrees [3] with respect to co-clockwise direction, respectively. Fast ions were originally tangentially co- and counter-injected with energy 150 keV into LHD hydrogen plasma. To provide both spectrometry and flux dynamic studies of tangential and perpendicular CX atoms, measurements were performed during experimental program of high energy ion task force with stationary and

modulated (200 ms – on / 200 ms – off) co- and counter- beam injection [1]. Applied NDDs were specially developed for fast (E > 18 keV) CX atom spectrometry [4]. Tangential NDD was placed at distance 6.8 m from the plasma center. It has input window with diameter 2 mm and additional aperture with diameter 1 mm installed at distance 285 mm from the detector. So this NDD has plane angle of its cone of view ~ 0.3 degree, and sees the plasma region with diameter ~ 6 cm at the axis. Measurements were performed in standard plasma configurations with magnetic axis at R_{ax} = 3.75 m and in inward shifted configurations with $R_{ax.}$= 3.6 and 3.53 m and average minor radius a = 0.6 m with values of magnetic field equal to 2.5, 1.5, 0.75 (co-clockwise) and -2.5 T (counter-clockwise). Electron density and temperature of plasma in these experiments were in the ranges $0.5 \div 2 \times 10^{19}$ m^{-3} and 1 ÷ 2 keV.

3. Results of Fast Ion Confinement Studies

3.1. Methodology of the Studies

Behaviors of co- (with respect to magnetic field (B_t)) and counter-moving fast ions were studied in plasma discharges with counter- and co-directed B_t, respectively.

To study the difference in confinement of co- and counter-moving tangential and perpendicular ions in a number of LHD plasma configurations the most of CX atom spectra measurements were performed in MHD-quiescent plasmas with similar parameters (n_e ~ $(0.75 \div 1) \times 10^{19}$ m^{-3}, $T_e \sim 1.8 \div 2$ keV).

Another way to study experimentally the efficiency of fast ion confinement is connected with measurements of the decay times of fast (E > 18 keV) CX atom fluxes after beam cancellation in experiments with modulated NBI and their comparison with calculated: 30 degree scattered times for tangential CX atom flux measurements and Coulomb slowing down time for perpendicular CX atom flux measurements. It was measured that after beam cancellation the perpendicular fast CX atom flux exist longer then tangential one. This indicates that due to reionization of CX atoms integrated from respective cone of view the tangential NDD has measured CX atom flux from more periphery region of plasma than perpendicular NDD. It was measured that perpendicular CX atom flux is increasing with plasma density and time delay of its maximum with respect of beam cancellation is diminishing with plasma density. Such relative behavior of tangential and perpendicular fast CX atom flux is in good agreement with pitch angle scattering by Coulomb collisions.

3.2. CX Atom Spectrum and Flux Measurements in MHD-quiescent LHD Plasma

Tangential spectra of co- and counter-moving CX atoms were very similar in whole energy range for plasma configurations with R_{ax} = 3.75 and 3.6 m and $|B_t|$ = 2.5 T. This demonstrated the absence of essential difference in confinement of fast co- and counter moving ions with energies up to 140 keV in these LHD plasma configurations.

Tangential spectra of co-moving CX atoms measured for R_{ax} = 3.53 m and 3.6 m plasmas were equal to each other and a bit lower than for R_{ax} = 3.75 m plasma in the energy range 20-85 keV. Similar, as shown in fig.1, tangential spectra of counter-moving CX atoms measured for R_{ax} = 3.6 m plasmas were a bit lower with respect to those measured from the R_{ax} = 3.75 m plasmas in the same energy range. Measured decay times of co- and counter-moving CX atom flux were slightly lower in R_{ax}= 3.6 m configuration with respect to R_{ax}= 3.75 m one and essentially lower in R_{ax}= 3.53 m (see fig.2) plasma. Fast beam ion minor radial distributions in standard and inward shifted plasma configurations were calculated using FIT code [5] for LHD discharges 45896 (R_{ax} = 3.75 m) and 45908 (R_{ax} = 3.6 m) using experimentally measured by Thomson scattering electron density and temperature minor radial distribution. Results of calculations shown, that the beam ion minor radius distribution

is becoming broader with the inward shift of plasma axis from standard configuration. In addition to this due to reionization of CX atoms the input of more periphery component in the integrated by NDD along its line of sight fast CX atom flux is increasing with the inward shift of the plasma axis. So, the obtained results of some diminishing of fast ion distribution function in low energy range and fast CX atom decay time after beam cancellation with the inward shift of LHD plasma axis could be treated as illustration of slightly higher losses of both co- and counter- moving fast ions from more periphery plasma regions (measurements in R_{ax} = 3.6 and 3.53 m configurations) than from more central regions (measurements in R_{ax} = 3.75 m configuration). Due to the absence of the loss cone for tangentially moving fast ions with studied energies in almost whole LHD cross section [5] these losses should be assigned to charge exchange processes of fast ions with residual in plasma atoms, that are increasing to plasma periphery due to higher atom density there.

As shown in fig.3, in plasma configuration with R_{ax}=3.6m tangential counter-moving CX atom spectra are slightly diminishing with B_t change from 2.5T to 1.5T and essentially diminishing for B_t=0.75T in whole energy range. The comparison of measured in these experiments fast CX atom flux decay times with calculated 30 degree scattered times are presented in fig.4. These results are showing that for lower axial magnetic field measured decay times are very slightly (B_t=1.5T) or essentially (B_t = 0.75T) shorter then calculated 30 degree scattered time. These decay time data could be treated as an illustration of some degradation of the confinement of counter-moving ions in plasma with B_t diminished down to 0.75T. But measured results, and spectrometry data in particular, could be also assigned to lower T_e in discharges with lower B_t and to wider fast ion trajectory excursions to plasma periphery at lower B_t and so lower slowing down time and higher CX loss there. Further detail mathematical modeling of measured by NDD CX atom fluxes is required for making the final conclusion.

The perpendicular CX atom spectra, $T_{eff,\perp}$ (see fig.5) and fast CX atom flux decay time shown in fig.6 were lower in R_{ax} =3.75m configuration than in cases of R_{ax} =3.6m and 3.53m. All this could be explained by better confinement of helically trapped ions in inward shifted configurations with respect to standard one [6].

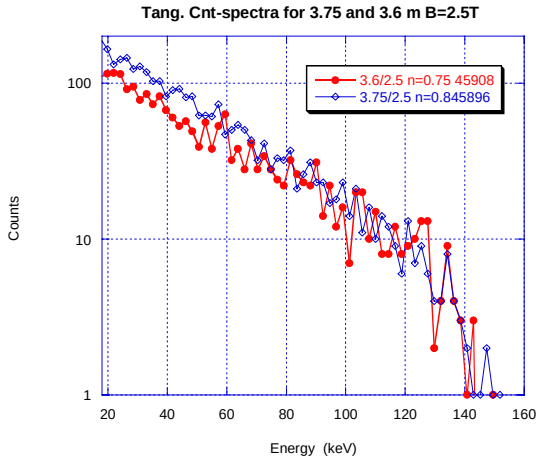

Fig.1. Tangential spectra of counter-moving CX atoms for B_t=2.5T, R_{ax}=3.6m (discharge 45908, n_e=7.5×10^{18}m^{-3}) and 3.75m (45896, n_e=8×10^{18}m^{-3}).

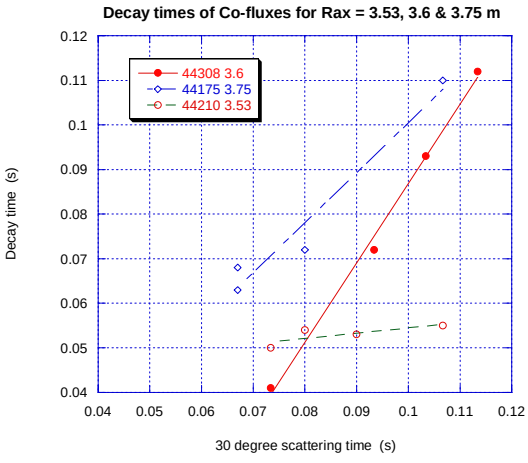

Fig.6. Comparison of measured Co-CX atom flux decay times with calculated 30 degrees scattered time of 50keV protons for R_{ax}=3.75m (discharge 44175, diamonds), 3.6 m (44308, circles), 3.53 m (44210, empty circles).

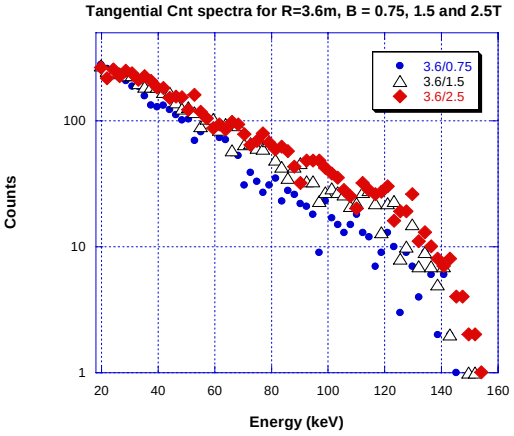

Fig.3. Counter-CX atom spectra (for E>18 keV) measured in plasmas with R_{ax}=3.6m and B_t=2.5T (diamonds), 1.5T (triangulars) and 0.75T (circles).

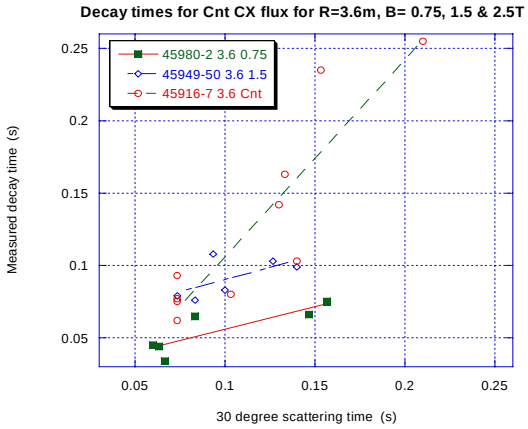

Fig.4.Counter-CX atom flux decay times (R_{ax}=3.6m, B_t=2.5T (open circles), 1.5T (diamonds), 0.75T (squares) upon 50 keV proton 30^0 scattered times.

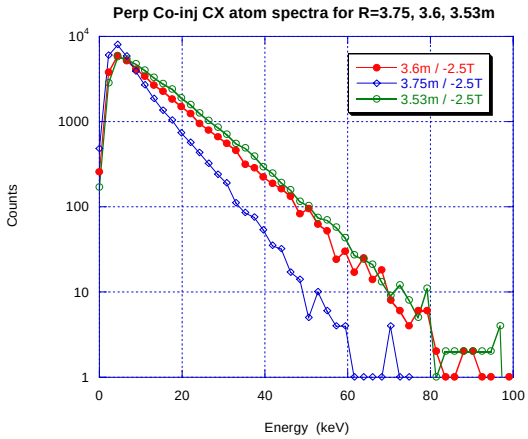

Fig.5.Perpendicular CX atom spectra (E>18 keV) in plasmas with B_t=-2.5T, R_{ax}= 3.75m (diamonds), 3.6m (circles) and 3.53 m (open circles).

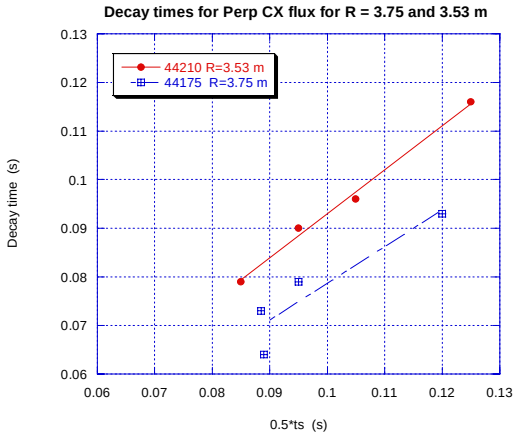

Fig.6. Perpendicular CX atom flux decay times for B_t=-2.5T, R_{ax}=3.75m (squares) and 3.53m (circles) upon calculated slowing down times t_s.

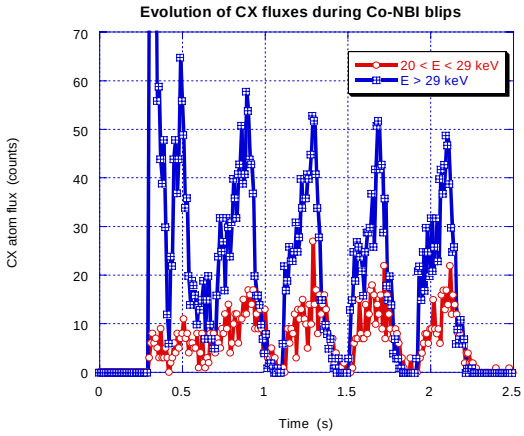

Fig.7. Tangential CX atom fluxes (E = 20-29 keV (circles) and >29 keV (squares), shot 44210, R_{ax}= 3.53m,co-NBI blips turned-off at 0.9, 1.3, 1.7, 2.1s.)

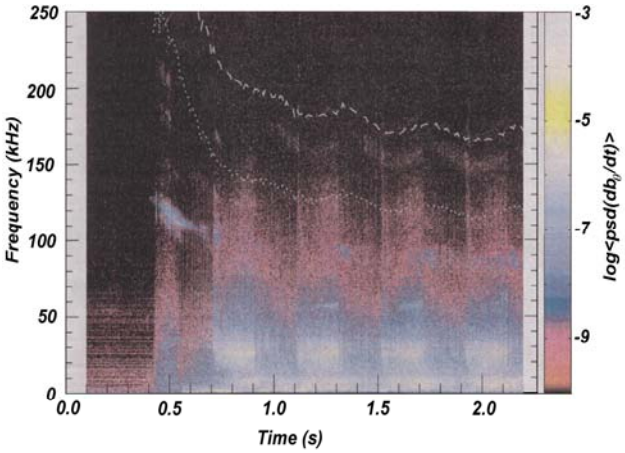

Fig.8. MHD activity during co-beam blips turned-off at 0.9, 1.3, 1.7, 2.1 s (44210, B_t = -2.5 T, R_{ax}= 3.53 m).

3.3. CX Atom Flux Measurements in LHD Plasma with MHD Activity

Sharp increases of co-moving CX atom fluxes were measured in experiments with 200ms co-beam blip injection in R_{ax}=3.53m and not so clear but also in R_{ax}=3.6m plasmas during the second part of the beam time (see Fig.7). Essential MHD activity was developed in these experiments with inward shifted LHD plasma and modulated co-NBI. Development of MHD activity in LHD discharge with R_{ax}=3.53m, which CX atom fluxes presented in fig.7 is shown in Fig.8. The evolution of fast CX atom flux from plasma with Rax=3.53m configuration was studied for different energy ranges. As shown on fig.7 it was measured that fluxes of CX atoms with energy 20–29 keV did not have fast increases during beam time but fluxes of CX atoms having energy higher than 29 keV have sharp peaks during second parts of beam time. Measured sharp increases of fast CX atom fluxes correlate with appearance in plasma 50-60 kHz MHD instabilities showing on fig.8. This effect was almost not seen in R_{ax}=3.75m plasma configuration. Instant beginning of co-CX atom flux decay after co-NBI termination and delay with decay of counter-CX atom flux after counter-NBI termination were also measured. Increase of fast co-moving ion transport from plasma center to periphery by 50-60 kHz energetic particle modes in R_{ax}=3.53 and 3.6m plasma configurations could be discussed as the reason caused measured increase of fast (E > 29 keV) CX atom flux.

4. Conclusions

Results of CX spectrum and flux dynamic measurements:

- Demonstrated that there is no essential difference in confinement of fast co- and counter-moving ions with energy up to 140keV in LHD plasma with R_{ax}=3.75 and 3.6m, $|B_t|$=2.5T.
- Could be treated as illustration of slightly higher CX losses of both co- and counter-moving fast ions from more periphery plasma regions (measurements in R_{ax} = 3.6 and 3.53m configurations) than from more central regions (measurements in R_{ax} = 3.75 m configuration).
- Could be treated as illustration of some degradation of counter-moving ion confinement in plasma with magnetic field decrease down to B_t = 0.75 T. But measured results could be also assigned to lower T_e in plasma discharges with lower B_t and to wider fast ion trajectory excursions to plasma periphery and so lower slowing down time and higher CX loss there.
- Demonstrated the better confinement of helically trapped ions in inward shifted (R_{ax}= 3.53 and 3.6 m) configurations with respect to standard one (R_{ax} = 3.75 m).

Increase of fast (E > 29 keV) co-moving ion transport from plasma center to periphery by 50-60 kHz energetic particle modes in R_{ax}=3.53 and 3.6 m plasma configurations could be discussed as the reason for measured increase of fast CX atom flux.

Acknowledgment. Work was performed in frame of the program of high energy ion task force of LHD team and under support of National Institute for Fusion Science

References

[1] M.Osakabe, et. al., presented at IAEA Fusion Energy conference (EX-P4/44) Villamura, Portugal (2004).
[2] S.Sudo, et.al., Plasma Phys.Control.Fusion, 45, A425-A443 (2003).
[3] M.Isobe, et.al., Rev. Sci. Instrum., 72, 611-614 (2001).
[4] A.V.Krasilnikov, et.al., Nuclear Fusion, 42, 759-767 (2002).
[5] S. Murakami, N. Nakajima, S. Okamura, M. Okamoto, Nucl. Fusion 36 789-796 (1996).
[6] S.Murakami, H.Yamada, M.Sasao,et.al. Fusion Science & Technology 46, 241-247 (2003)

Horizontal and Vertical Structure of the High-Energy Particle Distribution in Large Helical Device

T.Ozaki[1], P.Goncharov[1], S.Murakami[2], E.Veschev[3], S.Sudo[1], T.Seki[1], H.Sanuki[1], T.Watanabe[1] and LHD Experimental Group[1]

1) National Institute for Fusion Science, Toki, Gifu 509-5292, Japan
2) Kyoto University, Department of Engineering, Kyoto, Japan
3) Graduate University for Advanced Studies, Hayama, Kanagawa, 240-0193, Japan

e-mail address: ozaki@nifs.ac.jp

There are two neutral particle analyzers, the time-of-flight (TOF-NPA) and the silicon detector (SD-NPA), which are scannable horizontally and vertically. In horizontal scan, it is interesting to measure the pitch angle distribution and to investigate the loss cone feature obtained by it. It is very important to control the trapped particle by the helical ripple to realize the helical type plasma fusion device. Here the charge exchange neutral particle between the high-energy ion and the background neutral is measured to obtain the pitch angle of the high-energy ion in the plasma. Tangential injected NBI heating in long discharge is suitable for this purpose in LHD. The energy of the high-energy ion supplied from NBI decreases by the plasma electron. The pitch angle scattering is occurred by the collision of the plasma ion with several times energy of the electron temperature. Therefore we can easily compare the experimental pitch angle distribution with the simulation result, which is obtained by considering the initial pitch angle distribution and the atomic process. The pitch angle distribution from 40 to 100 degrees can be obtained by horizontal scanning the TOF-NPA during the long discharge over 100 seconds sustained by the NBI#2 (co-injection) at the magnetic axis (R_{ax}) of 3.6 m. The trapped particle by the helical ripple can be clearly observed around the pitch angle of 90 degrees. The loss cone feature is agreed with the result. It is interesting to investigate the dependence of R_{ax} of the loss cone feature. However it is not suitable to use the scanning of TOF-NPA during NBI plasma discharge although it can provide the precise structure of the loss cone because it is very difficult to sustain the long discharge at different magnetic axis. We use SD-NPA, which has ability of 6 different pitch angle measurement at R_{ax} =3.5, 3.6 and 3.75 m. More trapped particle can be observed at R_{ax} =3.5 m because the large helical ripple can be expected at inner magnetic axis.

In vertical scan, the heating deposition profile of the ion cyclotron resonance heating (ICH) has been discussed. In LHD, the long discharge over 30 minutes with the total energy of 1GJ can be sustained by the ICH. The deposition profile can be obtained by the vertical scan of the SD-NPA. The region where the high-energy particle is generated, is agreed with the resonance region of ICH. Similar result can be obtained by the pellet charge exchange measurement in the short discharge.

1. Introduction

On helical devices, particle orbits in plasma are very complicated due to the magnetic field ripple. The particle is trapped by the helical or/and the toroidal ripples. When these orbits are drawn in velocity space, some particles with large pitch angles are lost.[1] This phenomenon is known as a loss cone and it expresses well the features of particle confinement in helical device. One of the main subjects in helical devices and the future fusion reactor with the helical system is, how this loss cone can be reduced. This phenomenon can be reduced by the control of the magnetic configuration, the heating method and the electric field etc. In the Large Helical Device (LHD),[2] the device design is devised so that the loss cone at ρ (radial position on the magnetic surface) <1/2 may not exist.[3] Moreover, most of the particles heated by tangential NBI (Neutral Beam Injection)

do not have a pitch angle perpendicular to the magnetic field.

However, if the slowing down of the incident particle by electron collision occurs, not only in ICH (Ion Cyclotron resonance frequency Heating) heating but also in NBI heating, the particle with a large pitch angle actually will be generated due to the scattering between the particle and a plasma ion at several times the plasma temperature. These particles cause the drift motion and rotate poloidally. They can almost be confined in the plasma because the energy of these particles is not so large. However part of them are not confined by balance with the electric field *E*. [4] Here we are thinking about the single particle orbit model excluding the electric filed for simplicity.

The simulation of the single particle orbit in LHD magnetic field configuration had been precisely done by Kamimura [5] and Watanabe [6]. In calculation, test particles with uniform initial pitch angle are put on a certain poloidal surface grid. Typical simulation results are shown in Ref. [5]. Protons with the energy of 50 keV, which are settled on the poloidal surface initially, move on LHD magnetic configuration in vacuum. The figure shows alive particles map with major radius in horizontal axis and pitch angle in vertical axis. The symbols indicate the difference of the particle orbits. Particle confinement by the different magnetic fields are shown in Ref. [5]. The trapped particle sby the helical ripple are remarkably observed around 90 degrees of the pitch angle at the inner magnetic shifts. Some of the particles are lost when the pitch angle is slightly lower or higher than 90 degrees. However when the pitch angle becomes much lower (or higher), the particle has the transit orbit. Therefore many particles can be confined in this region. When the magnetic axis moves inward, the trapped particle is well confined because the orbit of the trapped particle closes the plasma magnetic surface.

2. Experimental arrangement

The time-of-flight (TOF) type neutral particle analyzer has a large S/N ratio for various kinds of radiation noise from soft X-rays. Its detail and experimental configuration are described in Ref. [7]. The analyzer with its driving stage is installed on the plasma mid-plane (port 10-O). As for the position of 10-O, NBI#1 and NBI#2 are installed at the right and left sides of the analyzer sight line, and especially the beam path of NBI#1, which crosses the sight line near the plasma center, can be expected to generate neutral particles because of charge exchange in the central part of the plasma.

The possible scanning angle is equivalent to the pitch angles from 40 degrees to 100 degrees. The pitch angle in this paper is defined as the angle between the magnetic axis and the sight line, not the actual pitch angle for each particle because it is difficult to find the generation point of each particle. About the vertical scan, it is possible from -12 to +15 degrees. A very high-speed scan of one degree per second in the vertical system is possible since a counter weight is used to compensate the weight of the analyzer (700kg).[8]

Silicon surface barrier diode type neutral particle analyzer (SD-NPA) is installed under the TOF-NPA.[9,10] It has 6 liquid nitrogen cooled detectors with different sight lines from 35 to 90 degrees. Minimum observable energy is 25 keV which is determined by the thickness of

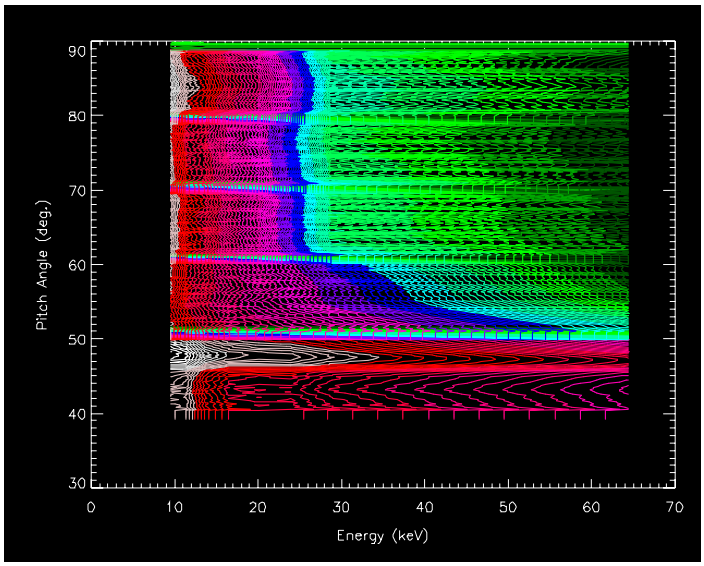

Fig. 1. The contour plot of the pitch angle distribution.
The color (or density) means the flux of the particle. The trapped particle around the pitch angle of 90 degrees is clearly observed. The effect of loss cone is not so large because the particle loss near the 20 keV is not remarkable.

aluminum coating for light protection and the inactive layer of the silicon detector. The simultaneous six energy spectra with energy resolution of several keV can be obtained by traditional pulse height analysis. The time resolution is 5 ms. It has vertical scanning mechanism by moving the aperture.

LHD has the toroidal mode number of *m=10* and helical mode number of *l=2*. The major radius and minor radius are 3.9 m, 0.6 m, respectively. The helical ripple is 0.25 and a magnetic field is a maximum of 3 T. Although the standard magnetic axis is 3.75 m, it can be changed from 3.4m to 4.1m by applying a vertical magnetic field. There are three kinds of heating system ECH (10MW), NBI (15MW) and ICH (3MW). As for electron temperature, a maximum of 10keV is observed by using Thomson scattering and ECE (Electron Cyclotron Emission). Electron density can be changed from 0.1 to $4x10^{19}$ m^{-3}. The density profile is measured with the multi-channel interferometer.

3. Experimental Results

Figure 1 shows the contour plot of the pitch angle distribution measure by the scanning of TOF-NPA during NBI long plasma discharge. Horizontal and vertical axes indicate the particle energy of hydrogen and the pitch angle, respectively. Here the pitch angle is defined as the angle between the magnetic axis and the sight line. The color (or density) means the flux of the particle. We must take account the line integration of the particle flux in experiment. The observed neutral particle flux is the products of the high-energy particle and the background neutrals amounts. The penetration depth of the background neutral depends on the plasma density. However main region of the neutral particle source is outer than 2/3 of the plasma radius. Loss cone appears outer than 1/2 of plasma radius. Therefore the experiment results are expected to reflect the simulation results. Horizontal axis in Fig. 2 is the particle energy not the major radius which is shown in Fig. 1. However the trapped particle around the pitch angle of 90 degrees is clearly found in Fig. 1. The magnetic axis of R_{ax} =3.6 m in this experiment is equal to the 0.15 m inner shift in the simulation. Both results are qualitatively agreed. Although some particles are disapperaed by escaping to the loss cone, most of particles with large pitch angle are well confined by the inner shift of the magnetic axis. The flux in the pitch angle of less than 90 degrees is smaller. In this experiment, the critical energy is expected to be 20 keV because the electron

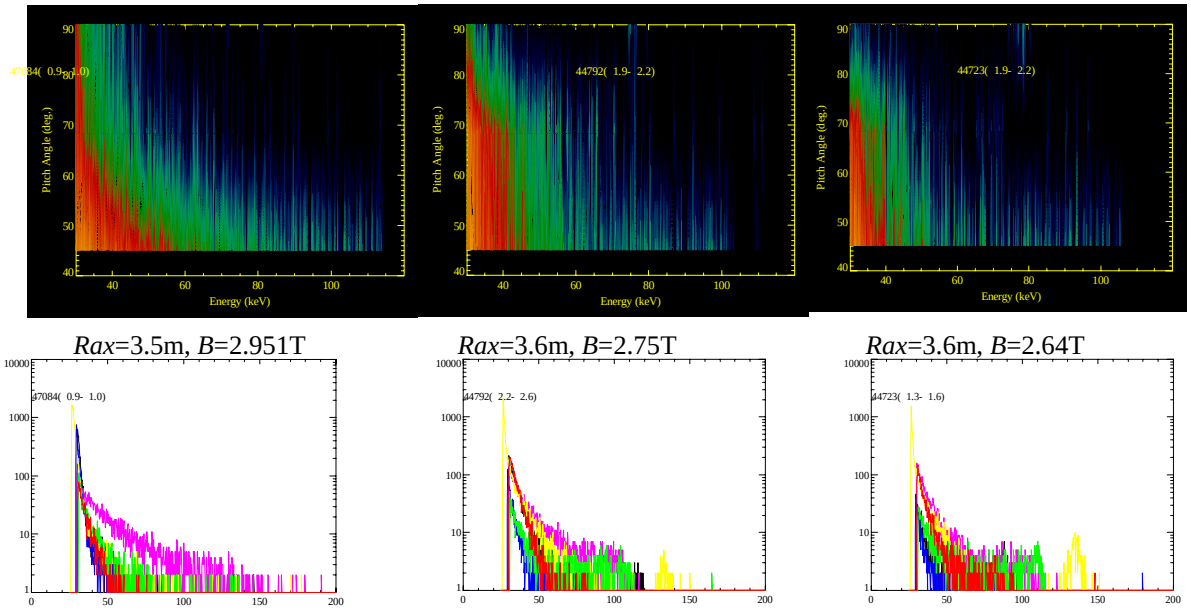

Fig. 2. The contour plots and spectra of the pitch angle distribution at three different magnetic axes.
. By inward shift of the magnetic axis, the trapped particle near the pitch angle of 90 degrees increases.

temperature is 4 keV. Uniform initial pitch angle distribution can be expected on 20 keV. The effect of loss cone is not so large because the particle loss near the 20 keV is not remarkable.

In the long discharge experiment, it is very difficult to choose the different magnetic axis position because the long discharge cannot maintain except R_{ax} =3.6 m. We use SD-NPA which has different 6 sight lines in order to obtain the pitch angle distribution in single short discharge. The pitch angle distribution in different magnetic axes can be obtained by using SD-NPA. Figure 2 shows the contour plots of the pitch angle distribution at three different magnetic axes, R_{ax} =3.53, 3.6 and 3.75 m. Horizontal and vertical axes indicate the particle energy of hydrogen and the pitch angle, respectively. The color (or density) means the flux of the particle. Each spectrum is also shown in Fig. 2. By inward shift of the magnetic axis, the trapped particle near the pitch angle of 90 degrees increases. This means the trapped particle is well confined because the orbit of the trapped particle closes the magnetic surface when the magnetic axis moves inward.

3. Vertical scan

In LHD, the long discharge over 30 minutes with the total energy of 1GJ can be succeeded by the ICH. SD-NPA has an ability of the vertical scan of 0.03 degree/seconds by the sliding of the pinhole in order to obtain the vertical distribution of neutral particle energy spectra. The deposition profile of ICH can be determined by the distribution. Much high-energy flux can be observed near the resonance region of ICH as shown in Fig. 3. Similar result can be obtained by the pellet charge exchange measurement in the short discharge. The details of

the results are mentioned elsewhere.[11]

4. Summary

Two neutral particle analyzers, TOF-NPA and SD-NPA, which are scannable horizontally and vertically, are used for observing the pitch angle distribution of high-energy particle and studying loss cone feature. In NBI long discharge, precise pitch angle distribution, which can be compared with the simulation, can be obtained. The dependence of tapped particle against the magnetic field can be obtained using SD-NPA. In LHD, large loss cone is not observed when the magnetic axis is shifted inward. The ICH heating near the resonance region can be observed using vertical scan of SD-NPA.

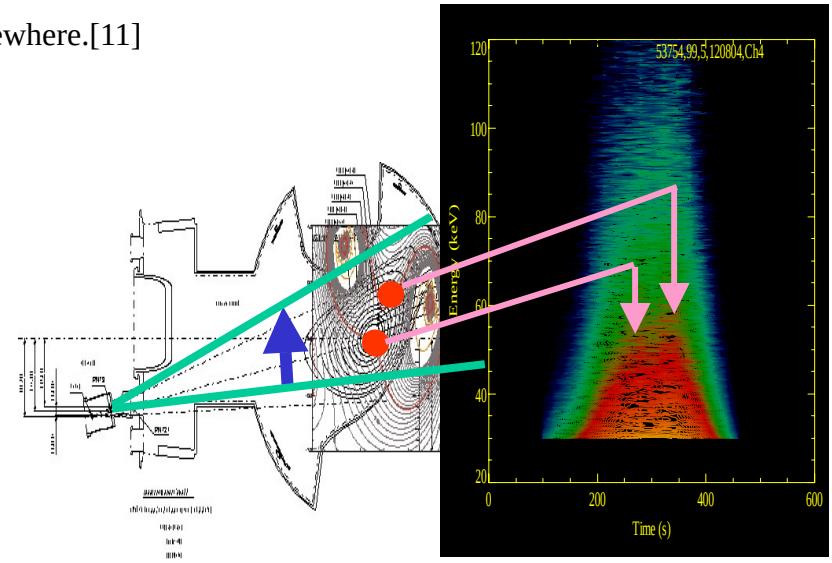

Fig. 3. The vertical scan of SD-NPA.
. SD-NPA is scanned from the bottom to top. During scanning, two peaks appears when the sight line cross the strong resonace positions of ICH.

Acknowledgements

This work is financially supported by the NIFS-PH021 and the aid of Japan Society for the Promotion of Science (17540475).

References

[1] K. Hanatani, *et al.*, Nucl. Fusion 25 (1985) p.259.
[2] A. Fujisawa, *et al.*, IAEA-CN-64/C1-5 (1996).
[3] M. Wakatani, *"Stellarator and Heliotron Devices"*, Oxford University Press (1998) p.262.
[4] H.Sanuki, *et al.*, Phys. Fluids B, Plasma Phys.Vol.2 No.9 (1990) 2155-61.
[5] T.Kamimura, *et al.*, *"Numerical Studies of Particle Drift Orbits in Helical System"*, Energy Tokubetsu-Kenkyu of MOE (in Japanese) (1987).
[6] T. Watanabe, Proc. of 3rd Toki Conf. (1989) 130-3.
[7] T. Ozaki, V. Zanza, *et al.*, Rev. of Sci. Instrum., 71(7), 2698-2703 (2000).
[8] T.Ozaki, P.Goncharov, *et al.*, Vol. 75, No. 10, pp. 3604-3606(2004).
[9] P.R. Goncharov, J.F. Lyon, T. Ozaki, *et al.*, ,Journal of Plasma and Fusion Research Series, Vol. 6 (2003), Vol. 6, (2004) 314-317.
[10] Lyon, J.F. Goncharov, P.R. Murakami, S. Ozaki, *et al.*, Rev. Sci. Instrum. (USA) vol.74, No.3, (2003) 1873-7.
[11] P.R. Goncharov, T. Ozaki, et al., proc. of 9th IAEA-TM (P18), Takayama, Japan.

Computational Analysis of Neutral Particle Fluxes from Non-Axisymmetric Magnetically Confined Plasmas

E.A. Veshchev[1], P.R. Goncharov[2], T. Ozaki[2], S. Sudo[2], J.F. Lyon[3]

1) Graduate University for Advanced Studies, Hayama, Kanagawa, 240-0193, Japan
2) National Institute for Fusion Science, Toki, Gifu 509-5292, Japan
3) Oak Ridge National Laboratory, Oak Ridge, TN 37831-8072, USA
Corresponding author's e-mail: veshchev.evgeny@lhd.nifs.ac.jp

Abstract

Energy and angle-resolved measurements of neutral particle fluxes from the plasma provide information about T_i. as well as non-maxwellian anisotropic ion distribution tails from NBI and ICH. Multidirectional diagnostics employing high resolution atomic energy spectrometers are being used to study the ion component heating mechanisms and fast ion confinement in helical plasmas. Since the natural atomic flux source is not localized in contrast to the diagnostic neutral beam or pellet charge exchange methods, the correct interpretation of such measurements in a complex toroidally asymmetric geometry requires a careful numerical modeling of the neutral flux formation and the knowledge of the charge exchange target distributions, relevant cross-sections and the magnetic surface structure. The measured neutral flux calculation scheme for LHD geometry is given. Calculation results for Maxwellian and NBI-induced ion distributions are shown. The behaviour of calculated and experimental suprathermal NBI tails is discussed along with the magnetic axis shift effect on energetic particle confinement.

1. Neutral Flux Formulation and Calculation Scheme

The atomic flux $\Gamma(E,\theta,t)$ [erg^{-1}s^{-1}] measured by passive diagnostics is an integral along the sightline L of the local differential atomic birth rate in the plasma $g(E,\mathbf{r},t)$ [erg^{-1}cm^{-3}s^{-1}], which contains the sought ion distribution:

$$\Gamma(E,\vartheta,t)=\frac{\Omega S_a}{4\pi}\int\limits_{(L)} g(E,\vartheta,\mathbf{r}(\xi),t)e^{-\int\limits_0^{\xi}\frac{d\xi'}{\lambda_{mfp}(E,\mathbf{r}(\xi'),t)}}d\xi\,, \qquad (1)$$

where Ω is the observable solid angle and S_a is the diagnostic aperture area. The exponential factor describes the attenuation of the atomic flux in the plasma. $\lambda_{mfp}^{-1}(E,\mathbf{r}(\xi'),t)$ is the mean number of ionizations per unit path length. Changing the integration variable in (1) from ξ to the effective minor radius ρ yields [1, 2]

$$\Gamma(E,\vartheta,\zeta)=e^{\int\limits_{\rho_{\min}}^{1} Q^-(\tilde\rho,\zeta)\lambda_{mfp}^{-1}(E,\tilde\rho)d\tilde\rho}\frac{\Omega S_a}{4\pi}\int\limits_{\rho_{\min}}^{1} g\left(E,\vartheta,\rho\right)\times\left[Q^+(\rho,\zeta)e^{-\int\limits_{\rho_{\min}}^{\rho} Q^+(\tilde\rho,\zeta)\lambda_{mfp}^{-1}(E,\tilde\rho)d\tilde\rho}-\right.$$
$$\left.-Q^-(\rho,\zeta)e^{-\int\limits_{\rho_{\min}}^{\rho} Q^-(\tilde\rho,\zeta)\lambda_{mfp}^{-1}(E,\tilde\rho)d\tilde\rho}\right]d\rho\,. \qquad (2)$$

The functions $Q^+(\rho,\zeta)=dX'/d\rho>0$ and $Q^-(\rho,\zeta)=dX'/d\rho<0$ on the intervals between $\rho=1$ and $\rho=\rho_{\min}$ are obtained from the structure of the isolines $\rho=const$ known from a numerical solution of Grad-Shafranov equation [3]. This enables one to use the relation (2) for computer simulations of the neutral particle diagnostic data. Fig. 1 illustrates the calculation of the positive Q^+ and negative Q^- branches of the integral transform (2) for

SDNPA diagnostic [4]. The ion temperature retrieval from the thermalized spectra and modeling results for suprathermal high energy tails from NBI induced $f_i(E,\theta,t)$ are discussed below for LHD heliotron configuration.

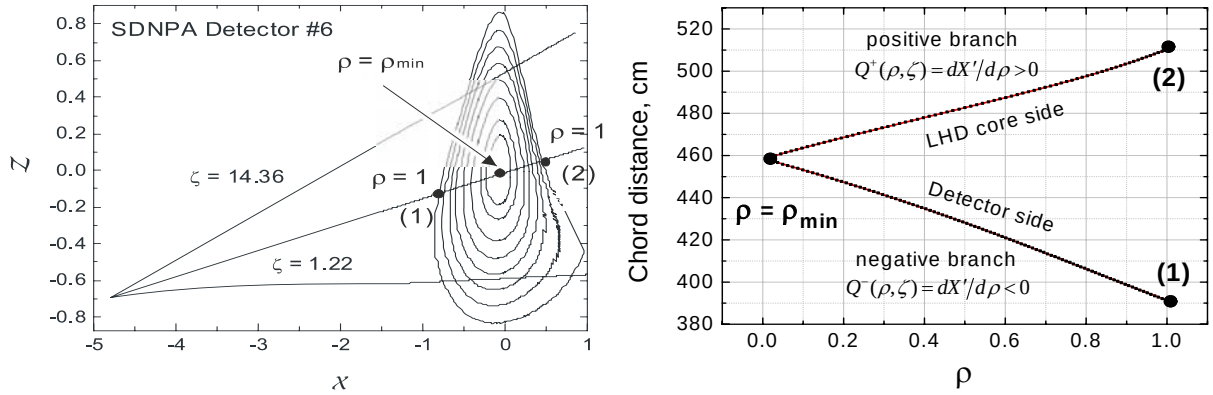

Fig. 1. Magnetic surface structure in SDNPA [4] detector #6 diagnostic cross-section (left) and the integral transform (2) kernel calculation for the middle vertical scan position (right).

2. Calculation Results for Maxwellian and Beam-induced Ion Distributions

The experimentally measured $\Gamma(E,\theta,t)$ has been calculated for hydrogen plasma on the following radial profile shape assumptions:

$$n_e(\rho) = n_e(0)\left(1-\rho^q\right)^s, \quad T_e(\rho) = T_e(0)\left(1-\rho^u\right)^w, \tag{3}$$

$$T_i(\rho) = T_i(0)\left(1-\rho^x\right)^y, \tag{4}$$

$$n_0(\rho) = n_0(0)\exp\left(B\rho^A\right) \tag{5}$$

with the unknown values taken as free parameters. The hydrogen charge exchange $H^+ + H^0 \leftrightarrow H^0 + H^+$ and proton impact ionization $H^+ + H^0 \leftrightarrow H^+ + H^+ + e^-$ cross-sections were taken from [5].

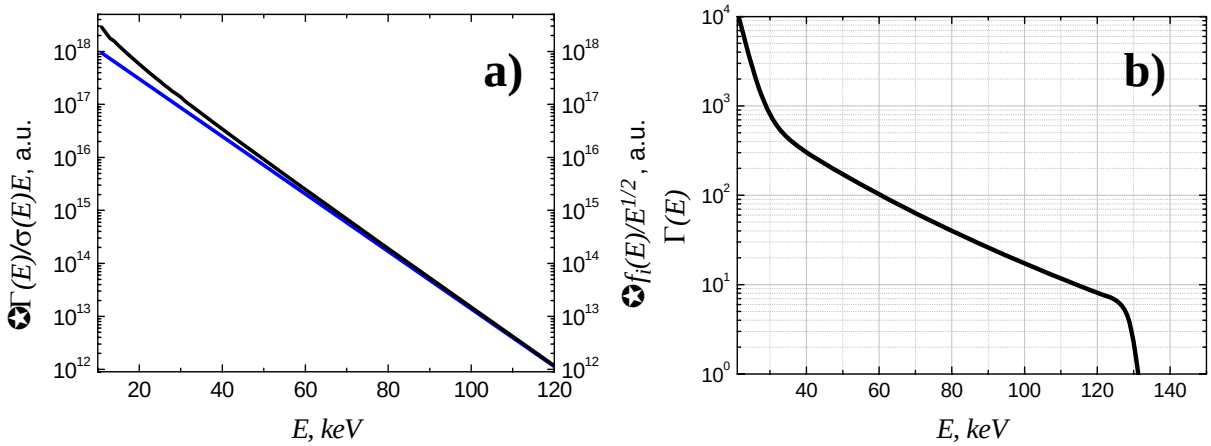

Fig. 2. a). Plasma with Maxwellian ion distribution: blue line – thermal exp(-E/T_i(0)) representing the central ion temperature; black line – calculation of the experimentally measured neutral spectrum corrected for σE factor; b). NBI-heated plasma: calculation of the experimentally measured neutral spectrum.

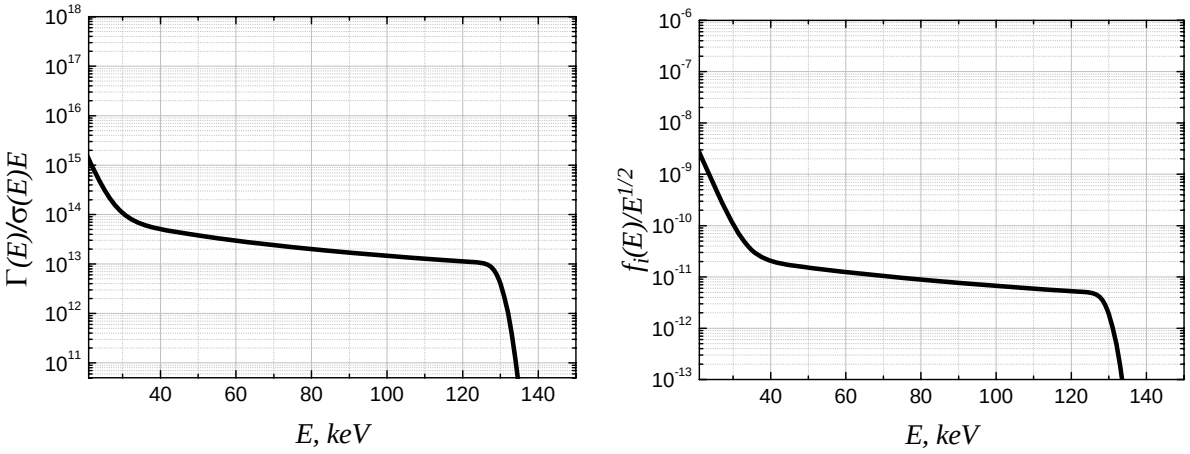

Fig. 3. NBI-heated plasma: calculated neutral spectrum corrected for σE factor (left); model ion distribution function (right)

Calculation results for the Maxwellian plasma ion distribution $f_i^{(M)}(E,\rho)=\frac{2\sqrt{E}}{\pi^{1/2}T_i^{3/2}(\rho)}\exp\left(-E/T_i(\rho)\right)$ are shown in Fig. 2 a). The calculated typical neutral hydrogen energy spectrum corrected for the charge exchange reactivity factor $\sigma\sqrt{E}$ combined with the Jacobian $\sqrt{E}$ (black line) and the Maxwellian exponent $\exp\left(-E/T_i(0)\right)$ in the core region (blue line) are scaled to match at the highest energy in the considered range. Taking the logarithmic slope of $\Gamma(E)/\sigma(E)E$ in the energy range below $\approx 5T_i(0)$ as an estimation of the core T_i results in a systematic 10-30% error while at the higher energies this error vanishes. This is consistent with the simple qualitative analysis for a flat plasma layer case [6]. However, in practice either the counting statistics is poor at the highest energies or the high-energy tail becomes substantially non-Maxwellian due to the strong distortion by the ion heating.

In order to calculate the tangentially measured neutral hydrogen spectrum from tangential NBI heated Maxwellian background plasma .the model ion energy distribution was assumed to be a combination of the Maxwellian distribution function and the fast ion slowing down distribution from a monoenergetic isotropic source $S\left(v-v_0\right)=\frac{S_0}{4\pi v^2}\delta\left(v-v_0\right)$ [7, 8]:

$$f_i^{(s)}(v,t)=\frac{S_0}{4\pi}\frac{\tau_s}{v^3+v_c^3}\left(h\left(v^*(v,t)-v_0\right)-h\left(v-v_0\right)\right), \tag{6}$$

where τ_s and v_c are the Spitzer's slowing down time and the critical velocity given by

$$\tau_s=\frac{3m_pT_e^{3/2}}{4\sqrt{2\pi}n_e e^4\Lambda m_e^{1/2}},\quad v_c^3=\frac{3\sqrt{2\pi}T_e^{3/2}}{2m_pm_e^{1/2}}, \tag{7}$$

Λ is the Coulomb logarithm, $h(x)$ is the Heaviside step function and $v^*(v,t)=\left(\left(v^3+v_c^3\right)e^{3t/\tau_s}-v_c^3\right)^{1/3}$.

Fig. 2 b) shows the resultant H^0 energy spectrum calculated in accordance with Eq. (2) with the integral kernel corresponding to detector #6 of the SDNPA diagnostic at the middle vertical scan position (see Fig. 1). The σE-corrected spectrum and the combined $f_i^{(M)}$ and $f_i^{(s)}$ ion distribution are shown in Fig. 3.

3. Analysis of Experimental Spectra from NBI-Heated Plasma

The calculation scheme described above taking into account the spectra superposition along the diagnostic chord and the isoline shape determined by the magnetic surface structure implies that a simple correction of the measured neutral spectra by the energy-dependent charge exchange reactivity factor $\sigma\sqrt{E}$ and the Jacobian $\sqrt{E}$ may appear insufficient in case of complex-shaped full 3D plasmas. The correct interpretation of the neutral spectrum shape is important to draw conclusions on physical mechanisms responsible for the ion distribution formation.

Consider the experimental results illustrated by Fig. 4 representing the spectrum from SDNPA detector # 6 closest to the tangential observation direction measured from $n_e = 0.4\times10^{13}$ cm^{-3} hydrogen target plasma at R_{ax} = 3.6 m heated by 130 keV H^0 NBI. The solid line shows the calculated neutral spectrum with free parameters chosen in such a way that the thermal slope and the value at the injection energy match the experimental ones (Fig. 4, left). The simple σE correction procedure leads to a U-shape tendency in the ion distribution (Fig. 4, right) with a decreased fast particle population. The calculation results suggest that this is an ion distribution property rather than a data misinterpretation. Fig. 5 shows the results for the similar plasma at R_{ax} = 3.5 m.

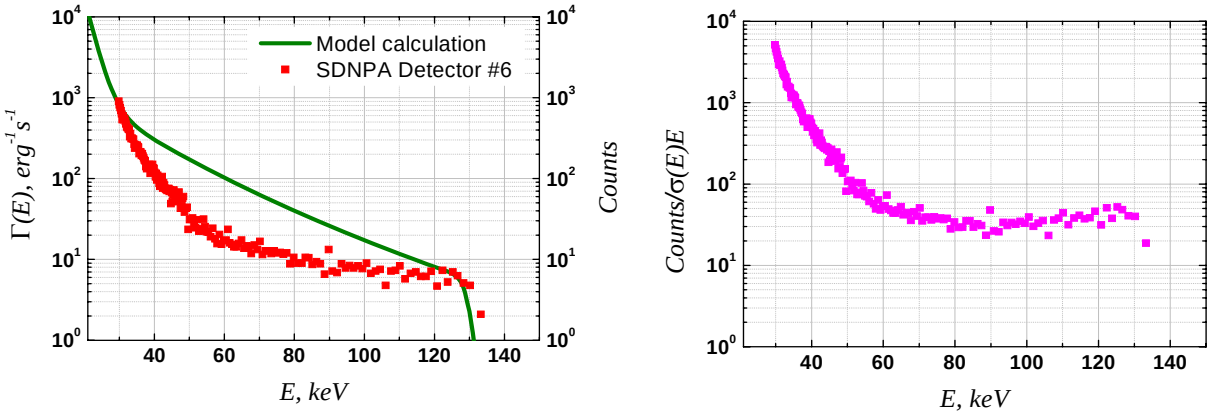

Fig. 4. R_{ax} = 3.6 m; left: experimental (squares) and calculated (solid) neutral spectrum; right: σE corrected spectrum reflecting the ion distribution.

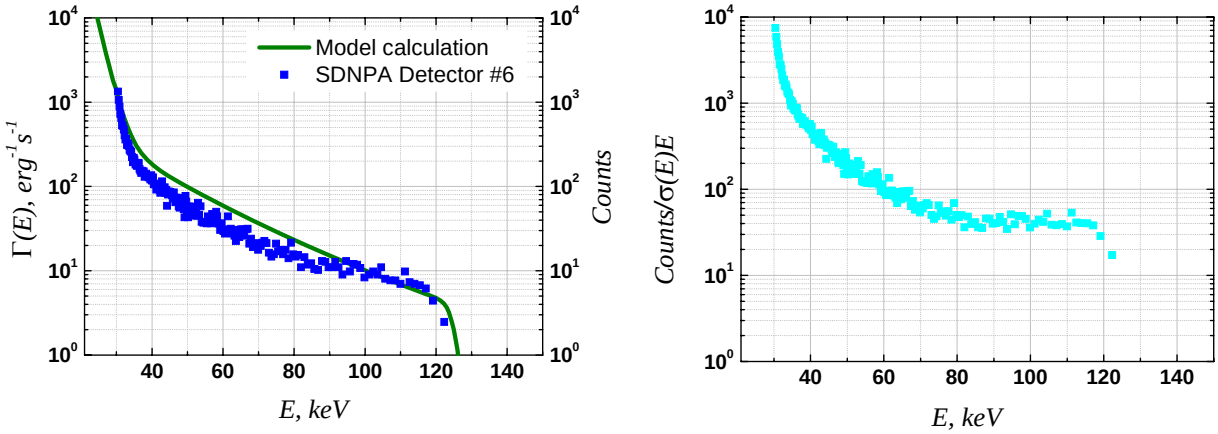

Fig. 5. R_{ax} = 3.5 m; left: experimental (squares) and calculated (solid) neutral spectrum; right: σE corrected spectrum reflecting the ion distribution.

In order to validate the possibility of making comparisons between these spectra obtained a different R_{ax} positions, it is necessary to confirm that the geometry of measurements is not substantially different for these two cases. The magnetic axis shift leads to a certain displacement of the plasma column with respect to the diagnostic sightlines. The values of the effective minor radius and the pitch angle cosines of particles measured from different locations along the sightlines for R_{ax} = 3.6 m and for R_{ax} = 3.5 m were calculated. Since no enormous differences could be seen, it was accepted that for the two different magnetic configurations under investigation, the comparisons should be sensible between the spectra measured with the corresponding SDNPA detectors. Inward shifted plasmas exhibit an increased fast ion population. This is interpreted as a reduction of fast particle losses in comparison with the outward shifted case [9, 10].

4. Summary.

A scheme has been realized to calculate the energy resolved flux of neutral particles escaping from the helical plasma column. Thermal distributions have been analyzed for T_i determination. The presence of a systematic error in case of lower energy range usage has been demonstrated. Suprathermal distributions induced by tangential NBI have been analyzed to clarify kinetic effects and the effect of particle confinement on the distribution function. The effect of increased fast ion population in inward shifted R_{ax} configuration has been verified via the computational modeling of the escaping neutral fluxes and the experimentally obtained spectra analysis.

References

[1] GONCHAROV, P.R., LYON, J.F., et al., J.Plasma Fusion Res. Series, **6** (2004), 314.
[2] GONCHAROV, P.R., et al., Proc. 31st EPS Conference on Plasma Physics and Controlled Fusion, ECA vol. **28G**, P-5.112 (London, 2004).
[3] LAO, L.L., HIRSHMAN, S.P., et al., Phys. Fluids, **24** (1981), 1431.
[4] LYON J.F., GONCHAROV, P.R., et al., Rev. Sci. Instrum., **74** (2003), 1873.
[5] BARNETT, C.F., ed., *Atomic Data for Fusion*, ORNL-6086, USA (1990).
[6] HUTCHINSON, I. H., Principles of plasma diagnostics, 2nd ed., Cambridge University Press, Cambridge (2002).
[7] DNESTROVSKII, Y.N., KOSTOMAROV, D.P., Numerical simulation of plasmas, Springer-Verlag, Berlin (1986).
[8] CORDEY, J.G., HOUGHTON, M.J., Nucl. Fusion, **13** (1973), 215.
[9] LYON J.F., et al., Proc. 29th EPS Conference on Plasma Physics and Controlled Fusion, ECA vol. **26B**, P-1.102 (Montreux, 2002).
[10] MURAKAMI, S., YAMADA H., et al., Fusion Sci. and Technol., **46** (2004), 241.

Observation of CX Neutral Particle Flux Injected by Diagnostic Neutral Beam in CHS

H. Matsushita[1], K. Ida[2], S. Okamura[2], M. Isobe[2], R. Akiyama[2], CHS Group

[1] The Graduate University for Advanced Studies, Toki 509-5292, Japan
[2] National Institute for Fusion Science, Toki 509-5292, Japan

Abstract

Diagnostic neutral beam (DNB) is applied to study a confinement of energetic ion in the compact helical system (CHS). The DNB can vary the injection angle in order to study confinement of energetic ions with different pitch angle. A charge-exchange (CX) neutral particle analyzer (NPA) to measure energetic ions injected by the DNB is also scannable and varies the observation angle on the equatorial plane in CHS. Combination of horizontally scannable DNB and NPA provides the information on whether the energetic ions with different pitch angle are confined in the plasma or immediately lost. When DNB is injected at loss cone region, observed neutral flux is significantly decreased. The experimental results are consistent with the prediction of single particle full orbit calculation. The good confinement of helically trapped ions is expected in the configuration with strong inward shift in CHS. Experimental result shows better confinement of perpendicularly injected energetic ions in the inward shifted configuration compared with that in the outward shifted configuration.

1. Introduction

The confinement of energetic ions having relatively high pitch angle is the interesting issue in heliotron experiments, because it gives a prospect for the efficiency of α-heating in future. In CHS, the loss cone region of energetic ions exists for the ions with a pitch angle nearly perpendicular to magnetic field line. Because of this loss cone, there is no increase of stored energy observed when the heating neutral beam is injected perpendicularly [1]. In order to investigate the loss cone structure of energetic ions experimentally, the scannable DNB and NPA systems have been developed in CHS [2]. The DNB can be scanned horizontally to vary the pitch angle of ions injected as test particles. The behavior of energetic ions injected by DNB is studied through the measurements of the ion energy distribution function with the NPA systems. In order to investigate the loss cone boundary in CHS, the injection angle of the DNB has been scanned for the plasmas with a magnetic axis position R_{ax} of 0.88 m. Furthermore, confinement property of energetic ions with different magnetic field configurations is also investigated by use of DNB and NPA systems. In this paper, the experimental results and initial analysis are reported.

2. Experimental Set-up

The DNB and NPA systems are installed at the outboard side on CHS (Fig. 1). Both systems are on the equatorial plane and separated by 180 degrees in the toroidal direction.

The beam line can be scanned from perpendicular injection to tangential injection both in co- to counter-direction with a pivot point of R = 1.58 m. Injected energetic ions are measured with the NPA at tangential radii (R_T^{NPA}) from 18 cm to 74 cm in this experiment. The DNB and NPA systems can be scanned horizontally by 0.1 degree increments using a pulse motor system. Beam energy (E_b) and extracted current (I_b) of the positive hydrogen beam are 28 keV and 2 A respectively. The DNB divergence angle measured with a calorimeter is 0.95 degrees at E_b of 28 keV. The beam diameter at the focal point is 9.8 cm while the averaged minor radius of CHS plasma is typically 20 cm. The proton ratio of DNB measured with spectroscopy system is 0.55. The NPA system consists of an electrostatic deflection plate and 16 microchannel plates. By changing the voltage of parallel plate of the NPA, the energy spectrum in the range of 0.1-50keV can be measured with a maximum count rate of 1×10^6 counts/s.

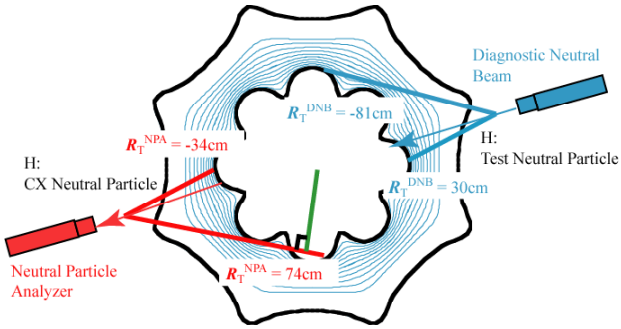

Fig. 1 *Experimental set up of the DNB and NPA systems as seen from the top of CHS. The beam line and NPA line of sight on the equatorial plane are plotted.*

3. Results and Discussion

3.1 Prompt loss of beam ions due to the Loss-cone

In order to investigate the loss cone boundary in CHS, the injection angle of the DNB has been scanned for the plasmas with a toroidal magnetic field B_t = 0.83 T and a magnetic axis position R_{ax} of 0.88 m. The target plasma is initiated and sustained by electron cyclotron resonance heating (ECRH) with a power of 220 kW for the duration of 100 msec. Line averaged n_e is 0.7×10^{19} m^{-3} and central electron temperature is 0.7 keV in this experiment. The heating power of DNB is small enough not to perturb these plasma parameters.

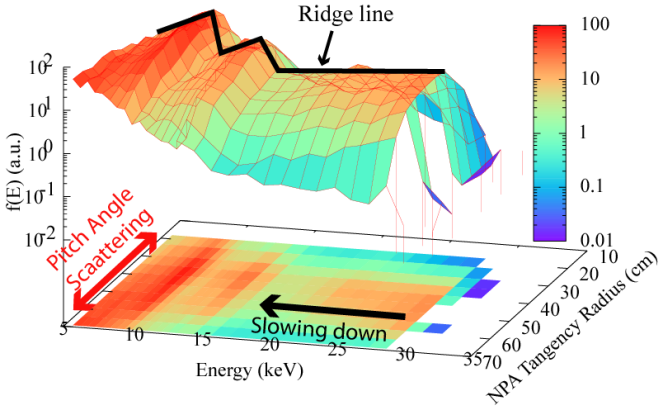

Fig. 2 *Energy spectrum of DNB at each tangency radius of NPA. DNB is injected at R_{tan} of 30 cm.*

Figure 2 shows the measured neutral energy spectra when the DNB is injected at tangential radius (R_T^{DNB}) of 30 cm in co-direction where the injected fast ions are expected to be confined in the orbit analysis. The NPA was scanned horizontally shot by shot from

tangential radius (R_T^{NPA}) of 18 cm to 74 cm and the neutral flux is integrated over 50 msec intervals in the discharge. Each energy component of the DNB, E_b (28 keV), $E_b/2$ (14 keV), $E_b/3$ (9.3 keV) was clearly observed. E_b component shows slowing down process while $E_b/2$ and $E_b/3$ components show pith-angle scattering. The ridge line of space resolved energy spectrum is used to estimate the loss time of energetic ions injected by DNB. For velocities less than the DNB initial velocity v_b, energy diffusion term of steady state Fokker-Planck equation is

$$f(v) \cong \left(\frac{S_0 \tau_{se}}{v^3 + v_c^3}\right)\left(\frac{v^3 + v_c^3}{v_b^3 + v_c^3}\right)^{\tau_{se}/3\tau_{loss}} \qquad (1)$$

where S_0 is the energetic ion source term, τ_{se} is Spitzer slowing down time, τ_{loss} is characteristic loss time of injected ions, v_c is the beam velocity at critical energy [3]. When the energy of injected ions is high enough not to be affected by pitch-angle scattering, eq.(1) is modified as[4]:

$$f(E) \cong \left(\frac{S_0 \tau_{se}}{2E_b}\right)\left(\frac{E_b}{E}\right)^{-\tau_{se}/2\tau_{loss}+1} \qquad (2)$$

In this experiment, slowing down time is estimated to be about 45 msec. Applying the eq.(2) as a fitting curve, τ_{loss} of E_b component is derived from energy spectrum (Fig.3(a)). As seen in Fig. 3(b), the τ_{loss} shortens as the DNB injection angle becomes vertical and significant depression of CX neutral flux is observed between R_T^{DNB} 17 cm and 8cm. This is because the fast ions injected to the loss cone are immediately lost before they travel to the sight line of NPA 180 degrees apart in the toroidal direction. Figure 4 shows the confinement and prompt loss domain of E_b component ions injected by DNB in the space of pitch angle and normalized minor radius. Test particles are launched from each point of origin on the beam line with an initial velocity vector parallel to the beam direction. The full gyro-motion of the particles is

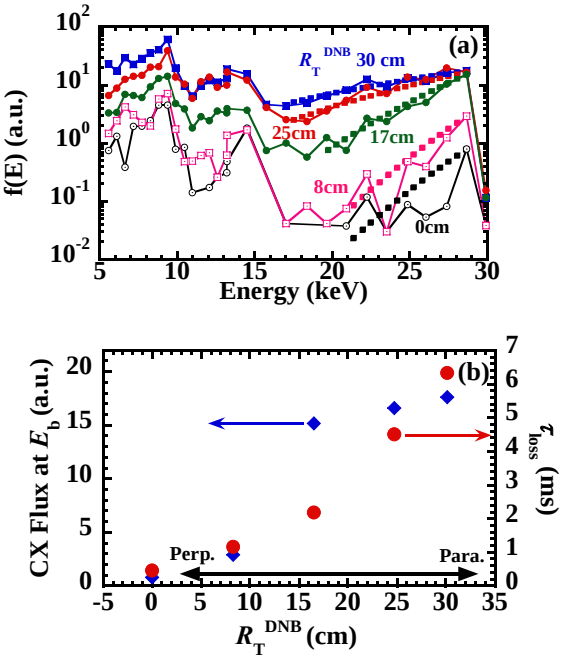

Fig. 3 *(a) Energy spectrum of each DNB injection angles. (b) DNB injection angle dependence of τ_{loss} and CX Flux Intensity at E_b*

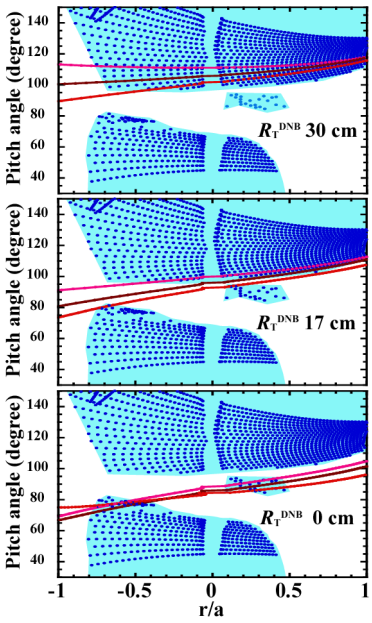

Fig. 4 *Calculated confinement/loss domain of the DNB-injected ions. The shadowd area corresponds to the confinement domain. The blank area corresponds to the prompt loss domain. The solid lines represent the beam line of DNB at each R_T^{DNB}. Center of three solid lines denotes beam path of DNB while neighbor lines show the edge of cylinder beam with beam diameter of 9.8 cm.*

tracked in a vacuum magnetic field in CHS and when a test particle intersects the vacuum vessel wall within 70 μsec, the particle is treated as lost. The loss cone boundary exists at R_T^{DNB} = 17 cm and calculated loss domain is consistent with experimental results.

3.2 R_{ax} Dependence of τ_{loss}

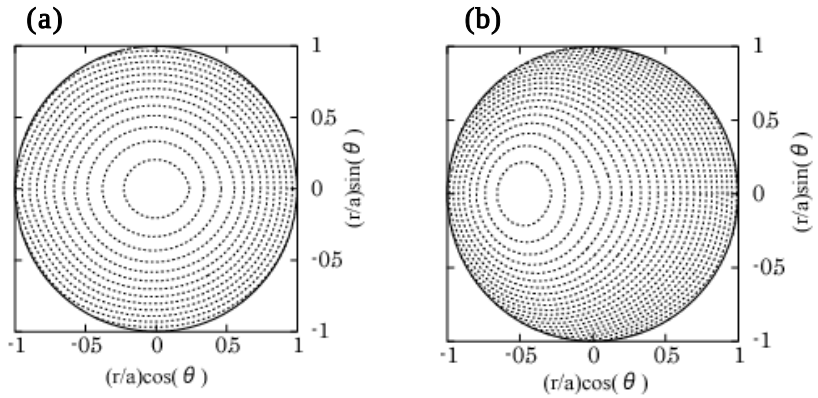

Fig. 5 *$|B_{min}|$ contours in the vacuum magnetic field of CHS. (a) Inward shifted configuration (b) Outward shifted configuration*

In CHS, confinement of collisionless trapped ion confinement depends on the magnetic field configuration. In the configuration with the strong inward shift, the distortion of $|B_{min}|$ contours from the magnetic flux surfaces is minimized (Fig. 5(a)). In this configuration, the drift motion of the helically trapped particles does not deviate significantly from the magnetic flux surfaces and good confinement of fast ions are expected. In contrast, in outward shifted magnetic field configuration, the distortion of $|B_{min}|$ contours from the magnetic flux surfaces is large and helically trapped ions crossing the magnetic flux surfaces will be lost (Fig.5(b)).

In order to investigate magnetic axis dependence of trapped ion confinement in CHS, DNB was perpendicularly injected into ECRH sustained plasma with magnetic axis position, R_{ax} of 0.87 m (inward shifted configuration), 0.92 m (standard configuration) and 99.5 cm (outward shifted configuration). In this experiment, estimated τ_{loss} is 6.33 msec for R_{ax} 88.8 cm, 3.97 msec for R_{ax} 92.1 cm and 1.21 msec for R_{ax} 99.5 cm respectively (Fig.6). This result indicates that inward shifted configuration has better confinement of perpendicularly injected energetic ions compared with that of outward shifted configuration.

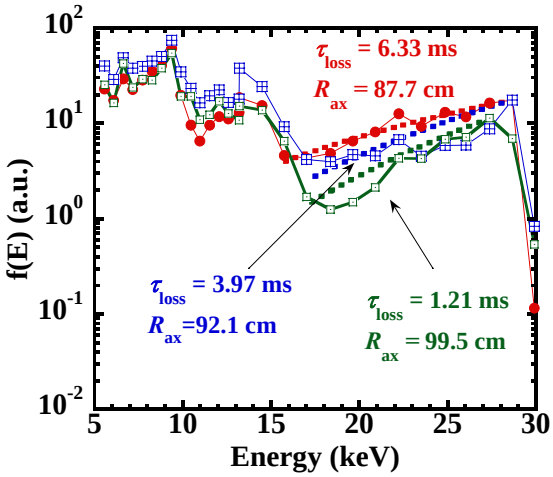

Fig. 6 *Energy spectrum of each magnetic field configurations.*

4. Summary

The behavior of energetic ions injected by DNB is studied with the NPA in CHS. The DNB injection experiments with different injection angle have been carried out to study energetic ion loss due to loss-cone. Only a few CX neutrals are observed when the DNB is injected into the loss cone region ($R_T^{DNB} < 17$ cm). This is because the fast ions injected to the loss cone are immediately lost before they travel to the sight line of NPA 180 degrees apart in the toroidal direction. The confined region in the space of pitch angle and normalized minor radius determined from measurements are consistent with that calculated with the orbit code. Then the dependence of the energetic ion loss time on magnetic field configuration is examined. Inward shifted configuration shows better confinement property of perpendicularly injected DNB ions. Estimated τ_{loss} is consistent to the previous experiment where it is deduced from the decay of DD neutron yield from beam-plasma reactions [5].

Reference

[1] S. Okamura et al., in Plasma Physics and Controlled Nuclear Fusion Research 1992 (Proc. 14th Int. Conf. Wurzburg, 1992), Vol. 2, IAEA, Vienna (1993) 507.

[2] H. Matsushita et al., Rev. Sci. Instrum. 75, 3607 (2004)

[3] J.D. Gaffey, J. Plasma Physics 16, 149 (1976)

[4] M. Osakabe et al., J. Plasma Fusion Res. 80, 971 (2004)

[5] M. Isobe et al., Nucl. Fusion 41, 1273 (2001).

Local Measurement of Energetic Particles in a Core Plasma by a Directional Probe Method

K. Nagaoka, M. Isobe, *K. Shinohara, M. Osakabe, S. Okamura, CHS group

National Institute for Fusion Science

**Japan Atomic Energy Agency*

Abstract. A directionnal probe method is applied for energetic particle measurements in outer and inside the last closed flux surface. The two experimental demonstrations have been performed in the compact helical system (CHS). One is neutral beam modulation experiment and the other is the measurement of MHD burst induced loss of energetic ions. The spatial variation of energetic particle response to MHD burst can be observed, which is considerd as a first experimental observation.

1. Introduction

Energetic particle transport is one of the most important issues for burning fusion plasmas, for example, international thermonuclear experimental reactor (ITER). In particular, the interaction between energetic particles and MHD instabilities is a key issue for energetic particle confinement. The significant enhancements of energetic particle loss due to MHD instabilities have been experimentally observed in many fusion devices, and the MHD instabilities have been strongly studied both experimentally and theoretically [1]. In these researches, it is considered that the distribution function of energetic particles is important, because the excitation of MHD instabilities is very sensitive to the distribution function of energetic particles [2]. However it is difficult to experimentally observe the spatial distribution of energetic particles in the core plasmas by conventional diagnostic tools, for example, neutral particle analyzer (NPA), lost ion probe (LIP), and so on, because of insufficient spatial resolution. In this paper, the application of directional Langmuir probe (DLP) method for energetic particle measurement is proposed in order to measure energetic particles with high spatial resolution in section 2, and the directional probe and two experimental demonstrations of this method are presented in sections 3 and 4, respectively.

2. Diagnostic Principal

A directional probe method is able to obtain deviations of the ion (electron) velocity distribution function from the dependence of ion (electron) current on the angle of normal vector of the particle-collecting surface. And it is well known as a plasma flow measurement method. However it also has sensitivity to beam component for ion and electron in case that beam component is relatively stronger than flow component, for example, toroidal plasmas sustained by tangentially injected neutral beam. In such case, the difference of the ion current measured with the angle of probe surface collecting flux flowing co-direction, I_{co}, and that flowing counter-direction, I_{ctr}, is assumed here to be proportional to the energetic ion current, I_b;

$$I_{co} - I_{ctr} \simeq I_b \qquad (1).$$

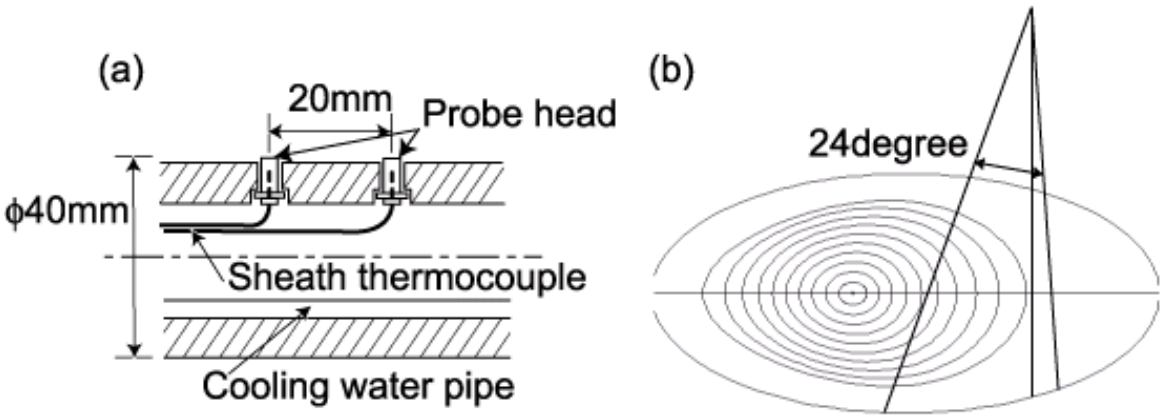

Fig. 1. (a)The schematic view of cross section of the DLP, and (b) the horizontally elongated cross section of CHS standard configuration and the area in which the DLP can scan.

The accuracy of this relation must b experimentally e confirmed by calibration for the high energy beam.

2. Experimental

A ten-channel probe array has been installed on a directional Langmuir probe (DLP), and each probe head set up a thermocouple. This probe is useful as a conventional DLP and a thermal probe measuring local heat flux (which is not mentioned in this paper). The water cooling channel is installed inside the probe and removes the heat load from energetic particles and the plasma. This probe has been vertically installed from upside in a horizontally elongated cross-section of CHS, and it can move in the directions of vertical, *z*, and major radius, *R*. The schematic and scan region of this probe are shown in Fig. (1). Moreover, this probe can be rotated along the probe axis, so measure co- and ctr-going fluxes separately. In this experiment, the probe head is negatively biased with the voltage of –120V to collect ion current. The temperature increase of the probe head is also measured as a monitor in order to prevent from melting down of the DLP, and is about 100 degree at maximum in the region of $r/a>0.8$. The scale of this probe is 40mm in diameter and the collector area of each probe tip is 4mm in diameter, so the spatial resolution of this probe is about 4mm. The sampling speed of data acquisition system is 1MS/sec and the time resolution of this probe system is <10μsec.

3. Results and Discussions

3.1. Neutral beam modulation experiment

The application of the directional probe method for energetic particle measurement has been performed using the neutral beam modulation discharges in CHS. The NBI has been injected into the co-direction and repeated turn on and off in a discharge. The DLP has been inserted in the plasmas and the co-and ctr-going ion current have been measured at $r/a= 0.84$. The modulation pattern and the probe currents are shown in Fig. 2-(a) and -(b), respectively. The co-going ion flux measured by the DLP is larger than the ctr-going one in the NBI heating phase, while the two fluxes are almost same in electron cyclotron heating (ECH) phase without NBI heating. The energetic particle flux evaluated by eq.(1) (which is shown in Fig.2-(c)) is synchronized with the neutral beam pattern and also consist with the energetic

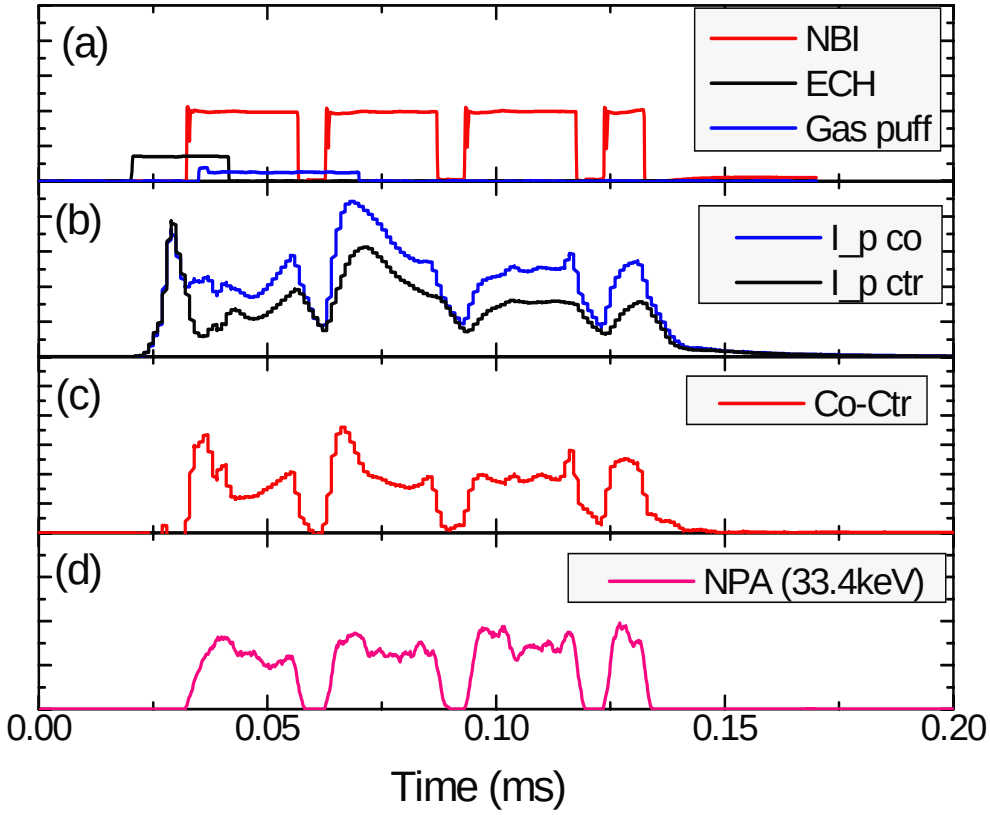

Fig.2 The wave form of neutral beam modulation experiment; (a) electron cyclotron heating and NBI heating, (b) ion currents measured by HP, I_{co} and I_{ctr}, (c) The difference of I_{co} and I_{ctr}, and (d) neutral particle flux with the energy of 33.4keV measured by a neutral particle analyzer.

particle fluxes measured by a neutral particle analyzer (the sample is shown in Fig.2-(d)). This result means that it is possible to evaluate energetic particle flux using eq.(1).

3.2. MHD burst experiment

The excitations of toroidal Alfven eigenmodes (TAE) and energetic particle mode (EPM) have been observed [3,4] and energetic particle losses synchronized with EPM bursts have been also observed by a lost ion probe (LIP) in CHS [5,6]. The energetic particle measurements by the DLP have been performed in plasmas in which EPM bursts are excited. The EPM burst I chirping down with the frequency range of 10-50kHz (The frequency range of TAE is >100kHz.) has been observed in NBI heating phase (80msec<t<180msec), and the significant increases of the co-going ion flux measured by the DLP have been also observed, while no response has been observed in ctr-going flux, which are shown in Fig.3-(a) and –(c), and each magnified figures are shown in Fig. 3-(b) and -(d), respectively. The perturbation amplitudes of the magnetic field are also shown in the magnified figures. The response of the co-going ion current is attributable to the energetic ion behavior by the EPM burst, because such response can not be observed in ctr-going one.

The responses of energetic particles to the EPM burst can be observed in wide area inside and outside of the LCFS (0.8<r/a<1.05, which is limited by the probe drive system), and is classified in two types; one is fast response in the burst glowing phase, and the other is slow response in the decay phase of the burst, which can be clearly seen in Fig. 3-(c). The fast response of energetic particle to the EPM burst can be observed only inner region of r/a<0.96,

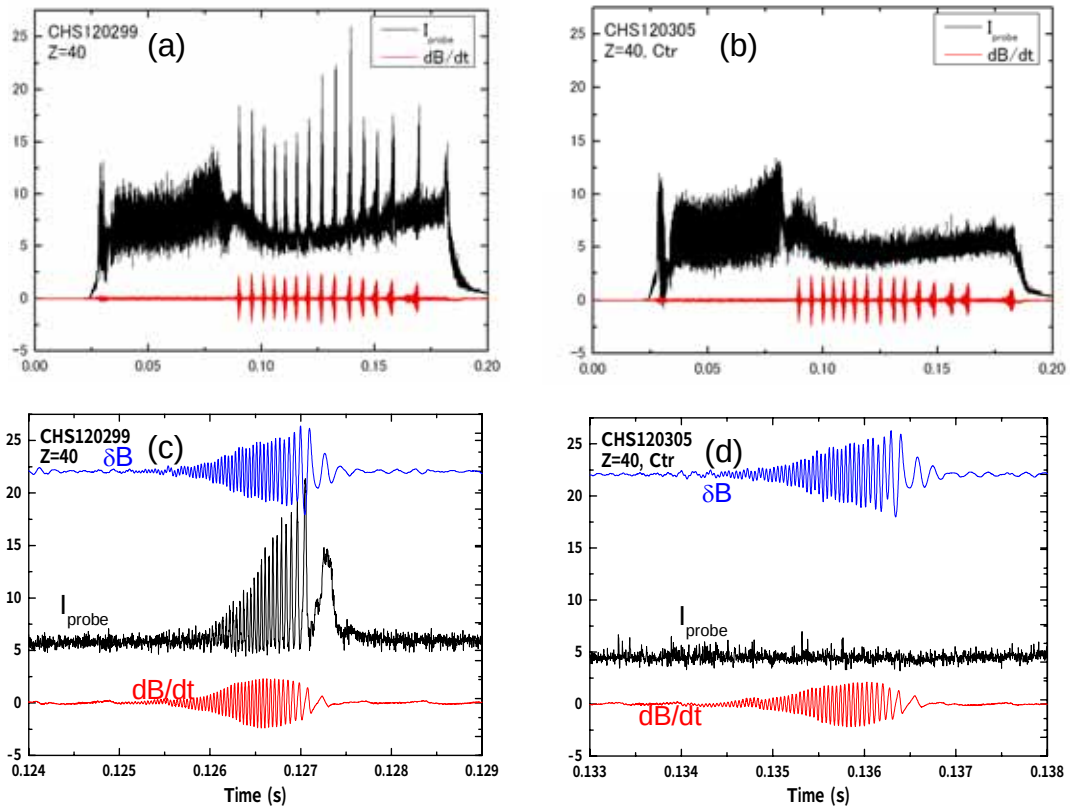

Fig.3. (a) The co- and (b) ctr-going ion fluxes measured by the DLP and magnetic field fluctuation measured by a magnetic coil. (c),(d) The magnified graphs of (a) and (b), and the amplitude of the magnetic field perturbations are also shown in (c) and (d).

and the amplitude of energetic particle flux of this fast response have a linear relation to the amplitude of magnetic field perturbation of the EPM and is also sensitive to the population of the energetic particles at the point, while further analysis is necessary for confirmation of these relation. Thus the fast response has information about distribution of energetic particle in the plasma and the eigenfunction of the EPM. The spatial profile of the fast response amplitude seems to be consistent with the EPM burst profile measured by a heavy ion beam probe [7].

On the other hand, the slow response can be observed in wide spatial area of $0.8<r/a<1.05$ and seems to be sensitive to the envelop of the burst, in particular, to that of the decay phase. The slow response of energetic particles observed by the DLP outside of the LCFS agrees well with the energetic particle loss measured by the LIP. So the spatial distribution and propagation of the slow response is significantly important for understanding the rule of energetic particle transport due to EPM bursts in toroidal fusion plasmas, which is left for future study.

4. Conclusion

In order to measure energetic particles with high spatial resolution, the application of directional probe method for energetic particle measurement was proposed, and two experimental demonstrations confirmed that this method is useful for high energy particle measurement inside the LCFS. Moreover, the new feature of energetic particles can be observed using this method, that is, the dynamic responses of energetic particles to EPMs and their spatial profile have been observed. The further investigation is necessary for understanding of energetic particle transport due to EPMs, which is left for future study.

ACKNOWLEDGEMENTS

The authors would like to thank Profs. K. Toi (NIFS), Y. Todo (NIFS) and H. Zushi (Kyushu Univ.) for fruitful discussions. This work is supported in part by a Grant-in-Aid for Scientific Research from Japan Society for the Promotion of Science, No. 15740333.

REFERENCES

[1] W.W. Heidbrink, G.J. Sadler, Nucl. Fusion **34**, 535 (1994).
[2] W.W. Heidbrink, Phys. Plasmas, **9**, 2113 (2002).
[3] K. Toi, *et al*., Nucl. Fusion, **40**, 1349 (2000)
[4] K. Toi, *et al*., J. Plasma Fusion Res. SERIES, **5**, 50 (2002).
[5] M. Isobe, *et al.*, Proceedings of 26th EPS Conf. on Contr. Fusion and Plasma Physics, **23**, 21 (1999).
[6] T. Kondo, M. Isobe, *et al*., Nucl. Fusion **40**, 1575 (2000).
[7] A. Fujisawa, *et al*., Proceedings of 16th International Conference on Fusion Energy, Vol. 2, IAEA-CN-64/C1-5 (1997).

Observation of Energetic Particle Mode by Using Microwave Reflectometer

T. Tokuzawa[1], S. Yamamoto[2], K. Kawahata[1], S. Sakakibara[1], K. Toi[1], M. Osakabe[1], and LHD Experimental Group[1]

[1] *National Institute for Fusion Science, Toki 509-5292, Japan*
[2] *Osaka University, Suita 565-0871, Japan*
e-mail of corresponding author : tokuzawa@nifs.ac.jp

Abstract
Two heterodyne reflectometer systems are utilized for the fluctuation measurement in the Large Helical Device (LHD). By using the extraordinary polarized wave, we can measure the corresponding value to the combined fluctuation with the electron density and the magnetic field in the plasma core region even if the radial electron density profile is flat. E-band system has three channels of fixed frequencies of 78, 72, 65 GHz. The system is very convenient to observe magnetohydrodynamics (MHD) phenomena such as energetic particle driven Alfvén eigenmodes, even if the system works as an interferometer mode. The detailed behaviour of the energetic particle mode is studied when low-*n* MHD burst is occurred. It seems to be caused that the spatial distribution of high energy particle is changed by such a MHD-burst. Also to know the radial distribution of MHD mode, frequency swept R-band reflectometer is applied for the first time. It seems to be successfully detected the energetic particle mode and toroidal Alfvén eigenmode.

1. Introduction

In the burning plasma energetic alpha particles enhance magnetohydrodynamics (MHD) modes such as toroidal Alfvén eigenmodes (TAEs). On the other hand MHD mode affects the alpha particle transport and changes plasma confinement. Therefore energetic particle driven MHD instability has been studying in several magnetic confinement devices [1-4]. Usually MHD phenomena are observed by magnetic probes and the excellent analytical technique is developed to know toroidal and poloidal mode number and travelling direction etc. Also theoretical analysis using three dimensional code has been developing [5]. For the comparison between the simulation code result and the experimental result, it is important to measure directly the radial distribution of these modes.

In Large Helical Device (LHD [6]) recently we have been applying two types of microwave reflectometer system for measuring the radial distribution of the fluctuation, because the microwave reflectometer has a potential of the localized measurement by using the cut-off effect in the plasma core. One system is the multi-channel heterodyne fixed frequency reflectometer [7]. Recently the real-time data acquisition system is applied with the sampling rate of up to 10 MSample/sec by using a compact-PCI based digitizer. Then it can measure the density and magnetic fluctuation in the core region during the whole plasma discharge. And another one is the frequency swept reflectometer system. When the plasma condition seems to be steady during the frequency sweeping period, the radial profile could be measured each sweep in one plasma discharge. By using these reflectometers it is quite easy to observe MHD phenomena such as energetic particle mode and Alfvén eigenmodes. In this paper we present these two reflectometer systems and some experimental results.

2. Frequency Fixed E-band Reflectometer System

E-band fixed frequency heterodyne reflectometer system is utilized for the fluctuation measurement [7]. Currently the system has three channels of fixed frequencies of 78, 72, 65 GHz. Power combined three microwaves are travelling to/from the LHD by using a corrugated waveguide for avoiding the transmission loss. The simplified super heterodyne detection technique is used for the receiver system. In LHD the real-time data acquisition system has been able to be utilized and the sampling rate is up to 10 MSample/sec by using a compact PCI based digitizer [8]. The system is very convenient to observe MHD phenomena such as energetic particle driven Alfvén eigenmodes, launching the extraordinary polarized wave. In Fig. 1 the temporal behaviours of the reflectometer signal of 78 GHz and magnetic probe signal and these power spectra are shown. Coherent spectra of around 8 and 16 kHz are caused by low-*n* mode oscillation. In the range of 100~150 kHz there are a lot of coherent

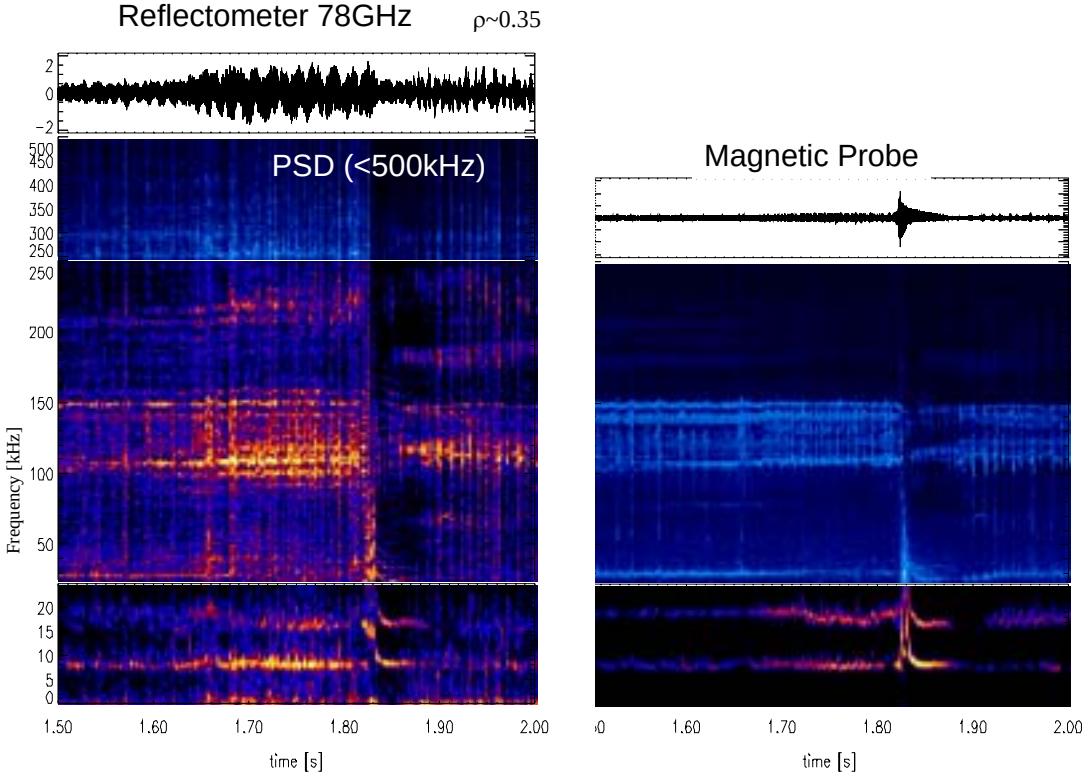

Figure 1 Time evolution of reflectometer signal and frequency spectrum (Left) and these of magnetic probe signal (right)

mode. These mode are identified the n=1 (n: toroidal mode number) TAE mode by the magnetic probe analysis. Also on the reflectometer signal it is observed higher mode around 230 kHz. Just after t=1.82s MHD-burst is occurred and TAE mode frequency components are rapidly disappeared and then passing 0.02s these mode are revived. This sudden disappearance may be caused that the distribution of high energy particle is changed by such a MHD-burst. In this experiment the birth source of energetic particle is generated by the neutral beam and this injection of neutral beam is kept constant during this phenomenon is occurred. Therefore the TAE mode is re-exited quickly and then it keeps to a next burst.

3. Frequency Modulated R-band Reflectometer System

To know the radial distribution of fluctuation there are two methods in reflectometry. One is the multi-channel system, and another is the wide band frequency source system. For the latter system, source frequency sweeps step by step in the whole frequency range. The step width is limited by the characteristic time of the desired fluctuation frequency. Of course, during the frequency modulation, the plasma condition and fluctuation level are assumed to be constant. Figure 2 shows the schematic of frequency modulated reflectometer system. The system uses voltage controlled oscillator (VCO) as a source. The output frequency of this source is easily changed by the external controlled signal. The output wave is amplified and also this frequency is multiplied by two. The reflected wave is mixed with a local wave for the heterodyne detection and IF signal is amplified and detected. Data acquisition system is the same as the previous E-band reflectometer system.

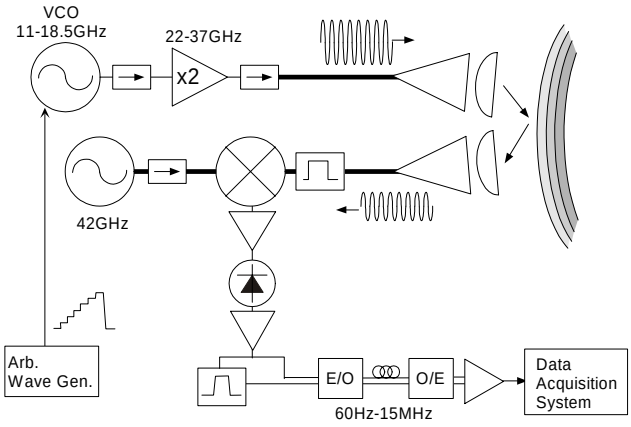

Figure 2 Schematic of FM-CW Reflectometer

The experiment is carried out that the axial magnetic field strength is 1.0 T, the averaged electron density is under $0.5 \times 10^{19} m^{-3}$, and neutral beam is injected with constant. The source frequency is swept full range every 200ms and the number of the stair step is 20. Each time of the launching frequency is 10ms and data sampling rate is 1μs, then the data

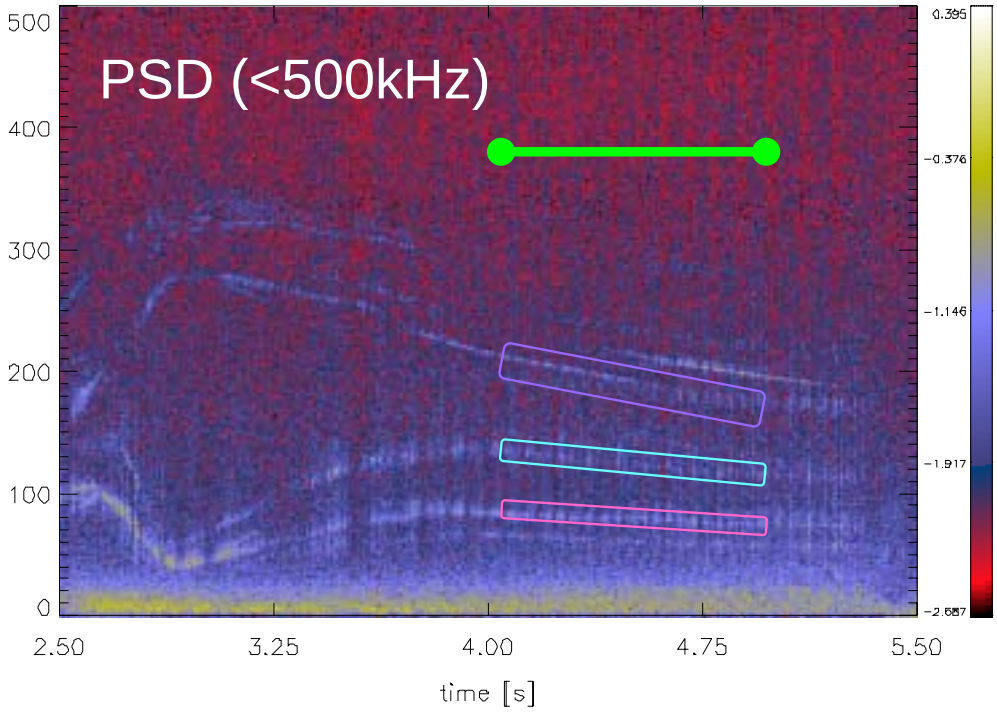

Figure 3 Frequency spectrum of interferometer mode CW Reflectometer

point is 10,000 and the frequency resolution is 100Hz. It is enough to observe the MHD phenomena such as TAE. Figure 3 shows the frequency spectrum of the previous frequency fixed 78GHz reflectometer signal. In this plasma condition there is no cut-off layer of 78GHz and this system is operated as an interferometer mode. We can see several continuous coherent frequency components. Figure 4 shows the radial profile of the fluctuation strength of the frequency swept reflectometer signal during t=4.0-4.8s (4 periods). It can be obtained that the frequency component around 200kHz is large near at ρ=0.8 and the other component around 150kHz is localized in the plasma centre. Here the meaning of the data points which are located under ρ=0 is that these frequency waves are not reflected from the plasma and they are come back from the opposite wall.

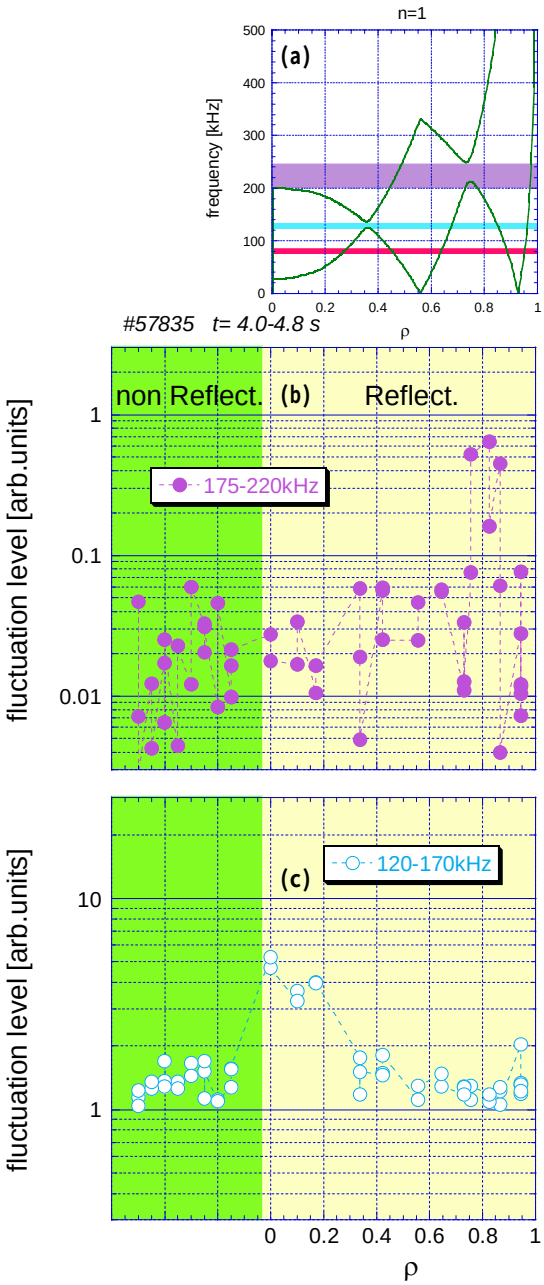

Figure 5 (a) Shear Alfvén spectra for n=1 and Radial profile of the fluctuation component of FM-CW reflectometer in the range that (b) 175-220 kHz and (c) 120-170kHz

Acknowledgements

This work was partially supported by a Grand-in-Aid for Young Scientists (B) (No.15760625, 2003) from the Japan Society for the Promotion of Science to one of the authors (TT) and also by NIFS05ULHH507 from the budget grant-in-aid of the National Institute for Fusion Science.

References

[1] S. E. Sharapov *et al.*, Phys. Rev. Lett. **93**, 165001 (2004)
[2] R. Najikian *et al.*, Phys. Rev. Lett. **91**, 125003 (2003)
[3] H. Kimura *et al.*, Nucl. Fusion **38**, 1303 (1998)
[4] S. Yamamoto *et al.*, Nucl. Fusion **45**, 326 (2005)
[5] C. Nührenberg, Phys. Plasmas **6** 137 (1999)
[6] O. Motojima *et al.*, Nucl. Fusion **43**, 1674 (2003)
[7] T. Tokuzawa *et al.*, 31st EPS Conf. P5-114 (2004)
[8] H. Nakanishi *et al.*, Fusinon Eng. Design **66-68** 827(2003).

P09

Energetic Ion Driven Alfvén Eigenmodes in High Beta Regime of the Large Helical Device Plasmas

S. Yamamoto[1)], K. Toi[2)], N. Nakajima[2)], S. Ohdachi[2)], S. Sakakibara[2)],
C. Nuehrenberg[3)], K.Y. Watanabe[2)], S. Murakami[4)], M. Osakabe[2)],
Y. Narushima[2)], S. Masuzaki[2)] and LHD experimental group

1) *Graduate School of Enginnering, Osaka University, Suita, Japan*
2) *National Institute for Fusion Science, Toki, Japan*
3) *Max-Planck-Institute fuer Plasmaphysik, IPP-Euratom Association, Greifwald, Germany*
4) *Graduate School of Engineering, Kyoto University, Kyoto, Japan*

In NBI heated LHD low density plasmas at low magnetic field (B_t < 1 T), the bulk plasma beta $<\beta_{bulk}>$ exceeds about 1 %, and calculated energetic ion beta $<\beta_{b//}>$ is comparable to $<\beta_{bulk}>$ on the assumption of classical slowing down of energetic ions. In the high beta plasmas, the bursting TAEs (toroidicity-induced Alfvén eigenmodes), of which amplitude is one order of magnitude larger than that of non-bursting ones, are often observed and appreciably affect the energetic ion transport. Moreover, HAEs (helicity-induced Alfvén eigenmodes), of which frequency is about eight times higher than that of TAEs, are also observed. In order to identify and estimate of important damping mechanisms of the observed AEs, we compared between the experimental data, such as observed mode frequency and profile, and the global mode analysis using CAS3D3. AEs can have a global mode structure and avoid the intersection of Alfvén continuum in high beta LHD plasma. We studied the observed region of AEs in parameter space, which are based on the database of AEs experiments, composed of the resonance and the stability conditions. In these studies, continuum and/or radiative damping, of which damping rate depends on the magnetic shear, is thought to be an important role in stabilizing AEs in LHD.

P10

MHD spectrum in the heliotron configurations allowing a large Shafranov shift

N.Nakajima 1), A.Fukuyama 2)

1) National Institute for Fusion Science, Oroshi-cho 322-6, Toki 509-5292, Japan
2) Kyoto University, Kyoto, 606-8501, Japan

e-mail contact of main author: nakajima@nifs.ac.jp

MHD spectrum in the heliotron configurations allowing a large Shfranov shift is considered. In such three dimensional toroidal configurations, the MHD spectrum in the stable side has many different points from that in the two dimensional axisymmetric tori, namely,

1. Helicity-induced shear Alfvén Eigenmodes [1] are theoretically expected and experimentally confirmed [2].

2. The shear Alfv'en continuum spectrum becomes discrete spectra in the high-wave-number limit by the three dimensional properties of the equilibrium quantities.

In order to clarify the whole structure of the MHD spectrum in the stable side, firstly ideal MHD spectrum with slow and fast magnetosonic branches are investigated by using the three dimensional stability code cas3d3 [3], and secondly kinetic effects on such an ideal MHD spectrum are examined by using a wave analysis module of task code [4]. Through those analyses, the similar points and different points of the ideal MHD spectra between three and two dimensional configurations will be clarified.

[1] N.Nakajima, C.Z.Cheng, and M.Okamoto, Phys.Fluids B **4**, (1992) 1115.
[2] S.Yamamoto, K.Toi, N.Nakajima, *et al.* Phys.Rev.Lett. **91**, (2003) 245001-1.
[3] C.Nührenberg, Phys.Plasmas **6**, (1999) 137.
[4] M.Honda, A.Fukuyama, *et al.*, J.Plasma Fusion Res. SERIES Vol.6, (2004) 160.

Observation of Compressional Alfven Eigenmodes in a Conventional Tokamak

W.W. Heidbrink (wwheidbr@uci.edu), M.S. Kim
University of California, Irvine
E.D. Fredrickson, N.N. Gorelenkov
Princeton Plasma Physics Laboratory
T. Rhodes, G. Wang
University of California, Los Angeles
M.A. VanZeeland
ORISE

Fast-ion instabilities with frequencies somewhat below the ion cyclotron frequency occur frequently in spherical tokamaks such as the National Spherical Torus Experiment (NSTX). NSTX and the DIII-D tokamak are nearly ideal for fast-ion similarity experiments, having similar neutral beams, fast-ion to Alfven speed v_f / v_A, fast-ion pressure, and shape of the plasma, but with a factor of two difference in the major radius. When DIII-D is operated at low field (0.6 T), compressional Alfven eigenmode (CAE) instabilities appear that closely resemble the NSTX instabilities. In particular, the mode frequencies, polarization, and beam-energy threshold are nearly identical to NSTX. CAE in high-field discharges and emission at cyclotron harmonics are also observed. As on NSTX, the basic stability properties are consistent with the idea that the instability is driven by anisotropy in the fast-ion velocity distribution and is damped predominately by Landau damping of electrons. The results suggest that these modes could be unstable in ITER.

Instabilities with frequencies f=0.4-1.1 f_{ci} are observed in most beam-heated discharges in the National Spherical Torus Experiment (NSTX). (f_{ci} is the ion cyclotron frequency.) Similar instabilities are also common in the Mega Ampere Spherical Tokamak (MAST). NSTX studies of the sub-cyclotron emission indicate that the instabilities are usually compressional Alfven eigenmodes (CAE), although some of the modes are probably global Alfven eigenmodes [1]. The phenomenology of CAEs was studied extensively in NSTX [2]. Although emission at harmonics of the ion cyclotron frequency is often observed in conventional tokamaks, emission at ~0.6 f_{ci} has never been reported. This raises the question: is sub-cyclotron emission peculiar to spherical tokamaks? Or can it occur in large-aspect ratio devices such as ITER?

Recent experiments in DIII-D show that CAE are also common in conventional tokamaks when the fast-ion speed exceeds the Alfven speed. Figure 1 shows an example from a 0.6 T discharge with modulated injection of a 80 keV deuterium neutral beam. CAE activity is also detected in some full-field (2 T) discharges, although it is less common. Phenomenologically, the instabilities in DIII-D are very similar to NSTX. The data are in qualitative agreement with the idea that the primary damping mechanism is parallel electron Landau damping, while the principal driving term is a bump in the fast-ion distribution function caused by finite orbit effects.

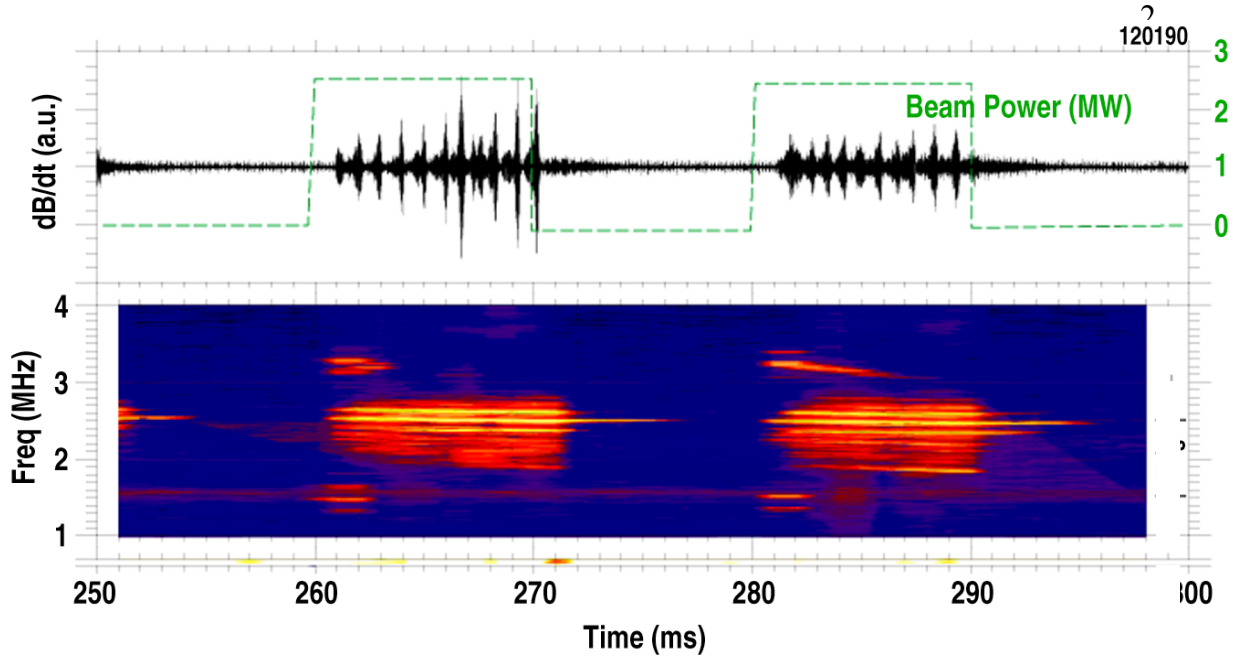

Figure 1. Magnetics signal and spectra in a low-field DIII-D discharge. The beam power is also shown.

A full-length paper on these observations was submitted to Nuclear Fusion in August 2005 [3]. Recent work is concentrating on the poloidal and radial structure of the modes. The origin of the frequency splitting is also under investigation.

References

[1] GORELENKOV, N.N., et al., Nucl. Fusion **43** (2003) 228.
[2] FREDRICKSON, E.D., et al., Phys. Plasmas **11** (2004) 3653.
[3] HEIDBRINK, W.W., et al., "Observation of Compressional Alfven Eigenmodes in a Conventional Tokamak," submitted to Nucl. Fusion (2005).

Effect of Ion Cyclotron Acceleration on Frequency Chirping Beam-Driven Instabilities in NSTX

E. Ruskov (eruskov@uci.edu), W.W. Heidbrink
University of California, Irvine
E.D. Fredrickson, D. Darrow, S. Medley, N. Gorelenkov
Princeton Plasma Physics Laboratory

The fast-ion distribution function in the National Spherical Torus Experiment (NSTX) is modified from shot to shot while keeping the total injected power at ~2 MW. Deuterium beams of different energy and tangency radius are injected into helium L-mode plasmas, producing a rich set of instabilities, including TAE modes, 50-100~kHz instabilities with rapid frequency sweeps or chirps, and strong, low frequency (10-20 kHz) fishbones. The experiment was motivated by a theory that attributes frequency chirping to the formation of holes and clumps in phase space. In the theory, increasing the effective collision frequency of the fast ions that drive the instability can suppress frequency chirping. In the experiment, high-power (~3 MW) harmonic fast wave (HHFW) heating accelerates the fast ions in an attempt to alter the effective collision frequency. Steady-frequency TAE modes excited early in the discharge are affected by the HHFW heating but there is no evidence that the chirping of 20-100 kHz modes is suppressed.

An understanding of the nonlinear dynamics of fast-ion instabilities is essential to predict the amplitude and subsequent fast-ion transport associated with alpha-driven instabilities in ITER and other burning plasmas. Some instabilities, such as the classic fishbone, have frequencies that change by a factor of two on a millisecond timescale while other instabilities, such as the TAE, have frequencies that are virtually constant on this timescale. In this paper, frequency ``chirping'' refers to large changes in frequency on a sub-millisecond timescale.

The phenomenon of rapid chirping driven by energetic particles is extremely common. The widespread nature of the phenomenon in systems with different instabilities and different energetic particle populations suggests that a generic theoretical model of the coupled wave-particle system might describe the essential features. Berk, Breizman, and collaborators have attempted to develop such a model. They explore a simplified system: the classic ``bump-on-tail'' Bernstein-Greene-Kruskal (BGK) problem of a distribution function that excites electrostatic waves. The basic idea is that the velocity-space gradient that drives the instability is analogous to the configuration-space gradient that drives fast-ion instabilities. Flattening of the distribution function in velocity space corresponds to fast-ion transport. Berk *et al.* find that several frequencies determine the nonlinear dynamics of such a system [1]. The response depends on the characteristic bounce frequency of the resonant particle trapped in the finite amplitude wave ω_B. The rate ν_{eff} that particles leave and enter the resonance region in phase space due to collisions (or other relaxation processes) affects the evolution of the system. The linear growth rate γ_L of the kinetic drive and the damping of the background plasma γ_d are also important. In their model [2], frequency chirping is associated with the formation of holes and clumps in the phase space that describes the fast-particle distribution function. When collisions are weak, these phase-space structures persist and frequency chirping is possible. When the effective collision rate is large, the structures are rapidly destroyed and no frequency chirping occurs.

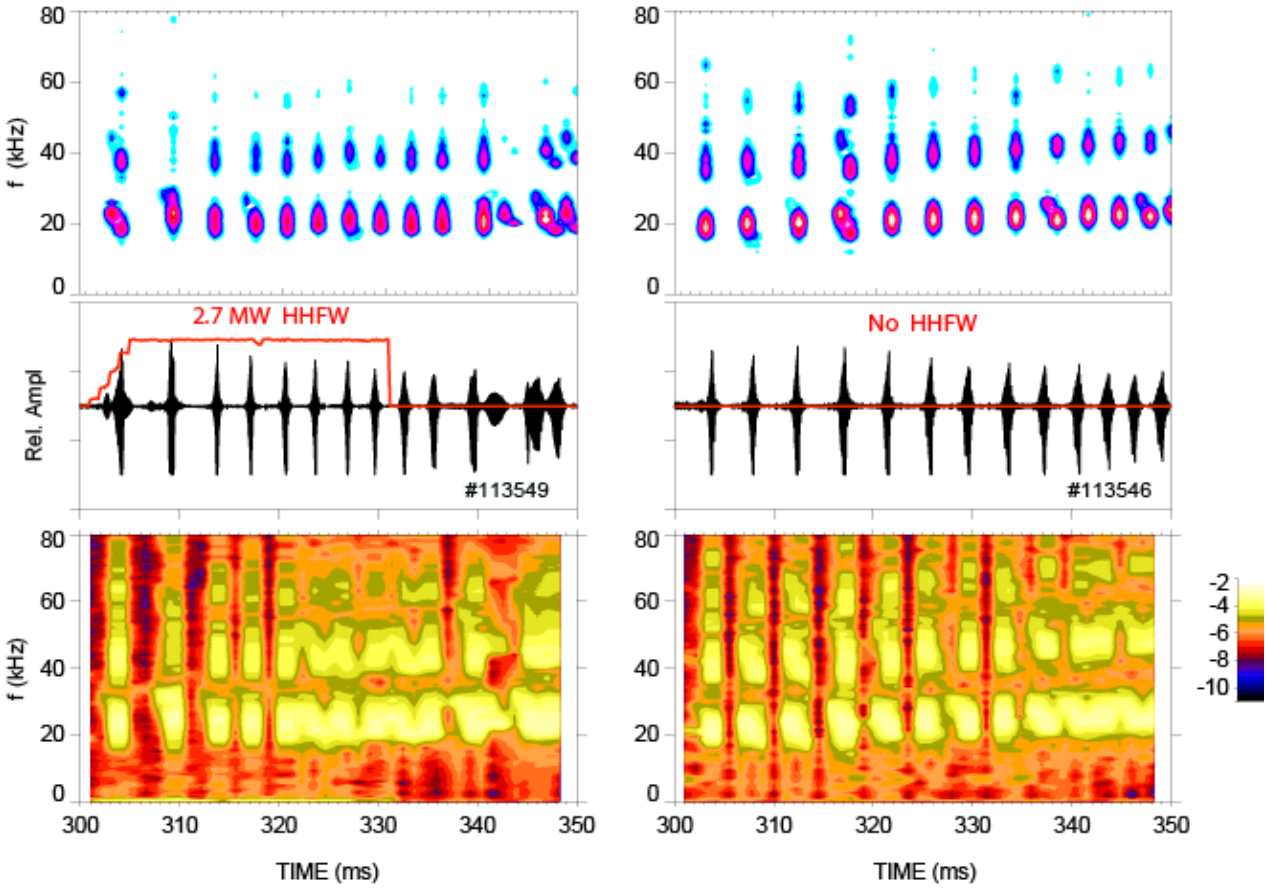

Figure 1. Magnetics spectra, raw signal, and cross power during fishbone activity for discharges with and without HHFW heating.

Recently, a detailed test of the Berk-Breizman model was performed in a dipole experiment [3]. A population of energetic electrons drove a strongly chirping interchange instablity. When electron cyclotron heating was added to increase the effective collision frequency of the resonant electrons, chirping was suppressed. Quantitative estimates of γ_L, γ_d, ω_b, and ν_{eff} explained the observations. The experiment reported here was motivated by this dipole experiment. The basic idea of the experiment was to use neutral beam injection to create chirping instabilities, then use high harmonic fast wave (HHFW) heating to increase ν_{eff} of the resonant fast ions, thereby suppressing the frequency chirping.

The results of the experiment were unexpected: HHFW had no effect on the strongest chirping instabilities. Figure 1 shows a pair of nominally identical discharges with strong fishbone instabilities. The HHFW has no detectable impact on the modes. Similarly, application of HHFW earlier in the discharge, when rapidly chirping modes in the TAE band occurred, also had no effect (Fig. 2). In contrast, application of HHFW did suppress TAE modes with steady frequencies. Also, chirping of ~ MHz GAE modes was altered by HHFW heating.

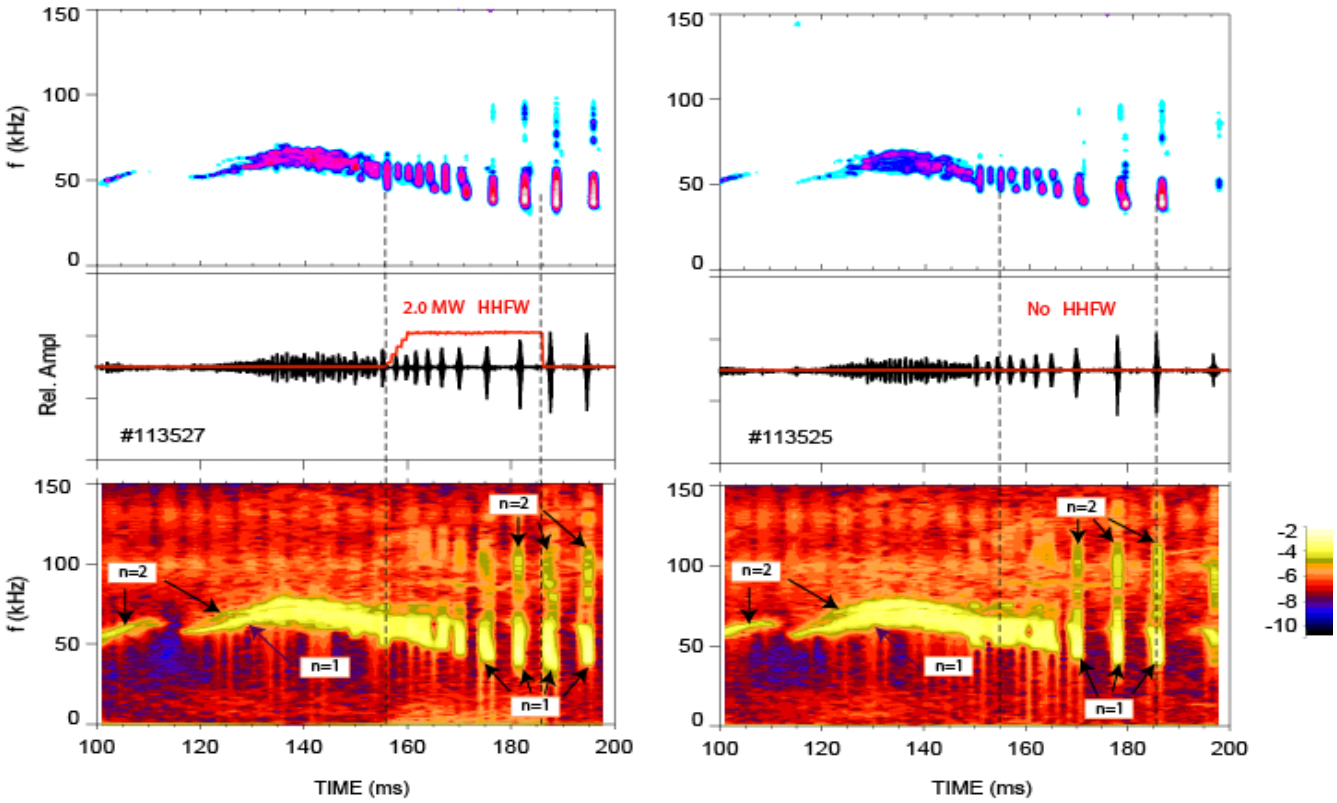

Figure 2. Magnetics spectra, raw signal, and cross power during chirping activity in the TAE band for discharges with and without HHFW heating. The toroidal mode numbers are indicated.

Neutral particle measurements show that fast ions were accelerated by the HHFW heating. Calculations suggest that the ion cyclotron waves interacted with fast ions throughout the plasma and in most of velocity space, so it is likely that the ions that resonate with the fast-ion driven instability were accelerated. Estimates indicate that the increase in ν_{eff} was more than adequate to suppress chirping if the Berk-Breizman model was applicable.

Recent calculations by Vann [4] suggest that strongly driven (called "non-perturbative" because the fast ions alter the mode structure) instabilities exhibit different frequency chirping behavior than the "perturbative" instability studied by Berk *et al*. A likely hypothesis is that the HHFW heating failed to suppress chirping of the ~20 kHz and ~50 kHz instabilities because these modes are Energetic Particle Modes [5]. In contrast, the interchange mode studied in Ref. [3] is a normal mode of the background plasma.

A full-length paper on this study will be submitted in late 2005 to the Physics of Plasmas.

References

[1] BERK, H.L., *et al.,* Phys. Rev. Lett. **68** (1992) 3563; Phys. Rev. Lett. **76** (1996) 1256.
[2] BERK, H.L., *et al.,* Phys. Plasmas **6** (1999) 3102.
[3] MASLOVSKY, D., LEVITT, B., MAUEL, M.E., Phys. Plasmas **10** (2003) 1549.
[4] R. Vann, paper presented at this conference (2005).
[5] CHEN, L., Phys. Plasmas **1** (1994) 1519.

Initial measurements of the beam ion profile in NSTX with the Solid State Neutral Particle Analyzer array

D. Liu (deyongl@uci.edu), W.W. Heidbrink,
University of California, Irvine
D. S. Darrow, S. S. Medley, A. L. Roquemore
Princeton Plasma Physics Laboratory

The Solid State Neutral Particle Analyzer (SSNPA) array on the National Spherical Torus Experiment (NSTX) utilizes silicon diodes coupled to fast digitizers to measure the energy distribution of charge exchange fast neutral particles (35~100 keV) at four fixed tangency radii (60, 90, 100, and 120 cm) to obtain the corresponding beam ion profile. Noise reduction techniques required to operate in the tokamak environment and post-shot pulse height analysis (PHA) methods are described. The results have been compared with those on the scanning E//B type Neutral Particle Analyzer (NPA) and good agreement was achieved. The redistribution and loss of beam ions during MHD activity including sawteeth events and internal reconnection events have been observed.

The initial design of the Solid State Neutral Particle Analyzer (SSNPA) array on the National Spherical Torus Experiment (NSTX) was described in an instruments paper by Shinohara *et al.* [1]. This poster highlighted recent improvements. An improved signal-to-noise ratio is obtained through fast digitization of the signal (Fig. 1). In software, the following algorithm is used to select valid pulses.

1. Find all points below a given threshold.
2. For adjacent points that exceed the threshold, locate the peak of this particular pulse.
3. Find the baseline and pulse height for each individual pulse.
4. After normalization, compare the pulse shape with the model pulse shape. If chi-squared is smaller than a specified value, accept the pulse as valid.

Initial results indicate that the SSNPA array has an energy resolution of ~ 10 keV. The diagnostic is able to detect redistribution of fast ions caused by MHD events.

A paper on recent improvements to the SSNPA diagnostic will be submitted to the Review of Scientific Instruments for inclusion in the proceedings of the 2006 High Temperature Plasma Diagnostics conference.

References

[1] SHINOHARA, K., et al., Rev. Sci. Instrum. **75** (2004) 3640.

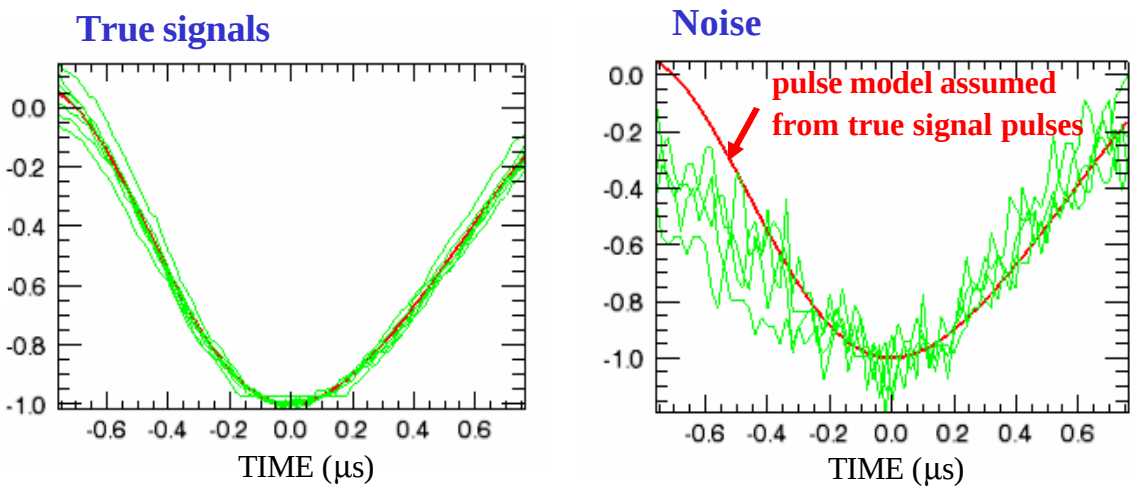

Figure 1. Normalized pulses archived by a fast digitizer. A shaping amplifier determines the pulse shape for true pulses from incident neutrals. Signals dominated by electronic noise deviate from this pulse shape.

Ripple Loss of Alpha Particles in a Low-Aspect-Ratio Tokamak Reactor

K. TANI, S. NISHIO, K. TOBITA,
H. TSUTSUI*, H. MIMATA*, S. TSUJI-IIO*, T. AOKI*
Japan Atomic Energy Agency, tani.keiji@jaea.go.jp
* Tokyo Institute of Technology

Abstract

Studies on the loss of alpha particles enhanced by toroidal field (TF) ripple in a low-aspect-ratio tokamak reactor (VECTOR) have been made by using an orbit-following Monte-Carlo code. In actual TF coil systems, the ripple loss of alpha particles is strongly reduced as the aspect ratio becomes low (the power loss $\propto A^{8.8}$ for $A \geq 2.5$) and the reduction of the number of TF coils results in a large amount of ripple loss even in a low-aspect-ratio tokamak. To reduce the number of TF coils from 12 to 6, about 40% of coil size enlargement is necessary in VECTOR. Ferrite plates are very effective to reduce ripple losses of alpha particles. By using ferrite plates, the coil size enlargement for N=6 can be relaxed to 15% and the number of coils can be reduced from 12 to 8 without enlargement of coil size in VECTOR.

1. Introduction

It has been shown in previous works that the toroidal field ripple shows a very strong decay in the plasma region in a low-aspect-ratio tokamak [1,2]. Moreover, the area of ripple-well region, the size of the ripple-enhanced banana drift and the area of stochastic orbit region are all become smaller, as the aspect ratio is reduced. By these synergetic effects, the ripple loss of alpha particles is strongly reduced as the aspect ratio becomes low (the power loss is proportional to $A^{4.3}$ for A>3) and consequently, alpha particles are well confined in a low-aspect-ratio tokamak reactor "VECTOR (the Very Compact Tokamak Reactor)" [2,3]. It has also been shown by numerical studies using an orbit-following Monte-Carlo (OFMC) code [4] that thanks to the good confinement of alphas in a low-aspect-ratio system, the number of TF coils can be reduced from 12 to 6 in VECTOR by keeping the maximum heat load due to loss alpha particles on the first wall within an acceptable level (~1MW/m^2).

These results, however, have been obtained by using a model field ripple [5]. In order to reexamine the ripple loss of alpha particles in an actual field ripple, a new code to calculate 3D magnetic field in a realistic TF coil system (Fig.1) has been developed and combined with the OFMC code. In the code, radial shift and radial expansion of coil configuration can be set by input data, radial coil expansion factor F_{exp} and radial shift R_{shft}, as shown in Fig.1. Calculations of the effect of ferrite plates on the field ripple are also available.

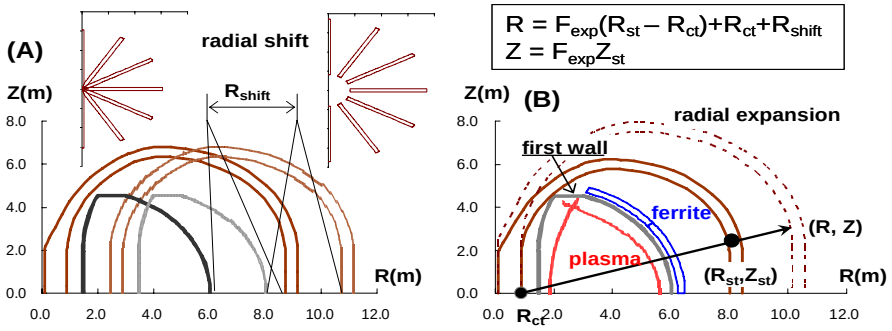

Fig.1 TF-coil system to calculate field ripple, radial shift (A) and expansion (B). Typical shapes of plasma and first wall of VECTOR are also shown in (B).

2. Reexamination of Loss of Alpha Particles in Actual Field Ripple

Qualitative studies on the ripple loss of alpha particles have been made by adopting an MHD equilibrium for a non-circular plasma [6]. Calculation parameters are summarized in Table 1 and shapes of first wall and TF coils are shown in Fig.1(B).

2-1 Dependence on the Aspect Ratio

Simulations were performed by changing the major radius only and keeping the relative positions of plasma, first wall and TF coils and the safety factor at plasma surface. Results for an actual field ripple are shown in Fig.2 (A) and those for a model field ripple (constant edge ripple γ_o =1%) are also shown in (B) for reference. The aspect-ratio dependence of the ripple loss in an acutual field ripple is much stronger ($\propto A^{8.8}$) than that in a model field ripple ($\propto A^{4.3}$) because the edge field ripple depends on A as shown in (A).

Table 1 Calculation parameters

Major radius	R_t = **3.7 ~9.2m**
Minor radius	a = 1.9m
Toroidal field @R=R_t	B_t = 3.1 T
Plasma temperature	$T_e(\Psi) = T_{e0}(1-\Psi)$
	$T_i(\Psi) = T_{i0}(1-\Psi)$
	$T_D(\Psi) = T_T(\Psi) = T_i(\Psi)$
	$T_{e0} = T_{i0}$ = 35 keV
Plasma density	$n_e(\Psi) = n_{e0}(1-\Psi)^{0.3}$
	$n_D(\Psi) = n_T(\Psi) = n_i(\Psi)$
	$n_{e0} = 2\times10^{20}$ m^{-3}
Plasma current	$j(\Psi) = j_0(1-\Psi^{1.3})$
Safety factor @Ψ=1.0	$q_a = q_s(a)$ = 2.56
Elongation	κ = 1.55
Tiangularity	δ = +0.5
Effective Z	Z_{eff} = 1.9 (uniform)
Charge number of impurity	Z_{imp} = 6.0 (carbon)
Number of TF coils	**N = 4 ~ 18**

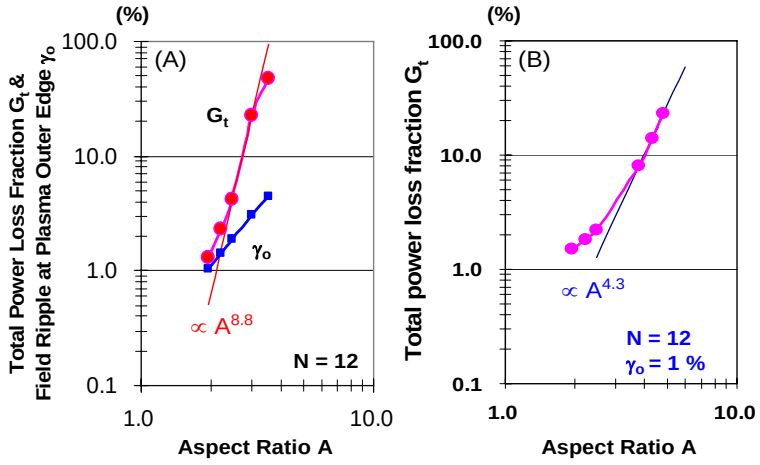

Fig.2 Dependence of the ripple loss loss of aplha particles on the aspect ratio in an acutual field ripple (A) and in a model field ripple (B).

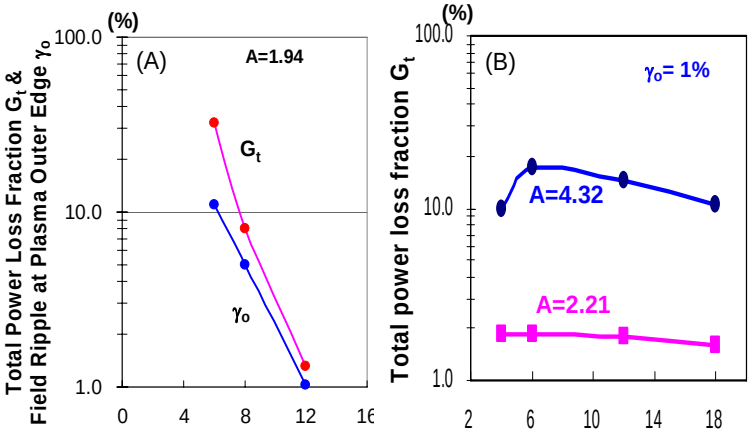

Fig.3 Dependence of the ripple loss of aplha particles on the aspect ratio in an acutual field ripple (A) and in a model field ripple (B).

2-2 Dependence on the number of TF coils

Results in an actual field ripple calculated by changing only the number of coils and keeping the safety factor at plasma surface q_a are shown in Fig.3(A). Results of the previous work for a model field ripple obtained by keeping the field ripple at outer plasma edge γ_o=1% shown in Fig.3 (B) for reference. In a realistic TF coil system, the edge field ripple strongly depends on the number of TF coils, consequently, the ripple loss is substantially increased as the number of coils is reduced.

3. Evaluation of TF Coil Parameters by 2-D Heat Load

Quantative studies on the ripple loss of alpha particles in VECTOR have been made for a realistic MHD equilibrium and an actual field ripple by adopting the same OFMC code. A bird's-eye view of VECTOR is shown in Fig.4. Shapes of the plasma and the first wall are shown in Fig.1(B). The major radius R_t=3.7m. Other parameters besides the major radius, such as the elongation, the triangularity and the plasa current are the same as those summarized in Table 1.

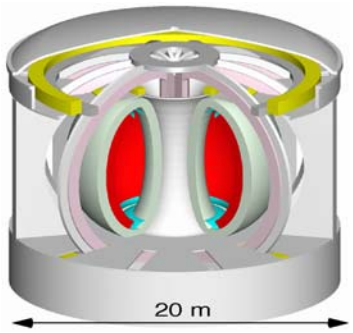

Fig.4 Bird's-eye view of VECTOR

Two dimensional distribution of the heat load due to loss particles have been evaluated by using 30,000 test particles. It took about 6 hours of CPU time by using 128 processors of SGI Altix3900.

Targets of the present work are as follows;

1. To evaluate two dimensional heat load due to loss particle,
2. To evaluate the effect of ferrite plates on the ripple loss of alpha particles, and
3. To find the minimum number and the size of TF coils to meet the allowable peak heat load.

A typical poloidal distribution of the heat load averaged over the toroidal angle is shown in Fig.5. Usually, there are three loss regions, top and bottom divertor regions and near the plsama outer edge. We concentrate our attention only on the peak near the midplane, because powerful cooling systems are ususally installed in the divertor regions.

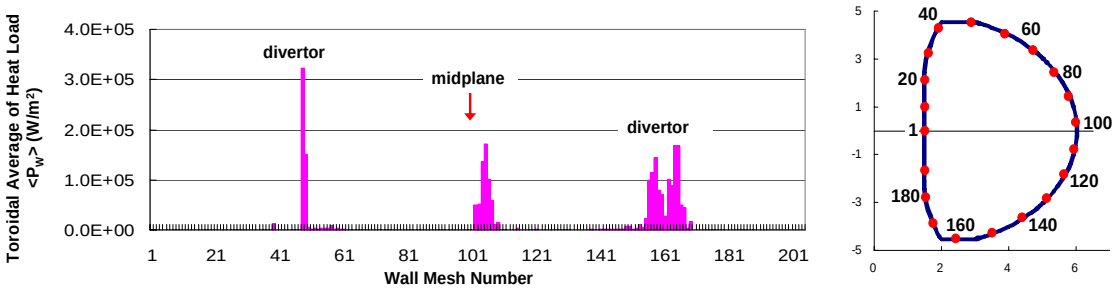

Fig.5 Typical poloidal distribution (toroidal average) of heat load on the first wall

Two dimensional heat load on an axisymmetric first wall for F_{exp}=1.2 and R_{shift}=0 with ferrite plates (0.25m thick at 0.63m from the plasma surface as shown in Fig.1(B)) is shown in Fig.6(A). The heat load is stlongly localized in both poloidal and toroidal directions. If the firs wall surface is corrugated along the magnetic field line, the heat load is substantially flattend in the toroidal

direction as shown in Fig.6(B).

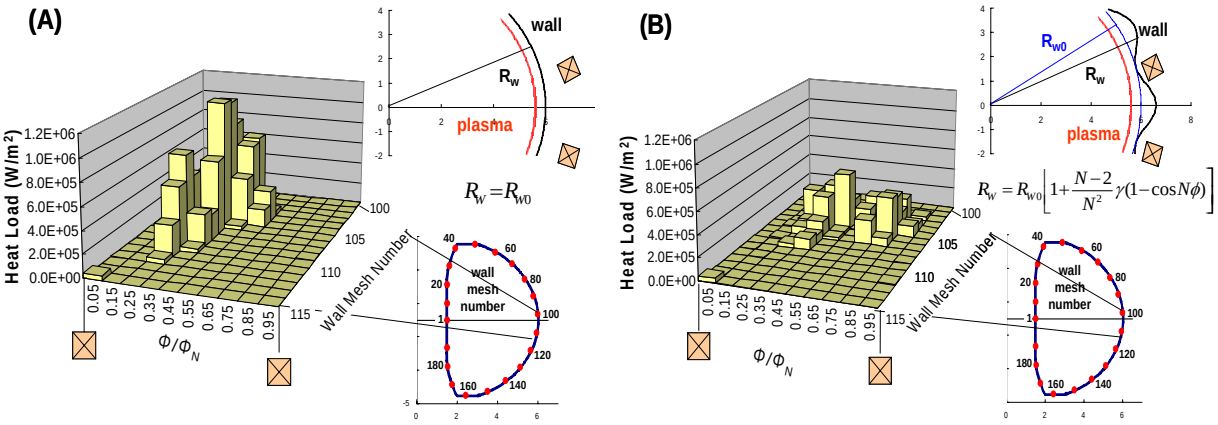

Fig.6 Two dimensional heat loads on an axi-symmetric and axi-asymmetric first wall for F_{exp}=1.2 and R_{sfift}=0 with ferrite plates.

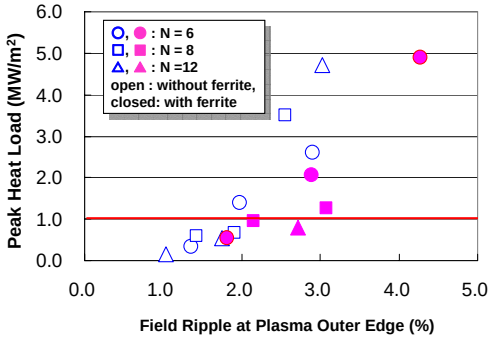

Fig.7 Peak heat load against edge field ripple for various cases.

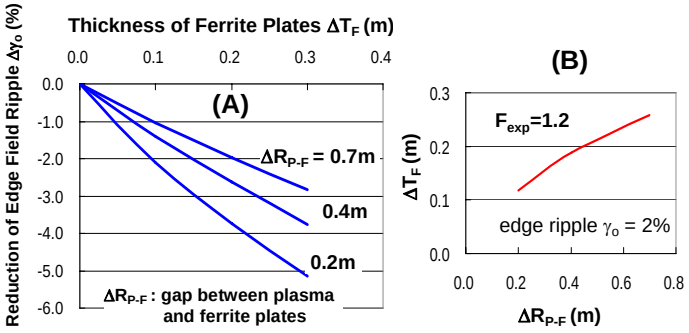

Fig.8 Reduction of field ripple by ferrite plates for various gaps between plqsma and ferrite plates against plate thickness (A) and a contour for edge ripple 2%(B).

The peak heat load against the edge field ripple is shown in Fig.7 for various cases. It is known that the allowable heat loads on the first wall is about 1MW/m^2 without cooling system [7]. Figure 7 shows that generally, allowable field ripple at plasma outer edge γ_o to meet the peak heat load less than 1 MW/m^2 is about 2.0%.

Reduction of field ripple by F82H ferrite plates for various gaps between plqsma and plates ΔR_{P-F} against their thickness ΔT_F and a ΔR_{P-F} - ΔT_F contour line of γ_o= 2% for F_{exp}=1.2 are shown in Fig.8 (A) and (B), respectively. In the calculation of field ripple with ferrite plates, a magnetization surface current $j_m(\phi) = j_m(1 + \cos N\phi)/2$ is assumed to remove higher haromonics of the field. Figure 8 shows that studies to optimize the gap ΔR_{P-F} and the thickness ΔT_F should be made in future. The higher harmonics of the field ripple might have an impact on the 2-D distribution of the heat load. These studies are left for furure works.

Finally, contours of peak heat load of 1MW/m^2 with respect to the number of TF coils N and coil expansion factor F_{exp} with and without ferrite plates (ΔR_{P-F} =0.63m, ΔT_F =0.25m) are shown in Fig.9. Even in a low-aspect-ratio system, if the number of TF coils is reduced, it is necessary to allow some enlargement of the coil size to control the edge field ripple less than 2% and consequently the ripple

loss of alpha particles. Figure 9 shows that about 40% of enlarghement of coil size is necessary to meet the requirement for the allowable peak heat load without cooling system to reduce the number of TF coils by one half (from 12 to 6) in VECOR. The enlargement can be relaxed to 15 % by using ferrite plates. It is noted that by using ferrite plates, the number of coils can be reduced to 8 without any enhancement of coil size.

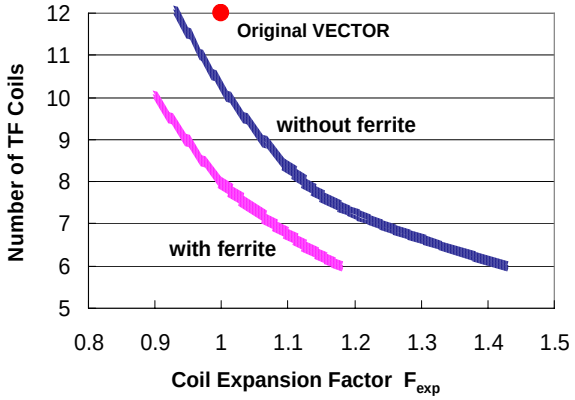

Fig.9 Contours of number of TF coils and coil expansion factor to meet peak heat load of 1MW/m^2 with and without ferrite plates ($\Delta R_{P\text{-}F}$ =0.63m, ΔT_F =0.25m)

4. Conclusions

Conclusions of the present work can be summarized as follows:

1. In actual TF coil systems, the ripple loss of alpha particles is strongly reduced as the aspect ratio becomes low (the power loss $\propto A^{8.8}$ for $A \geq 2.5$) .
2. In actual TF coil systems, the reduction of the number of TF coils results in a large amount of ripple loss even in a low-aspect-ratio tokamak.
3. Corrugation of the first wall surface along the magnetic field line is effective to reduce the peak heat load due to loss particles.
4. To reduce the number of TF coils from 12 to 6, about 40% of coil size enlargement is necessary in VECTOR. Ferrite plates are very effective to reduce ripple losses of alpha particles. By using ferrite plates, the coil size enlargement for N=6 can be relaxed to 15% and the number of coils can be reduced from 12 to 8 without any enlargement of coil size in VECTOR.

Following studies are left for future works;

1. To optimize the configuration of ferrite plates (position, thickness etc.).
2. To evaluate the effect of higher harmonics of TF ripple by ferrite plates on the peak heat load due to loss particles.

References

[1] K.Tani, et al., The 10th Spherical Tokamak Workshop STW2004, Kyoto,(2004).
[2] K.Tobita, et al., Plasma Phys. Controlled Fusion **46**, S95-S105 (2004).
[3] S. Nishio, et al., IAEA-CN-94FT/P1-21, Lyon, France (2002).
[4] K.Tani, et al., IEEJ Trans. FM, **125**, No.11 (2005).
[5] K.Tani, et al., Nucl. Fusion **23**, (1983) 657-665.
[6] K.Tani, et al., Nucl. Fusion **33**, (1993) 903-914.
[7] S.Nishio, et al., J. Plasma and Fusion Research, **78,** No.11, (2002) 1218-1230

Orbit following calculation of energetic ions for design of ferritic insertion on JT-60U

K. Shinohara, Y. Suzuki, S. Sakurai, K. Masaki, T. Fujita, and Y. Miura
Naka Fusion Research Establishment, Japan Atomic Energy Agency, Naka, Ibaraki, 311-0193, Japan
shinohara.koji@jaea.go.jp

The design work for ferritic inserts is described from the viewpoint of the behavior of energetic ions. The confinement of energetic ions and the absence of the unfavorable heat flux on the first wall was assessed by using the Fully three Dimensional magnetic field OFMC code, which was developed for a ferrite insert program in JFT-2M. In the final design, the confinement of energetic ions is improved by a factor of about 1.3 times in a particular large volume plasma with Bt_0 = 1.9T.

1. Introduction

The toroidal field (TF) ripple induces loss of energetic ions due to local mirror trapping (ripple trapped loss) and/or due to lack of the up-down symmetry of banana orbit (banana diffusion). Such enhanced transport of the energetic ions reduces the efficiency of the heating and current drive. To avoid such enhanced transport due to the ripple induced loss, installation of ferritic steel was proposed [1]. The first experiment was carried out on JFT-2M to investigate the reduction of energetic ion loss by using ferritic steel. And the reduction of NB ion loss and the compatibility of ferritic steel with high performance plasmas were demonstrated [2, 3].
Through the valuable experience and results on ferritic insert experiments on JFT-2M, ferritic insertion on JT-60U was proposed. The TF ripple reduction by the ferritic insertion is expected to contribute to the steady-state high-beta plasmas research on JT-60U, because the reduction of energetic ion loss brings: 1) enhancement of the heating and current drive "effective" efficiency, 2) extended pulse length of RF injection due to the reduced heat flux by energetic ions on antennas and, as a result, improved coupling between antennas and a plasma with a smaller gap, 3) availability of wall stabilization without losing the net heating power, and 4) possibility of enhanced availability of the rotation control to improve the MHD stability and transport.

The design work of the ferritic insertion was carried out in 2004, and its installation has finished at the summer of 2005. Here, the design work using orbit following calculations of energetic ions are described. The design work was carried out aiming at effective, machine-safe, and short-term installation. In the design work, the enhanced confinement of energetic ions and absence of the large heat flux on the first wall has been assessed for the NB ions by using the Fully three Dimensional magnetic field Orbit-Following Monte-Carlo code, which was revised from an original code [4] under the ferritic insert program in JFT-

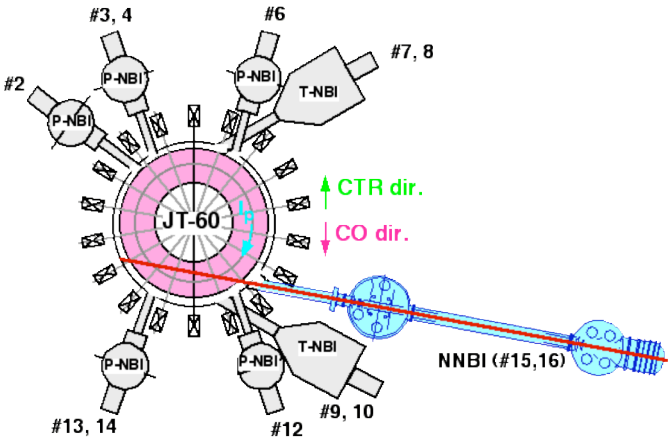

Figure 1. NB systems on JT-60U. #2,3,4,6,12,13,14 are perpendicular PNBs. #7,8,9,10 are tangential PNBs. #15,16 are tangential NNBs. Total power of PNBs is 24.75 MW, and that of NNBs is 4 MW in this calculation.

2M [2].

2. Trials and Final Design

JT-60U has eleven positive ion-based NBs (PNBs) with the injection energy of ~85keV and two negative ion-based NBs (NNBs) with the energy of 350-420 keV. On PNBs, two beams are co-tangential to the direction of the plasma current and the toroidal field, two beams are counter(ctr)-tangential, and seven beams are perpendicular. And NNBs are co-tangential.

As mentioned above, the ripple reduction is expected to bring four benefits mainly. The wall stabilization and better RF efficiency are mainly obtained in a large volume plasma. Thus, our assessment has been carried out intensively for the large volume plasma configuration. An example of the configuration is shown in Fig. 2 (E34797, t=3.8s, Bt0/Ip = 1.86T/1.1MA, β_N= 1.9, ne ~ 1.5x1019m-3). At first, the reference results, namely without ferritic steel plates (FP), are shown in Tab 1. The loss of perpendicularly injected beams is large and 63 % of the deposited power. The loss of tangentially injected beams is also not negligible. In the distribution of escaping energetic ions, most of the escaping ions hit on the first wall on the mid-plane of plasma as an orbit loss in this configuration.

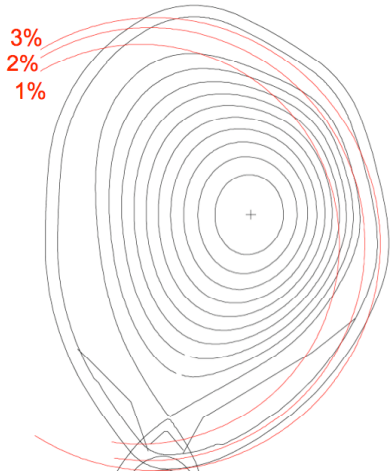

Figure 2. Shape of analyzed large volume plasma with ripple rate contour of TF coils alone.

	Absorbed power for full injection [%]	Loss power for full injection [%]	Absorbed power for perp. PNB [%]	Loss power for perp. PNB [%]	Absorbed power for co. PNB [%]	Absorbed power for ctr. PNB [%]	Absorbed power for co NNB [%]
w/o FP	54	46	40	60	73	59	75
Case I	72	28	63	37	87	67	88
Case II	72	28	63	37	87	69	88
Case III	70	30	61	39	87	68	86
Final Design	68	32	58	42	84	67	84

TABLE 1. POWER FRACTION OF NB ION DESTINATION. FRACTION IS THE RATIO TO THE DEPOSITED POWER IN PLASMA, NOT TO THE INJECTION POWER.

We used the ferritic steel with the ingredient of 8Cr-2W-0.2V [5]. This steel has a similar saturation magnetization (1.7T @573K) to F82H ferritic steel (8Cr-2W-0.2V-0.04Ta), which is a reduced-activation ferritic steel developed by JAERI [6].

We analyzed several configurations of ferritic insertion in design works. Here, results from three key configurations are shown. In these configurations, we considered only a few important limitations: 1) installation inside vacuum vessel

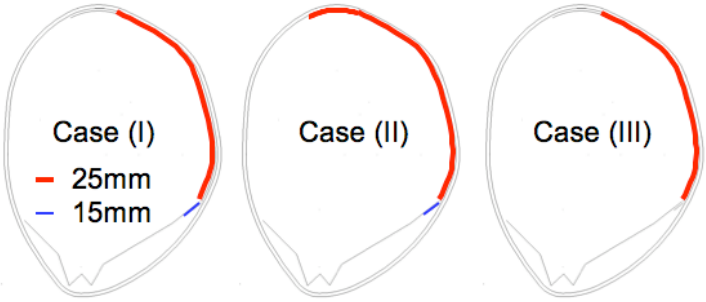

Figure 3 Trial configurations of ferritic insertion, Case (I), (II) and (III). The Note: line thickness is not proportional to the thickness of ferritic steel. The line thickness is exaggerated for illustration.

because a realistic space of its installation is not available outside the vacuum vessel. 2) plate thickness, which should be thinner than that of carbon tiles of 27mm. 3) typical port shape. Namely, detailed port shape and interference with diagnostics such as magnetic sensors was not taken into account. In these configurations, the ferritic steel was placed in 18 fold toroidal symmetry. The configurations are illustrated in Fig. 3.

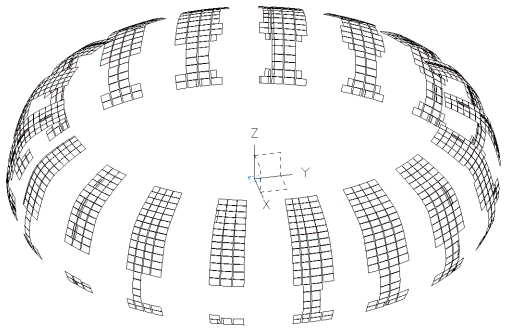

Figure 4. Bird's eye view of ferritic insertion. Thickness of FP is 23 mm

The ripple amplitude is large around the mid-plane of the vacuum vessel. In the case (I), the ferritic inserts are placed around the mid-plane as possible in order to reduce the ripple amplitude around the mid-plane. However, because of a relatively weak support structure, the region of ferritic inserts is limited on the baffle board of the divertor.

In the case (II), the ferritic inserts are added on the ceiling of the vacuum vessel. Because there is a thin region with relatively large ripple amplitude on the top of the plasma (Fig. 2), which might induce banana diffusion by affecting the excursion of banana tips. The ferritic inserts on the ceiling of the vacuum vessel can reduce the ripple in this region.

In the case (III), the ferritic steel on the baffle board of the divertor was removed compared with the case (I) because the ferrite installation on the baffle board can restrict the operation at high plasma current due to the weak support structure of the baffle board.

The simulation results for these three cases are shown in Tab 1. The differences among these three results are small, but the technical difficulty is increased in the cases of (I) and (II) compared with case (III). From these results, we decided to choose the minimum installation of case (III) as a base of a final design. In the final design, we imposed more restrictions for a realistic installation. The restrictions are: detailed port shapes, e.g. for tangential ports, the interference with diagnostics such as magnetic sensors, the opposed wall of NNB injection. As a result, the 18-fold toroidal symmetry was lost in the magnetic field. The bird's eye view of the ferritic inserts is depicted in Fig. 4. In this configuration, carbon tiles were replaced by ferritic steel on about 10% of the surface area inside the vacuum vessel. The calculation result is shown in Tab 1. Compared with the reference case without FPs, the absorbed power is increased by a factor of about 1.3 times as a whole for a full injection, and the absorbed power of perpendicularly injected beams is increased by a factor of 1.5. We also estimated the heat load on the LH antenna region. The heat load was reduced from 0.6 to 0.2 MW/m^2 in this particular discharge.

These results are encouraging for our coming experiments. Namely, because of the increases of the absorbed heating power, the MHD stability, the controllability of the current profile , and the controllability of the rotation profile, we are expecting 1) longer discharges with high β_N and high confinement for ITER hybrid scenario, 2) higher β_N beyond an ideal limit of free boundary, 3) longer discharges with high f_{BS} .

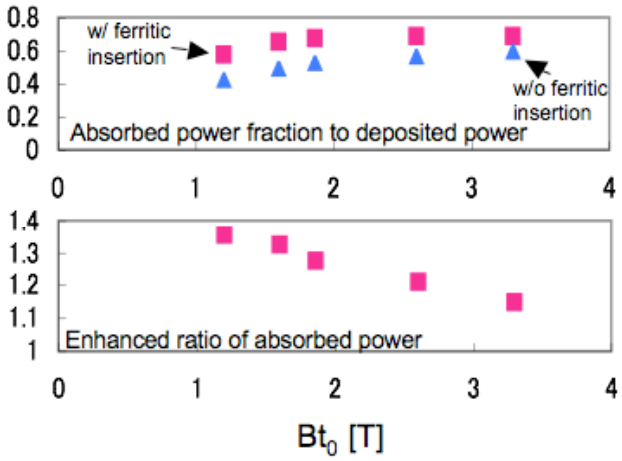

Figure 5. Variation of the absorbed power fraction for cases with and without ferritic insertion, and the ratio of the absorbed power with ferritic insertion to that without ferritic insertion.

3. Dependence on Toroidal Field

Strength

The magnetic field produced by ferritic plates is saturated in above the external vacuum magnetic field of about 0.6 T. Thus, the magnetic field produced by ferritic plates is almost constant in the typical operational toroidal magnetic field, namely > 1T, on JT-60U. This means ferritic plates might "over-cancel" the TF ripple in the lower magnetic field, and work less effectively in the higher magnetic field. It is interesting to investigate the effectiveness of the ferritic insert in the different strength of the magnetic field produced by TF coils. We have assessed the effectiveness in the magnetic field of 1.2T, 1.6T, 2.6T and 3.3T. The most of the plasma parameter is same with the case of 1.9T. The plasma current and poloidal coil current was varied, depending on the value of the toroidal field. Namely, the safety factor, q, profile is identical to the case of 1.9T. The strength of the toroidal magnetic field at R=4.4 m and Z= 0.2m are compared for these 4 cases. The ripple amplitude for 2.6 T and 3.3T is less reduced compared with the case of 1.9 T, however we can see the reduction of the ripple amplitude. In Fig. 5, the variation of the absorbed power fraction for cases with and without the ferritic insertion and the ratio of the absorbed power with the ferritic insertion to that without the ferritic insertion. The ferritic insertion is less effective for the case of 2.6T and 3.3T, compared with 1.2, 1.6 and 1.9T. Even so, the absorbed power was enhanced by about 1.2 for both the case of 2.6T and 3.3T.

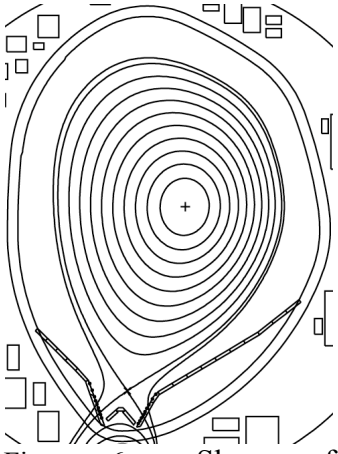

Figure 6. Shape of analyzed middle-size volume plasma

	Absorbed power for full injection [%]	Loss power for full injection [%]	Absorbed power for perp. PNBI [%]	Absorbed power for co. PNBI [%]	Absorbed power for ctr. PNBI [%]	Absorbed power for co NNB [%]
w/o FP	73	27	60	92	76	94
Final Design	81	19	73	95	78	95

TABLE 2. POWER FRACTION OF NB ION DESTINATION. FRACTION IS THE RATIO TO THE DEPOSITED POWER IN PLASMA FOR THE MIDDLE-SIZE VOLUME PLASMA.

4. Effectiveness of ferritic inserts in a middle-size volume configuration

In the large volume plasmas above analyzed, the major loss is the orbit loss around the mid-plane of the plasmas. Thus it is considered that the final design, in which most of the ferritic plates are installed above the mid-plane, is effective in the large volume plasma, however it was not obvious whether such an installation was effective even in a middle-size volume plasma, in which the ripple trapped loss appears clearly.

We have investigated the effectiveness of ferritic insertion of the final design in a middle-size volume configuration of B_{t0}/Ip=1.9T/1.1MA. The plasma configuration is shown in Fig. 6. The results of the comparison are shown in Table 2. The ferritic insert of the final design works even in the case of the middle-size configuration. Without ferritic inserts, there are heat loads on the first wall of the downward

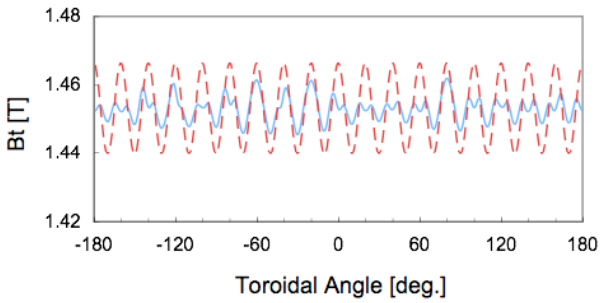

Figure 7. Toroidal variation of the toroidal field strength at R=4.25m Z=0.2

position of plasma. These heat loads come from the ripple trapped loss. With ferritic inserts the heat loads were reduced much. It is considered the ferritic plate around the mid-plane of the vacuum vessel effectively can reduce the TF ripple around the position of the plasma, where it is far from ferritic plates. Fig. 7 shows the toroidal variation of the toroidal field strength at R=4.25m Z=0.2, where is the outer edge on the mid-plane in this configuration. The TF ripple amplitude is reduced even at this position. This result is similar to the experimental results of external ferritic plate installation on JFT-2M [2].

5. Summary

For the further pursuit of the steady-state advanced tokamak research on JT-60U, the ferritic insertion was proposed to reduce the TF ripple. The ripple reduction in large volume plasmas is expected to bring 1) the improved heating and current drive "effective" efficiency, 2) the extended pulse length and the improved efficiency of the RF injection, 3) the availability of wall stabilization without losing heating power, 4) the possibility of the enhanced availability of the rotation control to improve the MHD stability and transport. This proposal of ferritic insertion is based on the successful experience under the ferritic insert program on JFT-2M. In the design work of ferritic insertion, the confinement of energetic ions and absence of the unfavorable heat flux on the first wall was assessed by using the F3D OFMC code, which was developed for a ferrite insert project in JFT-2M.
A large volume plasma of B_{t0}/Ip=1.9T/1.1MA was investigated to determine the final configuration of the installation. In the final design, the confinement of energetic ions is improved by a factor of 1.3 for the full injection. We also assessed the effectiveness dependence on the several different toroidal field strengths. Some benefits of ferritic insertion can be available to the higher Bt. A medium sized plasma was also analyzed. The ripple trapped loss was reduced and the confinement of energetic ions is improved by a factor of 1.1.

Acknowledgment

The authors would like to appreciate the JT-60 team and the JFT-2M group for their supports. We would like to acknowledge the support and useful comments of Dr. Y. Kamada of JAEA. We also would like to thank Mr. M. Suzuki of CSK Corporation for his support in the development of the F3D OFMC code.

References

[1] L. R. Turner, S-T. Wang and H. C. Stevens 1978 Iron shielding to decrease toroidal field ripple in a tokamak reactor Proc. 3rd Topical Meeting on Technology of Controlled Nuclear Fusion (Santa Fe) p 883
[2] K. Shinohara, et.al. , Nucl. Fusion **43**, 586 (2003)
[3] K. Tsuzuki, et.al., Nucl. Fusion **43**, 1288 (2003)
[4] K. Tani, et. al., J. Phys. Soc. Jpn., **50** 1726 (1981)
[5] Y. Kudo, et al. submitted to J. Korean Phys. Society.
[6] M. Tamura, et al., J. Nucl. Mater. **155–157** 620–625 (1988).

P16

Stability of the Alfven eigenmodes in JT-60U reversed shear plasmas

M. Takechi 1), A. Fukuyama 2), G. Matsunaga 1), M. Ishikawa 1), K. Shinohara 1), T. Fujita 1), T. Ozeki 1), JT-60 team

1) Japan Atomic Energy Research Institute, Naka 319-0193, Japan
2) Department of Nuclear Engineering, Kyoto University, Kyoto 606-8501, Japan.

A reversed shear (RS) plasma is potentially an efficient operation mode for steady state tokamak reactors with good confinement and a large bootstrap current fraction. However, the behavior of AEs in RS plasmas has not been systematically studied as those in PS plasmas. The stability of toroidal Alfven Eigenmodes (TAEs) in RS plasmas was first calculated by using the NOVA-K code and the results indicated that TAEs in the RS configuration are more stable than those in the PS configuration and are more stable in the RS plasma with internal transport barrier (ITB) than that without ITB. Recently, the observation of AEs with a rapid frequency sweeping and then saturation of frequency as q_{min} decreases in RS discharges can be explained by considering the properties of reversed-shear-induced Alfven Eigenmode (RSAE) near q_{min} and their transition to TAEs. AEs change from RSAEs to TAE as q_{min} decreases. It is found by the experimental results of JT-60U and the numerical calculation with TASK/WM that AE is most unstable during transition from RSAE to TAE and TAE is most stable. We investigate the stability of AEs in RS plasmas including RSAE and transition from RSAE to TAE. The *q*-profile measurement is more accurate with higher magnetic field. Therefore, the experiments for AEs destabilized by NNB in JT-60U RS plasmas were carried out with a relatively high toroidal field. To investigate the effect of *q*-profiles on AE stability, the *q*-profile is changed during NNBI by changing the ramp-up rate of plasma current and the injected power of positive neutral beams as shown in Fig. 1. The n=1 AE at the transition from RSAE to TAE is excited from t~5.85s and stabilized after changing to TAE at t~6.05s and the other n=1 TAE is observed from t~6.4s after changing PS configuration. We also systematically calculate AE stability with TASK/WM code.

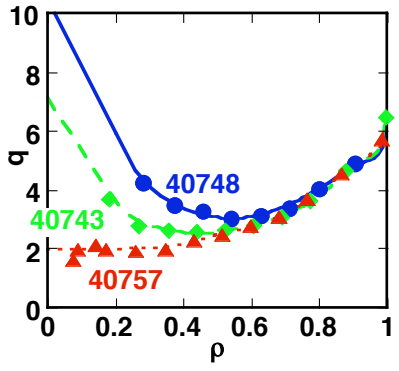

Fig. 1 The profile of safety factor when NNBI was injected.

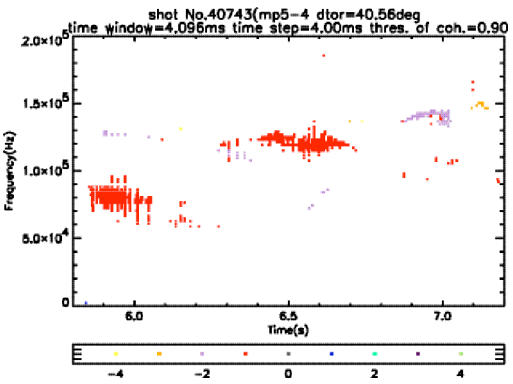

Fig. 2 The observed AE in the 40743 discharge.

Excitation of Alfven Eigenmodes using the DED Coil in the TEXTOR Tokamak

T. Shoji[1)], Y. Kikuchi[5)], A. Tsushima[2)], K. Toi[3)], N. Noda[3)], G. Matsunaga[4)]
K.H. Finken[5)], M. Jakubowski[5)], M. Lehnen[5)], O. Zimmermann[5)], R. Wolf [5)], A.G. Elfimov[6)]

1) Department of Energy Engineering and Science, Nagoya University 464-8603, Nagoya Japan

2) School of Engineering Division of Physics , Yokohama National University, Yokohama 240-8501, Japan

3) National Institute of Fusion Science, Toki-shi 509-5292, Japan

4) Japan Atomic Energy Research Institute, Ibaraki, Japan 311-0193

5)) Institute für Plasmaphysik, Forschungszentrum Jülich GmbH, EURATOM Association, Trilateral Euregio Cluster, Jülich D-52425, Germany

6) Institute of Physics, University of San Paulo, 05508-900, San Paulo, Brazil

Results from the first experiments to excite Alfven eigenmodes (AEs) in the TEXTOR tokamak plasma by using the dynamic ergodic diverter (DED) coils as an external antenna are presented. Notable features of AEs experiments using DED coils are exciting different modes around m/n=12/4, 6/2, 3/1 by changing the coil configuration, studying the effects of magnetic islands and edge magnetic fields ergodization on AEs when the rf current is applied for dc and AC DED operation, etc. The rf current of ≤ 4A with scanning the frequency 100kHz-1MHz is applied on the one of the DED coils. The coil impedance versus frequency is measured for the plasma (Ip = 350 kA, Bt = 2.25 T, n_e=2-3x10^{19} m^{-3}) with AC DED (1kHz, 1.5kA) and compared with the theoretical calculation. The excited waves are detected by the Mirnov coils installed around the torus.

1, Introduction

Weakly damped Alfven eigenmodes (AEs) excited by high energy ions such as alpha particles created by DT fusion reaction are recognized as one of important topics for confinement of alpha particles themselves in the International Thermonuclear Experimental Reactor (ITER). Due to the interaction of AEs with energetic ions, the modes become possibly unstable and the particle orbits are modified to enhance the loss and affect the ignition process in fusion reactors. Alfven eigenmodes activity driven by resonant energetic particles produced by ion cyclotron heating (ICH) and neutral beam injection (NBI) has been studied in different tokamak experiments [1, 2]. Energetic ion losses and resultant reduction of the neutron production accompanied with the appearance of toroidicity induced AEs (TAEs) have been

observed [3]. Passively excited AEs in such experiments have difficulties in studying the characteristics of the damping and stabilities of the modes due to the driving terms of NBI and ICH. The active method combining excitation by externally introduced antenna with coherent detection of proving signals at the plasma edge and core has been performed in JET [4]. We use the DED coil in TEXTOR [5] as an antenna to excite AEs and aim to investigate not only their characteristics but also the effects of edge field ergodization on AEs.

2, DED antenna system and diagnostics

The DED consists of 16 perturbation coils wrapped around the high field side of the torus (poloidal extension: 70^0) as shown in Fig. 1 and generate a perturbation field which has Fourier components having resonance near the plasma edge. The perturbation field is not only static but also rotatable in the helical direction (predominantly in the poloidal direction). The AC frequency of the field goes up to 10 kHz, and the resulting poloidal rotation velocity can exceed the diamagnetic drift at the plasma edge. A four phase current up to 15 kA on the DED coils ergodise the surface magnetic field structure.

One or two pairs of the DED coils are used as the antennas for AEs excitation. The maximum rf frequency, current and voltage induced in the coils by using the rf amplifier are 1MHz, 5A and 75V (zero to peak values), respectively. The coil set can be chosen in several ways that excite the perturbation fields of the poloidal and toroidal modes m/n=12/4. 6/2 and 3/1 (the effective poloidal mode numbers are 20, 10 and 5, respectively) by using two rf amplifiers with phasing each other. The coil inductance is ~15 μH for m/n=3/1 mode at 100kHz. The magnetic perturbation field against the total field δB/B is estimated as ~5×10^{-6} (rf current ~5A) at r/a=0.9 (q=3) for m/n=3/1. In order to estimate the antenna loading for AEs excitation, the coil current and the voltage are measured by the Rogowski coil and the capacitive pick-up (Fig. 2). The capacitive pick-up uses a thin dielectric ceramic plate for the isolation from the high voltage in the DED operation. The small rf signal can be superimposed on the large DED current to study the effects of edge field ergodization on AEs. The excited AEs fields in the plasma are measured by the Mirnov coils located at several positions in toroidal and poloidal directions.

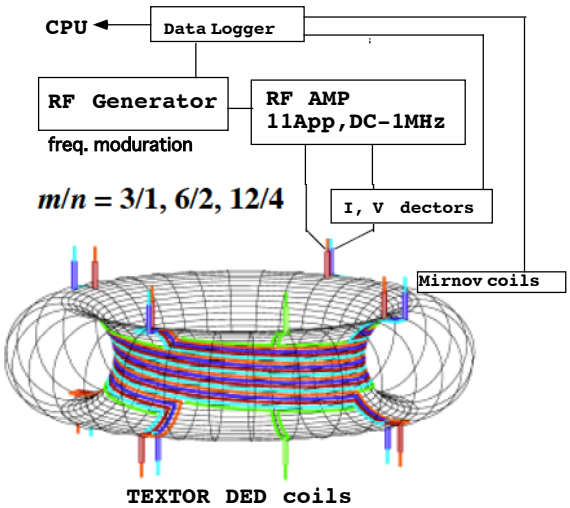

Fig. 1 DED coils and AEs antenna system

2, Coil impedance measurements

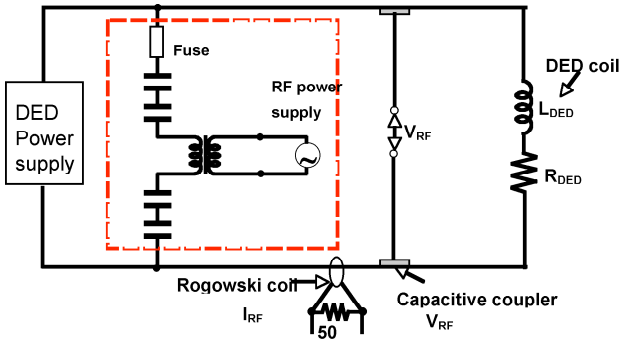

Fig. 2 Rf antenna circuit and impedance diagnostics

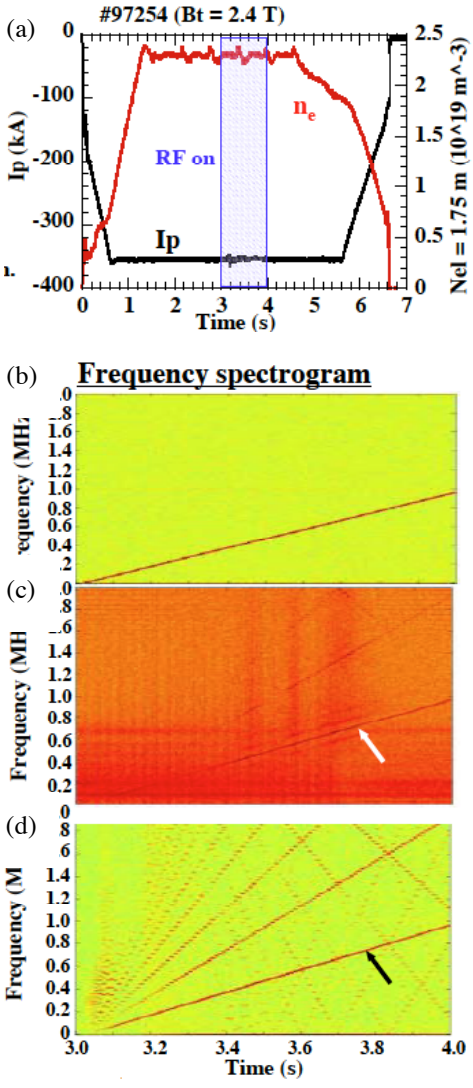

Fig. 3 (a) Ip and ne of TEXTOR shot. Frequency spectrum of rf generator (b), coil voltage (c) and current (d), respectively.

In Fig. 3, an example of the coil voltage and the current are shown for typical TEXTOR plasma discharge where toroidal field Bt, line averaged electron density ne and plasma current Ip are 2.4 T, 2.3×10^{19} m^{-3} and 350 kA, respectively. The preliminary results shown here are obtained by using the DED coil configuration of 3/1 mode. The rf current with the frequency sweeping from 100 to 300kHz in 1 sec is applied during the flat top period of the discharge (Fig. 3(b)). The frequency spectrum of voltage pick-up and current signals show the driving frequency peaks and also its higher harmonics. The voltage pick-up is more affected by the plasma noise than current one due to the high impedance detection system. We observed some high impedance peaks in the frequency spectrum which is attributed to the parallel resonance with the stray capacitance of the DED cables. When the plasma exists the real part of the coil impedance (same phase with the coil current) increases and the circuit resonance peaks become small and broader. The Mirnov coil placed almost 90 degrees away from the rf coil in poloidal direction detects the rf magnetic field perturbation during the plasma shot. The analysis on the AEs evidences in Mirnov signal is now underway.

3, Impedance measurement with DED operation

The unique feature of DED is the rotation of the magnetic perturbation. It is observed that the induction of the plasma toroidal rotation comparable to the one achieved by ~1MW of unidirectional NBI [6]. These features are expected to influence on the damping and the stability of AEs. The AC DED current is ramped up to 1.5kA (1kHz) during the plasma shot and the rf current of ~4A (the frequency is swept in 1 second) is superimposed on the DED current at almost the end of the rump as shown in Fig. 4(a). The rf signals of coil current and voltage can be still obtained under this condition with a little DED AC frequency (1kHz) modulation (Fig. 4(b)). An example of the power spectrum of the change in the coil loading resistance from the vacuum shot $\Delta r_p(\omega)$ is shown in Fig. 5. There are some peaks around 370kHz in this case. The TAE modes and the coil impedance for m/n=3/1 are calculated to compare with the experiments. The cylindrical plasma density and current profiles are assumed as $n_e=n_0(1-0.95\cdot r^2)^{1.1}$, $j_p=j_0(1-0.95\cdot r^2)^{2.5}$ which are determined from the experimental data. The profile of Alfven continuum frequency is shown

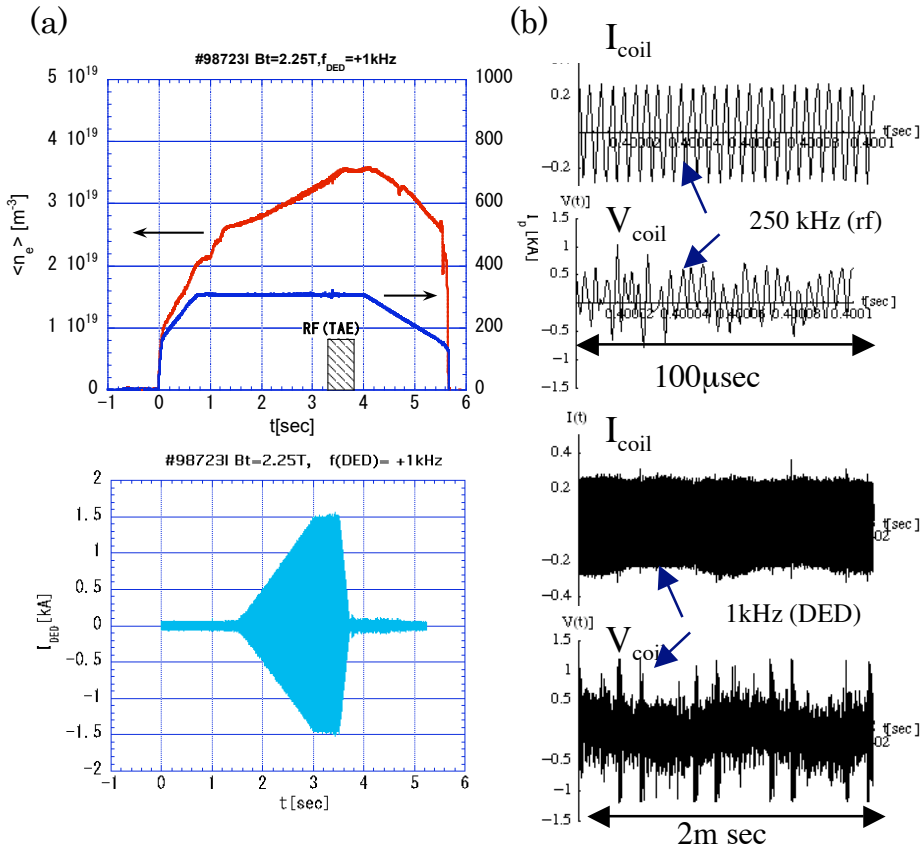

Fig. 4 (a) Ip and ne and DED current in AC(1KHz, 1.5kA max) mode, and (b) the coil rf current and Voltage signals in different time scales.

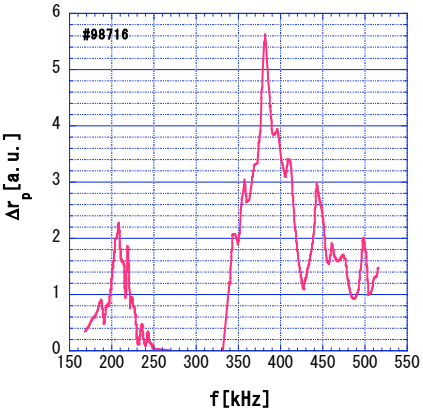

Fig. 5 Power spectrum of the change in the coil loadoing resistance from the vacuum. Bt=2.25T, <ne>= $3.2\times10^{19}m^{-3}$,I_{DED}=1.5kA, +1kHz.

for n=-1, m=1, 2, 3, 4 which are dominantly excited by the m/n=3/1 coils (Fig. 6(a)). The coil impedance has peaks around 209 kHz and 373 kHz (Fig.6 (b)). The lager is similar to the one observed in the experiment. The radial absorption profiles of the wave in these frequencies indicate that the absorption occurs at the plasma periphery region (Fig. 6(c)).

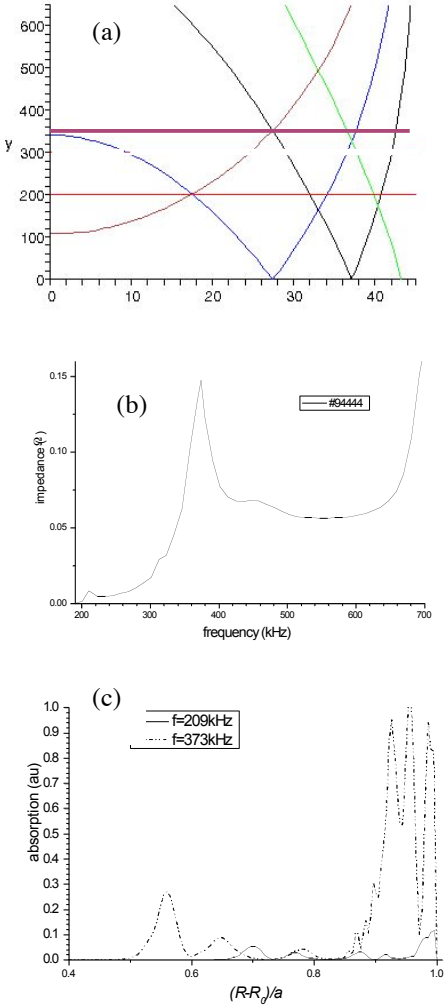

Fig.6 (a) Alfven wave continuum frequency for n= -1, m=1,2,3,4, (b) coil impedance spectrum and (c) power absorption profile. n_{e0}=3.2x $10^{19}m^{-3}$, Bt=2.25T, D_2 q_0=1.25, Ip=300kA

4, Summary

The DED coils are used as an antenna to excite AEs (TAE) and the preliminary experiment for impedance measurement has been performed with AC DED operation. The further detailed measurements are needed to investigate the effects of the active modification of the plasma periphery by DED on AEs (TAE).

5, Acknowledgement

This work was supported in part by the Grant-in-Aid for Scientific Research on Priority Areas from MEXT, No. 17044003 and 16082209.

References

[1] WONG, K.L., et al., Phys. Rev. Lett. **66** (1991) 1874

[2] ALI-ARSHAD, S., CAMPBELL, D.J., Plasma Phys. Control. Fusion **37** (1995) 715.

[3] DOUNG, H.H., et al., Nucl. Fusion **33** (1993) 749

[4] FASOLI, A., et. al., Nucl. Fusion. **35**(1995)1485.

[5] FINKEN, K. H., Special issue, Fusion Eng. Des. **37**(1997) 335

[6] FINKEN, K. H., et. al., Phys. Rev. Lett. **94**(2005)015003

Progress in the Pellet Charge Exchange Diagnostics on LHD and Local Neutral Particle Spectra Analysis

P.R. Goncharov[1], T. Ozaki[1], E.A. Veshchev[2], V.Yu. Sergeev[3], S. Sudo[1], N. Tamura[1], D.V. Kalinina[1], TESPEL Group[1] and LHD Experimental Group[1]

1) National Institute for Fusion Science, Toki, Gifu 509-5292, Japan
2) Graduate University for Advanced Studies, Hayama, Kanagawa, 240-0193, Japan
3) St.Petersburg Polytechnical University, St.Petersburg, 195251, Russia
Corresponding author's e-mail: pavel@nifs.ac.jp

Abstract

Production, confinement and thermalization of high-energy particles are the fundamental issues in fusion plasma ion kinetics. The ion distribution function $f_i(v, \theta, t)$ and its evolution under the ion cyclotron heating (ICH) and neutral beam injection (NBI) are studied by energy resolved charge exchange neutral particle flux measurements. For helical systems, such as LHD, local diagnostics are required due to the complex 3D magnetic configuration. First radially resolved measurements of local H^0 atomic energy spectra have been made on LHD by the pellet charge exchange (PCX) method with a Compact Neutral Particle Analyzer (CNPA). The diagnostic technique, the initial measurement results in the range 10-100 keV and the data analysis are described.

1. Experimental Method

An impurity cloud $r_{cloud} << r_{plasma}$ surrounding an ablating solid pellet provides a localized charge exchange target scanning the plasma radially. This is an advantageous approach to the local charge exchange neutral particle analysis [1] alternative to the use of a diagnostic neutral beam. The PCX atomic flux $\Gamma^{PCX}(E, \mathbf{r}(t))$ substantially exceeds the naturally occurring neutral flux and reflects the local plasma ion distribution function at the pellet position. Pellet-induced neutral fluxes were previously measured on LHD with a natural diamond detector [2]. However, obtaining the energy spectra from these data in the main energy range of interest (10^1-10^2 keV in the present experiments) is complicated due to the high operating speed, i.e. the spatial resolution requirement [3].

The new diagnostic presented here is based on a Compact Neutral Particle Analyzer (CNPA) [4] installed on LHD for measurements in the H_0 energy range 1 - 170 keV. CNPA employs a thin 50 Å diamond-like carbon stripping film instead of a traditional gas stripping cell to ionize the incoming neutrals, a strong permanent analysing magnet ($\gtrsim$ 1 T) sorting the resultant protons by energies (Larmor radii) and an array of 40 channel electron multipliers (CEMs) for particle detection. Pneumatically accelerated polystyrene $(-C_8H_8-)_n$ balls are injected transversally; typical D_{pel} = 500-900 μm, v_{pel} = 300-400 m/s resulting in 1-2 ms pellet flight time to the full ablation in the core plasma. The angle between the analyzer sight line and the pellet injection axis is 2° on the horizontal midplane projection and 1° in the poloidal plane. The values of the local $v_{||}/v$ for the observable particles are usually in the range -0.2 to +0.2 along the average pellet flight length.

The operating count rate C in PCX experiments is dictated by the desired radial resolution $\delta l \lesssim 10^{-1}\,\mathrm{m}$, the pellet velocity v_{pel} and the minimum statistically acceptable number of counts per one spectrum $N \approx 10^3$. Therefore, the analyzer should be able to process $C \gtrsim N v_{pel}/\delta l \approx 10^7\,\mathrm{s}^{-1}$. For such high particle fluxes CEMs can be used in the current mode in addition to the pulse counting mode. CEM signals are fed to two independent counting and current mode electronic sections Thus, the system is suitable for both passive measurements of naturally occurring neutrals and the active probing with a diagnostic pellet.

2. Initial Measurement Results

A clear response of the neutral fluxes to the diagnostic pellet injection has been observed and the energy spectra of PCX neutrals have been obtained with CNPA. The CEM current signals were recorded with 100 μs time resolution. The measurable energy range was 10 – 100 keV (due to 16 of 40 channels initially available). Ar/He plasma-forming gas was used. The experimental conditions and the obtained energy resolved pellet-induced neutral fluxes are summarized in Fig. 1 illustrating the heating time diagrams and the general discharge waveforms. The left side corresponds to D_{pel} = 834 μm, v_{pel} = 385 m/s pellet injection in the steady state of H minority ICH sustained plasma at R_{ax} = 3.6 m, β = 0.09%. The right side corresponds to D_{pel} = 867 μm, v_{pel} = 400 m/s pellet injection in the steady state of compensated tangential H^0 NBI heated plasma at R_{ax} = 3.8 m, β = 0.23% (unbalanced NBI is likely to cause the pellet trajectory deviation and thus is objectionable for PCX measurements).

The diagnostic pellet injection time corresponds to the spike on the total radiation power curve for each discharge. The millisecond-range pellet ablation time intervals are expanded on the lower two plots showing Hα light intensity from the pellet cloud at 656.3 nm and the synchronous increase in the CEM current signals reflecting the neutral particle flux. Different curves on the lower plots correspond to different energy channels. Fig. 2 shows the measurement geometry calculation for the ICH heated plasma discharge. This is required to recalculate the time into the effective radius and to interpret the observed particle pitch angles.

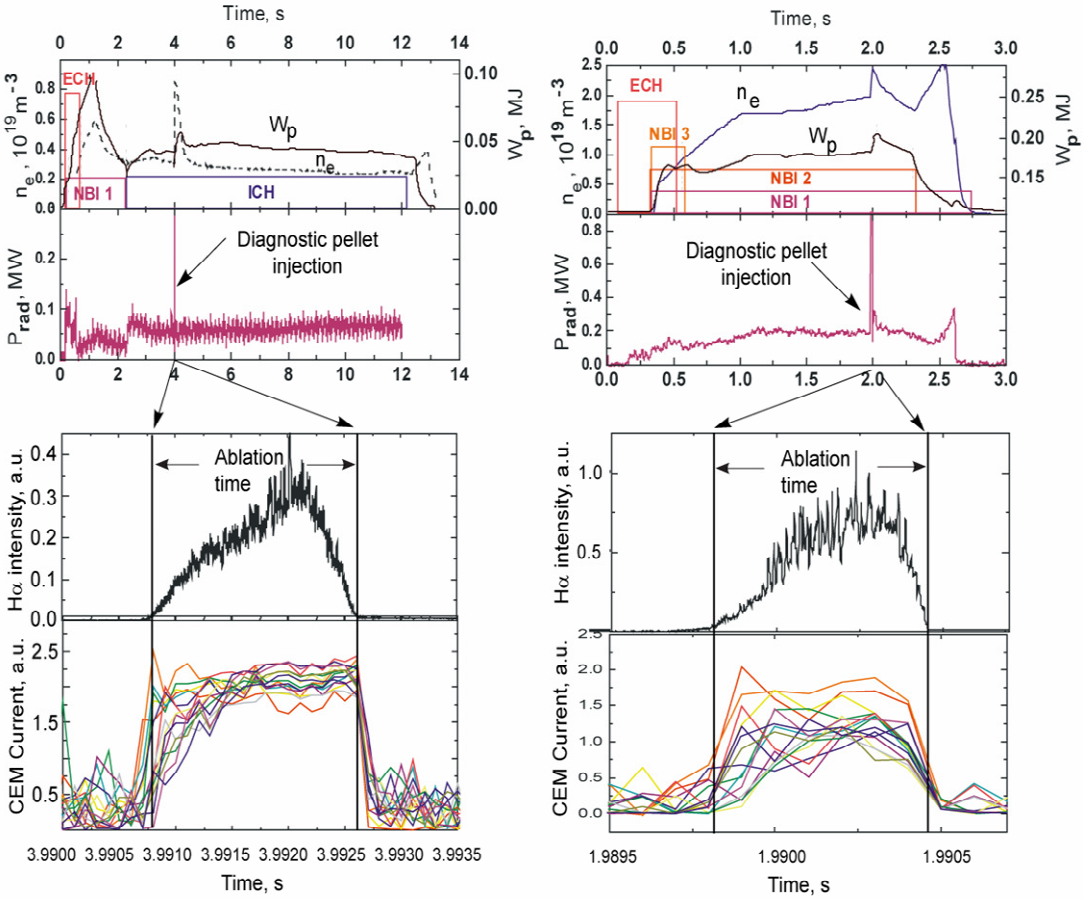

Fig. 1. Energy resolved H^0 fluxes synchronous with the visible light from the diagnostic pellet injected into H minority ICH sustained $n_e = 0.4\times10^{13}$ cm^{-3} Ar/He plasma (left) and H NBI sustained $n_e = 2\times10^{13}$ cm^{-3} Ar/He plasma (right).

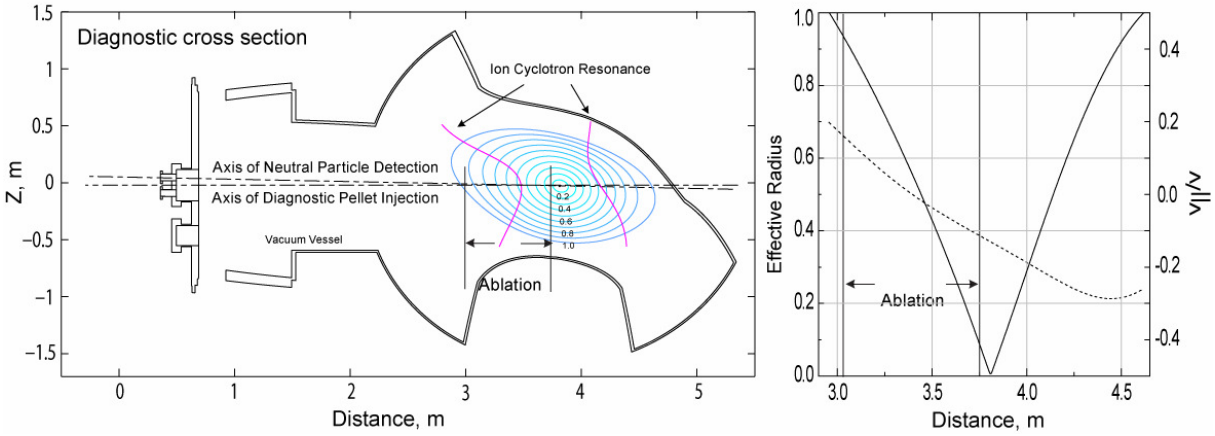

Fig. 2. Range of the radial scan of ICH plasma by the D_{pel} = 834 μm, v_{pel} = 385 m/s diagnostic pellet (ablation region) and observable particle pitch angle cosines at R_{ax} = 3.6 m, β = 0.09%.

3. Data Analysis

The naturally occurring neutral flux $I^{\theta}(E, t)$ depends on the charge exchange target density profile and is calculated as a superposition along the diagnostic sight line expressed by an integral equation with respect to the local neutral source function [5]. The PCX atomic flux $I^{PCX}(E, \mathbf{r}(t)) >> I^{\theta}(E, t)$ originates from a localized source and thus one only needs to correct it for all energy-dependent factors to obtain the local ion distribution function.

First, the CEM signals $S(E, t)$ should be corrected for the known detection efficiencies at the corresponding energies since $S(E, t) = \kappa(E) I^{PCX}(E, \mathbf{r}(t))$. The obtained PCX atomic flux itself is expressed as [2]

$$\Gamma^{(PCX)}(E,\mathbf{r}(t)) = \frac{S_a S}{4\pi L^2} e^{-\tau(E,L)} F_0(E)\, n_i(\mathbf{r}(t))\, \mathrm{v}_i f_i(E,\mathbf{r}(t)) \tag{1}$$

where the geometric factor contains the aperture area S_a, the visible area of the pellet cloud S and the distance to the cloud L; the exponent accounts for the attenuation of the neutral flux in the plasma on the way out to the periphery; $F_0(E)$ is the neutralization factor in the pellet ablation cloud; $f_i(E, \mathbf{r}(t))$ is the local ion distribution function in the plasma. $F_0(E)$ can be calculated from the ionization-recombination balance in the cloud [6]:

$$F_0(E) = \frac{1-\exp\left(-\left(\sigma_{0\to1}(E)+\sigma_{1\to0}(E)\right)\cdot S_n\right)}{1+\sigma_{0\to1}(E)/\sigma_{1\to0}(E)} \approx \frac{1}{1+\sigma_{0\to1}(E)/\sigma_{1\to0}(E)} \tag{2}$$

where $\sigma_{1\to0}$ and $\sigma_{0\to1}$ are hydrogen neutralization and ionization total cross-sections in the cloud respectively and S_n is the line-integrated cloud density (across the cloud). If this value is high enough, the approximate formula can be used. Thus, the knowledge of the cloud density and the dominating ion charge states in the cloud during the pellet flight is required as well as the experimental data or theoretical estimations of the relevant charge exchange cross-sections. For a polystyrene $(-C_8H_8-)_n$ pellet the relevant elementary processes are:

$$H^+ + C^{k+} \to H^0 + C^{(k+1)+},\quad H^+ + H^0 \to H^0 + H^+$$

and $H^0 + C^{k+} \to H^+ + C^{(k-1)+}$.

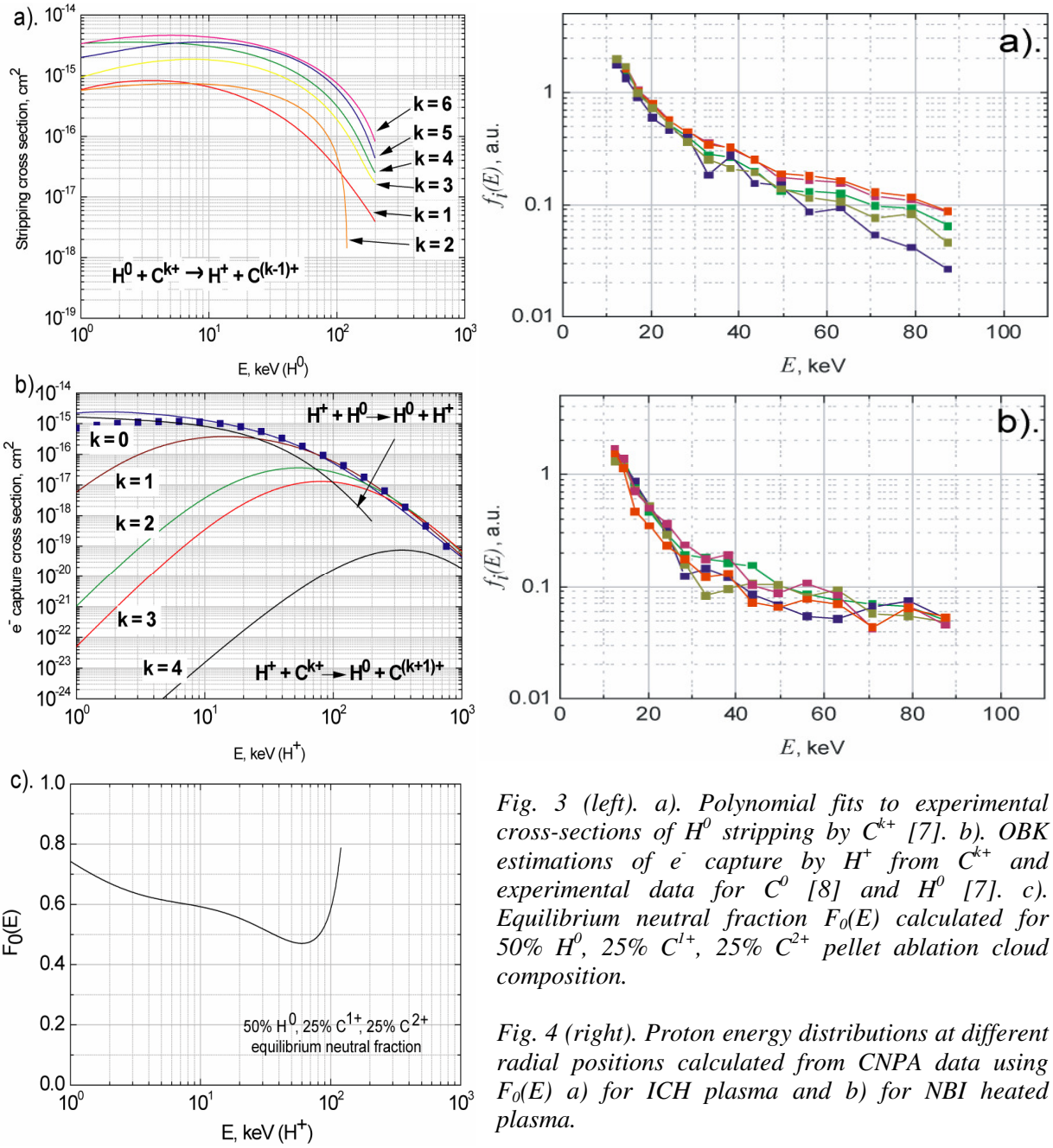

Fig. 3 (left). a). Polynomial fits to experimental cross-sections of H^0 stripping by C^{k+} [7]. b). OBK estimations of e^- capture by H^+ from C^{k+} and experimental data for C^0 [8] and H^0 [7]. c). Equilibrium neutral fraction $F_0(E)$ calculated for 50% H^0, 25% C^{1+}, 25% C^{2+} pellet ablation cloud composition.

Fig. 4 (right). Proton energy distributions at different radial positions calculated from CNPA data using $F_0(E)$ a) for ICH plasma and b) for NBI heated plasma.

The experimental stripping cross-sections for H^0 by carbon ions are available [7] as well the very well known hydrogen charge-exchange cross-section. However, the cross-sections of the electron capture by H^+ from carbon have only been experimentally determined for C^0 [8]. Therefore, Oppenheimer-Brinkman-Kramers approximation [9] has been used to estimate them. The cross-sections that contribute to $\sigma_{1\rightarrow 0}$ and $\sigma_{0\rightarrow 1}$ are shown in Fig.5 a) and b). The ion charge state composition of the pellet cloud has not been experimentally characterized. The assumption made to calculate the neutral fraction is 50% H^0, 25% C^{1+}, 25% C^{2+}. The resultant equilibrium $F_0(E)$ is shown in Fig. 3 c). The PCX atomic flux attenuation was assumed to be negligible.

The obtained $F_0(E)$ allows one to calculate the ion distributions from the measured escaping neutral energy spectra. Fig. 4 shows $f_i(E)$ at different radial positions.

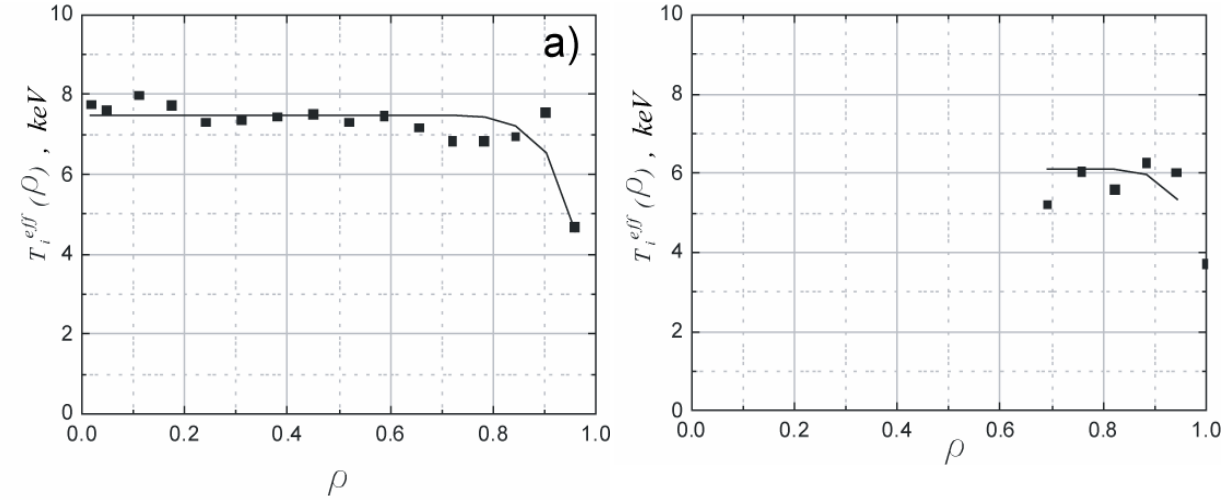

Fig. 5 (left). Radial profiles of effective H^+ ion temperature in ICH plasma a). in the lower energy range and b) in the upper energy range.

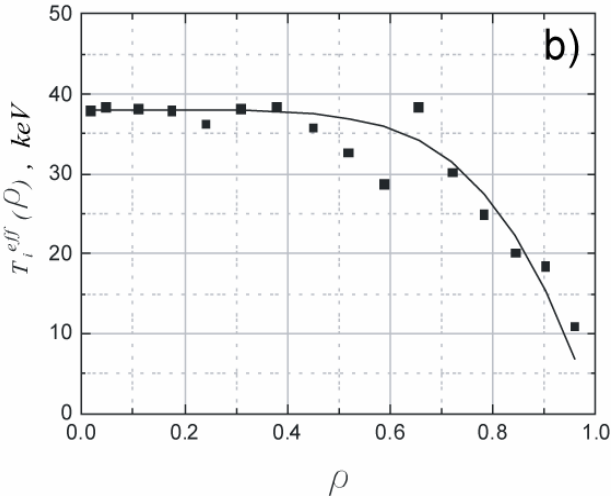

Fig. 6 (right). Radial dependence of effective H^+ ion temperature in NBI heated plasma (lower energy range).

The lower energy distributions below 25 keV are attributed to the thermalized proton population. The high energy tails from tangential NBI heated plasma correspond to the particles that have undergone a significant pitch angle scattering. These tails at different ρ depend on the NBI source function, i.e. the initial NBI particle angular distribution. In the energy range corresponding to thermalized protons from ICH and NBI and also for high energy tails from ICH an effective temperature is defined as $T_i^{eff}(\rho) = -1/k(\rho)$ where $k(\rho)$ is the logarithmic slope of $f_i(E)/\sqrt{E}$. Fig. 5 shows the effective proton temperature radial profiles calculated from the thermalized particle energy range (a) and also from the high energy tails (b) in ICH plasma. Fig. 6 shows T_i^{eff} radial dependence calculated from the thermalized NBI particle energy range. The simple polynomial fits (solid curves) on all plots have the form $T_i^{eff}(\rho) = T_i^{eff}(0)\left(1-\rho^{\alpha}\right)^{\beta}$.

References

[1] FISHER, R.K., LEFFLER, J.S., et al., Fusion Technol., **13** (1988), 536.
[2] GONCHAROV, P.R., SAIDA, T., et al., Rev. Sci. Instrum., **74** (2003), 1869.
[3] GONCHAROV, P.R., OZAKI, T., et al., Rev. Sci. Instrum., **75** (2004), 3613.
[4] CHERNYSHEV, F.V., AFANASYEV, V.I., et al., Instr. and Exp. Tech., **47** (2004), 214.
[5] GONCHAROV, P.R., LYON, J.F., et al., J. Plasma Fusion Res. Series, **6** (2003), 314.
[6] SERGEEV, V.Yu., et al., Proc. 29th EPS Conference on Plasma Physics and Controlled Fusion, ECA vol. **26B**, P-2.120 (Montreux, 2002).
[7] BARNETT, C.F., Ed., Atomic Data for Fusion, ORNL-6086, USA (1990).
[8] STANCIL, P.C., GU, J.P., et al., J. Phys. B: At. Mol. Opt. Phys. **31** (1998) 3647.
[9] MAPLETON, R.A., Theory of Charge Exchange, John Wiley & Sons, New York (1972).

Application for Plasma Diagnostics with D(α,γ)^{6}Li Gamma-ray

Kentaro Ochiai[1], Naoyoshi Kubota[1], Akira Taniike[2], Akira Kitamura[2], Takeo. Nishitani[1]

[1]Japan Atomic Energy Research Institute, Tokai-mura, Naka-gun, Ibaraki 319-1195, Japan
[2] Department of Environmental Energy Science, Faculty of Maritime Sciences, Kobe University

Introduction

The gamma ray measurement from fusion plasma is one of the important techniques to clarify fast ion properties in plasma. Some observation of the gamma-ray in JET plasma was reported. ^{12}C(d,pγ)^{13}C and ^{9}Be(α,nγ)^{12}C reactions on the JET observation are mainly recommended as the actual prospective nuclear reaction on the gamma-ray measurement [1]. However, it is thought that the gamma-ray observation by means of these reactions significantly depends on the conditioning (i.e. densities of the beryllium and carbon in plasma). Therefore, it is also important to examine the availabilities concerning the methods of gamma ray. We have tried to measure the 2.18 MeV gamma ray of D(α,γ)^{6}Li reaction and the properties of the another gamma ray emission by MeV-He^{++} beam irradiation experiment.

Irradiation experiment and gamma ray spectroscopy

We carried out the irradiation experiment to measure the gamma spectroscopy induced by He^{++} beam. Figure 1 shows the schematic view of the irradiation experiment. Tandem van de Graaff accelerator (5SDH-II) in Kobe University was used. A deuteride polystyrene (C_6D_6) thick target was implanted with He^{++} beam in the energy range of 2-4 MeV. Also thick targets of a carbon and a deuteride titanium (TiD_x) were implanted to compare with the result of the C_6D_6 target irradiation respectively. The mean of He-beam current was about 400nA. The emitted gamma ray was detected by a HpGe detector. The HpGe detector's relative efficiency was about 25% and was surrounded with the lead block assembly to intercept background gamma ray and unnecessary gamma-ray as much as possible. The energy calibration of the detector was done with the Co-60 and Cs-137 checking source. In order to monitor the production of neutron by the irradiation, we used the BF_3 counter which installed on the experimental room wall.

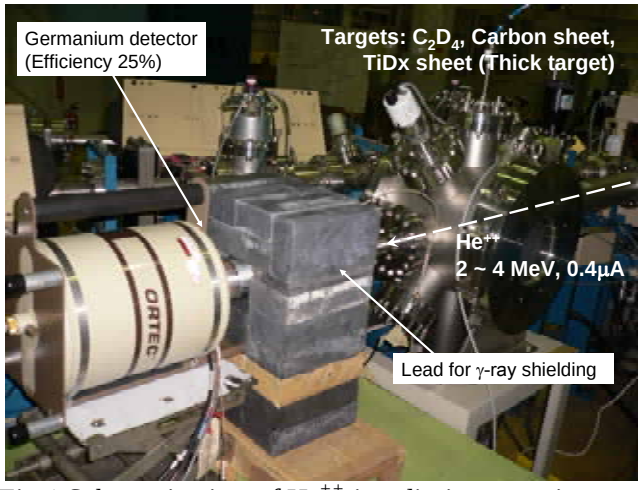

Fig.1 Schematic view of He^{++} irradiation experiment.

Result and discussion

Figure 2 shows the detected background gamma spectrum with our Ge detector. Some typical background peak (K-40, Tl-208, Bi-214 and Pb-214) was mainly observed. In order to detect gamma ray from the samples effectively, there is no shielding material between the head of detector and the target backing material. Therefore, the level of background yield was more several time than a while covered case.

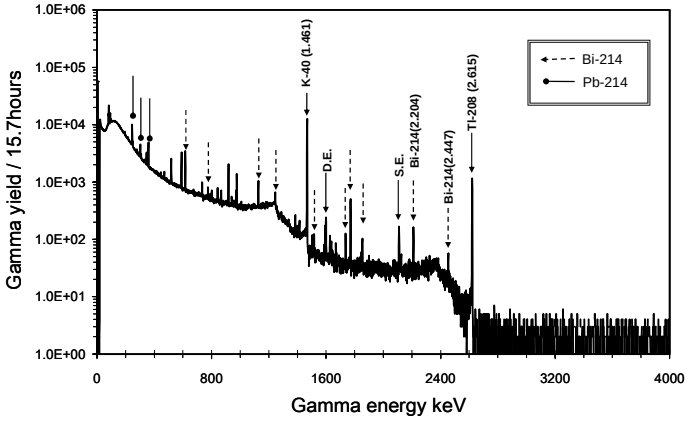

Fig.2 Measured background for 15.7 hours. Some typical photo peaks (K-40, Tl-208, Bi-214 and Pb-214) was observed.

Figure 3 shows the measured gamma-ray from used C_6D_6, carbon and TiD_x under 3.5-MeV He^{++} irradiation. each yield was normalized with incident coulomb of He^{++} ion. Below 1MeV, it is thought that the count of gamma ray was dominant at gamma-ray by $^{nat}Ge(n,n\gamma)$ inelastic reaction and $Al(n,x\gamma)$ reaction. Especially, the profile of spectra in the range of 0.5 and near 1 MeV corresponds with the past results [2]. It could be considered that the the neutron emission was due to the $^{13}C(\alpha,n)^{16}O$ reaction and D-D reaction between the recoil deuteron by He^{++}

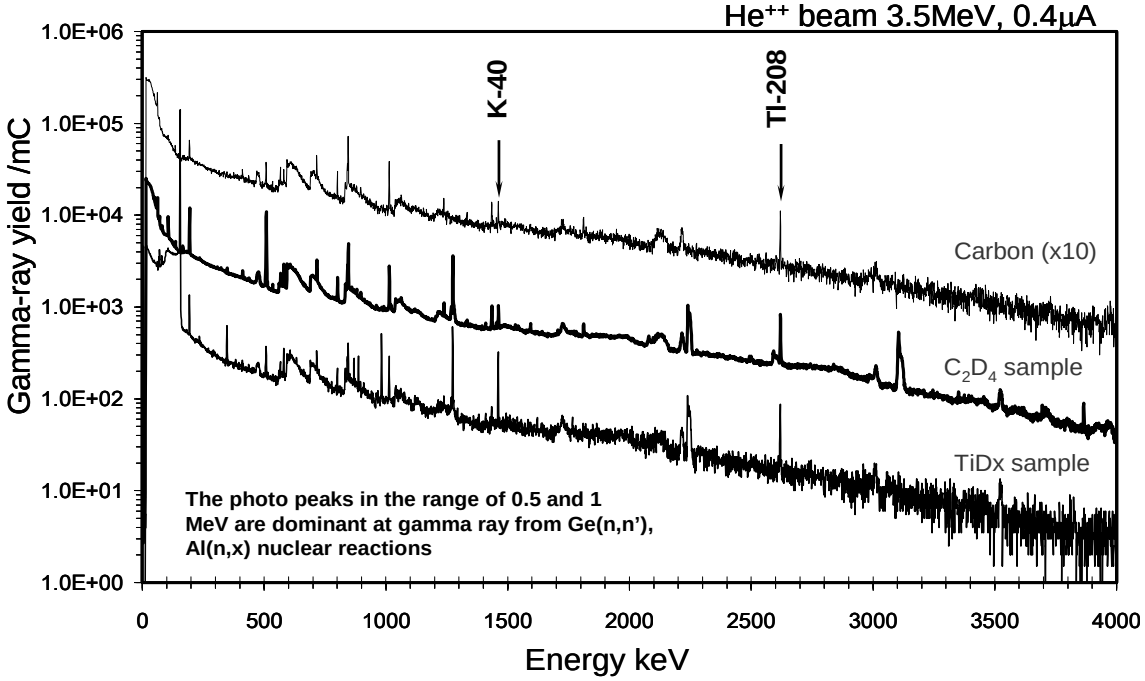

Fig. 3 shows the measured gamma-ray from used C_6D_6, carbon and TiD_x under 3.5-MeV He^{++} irradiation.

and deuterium in the sample. From the monitoring of the BF_3 detector, the neutron counting rate on the irradiation of the C_6D_6 and the carbon samples increased more than TiD_x case. Therefore, it is due to the neutron from $^{13}C(\alpha,n)^{16}O$ reaction. In the energy range between 2.1MeV and 2.2 MeV, that is, near 2.18 MeV gamma-ray from $D(\alpha,\gamma)^6Li$ reaction, we observed some shape and broad peak.

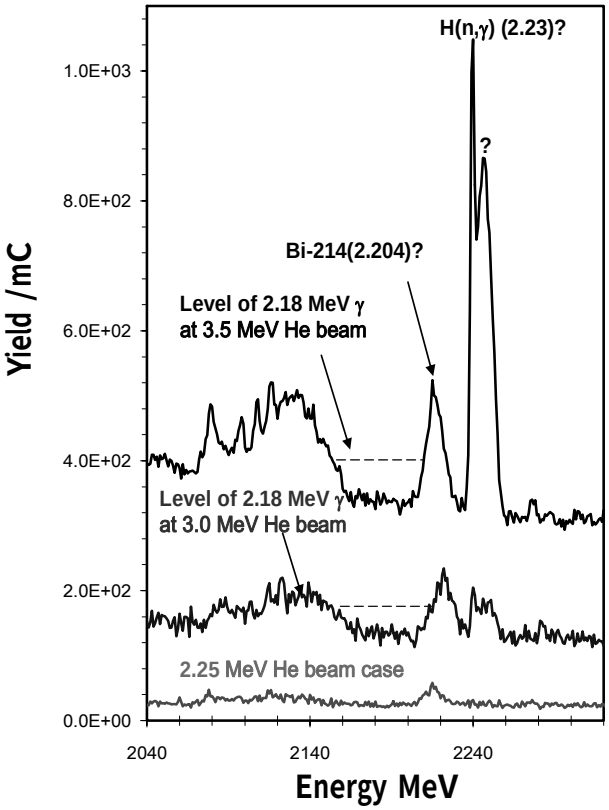

Fig.4 The detail spectrum in the range of 2.04 -2.24 MeV on 2.25-, 3.0- and 3.5-MeV H^{++} irradiations to the C_6D_6 sample.

Figure 4 shows the detail spectrum in the range of 2.04 -2.24 MeV on 2.25-, 3.0- and 3.5-MeV H^{++} irradiations to the C_6D_6 sample respectively. On the case of 3.5 MeV irradiation, we observed 2.24-MeV sharp peak and satellite peak, a somewhat broad peak near the 2.22 MeV and a broad peak with some structure near 2.06-2.16 MeV. However 2.18 MeV peak which agree with $D(\alpha,\gamma)^6Li$ reaction could not be found. The dash horizontal line in Fig.4 means the yield level estimated with the past cross section data [3]. As our preliminary view, it was thought that the sharp peak on 2.24 MeV is due to H(n,γ)D and 2.22-MeV peak is Bi-214 (2.204MeV). Furthermore, it is considered that the broad peak in 2.06-2.16 MeV is constructed from the single escape peak of Tl-208 and some gamma-ray from $^{nat}Ge(n,n\gamma)$. As above mentioned, we need to improve our measurement system to observe the 2.18 MeV gamma-ray from $D(\alpha,\gamma)^6Li$ reaction. Especially, the shielding of the background gamma ray precisely should be improved.

On the other hand, 3.09, 3.68 and 3.85-MeV peak was obviously observed on the He^{++} beam irradiation. Also the 3.09- MeV peaks have the distortion of the profile. Figure 5 shows the measured gamma profile. The three peaks is significantly thought that the 3.09-MeV peak was induced by $^{12}C(d,p\gamma)^{13}C$ reaction. For the reason of the observation, we suggest that elastic recoil deuteron with He^{++} bombardment induced the sequential $^{12}C(d,p\gamma)^{13}C$ reaction (see Fig.5). Also it is suggested that the distortion of the 3.09-MeV peak profile was due to the Doppler effect. The half life time ($T_{1/2}$) of 3.09 MeV gamma from the $^{12}C(d,p\gamma)^{13}C$ reaction is estimated about 1 fsec [4]. Also the maximum kinematics energy of the residual ^{13}C nucleus can estimate about 0.2 MeV. Considering the range of 0.2-MeV ^{13}C nucleus in the sample (C_6D_6), the stopping time is in order of 1 nsec and corresponds with the

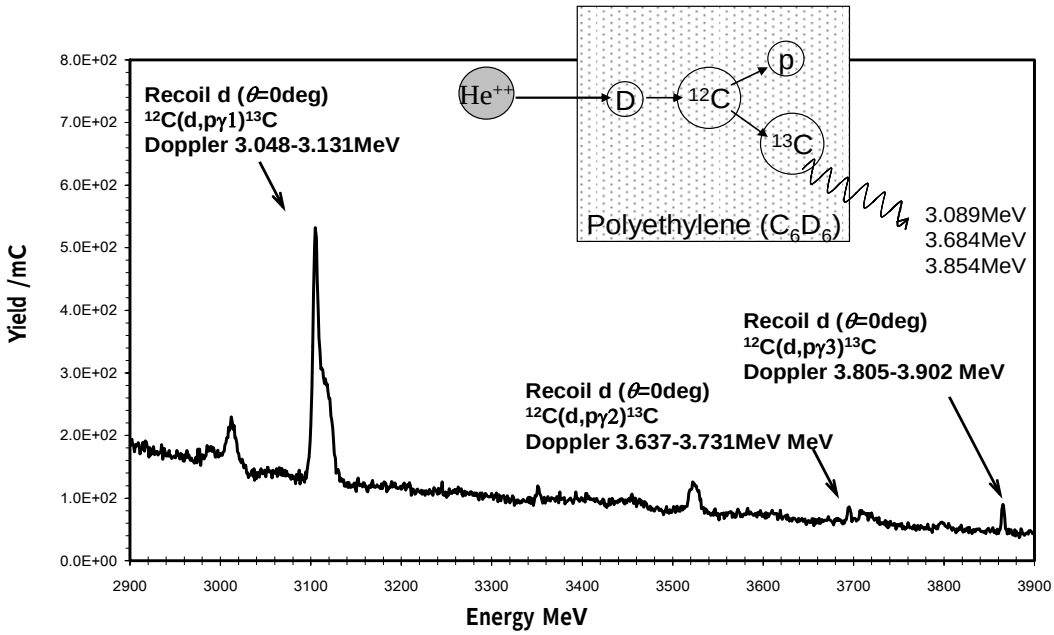

Fig.5 The gamma-peak from sequential $^{12}C(d,p\gamma)^{13}C$ reaction induced elastic recoil deuteron.

$T_{1/2}$ of 3.09 MeV gamma from the $^{12}C(d,p\gamma)^{13}C$ reaction. Therefore, it is considered that the edge shoulder of 3.09-MeV peak is the gamma-ray emitted from ^{13}C particle running in the sample.

Summary

In order to observe the γ-ray induced with high energetic α particles, we carried out the irradiation experiment with He^{++} beam. Especially, we tried to measure 2.18-MeV γ ray by $D(\alpha,\gamma)^6Li$ reaction and examined the propriety of the availability to plasma diagnostics.

Some broad peak in the range between 2.1 and 2.3 MeV was observed. However, it was difficult to identify 2.18-MeV γ ray from $D(\alpha,\gamma)^6Li$ reaction because of the background gamma-ray (Bi-214 (2.204MeV) and single escape peak from the Tl-208) and 2.2-MeV photo peak from H(n,γ)D reaction.

3.09- and 3.85-MeV peak was obviously observed and the peaks the sequential $^{12}C(d,p)^{13}C^*$ due to the elastic recoil deuteron with α particle bombardment (knock-on deuteron). Also It is suggested that the distortion of the 3.09-MeV peak profile is due to the Doppler effect. By the influence of the Doppler effect, it is thought that high energy α particle flux is able to measure.

Acknowledgement

This work is supported by Ministry of Education, Culture, Spots, Science and Technology (MEXT) under the Scientific Research of Priority Areas, “Advanced Diagnostics for Burning Plasma Experiment”.

References

[1] V.G. Kiptily et al., “Gamma-ray imaging of D and 4He ions accelerated by ion-cyclotron-resonance heating in JET plasmas” Nucl. Fusion 45 (2005) L21-L25.

[2] R.L. Bunting et al.,”Short-Lived Radioactivity Induced in Ge(Li) Gamma-ray Detectors by Neutron” Nuclear Instrument and Methods 118 (1974) 565-572.

[3] P. Mohr et al., “Direct capture in the 3+ resonance of $^{2}H(\alpha,\gamma)^{6}Li$” PHYSICAL REVIEW C Vol.50, Number 3 (1994)

[4] R.B. Firestone, V.S. Shirley, C.M. Baglin, *et al*., Table of Isotope 8^{th} edition Vol. 1(A = 1-150), Awiley-Interscience Publication, John Wiley & Sons, New York, (1996).

Production of Helium and Helium-Hydrogen Positive Ion Beams for the Alpha Particle Measurement

H. Sakakita 1), S. Kiyama 1), Y. Hirano 1), H. Koguchi 1), Y. Yagi 1), M. Sasao 2)

1) National Institute of Advanced Industrial Science and Technology (AIST), Tsukuba Central 2, 1-1-1 Umezono, Tsukuba 305-8568, Japan
2) Tohoku University, 6-6-01-2 Aoba, Aramaki, Sendai 980-8579, Japan

e-mail contact of main author: h.sakakita@aist.go.jp

Abstract. In order to produce diagnostic helium neutral beam for alpha particle measurement in nuclear fusion plant of deuterium-tritium reaction, helium ion (He^+) or helium-hydrogen ion (HeH^+) beams of ~20 keV have been considered as a primary beam. For He^+ beam, it is important to produce focused high-current-density ion beam in order to pass through small apertures of alkali gas cell with an enough signal level. For HeH^+ beam, conditions producing HeH^+ has not been investigated in detail as yet. In order to extract these beams, focused high-current-density neutral beam system is applied. For He^+ beam extraction of ~22 kV, it is confirmed that current density of ~86 mA/cm^2 is achieved, whose value is close to necessary value in ITER. For HeH^+ beam extraction in the case of ~300 V acceleration, the production rate of HeH^+ component increases with the increase of helium gas pressure ratio to hydrogen gas pressure when its value is > ~75 %. In the case of 25 kV acceleration, if 15 % of total current (which includes H^+, H_2^+, H_3^+, He^+ and HeH^+ components) is HeH^+ component, current density of HeH^+ is estimated as ~13 mA/cm^2, whose value is larger than necessary value in ITER. From melted traces of the target plate, it is estimated that the divergence angle is about ±0.8 deg.

1. Introduction

It is very important to measure the behavior of alpha particles which contribute for the continuous plasma burning in nuclear fusion plant of deuterium-tritium reaction. In order to measure the spatial and velocity profiles of alpha particles, injection of permeable helium neutral beam of ~1 MeV to the burning plasma has been considered [1]. The helium neutral (He^0) beam exchanges charges with helium ions (alpha particles), and produced high-energy helium neutral particles are measured by the energy analyzer. In order to produce diagnostic He^0 beam, following two methods are being considered. Helium ion (He^+) beam of ~20 keV and ~100 mA/cm^2 is converted to negative helium ion (He^-) through the alkali gas cell (conversion rate~1 %) [2,3], and accelerated to ~1 MeV, then He^- of ~1 MeV spontaneously becomes He^0 (~0.2 mA/cm^2) by passing through a reasonable length (neutralization efficiency~20 %). In this system, it is important to produce focused high-current-density ion beam in order to pass through small apertures of alkali gas cell with an enough signal level.
Another method which can give a simple way to realize the 1 MeV He^0 beam is to use the helium-hydrogen ion (HeH^+) beam of ~20 keV and ~2 mA/cm^2. This beam can be accelerated to ~1 MeV, and neutralized through the gas cell with sufficient probability (neutralization efficiency~10 %) [2,4]. In this concept, conditions producing HeH^+ beam has not been investigated in detail as yet.
We had already developed a high-current-density neutral hydrogen beam system with strong focusing in order to inject the beam through a narrow port in the vacuum vessel [5]. For the purposes of deep understanding of beam characteristics, we had also tried to extract ion beams of various kinds of elements (hydrogen, deuterium, helium and nitrogen). In the present paper, we will report characteristics of He^+ beam with strong focusing and high-current-density, and the results on optimized conditions for obtaining sufficient HeH^+ beam intensity, in our beam system.

2. Experimental Setups

In our ion beam system, three concave-type electrodes, acceleration, deceleration and grounded electrodes are used. The extraction aperture diameter of the concave acceleration electrode with a meniscus structure is 4.0 mm at the ion-source side [6]. The transparency of each electrode is ~50 %. The distance between the acceleration and deceleration electrodes is 5.5 mm, and that between the deceleration and grounded electrodes is 2.0 mm. The thickness of all electrodes is 2.0 mm. The plasma is produced using a bucket type ion source whose inside surface is covered by a copper sheet 2.0 mm thick to prevent accidental arc erosion. Cusped magnetic field is larger than 1500 G at the inside surface of the chamber, and residual magnetic field in the plasma region is smaller than 5 G. The magnetic field measured by a gauss meter shows a fairly good agreement with the designed value. A power supply (PS) system with capacitor banks is adopted. Specifications of PSs are 30 kV and 50 A with voltage ripples less than 5% for the acceleration PS, -5 kV and 6 A for the deceleration PS, and 300 V and 1 kA for the arc PS. The filament PS of DC operation (30 s) has the specifications of 20 V and 2700 A (= 180 A x 15 sets of filaments), and constant-voltage control is programmed with the setting accuracy of 0.1%. Narrow hairpin tungsten filaments of ϕ2 mm are adopted as cathodes [7]. The designed beam duration is 30 ms.
In order to measure beam species, mass analyzer (Balzers Instruments, PPM422) whose maximum energy is limited less than 500 V is used. Therefore, in the case of mass analysis, DC power supply system of 300 V and 20 A is used as an acceleration PS.

3. Experimental Results

At first, experimental results on helium acceleration of ~25 kV are described (in this case, helium gas is not puffed into the neutralization cell). Figure 1(a) shows the dependency of extracted ion current on filament voltage, which current is estimated as $I_{acceleration} - I_{deceleration}$. These currents are the circuit currents measured between the power supply and electrodes. In

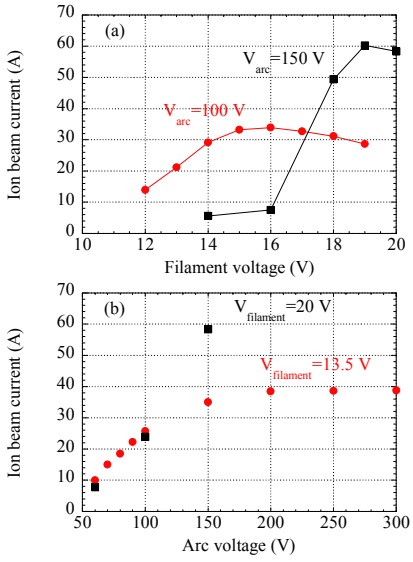

Fig. 1. (a) Filament voltage dependency, and (b) arc voltage dependency. Circle and square symbols indicate helium gas and hydrogen gas discharge cases, respectively.

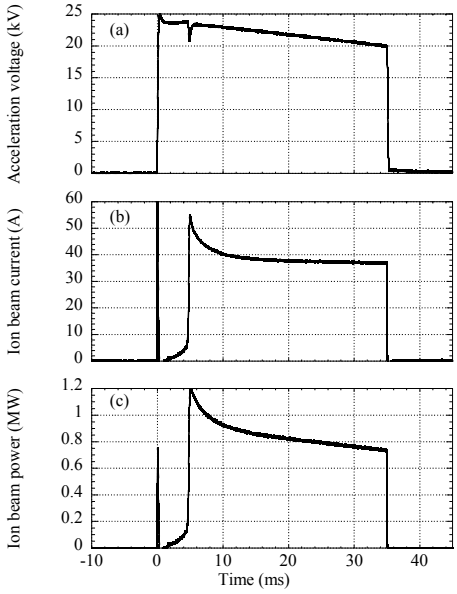

Fig. 2. Time evolutions of (a) acceleration voltage, (b) extracted ion beam current and (c) ion beam power.

the case of helium discharge, the extracted current has the maximum value at an optimized filament voltage. In the case of hydrogen gas discharge, filament voltage that achieves the maximum current value increases. This result suggests that it is possible to operate filament voltage at lower value. Figure 1(b) shows the dependency of extracted He^+ current on arc voltage. There is a tendency that beam current saturates over V_{arc}= 200 V. It is noticeable that He^+ beam can be extracted at low filament voltage, because we can reduce the heat flow into the acceleration electrode. Figure 2 shows time evolutions of each parameter in the case of $V_{acceleration}$ = 25 kV, $V_{deceleration}$= -1.2 kV, V_{arc}= 200 V, $V_{filament}$= 13.7 V. He^+ beam of ~22 kV and ~40 A is obtained, then current density of ~86 mA/cm^2 (= ~40/(πr^2x0.5)) is achieved, whose value is close to necessary value (~100 mA/cm^2) in ITER (International Thermonuclear Experimental Reactor). Here, r indicates effective radius of the electrode.

Next, in order to produce HeH^+ component in the ion source, helium and hydrogen gases are mixed in the gas reserve tank. Figure 3 shows time evolutions of each parameter in the case of $V_{acceleration}$ = 300 V, $V_{deceleration}$= -4.5 kV, V_{arc}= 110 V, $V_{filament}$= 10.5 V and He gas pressure ratio to hydrogen gas pressure= 75 %. Ion beam of ~6 A which includes H^+, H_2^+, H_3^+, He^+ and HeH^+ components is extracted. Figure 4 shows the number of HeH^+ particles measured by the mass analyzer as a function of beam energy, in the case of $V_{acceleration}$ = 300 V, $V_{deceleration}$= -4.5 kV and $V_{filament}$= 10.5 V. Here, in order to detect the maximum number of particles at each arc voltage condition, the energy of the detector is scanned. As arc voltage increases, the number of HeH^+ particles increases, but saturates around 130-140 V which almost corresponds to electron energy that ionization cross section to He^+ becomes maximum.

Figure 5 shows the number of HeH^+, He^+ and H^+ particles as a function of He gas pressure ratio to hydrogen gas pressure, $P_{He\text{-}ratio}$, in the case of $V_{acceleration}$ = 300 V, $V_{deceleration}$= -4.5 kV, V_{arc}= 110 V, $V_{filament}$= 10.5 V and ion beam current = ~6 A. It is clear that the production rate of HeH^+ component increases, when helium gas pressure ratio is larger than ~75 %. In the case of $P_{He\text{-}ratio}$= 90 %, the number of HeH^+ particles corresponds to ~15 % of total counts for H^+, He^+ and HeH^+ particles. (The analyzer sensitivity for H_2 gas is qualitatively larger than that for He gas. However, we cannot conclude the precise ratio, since absolute sensitivity calibration has not been conducted). Figure 6 shows the number of HeH^+, He^+ and H^+ particles as a function of beam energy (here, x axis in Fig. 5 is converted to the beam energy). As the amount of helium gas component increases, space potential in the ion source increases.

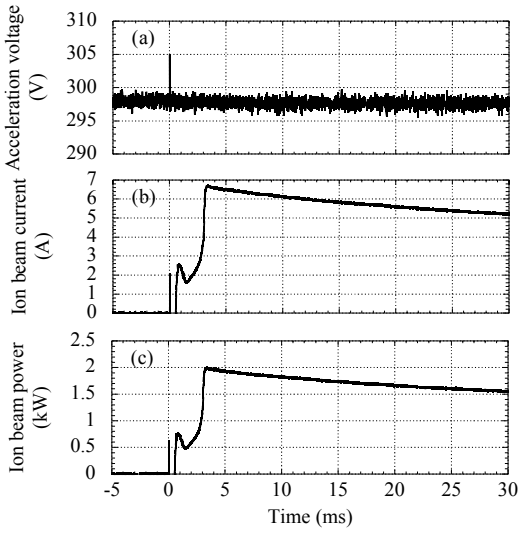

Fig. 3. Time evolutions of (a) acceleration voltage, (b) extracted ion beam current and (c) ion beam power.

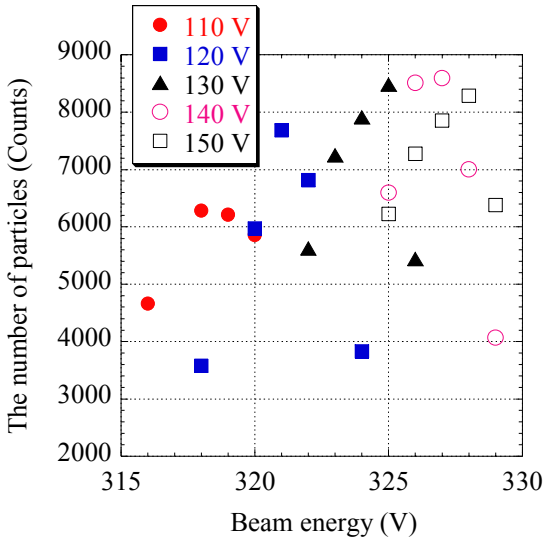

Fig. 4. The number of HeH^+ particles measured by the mass analyzer for several arc voltages.

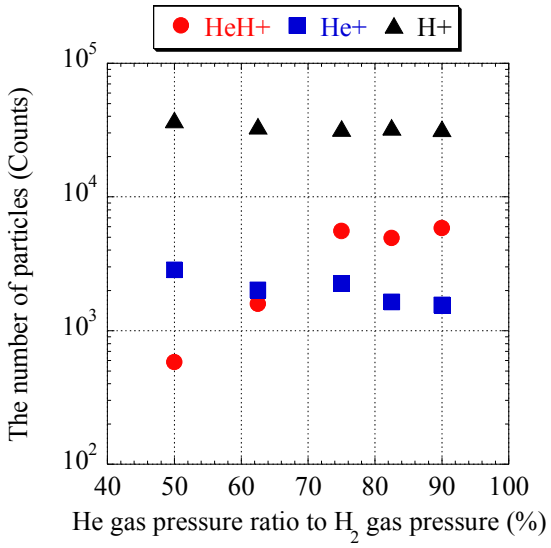

Fig. 5. The number of HeH^+, He^+ and H^+ particles as a function of He gas pressure ratio to hydrogen gas pressure.

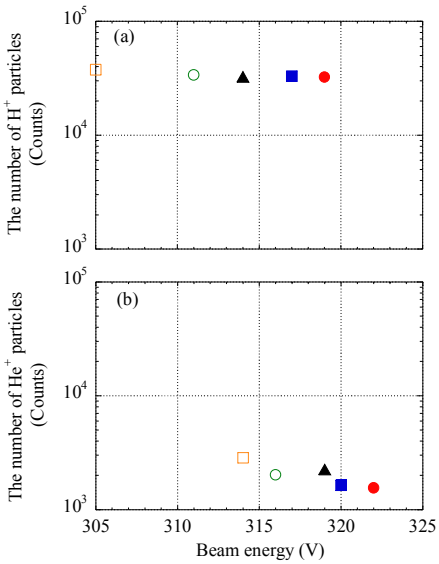

Fig. 6. The number of H^+ and He^+ particles as a function of beam energy. Empty square, empty circle, solid triangle, solid square and solid circle indicate the cases of 50, 63, 75, 83 and 90 % helium gas, respectively.

In order to study the beam performance of high-energy particles, total beam of H^+, H_2^+, H_3^+, He^+ and HeH^+ components is accelerated. Figure 7 shows time evolutions of each parameter in the case of $V_{acceleration}$ = 25 kV, $V_{deceleration}$= -1.2 kV, V_{arc}= 250 V, $V_{filament}$= 13.9 V and $P_{He\text{-}ratio}$= 75 %. Ion beam of ~40 A is extracted. If 15 % of total current is HeH^+ component, current density of HeH^+ is estimated as ~13 mA/cm^2 (= 40x0.15/(πr^{2}x0.5)), whose value is larger than necessary value (~2 mA/cm^2) in ITER. However, in order to measure only HeH^+ beam current, we must separate HeH^+ component from total beam of H^+, H_2^+, H_3^+, He^+ and HeH^+ by using the magnetic field system.

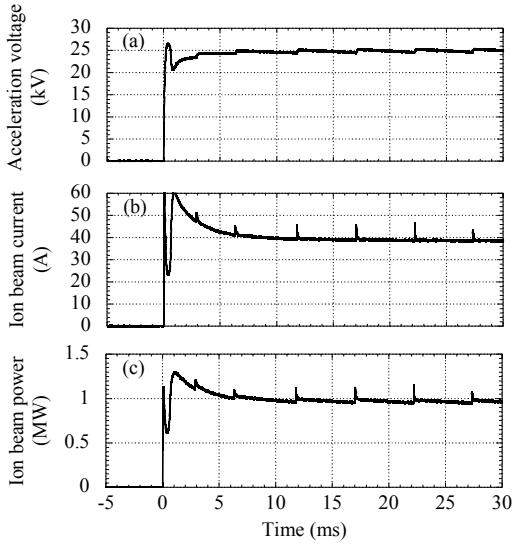

Fig. 7. Time evolutions of (a) acceleration voltage, (b) extracted ion beam current and (c) ion beam power.

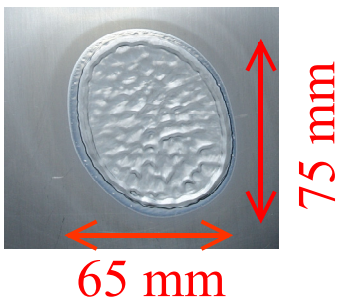

Fig. 8. The beam trace of the stainless steel target plate at X= 1530 mm.

In order to examine beam shape, focal point and beam divergence angle, high energy beam of ~25 keV is irradiated to a stainless steel target plate which is installed at the target chamber. The melted patterns on the plate are taken at several positions (X= 1530, 1735, 1835 and 1920 mm) shot by shot. Here, X indicates the distance from the electrode. As an example, the beam trace of the target plate at X= 1530 mm is shown in Fig. 8. From these melted traces, it is estimated that the focal length is ~1400 mm and the divergence angle is about ±0.8 deg.

4. Summary

Characteristics of He^+ and HeH^+ beams which produce He^0 beam used for the alpha particle measurement are described. In order to extract these He^+ and HeH^+ beams, the strongly focused high-current-density hydrogen neutral beam system is used [5]. It has been shown that this beam is strongly focused into a diameter of ~36 mm at the focal point with the divergence angle of about ±0.8 deg. As a result, a power density as high as ~1 GW/m^2 is attained at the focal point of the neutral beam.
For He^+ beam extraction of ~22 kV, current density of ~86 mA/cm^2 is achieved, whose value is close to necessary value (~100 mA/cm^2) in ITER. It is noticeable that He^+ beam can be extracted at low filament voltage, which mitigates heat flow into the acceleration electrode.
In the case of $V_{acceleration}$ = 300 V, $V_{deceleration}$= -4.5 kV, V_{arc}= 110 V, $V_{filament}$= 10.5 V, it is measured by the mass analyzer that the production rate of HeH^+ component increases with the increase of helium gas pressure ratio to hydrogen gas pressure when its value is > ~75 %. In the case of 25 kV acceleration, if 15 % of total current (which includes H^+, H_2^+, H_3^+, He^+ and HeH^+ components) is HeH^+ component, current density of HeH^+ is estimated as ~13 mA/cm^2, whose value is larger than necessary value (~2 mA/cm^2) in ITER. However, in order to measure only HeH^+ beam current, we must separate HeH^+ component from total beam of H^+, H_2^+, H_3^+, He^+ and HeH^+ by using the magnetic field system. From melted traces of the target plate installed at several positions from the electrode shot by shot, it is estimated that the focal length is ~1400 mm and the divergence angle is about ±0.8 deg, which reveals almost the same superior characteristics as the case in neutral hydrogen beam [5].

A part of this study was financially supported by the Budget for Nuclear Research of the Ministry of Education, Culture, Sports, Science and Technology of Japan, based on the screening and counseling of the Atomic Energy Commission, and a part of this study was financially supported by the Grant-in-Aid for Scientific Research based on the screening of the Japan Society for the Promotion of Science.

References

[1] SASAO, M., Proc. 9th IAEA Technical Meeting on Energetic Particles in the magnetic confinement systems, Takayama, OT11 (2005).
[2] SASAO, M., et al., Proc. Int. Workshop on Diagnostics for ITER, Varenna (2005) 51.
[3] SHINTO, K., et al., Proc. 9th IAEA Technical Meeting on Energetic Particles in the magnetic confinement systems, Takayama, P21 (2005).
[4] WARREN, J., et al., Phys. Rev. A **4** (1971) 1960.
[5] SAKAKITA, H., et al., Proc. 32nd Eur. Phys. Conf. on Control. Fusion and Plasma Phys., Tarragona, P4-109 (2005).
[6] COUPLAND, J.R., et al., Rev. Sci. Instrum. **44** (1973) 1258.
[7] KURIYAMA, M., et al., JAERI Reports, JAERI-M87 (1987) 169 [in Japanese].

Conceptual Design of Confined Alpha Particle Diagnostic System for ITER Using an Energetic He^0 Beam

K. Shinto*, M. Sasao, M. Isobe[A], M. Nishiura[A], O. Kaneko[A], M. Wada[B], C. I. Walker[C], H. Haskell[C], S. Kitajima, A. Okamoto, H. Sugawara, S. Takeuchi, N. Tanaka, H. Aoyama and M. Kisaki

Tohoku University, Aoba, Sendai 980-8579, Japan

[A] National Institute for Fusion Science, Toki, Gifu 509-5292, Japan

[B] Doshisha University, Kyotanabe, Kyoto 610-0321, Japan

[C] Max-Planck-Institut für Plasmaphysik, Garching, Germany

A conceptual design of an active-neutral-beam-probe-diagnostic-system for alpha particles produced by D-T nuclear reaction in a plasma confined by a magnetic fusion reactor has been examined. An energetic He^0 beam plays an important role in the system. To detect a signal of neutralized alpha particles from the fusion plasma with enough S/N ratios, a high brightness He^0 beam produced by spontaneous electron detachment from He^- ions is required. A prototype of a He^+ ion source has been designed and assembled to test the performance in producing a source beam for high intensity He^- beam through a double-charge-exchange process in alkali metal vapor.

1. Introduction

In the next generation magnetically confined fusion experimental reactors, such as ITER (International Thermonuclear Experimental Reactor), plasmas will be self-heated by high-energy alpha particles produced by D-T nuclear fusion reaction. The spatial and energy distributions of alpha particles in the core plasma are one of the most important issues for burning plasma diagnostics. Several methods to measure the velocity distribution of alpha particles have been proposed. One of the most promising methods is based upon the double-charge-exchange reaction of a fusion produced alpha particle in a core plasma to capture two electrons to escape from the plasma and detected by an energy analyzer installed outside the confined magnetic field. Post *et al.* proposed an active beam probe method to neutralize the alpha particles by injecting an energetic neutral helium (He^0) beam into the core plasma.[1] Sasao and Sato showed the possibility of producing an energetic ground state He^0 beam by spontaneous electron detachment from negative helium ions (He^-) to diminish impurities of the metastable states of He^0.[2]

In this paper, a conceptual design of the measurement system of the velocity distribution function of alpha particles in the core plasma using an energetic He^0 beam

* katsuhiro.shinto@qse.tohoku.ac.jp

with a neutral particle energy analyzer is shown. In section 2, a measurement scheme is described. The counting rate of the neutralized alpha particles produced by double charge exchange reaction due to incident energetic He^0 beam is estimated taking into account of the beam attenuation in the plasma. In section 3, the measurement system employing the active probing beam with the energy analyzer for the neutralized alpha particles is described. Components of the system are listed, and specifications of a high intensity He^+ ion source with three concave multi-aperture electrodes are described.

2. Measurement scheme

Sasao *et al*. described the diagnostic beam system for alpha particle measurement on ITER previously.[3] However, the system should be modified to be adaptable to the new ITER design. A schematic illustration of a possible geometry for tangential injection of an energetic probing beam into ITER plasma is shown in Fig.1. Fusion produced alpha particles after being neutralized by the injected beam are detected by the energy analyzer installed outside of the plasma confining magnets. With this configuration, the detector can cover the entire region of radial position in the plasma.

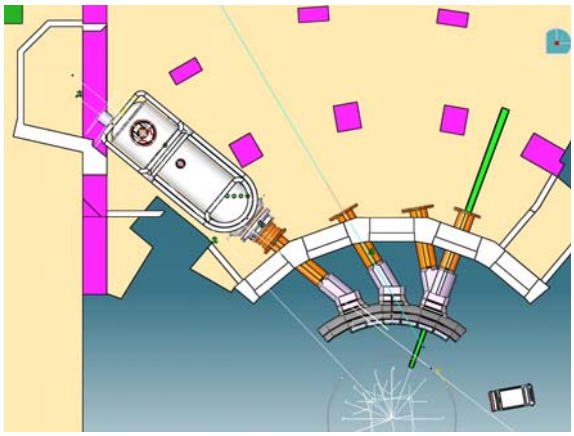

Fig. 1 Schematic illustration of a possible geometry of tangential injection of an energetic He^0 probing beam into ITER plasma. Diagnostic NBI system is left-up side behind the third NBI heating system and the energy analyzer is installed right-down side in the figure.

In the previous report [3], the velocity of the He^0 beam is required to exceed $0.6v_\alpha$, where v_α is the velocity of the fusion alpha particle at its birth. This velocity was considered necessary for the incident beam to penetrate to the center of the plasma. The number of neutralized alpha particles per a velocity interval, $C(v)dv$, is derived by,

$$C(v)dv = \eta(v)n_a(v,r)n_b(r)\sigma_{20}(v)v_{rel}Vd\Omega dv,$$

where $\eta(v)$, $n_\alpha(v,r)$, $n_b(r)$, $\sigma_{20}(v)$, v_{rel}, V are transmission coefficient of outgoing

neutralized alpha particle, local density of alpha particles, that of beam particles, cross-section of two electron capture of alpha particles, relative velocity between an alpha particle and an injected neutral particle, plasma volume respectively. The charge-exchange cross-section decreases rapidly when the relative energy is greater than 200 keV.[4] The total counting rate for an ITER plasma of $n_e(r=0) = 10^{20}$ m^{-3} with 1% produced alpha particle density and 10% attenuation of He^0 beam with the velocity of $0.8v_\alpha$, the atomic current of 10 mA in the area of 200 mm × 50 mm is estimated to be 10^5-10^6 particles per second.

3. Active beam probe system using He^0 beam

In order to diagnose the velocity distribution of the alpha particles produced by D-T nuclear fusion reaction, an active beam probe system using He^0 beam with an energy analyzer has been designed as shown in Fig. 1. In the conceptual design, the system consists of a high-brightness positive helium (He^+) ion source, an alkali-metal vapor cell to produce He^- ions by double charge exchange reaction, a magnetic deflection type ion separator with a stigmatic beam focusing, an electrostatic pre-accelerator, a radio-frequency quadrupole (RFQ) linac, a long-free-flight beam transport line and a neutralized alpha particle detector. The ion beam production and acceleration devices are designed to be installed behind the third neutral beam injection (NBI) heating system. The schematic diagram of the He- beam production and acceleration devices is shown in Fig. 2. The accelerated He^- beam is injected into the beam transport line of the NBI heating system and the neutralized He^0 beam produced by auto-detachment process during the long beam transport line is directed to the fusion reactor. The element species, the beam energy and the beam current in each component are tabulated in Table 1. The efficiency for the double charge exchange from He^+ to He^- is referred in Ref. [5] and the lifetime of He^- is referred in Ref. [6] which is recently measured by utilizing an electrostatic ion storage ring.

Table 1 Element species, beam energy and current in each component (expected values).

	Exit of He^+ ion source	Exit of alkali metal vapor cell	Downstream of ion separation	Exit of Electrostatic Accelerator	Exit of RFQ linac	Downstream of 40 m free flight tube
Element	He^+	He^+, He^0, He^-	He^-	He^-	He^-	He^0
Energy	10-30 keV	10-30 keV	10-30 keV	~200 keV	~ 2 MeV	~ 2 MeV
Current	3 A	3 A (total)	~60 mA	~55 mA	~ 50 mA	~ 10 mA

There have been many investigations on the production of a high-intensity He^- beam in accelerator applications. The most reliable method is to employ double-charge-exchange reaction of a He^+ beam in an alkali metal vapor.[7],[8] A high intensity He^+ ion source is required to produce enough intensity of He^- beam with a low divergence. At National Institute of Advanced Industrial Science and Technology, an ion source with three concave multi-aperture extraction electrodes to converge the formed beam into a narrow spot has been developed.[9] A He^+ beam extracted from this type of ion source injected into an alkali metal vapor cell will produce a high intensity He^- beam. A prototype of the He^+ ion source based on this idea has been designed. The specifications of the He^+ ion source are tabulated in Table 2.

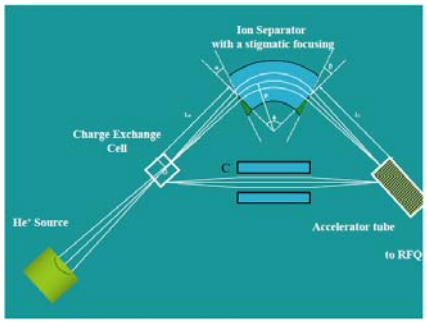

Fig. 2 Schematic diagram of He^- beam production and acceleration devices.

Table 2 Specifications of He^+ ion source.

Beam Current	3 A
Beam Energy	10-30 keV
Beam Divergence	< 1.0 deg.
Extraction Range	100 mm in diameter
Focal Length of the Concave Electrodes	750 mm

Meanwhile, a proof-of-principle low beam current test stand is also under construction to check necessary components for the active beam probe system and to investigate the beam qualities.[10]

4. Summary and future plans

A conceptual design of confined alpha particle diagnostic system for ITER using an energetic He^0 beam produced from auto-detachment of an electron from He^- ions has been described. In the system, the energy analyzer can detect the neutralized alpha particles distributed the entire region of radial position in the plasma. In order to obtain the signal with enough S/N ratio detection, the injected energetic He^0 beam is required to possess the intensity of about 10^{15} particles per second.

The prototype of the He^+ ion source for producing the high intensity He^- beam by double-charge-exchange reaction will be assembled in 2006 spring at National Institute for Fusion Science in Japan, where a high technology for neutral beam heating has been developed. The beam quality of the high brightness He^+ beam will be investigated.

Further development of the acceleration and neutralization of He^- beam is desired. Especially, RFQ acceleration of the high intensity He^- beam up to 2MeV is one of the most challenging subjects. It is also necessary to survey the possibility of neutralization of He^- beam by photo-detachment process in order to replace the long beam transport line for electron auto-detachment process to a short high efficiency photo-neutralizer.

Acknowledgements

This work was supported by a Grant-in-Aid of the Scientific Research of Priority Areas, “Advanced Diagnostics for Burning Plasma Experiment” from the Ministry of Education, Culture, Sports, Science, and Technology (MEXT) in Japan.

References

[1] POST, D. E., et al., “Techniques for measuring the alpha-particle distribution in magnetically confined plasmas”, Bulletin of the American Physical Society **24**(1979) 987.

[2] SASAO, M., and SATO, K. N., “Alpha-particle diagnostics with high-energy neutral beams”, Fusion Technol. **10**(1986) 236.

[3] SASAO, M., et al., “Development of diagnostic beams for alpha particle measurement on ITER”, Nucl. Fusion **35**(1995) 1619.

[4] ITO, R., et al., “Analytic cross sections for collisions of H, H_2, He and Li atoms and ions with atoms and molecules I”, JAERI-M 93-117(1993).

[5] SCHLACHTER, A. S., “Formation of negative ions by charge transfer : He^- to Cl^-”, Production and neutralization of negative ions and beams (3rd int'l symposium, Brookhaven, 1983) (Prelec, K., ed.), AIP conference proceedings No. 111 (1984) 300-311.

[6] PEDERSEN, U. V., et al., “Lifetime measurement of He- utilizing an electrostatic ion storage ring”, Phys. Rev. A **64**(2001) 012503.

[7] HOOPER, E. B., et al., “High-current source of He^- ions”, Rev. Sci. Instrum. **51**(1980) 1066.

[8] SASAO, M., et al., “Development of a double-charge exchange He^- source”, Rev. Sci. Instrum. **69**(1998) 1063.

[9] SAKAKITA, H., et al., “Production of helium and helium-hydrogen positive ion beams for the alpha particle measurement”, in these proceedings.

[10] SHINTO, K., et al., “Design of a fast neutral He beam system for feasibility study of charge-exchange alpha-particle diagnostics in a thermonuclear fusion reactor”, Proc. 21st Particle Accelerator Conference (PAC05) (in press).

CO_2 Laser Collective Thomson scattering for Alpha-particle Diagnostics

T. Kondoh, T. Hayashi, Y. Kawano, T. Sugie *, Y. Kusama , Y. Miura
Japan Atomic Energy Agency, Naka, Ibaraki, 311-0193, Japan
**ITER International team, Naka Joint Work Site, Naka, Ibaraki, 311-0193, Japan*
e-mail address; kondoh.takashi @ jaea. go. jp

In JT-60U (JAEA Tokamak 60 - Upgrade), a collective Thomson scattering (CTS) technique based on a CO_2 laser is being developed in order to establish a diagnostic method of confined alpha-particles in burning plasmas. In order to the demonstrate feasibility of the CTS system, a new laser systems is being developed, with which improved signal-to-Noise (S/N) ratio of a detection signal and temporal resolution will be obtained. The laser has cavity length of ~ 4 m and has high repetition rate (10 Hz). To improve the spectral purity of the laser, cavity length will be feedback-controlled and a spectral filter will be installed in the output of the laser. Numerical calculation shows that ion temperature will be evaluated from the scattered spectrum with the new CO_2 laser.

1. Introduction

In order to understand the behavior of alpha-particles which are the dominant heat source in a burning plasma, it is necessary to measure the spatial distribution of the density of the alpha-particles and their energy spectrum. In a collective Thomson scattering (CTS) technique, the plasma scatters a laser light and the frequency broadens due to the Doppler shift, and the scattered radiation is detected. In principle, the number density and energy spectrum of the fast ions can be determined from the spectrum of scattered radiation, however, the development of measurement techniques and hardware are at a very early stage. A technique based on CTS is being developed using CO_2 lasers [1-5] and gyrotrons [6] to measure spatial distribution and energy spectrum of the alpha-particles. The CTS technique based on the CO_2 laser has the advantage of small plasma refraction, simplifying the tracking of the scattered radiation. On the other hand, it is necessary to choose a small scattering angle, θ, so that the scattering wave length is larger than Debye length λ_D which satisfies $\alpha_s = (k \cdot \lambda_D)^{-1} > 1$, where k is the scattering wave number, $k = 2 \cdot k_i \cdot \sin(\theta/2)$, k_i is the wave number of incident beam. In the JT-60U parameter region (T_e > 1 keV、 $n_e > 10^{19} m^{-3}$), it is necessary to take the scattering angle of 0.5 degree or less.

A preliminary design of a beam line and a receiver system with the vertical scattering geometry has been developed for International Thermonuclear Experimental Reactor (ITER). To realize the CTS measurement, a proof-of-principle test on the CTS system using the JT-60U plasma is being conducted. Also present status of newly developed CO_2 laser is described.

2. Collective Thomson Scattering System proposed for ITER

ITER requires diagnostics of confined alpha-particles with time resolution of 0.1 s and spatial resolution of $a/10$, where a is minor radius of the plasma. A CTS system based on a pulsed CO_2 laser is under consideration for alpha-particle measurements on ITER, because there is no experimental data obtained at present tokamaks. Therefore demonstration of the CTS system is strongly required.

Heating neutral beams (NB) (E = 1 MeV) are normally co-injected in ITER and have a velocity similar to alpha-particles at birth. An important point is that the CTS measurement cannot, in general, distinguish between beam ions and alpha-particles which have the same velocity. The diagnostic scattering geometry must be oriented so that the scattering $\boldsymbol{k}$ vector is

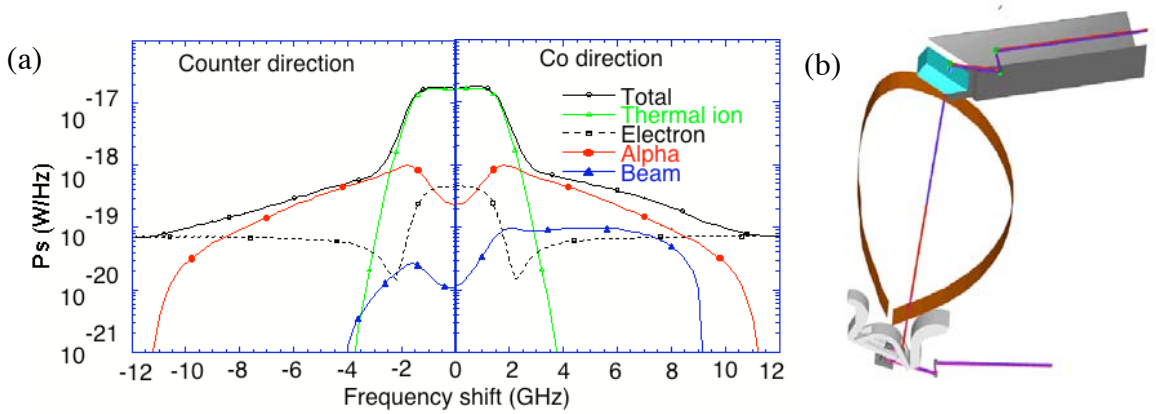

Fig.1 (a) Calculated spectra of CTS system on ITER. (b) Preliminary design of vertically viewing CTS on ITER.

near the toroidal direction to minimize contributions of NB-ions to the scattering spectrum. The distribution function of co- and counter-direction can be measured with the vertical geometry.

Figure 1 (a) shows the calculated spectrum of scattered radiation for the proposed ITER CTS system shown in Fig. 1 (b). Individual contributions to the scattered power due to alpha-particles, beam ions, electrons and thermal ions are indicated in Fig. 1(a). In the calculation, $n_e = n_i = 1\text{x } 10^{20}\ \text{m}^{-3}$, $T_e = T_i = 20$ keV, $Z_{eff} = 1.8$, laser power $P_{laser} = 50$ MW, scattering angle $\theta = 0.5°$, and solid angle, $\Delta\Omega = 0.1$ sr were assumed. It is clearly shown that the vertically viewing CTS could resolve counter-travelling alphas without being masked by beam ions.

The laser is injected to the plasma through the divertor. The scattered radiation is collected by a mirror optics located in the upper port and is transferred to the diagnostic room. The present CTS system in JT-60U cannot distinguish between co- and counter-ions because the frequencies of the local oscillator of the heterodyne receiver and the pulsed laser are the same (10.6 μm). In this case, the spectrum obtained is the summation of co- and counter-directions. In order to distinguish co- and counter-ions, isotope CO_2 and N_2O lasers which have shifted frequencies (2 - 10 GHz) from the pulsed laser can be used as the local oscillator laser and this was proposed for ITER[7].

Since the scattering angle, θ, must be small (~0.5˚), optimization of spatial and spectral resolution is one of the major task for CO_2 laser CTS in ITER. Scattering length (84% of the CTS signal comes from the length of L), and spectral resolution (FWHM), $\Delta f/f$, which is equal to the velocity resolution $\Delta v/v$, is described as follows;

$$L = w/\sin(\theta/2) \qquad (1)$$

$$\frac{\Delta f}{f} = \frac{6.7/w}{2k_i \sin(\theta/2)} \qquad (2)$$

where, w is radius of Gaussian beam waist (e^{-2} power level) which is equal to the radius of Gaussian sensitivity profile, and k_i is the wave number of incident laser at the plasma. Scattering length and spectral resolution as a function of the beam radius is shown in Fig. 2 (a) and (b). Scattering length of L ~ 0.92 m and spectral resolution of $\Delta f/f$ ~ 0.32 is obtained with beam radius of 4 mm, or L ~ 0.69 m and $\Delta f/f$ ~ 0.43 is obtained with beam radius of 3 mm. Beam radius of 3 mm is easily obtained with the mirror of 3 cm in diameter in the beam propagation optics of ITER. To obtain better spatial and spectral resolution, combination with tangentially viewing CTS system is needed to be considered.

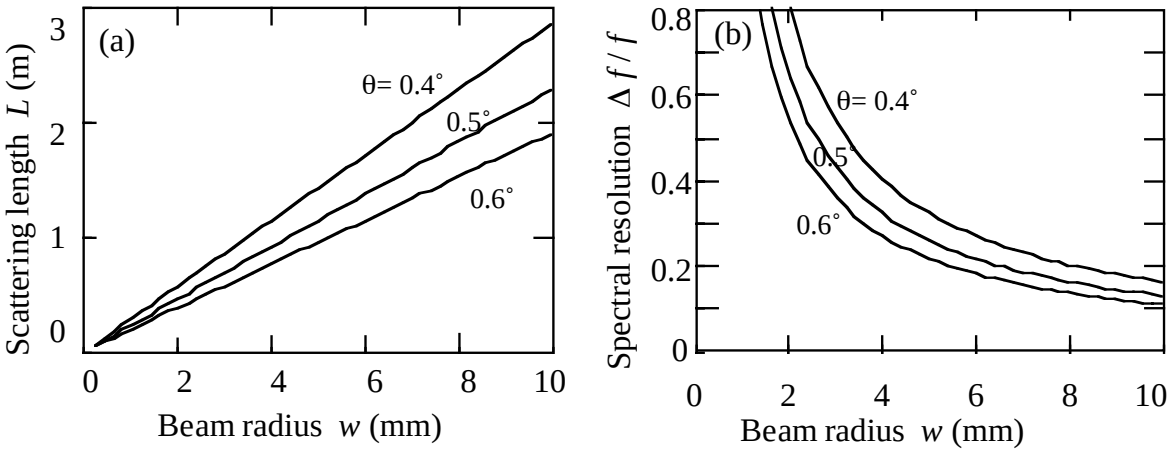

Fig. 2. (a) Scattering length L and (b) spectral resolution Δf/f as a function of beam radius w.

3. Test of the Collective Thomson Scattering System on JT-60U

In order to demonstrate the feasibility of the measurement, the CTS technique is being developed in the JT-60U tokamak [3-5]. A schematic view of the CTS system in JT-60U is shown in Fig. 3. A CO_2 laser system, a stray light filter, and a heterodyne receiver system are developed in collaboration with Oak Ridge National Laboratory (ORNL). The pulse shape and wavelength of a transversely excited atmospheric pressure (TEA) laser are controlled by injecting a beam from a 10W continuous wave (CW) CO_2 laser. It has a pulse width of about 1 μs and repetition rate of 0.5 Hz. The maximum output energy is about 15 J. The beam diameter is about 4 cm and divergence of the beam is 0.5 mrad. He-Ne laser beam is combined with the CO_2 laser and also combined with line of sight of the receiver for optical axis alignment. The scattering angle must be small (0.5°) to obtain large ion contribution on the scattered spectrum. Vacuum windows on JT-60U are made of zinc selenide (ZnSe) with antireflection coatings that have high damage thresholds (19.9 J/cm^2). Distance between the CO_2 laser and the plasma center is about 70 m. The laser beam is focused at the plasma center using a molybdenum spherical mirror (focal length f = 13.1 m) of 150 cm in diameter. The scattered light is collected by a spherical mirror (f = 7.8 m) 50 cm in diameter. Stray light is

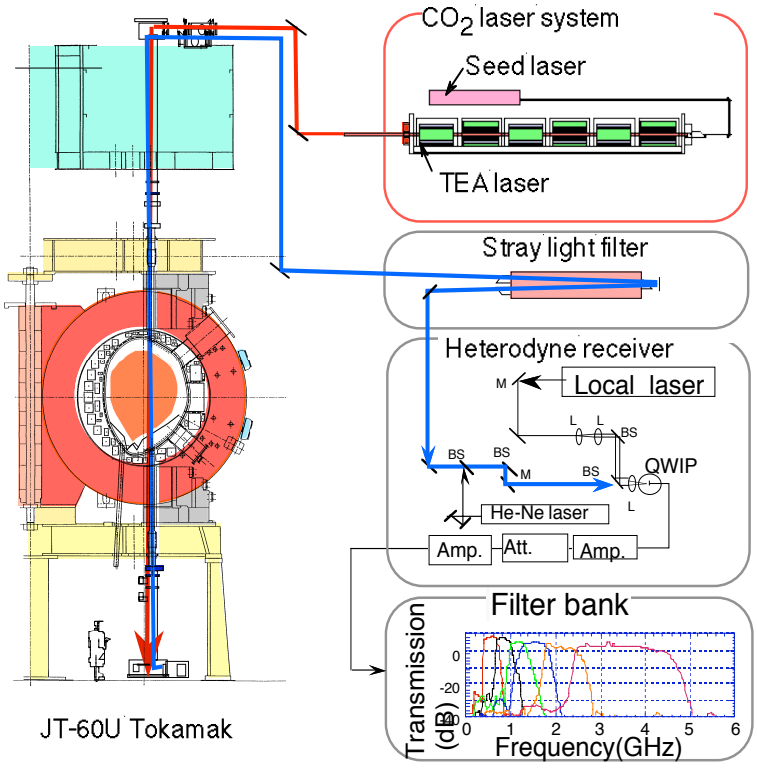

Fig. 3 Schematic diagram of the Collective Thomson scattering system in JT-60U

reduced by a notch filter with hot CO_2 gas. The scattered signal is detected by a heterodyne receiver and the spectrum is analyzed by a filter bank with six channels.

Measurements of the scattered signal from the JT-60U plasma were performed with a NB heated plasma. However, scattered signal was not detected due to electrical noise originating from the pulsed laser discharge and stray signal coming from mode impurities in the laser.

4. Development of CO_2 Laser

In order to improve *S/N* ratio of detection signal and to improve temporal resolution and spectral purity, a new laser systems is being developed. The laser has unstable cavity which has a length of ~ 4 m and has high-repetition rate. Schematic view of the newly developed CO_2 laser is shown in Fig. 4. Expected performance of the laser are as follows; repetition-rate is 20 Hz, output energy is 18 J, beam divergence is 1 mrad, and diameter of the beam is 4 cm. The cavity is comprised of six discharge units, which consists of main-discharge electrodes, pre-ionization pins (not shown in the figure), and two heat exchangers. To achieve high-repetition rate, working gas is cooled by the heat exchangers. Though the electrodes and the heat exchanger are designed to have capability of 20 Hz operations, the laser will be operated at a frequency of 10 Hz at first. Since discharge unit and power supply are component of a commercial laser, it is easy to improve its performances. To improve the spectral purity of the laser, cavity length will be feedback-controlled and a spectral filter will be installed to the output of the laser.

5. Summary

One of the candidates to measure confined alpha-particles is collective Thomson scattering technique using a pulsed CO_2 laser. By using a vertical viewing CTS geometry, it is possible in principle to distinguish the alpha-particle distribution from the energetic NB ions. Scattering length of $L \sim 0.92$ m and spectral resolution $\Delta f/f \sim 0.32$ will be obtained with beam radius of 4 mm. New laser system is being developed in order to improve the measurement performance (S/N ratio, temporal resolution) and proof-of-principle test will be performed with the improved laser system on JT-60U in next year.

6. Acknowledgements

The authors would like to acknowledge the many informative discussions with Drs K. Muraoka of Chubu Univ., K. Sasaki of Nagoya Univ. and M. Nagatsu of Shizuoka Univ. The authors also would like to acknowledge to Drs. D. P. Hutchinson, R. K. Richards, and C. A. Bennett for development of CO_2 laser and receiver systems. The authors also would like to acknowledge to Dr. A. E.

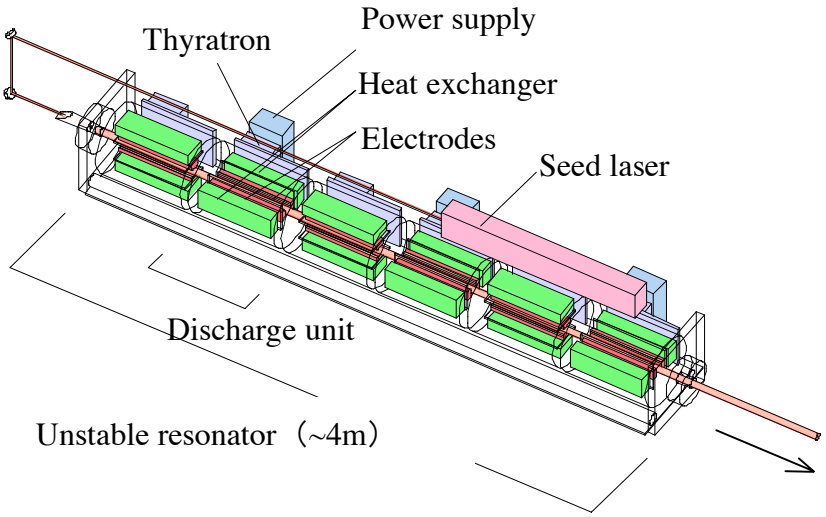

Fig. 4. Newly developed high-repetition CO_2 TEA laser.

Costley and members of ITER International Team.

This work is partly supported by Grant-in-Aid for Scientific Research Scientific Research on Priority Areas No. 16082210.

References

[1] HUTCHINSON, D. P., et al., Rev. Sci. Instrum. **56** (1985) 1075.
[2] RICHARDS, R. K., et al., Appl. Phys. Lett. **62** (1993) 28.
[3] LEE, S., KONDOH, T., et al., Rev. Sci. Instrum. **71** (2000) 4445.
[4] KONDOH, T., LEE, S., et al., Rev. Sci. Instrum. **71** (2001) 1143.
[5] KONDOH, T., MUIRA, Y., et al., Rev. Sci. Instrum. **74** (2003) 1642.
[6] BINDSLEV, H., et al., Phys Rev. Lett. **83** (1999) 3206.
[7] KONDOH, T., et al., "Prospects for Alpha-Particle Diagnostics by CO_2 Laser Collective Thomson Scattering on ITER", Proc. 30th EPS Conference on Contr. Fusion and Plasma Phys., St. Petersburg, Vol. 27A, (2003) P-4.65.

Lost Fast Ion Behavior in the Large Helical Device

M. Nishiura, M. Isobe, T. Mutoh, N. Kubo[1], M. Sasao[1], S. Murakami[2], M. Osakabe, J. Miyazawa, S. Sakakibara, K. Toi, T. Ido, T. Nagasaka, D.S. Darrow[3], D. A. Spong[4], LHD experimental group

e-mail: nishiura@nifs.ac.jp

National Institute for Fusion Science, 322-6 Oroshi, Toki, Gifu,509-5292 Japan
[1]Tohoku University, Aoba, Aramaki, Sendai 980-8579, Japan
[2]Kyoto University, Kyoto, 606-8501, Japan
[3]Princeton Plasma Physics Laboratory, Princeton, NJ
[4]Oak Ridge National Laboratory, P.O.Box 2008, Oak Ridge, TN 37831-6169

Abstract. For fast ion studies in confined plasmas, the scintillator probe has been designed and was installed into the Large Helical Device (LHD). A periscope with eyepiece, relay, and objective lenses is coupled with optical fiber bundle to transmit the scintillator light to an image intensified charge coupled device camera and 3x3 photomultiplier arrays. Using the scintillator probe, we show the experimental results of the fast ion loss profile at the edge plasma of LHD and the fluctuation signals of fast ion loss in the plasma detachment experiment. In these experiments, the scintillator rises in temperature of around 190 ºC.

1. Introduction

The fast ion behavior is studied by using the scintillator probe in the Large Helical Device(LHD) with $l = 2$ / $m = 10$ heliotron configuration, where l and m are the poloidal and the toroidal mode numbers of the helical plasma, respectively, because fast ion driven instabilities have possibilities of the substantial ion losses. In particular, the understanding of fast ion and alpha particle behaviors created in burning plasmas is the common interest for stellarator and tokamak devices in view of the performance of thermo nuclear reactor.

The scintillator probe can measure the pitch angle and energy of fast ions escaped from confined plasmas simultaneously. Zweben et al. studied MeV ions produced from DD reaction using poloidal array probes in Tokamak Fusion Test Reactor(TFTR) [1]. The same principle of the detector is used in other devices [2-4]. We have developed the same principle of the scintillator probe and have installed it into LHD. The moveable scintillator probe can access to the outer edge plasma region from outer port of the oblong cross section of plasma. The detail of the scintillator probe system is written in Ref. [5]. We show the typical results obtained using the scintillator probe.

2. Dependence of pitch angle and gyro radius of lost ions

Figure 1 shows the dependence of pitch angle on the magnetic axis, R_{ax} = 3.5, 3.6, and 3.75 m with the toroidal magnetic field from 1.0 to 2.8 Tesla. Two spots are observed usually on the scintillator plate around the pitch angle of 90 degrees, when the neutral beams (NB) are injected.

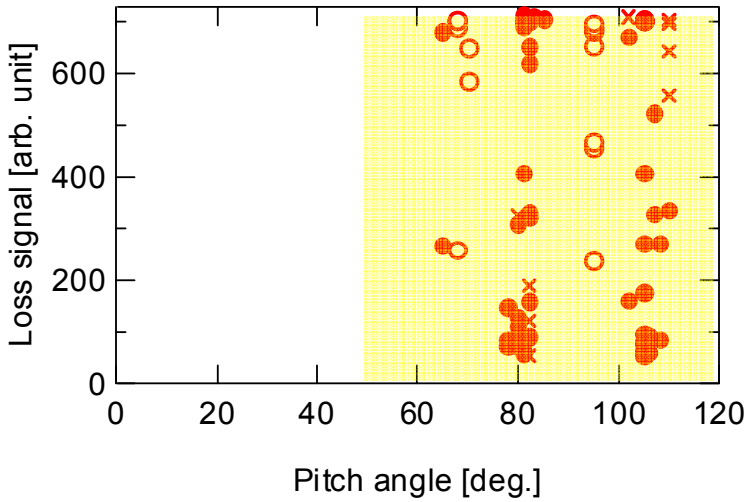

Figure 1. Pitch angles with Rax = 3.5 m (open circles), 3.6 m (closed circles), and 3.75 m (x) are plotted. The observable region is hatched from 50 to 120 degrees.

The gyro radius estimated from the peaks of striking points on the scintillator plate is plotted as a function of the magnetic field at the probe head position, B_{probe} in the figure 2. In this case, the toroidal magnetic field changes from 1.0 to 2.8 Tesla. Two curves are drawn in this figure for the comparison. They correspond to the energies of 160 keV for the NBs and 1.6 keV for the thermal ions. The observed signals do not exceed the gyro radius estimated from the energies of NB, and eliminate the thermal ion components. Thus the signals of fast ion loss are detected. The acceptable difference between measured and NB energies would come from the slowing down of fast ions, the resolution of the probe, and the error of the probe position.

The loss signal of fast ions with the pitch angle of approximately 80 degrees and the energy of 160 keV is shown in Figure 3. Before the injection timing of NB#3, fast ion loss is bellow the noise level. As NB#3 is injected, the fast ion loss increases. When the fast ion loss during only NB#2 injection is subtracted from that during NB#2 and #3 injections, we can estimate the amount of fast ion loss induced by NB#2. The amount of fast ion loss induced from NB#2 and #3 are almost same after NB#3 injection. However the change of fast ion loss before/after t = 1.9 s is not understood.

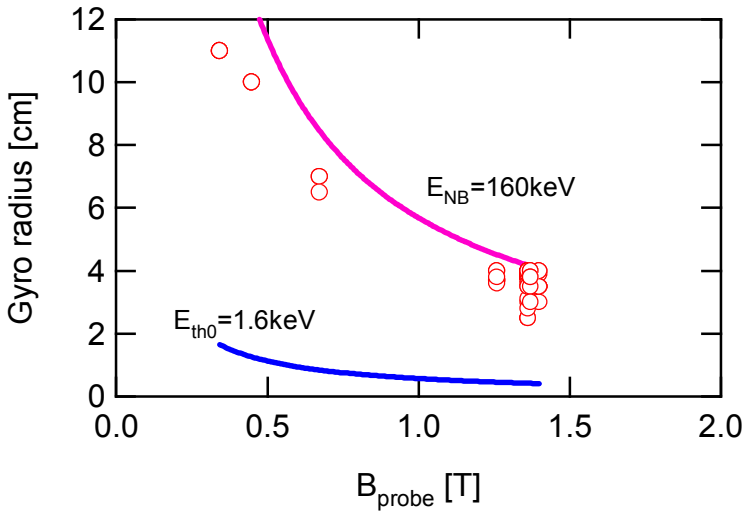

Figure 2. Gyro radii are plotted with the magnetic field at the probe position. Two curves are calculated from the N-NB energy and thermal ion temperature.

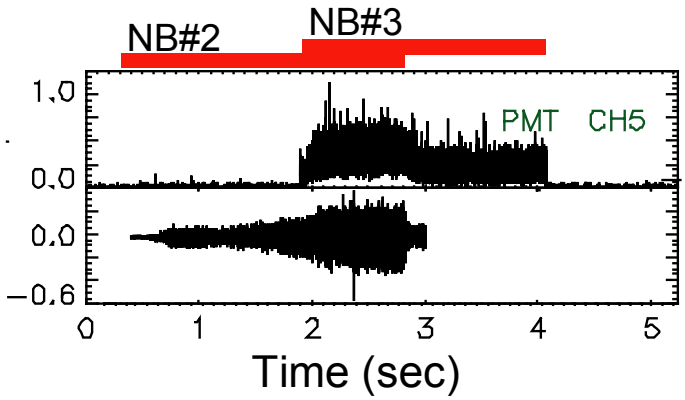

Figure 3. Fast ion loss signal and magnetic probe signal during the co-direction (NB#2) and counter direction(NB#3) NB injections.

3. Fast ion behavior at the plasma edge

To obtain the spatial distribution of lost fast ions, the scintillator probe is scanned at the edge of the LHD plasmas, where the major radius, R, is from 5040 to 5240 mm, shown in figure 4. The relative intensities of fast ion loss signals measured by the photomultiplier agree well with those measured by the image intensified CCD camera from the figure 4. At the probe position of 5100 mm, the decrease of the intensities of fast ion loss is observed. These data are useful for the estimation of deposition profile of NBs with the computer simulations.

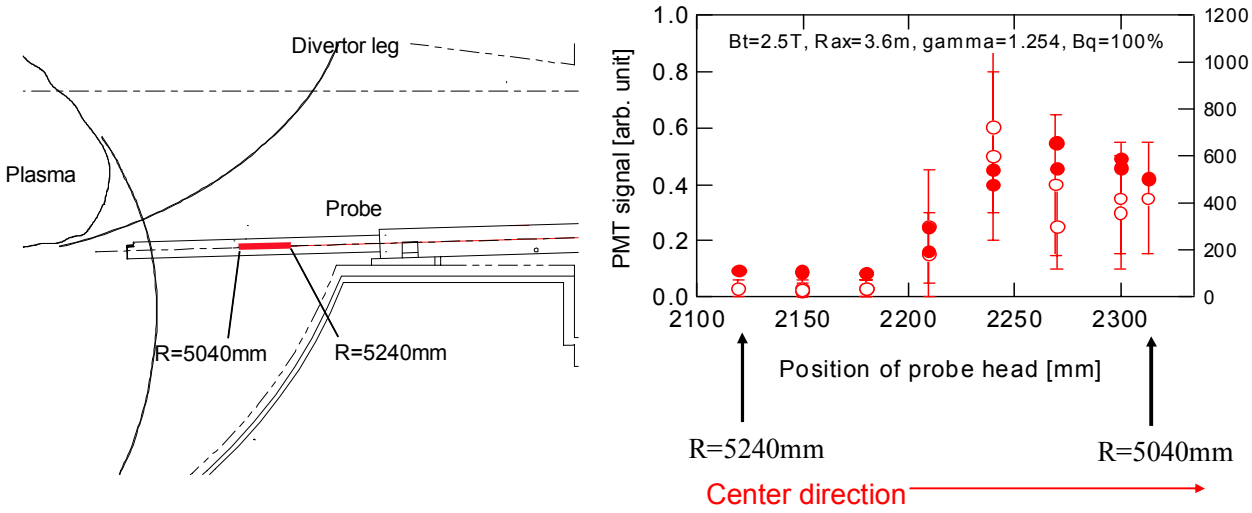

Figure 4 Spatial profile measurements of lost fast ions in edge plasmas. The open circles and closed circles indicate the photomultiplier signals, and the image intensified CCD signals, respectively.

4. Fluctuation signals before and after the plasma detachment phase

After the strong gas puffing, the self-sustained detachment plasma is observed in LHD [6]. As shown in figure 5, before the detachment, the significant loss of fast ions with the pitch angle of approximately 90 degrees is detected from t = 0.8 to 1.2 s by the scintillator probe. But after the detachment, the loss of fast ions disappears to the noise level. During the time window of pre-detachment, the fluctuation frequency of approximately 5 kHz is appeared in the signals of both the magnetic probe and the scintillator probe, but the fluctuation signal becomes quiescent in the detachment phase. From the mode analysis of the magnetic probe, this fluctuation signal is considered to come from the edge plasma region. In addition, the hot plasma boundary shrinks to approximately 90% of the pre-detachment plasma boundary [6]. From these results, two explanations are considered for the decrease of fast ion loss. With the plasma shrinking, the NB penetration at the edge region becomes larger, and it leads to the decrease of the total number of ionized ions. As another possibility, with the plasma shrinking, the exhaust of fast ions by the edge plasma fluctuation disappears. Further investigations are required to explain the fast ion behavior at the edge region in detachment plasmas.

5. Scintillator characteristics

The emission intensities of the scintillator (ZnS:Ag) depend on the temperature. The enough emission light is obtained without any degradation at the substrate temperature of up to 190 ºC in the plasma experiments. Throughout the 6 month plasma experiments of LHD, the scintillator surface is not damaged apparently. However the qualitative study for the emission efficiency should be carried out in higher temperature region to estimate fast ion losses.

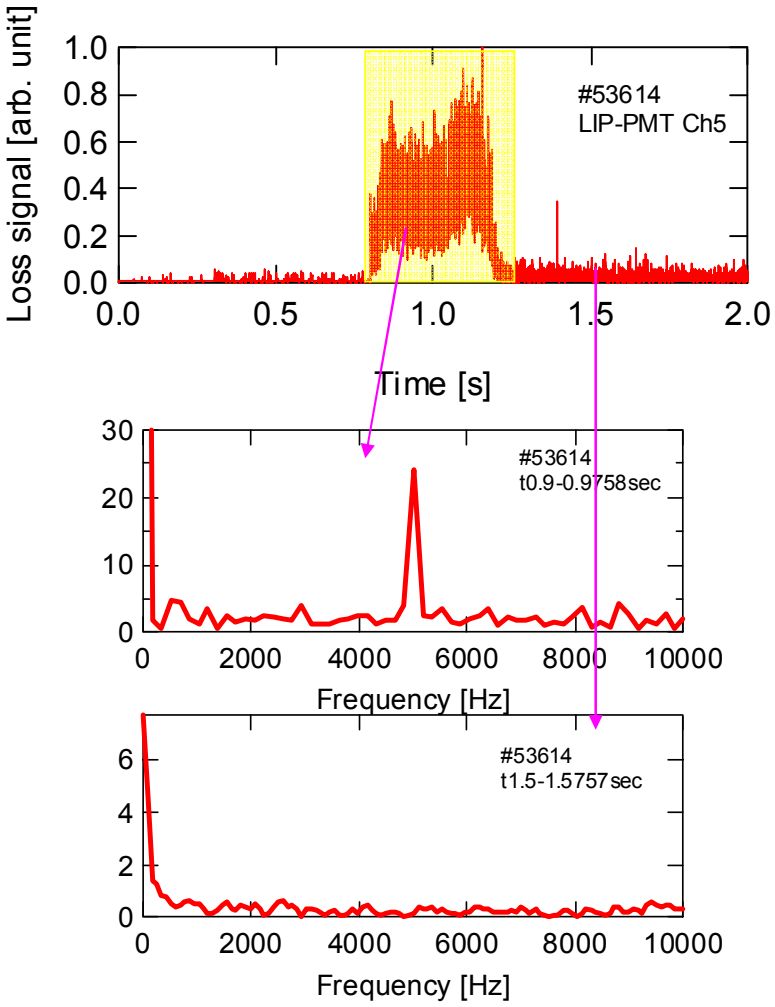

Figure 5 Fluctuation signals of fast ion losses in the detachment discharge. The detachment phase starts from t=1.2 to 3.2 s (this figure shows until t=2.0 s).

This work is supported by Grants-in-Aid for Scientific Research of the JSPS #17044006 and NIFS05ULRR511.

References

[1] S.J. Zweben et al. Nuclear Fusion **40**, 91(2000).

[2] M. Isobe, D. S. Darrow, T. Kondo, M. Sasao, K. Toi, M. Osakabe, A. Shimizu, Y. Yoshimura, C. Takahashi, S. Murakami, S. Okamura, and K. Matsuoka, Rev. Sci. Instrum. **70**, 827 (1999).

[3] S. Baeumel et al. Rev. Sci. Instrum. **75**, 3563(2004).

[4] M. Garcia-Munoz, H.-U. Fahrbach, J. Neuhauser, H. Zohm, A. Herrmann, V. Rohde and ASDEX Upgrade Team, Proc.European Physical Society (2005).

[5] M. Nishiura, M. Isobe, T. Saida, M. Sasao, D. S. Darrow, Rev. Sci. Instrum. **75**, 3646(2004).

[6] J. Miyazawa et al. J. Plasma Fusion Res. **81**, 331(2005).

Lost alpha diagnostic based on an imaging bolometer and a multi-foil thermal detector

B. J. Peterson[1], A. G. Alekseyev[2], S. Konoshima[3], N. Ashikawa[1], H. Parchamy[1], Y. Miura[3], M. Sasao[4]

[1]*National Institute for Fusion Science, Toki, 509-5292 Japan*
[2]*Troitsk Institute for Innovation & Fusion Research, Troitsk, 142190 Russia*
[3]*Japan Atomic Energy Agency, Naka-shi, Ibaraki-ken 311-0193, Japan*
[4]*Tohoku University, Aoba, Aramaki, Sendai 980-8579, Japan*

e-mail of corresponding author: peterson@LHD.nifs.ac.jp

The diagnosis of lost alpha particles is important for the operational safety and evaluation of an experimental fusion reactor. A radiation-hard diagnostic device has been proposed based on an imaging bolometer and a multi-foil thermal detector. In this paper we discuss ongoing work with testing prototype imaging bolometers on JT-60U and the testing of a prototype multi-foil thermal detector on an ion accelerator.

1. Introduction

The confinement of alpha particles is an important topic for the operation of a fusion reactor as they should transfer their energy to the fuel plasma and then be exhausted safely through the divertor. If their confinement is poor the 3.5 MeV helium nuclei could escape through the last closed flux surface and scrape-off layer in a spatially localized manner that could do serious damage to the first wall of the reactor. Therefore the diagnosis of lost alpha particles is important for the operational safety and evaluation of an experimental fusion reactor. A lost alpha detector has been identified as one of the key diagnostics for the ITER experiment which will soon enter the construction phase. The diagnostic requirements specified by the ITPA diagnostics group are given in a Table 1 [1].

In spite of this importance, a suitable diagnostic solution has yet to be found for the ITER device. Two options have been deployed on magnetic plasma confinement devices to study the loss of energetic ions. The first is the scintilator probe that has been used successfully on various plasma confinement devices to diagnose the energy

PARAMETER	CONDITION	RANGE	RESOLUTION			
			Temporal	Spatial	Energy	Accuracy
First wall flux	**Default**	2 MW/m2 + (with FI -?)	100 ms	*a*/10 -poloidal direction*	250 keV (desired)	10%
	Transients	20 MW/m2 (with FI - ?)	10 ms	TBD	-	30%

Table 1 Measurement requirements for lost alphas on ITER [1].

distribution and pitch angle of escaping energetic ionized particles [2]. The second are Faraday cup detectors, which provide information on the energy distribution of lost ions [3]. However, both of these concepts are subject to questions regarding their applicability in a neutron-rich fusion reactor environment. For the former, a suitable scintilator material should be found that can operate at high temperature and withstand the high neutron fluxes. For the later, problems with detecting the expected nanoampere level electrical currents in the presence of radiation induced electromotive forces are anticipated. These problems call for a new technique which is durable and reliable in a fusion reactor environment and can provide the necessary information on the escaping alpha particle energy distribution and pitch angle.

A new concept for measuring energetic ions escaping from a fusion reactor has been proposed based on the combination of a multifoil thermal discriminator and an imaging bolometer [4] and is known as the InfraRed MultiFoil Thermal Detector (IRMFTD) The imaging bolometer is a radiation-hard energy detector which uses a thin metal foil to absorb the energetic radiation or particles from its front side facing the plasma and is imaged on the back side by an infrared camera through a periscope infrared optical path [5]. The infrared camera measures the change in temperature of the thin foil and then this information is used in the solution of the two-dimensional heat diffusion equation for the power deposition distribution in the foil. A stack of multiple thin foils is placed in front of the imaging bolometer to discriminate the energy distribution of the absorbed particles as shown in Figure 1. By layering the discriminating foils in a stair-step fashion, one dimension can be used for energy discrimination and by proper orientation of the detector with respect to a slit and the magnetic field the other dimension can be used for pitch angle discrimination as shown in the conceptual design in Figure 2.

In this paper we report on ongoing research into the development of this diagnostic.

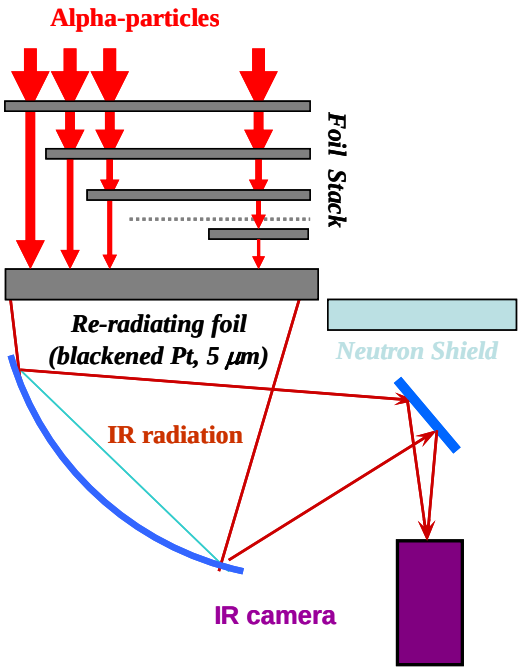

Figure 1 Conceptual design of IR multi-foil thermal detector.

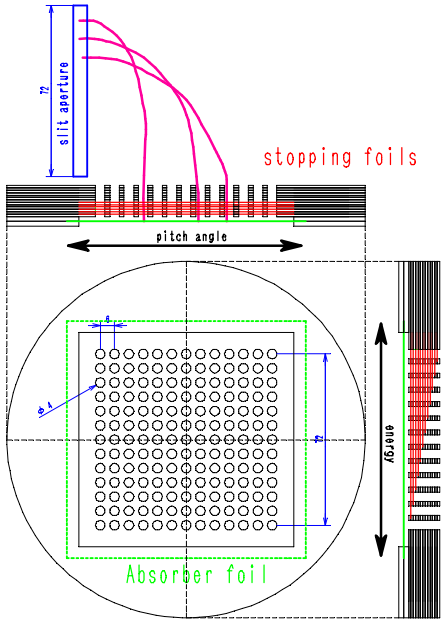

Figure 2 Conceptual design of discriminator stack and re-radiating foil for IR multi-foil thermal detector.

This R&D can be separated into two areas: development of imaging bolometers; designing, fabricating and testing prototype multi-foil thermal detectors on ion beam facilities. In the following we report on the current status and future plan for each of these areas.

2. Imaging bolometer testing on JT-60U

An integral part of the IRMFTD is the imaging bolometer. Imaging bolometers have been operated recently on the helical devices LHD and CHS [6,7]. However this is not a sufficient test of the viability of an imaging bolometer for a tokamak device because of the lack of disruptions in a helical device. There for we embarked on a project to test an imaging bolometer on the JT-60U tokamak. The bolometer foil, pinhole camera and vacuum IR window were installed in JT-60U in August of 2003 [8]. The IR camera was installed in 2004 and initial data were taken during the 2004-2005 campaign as shown in Figure 3 [9]. Loss of IR camera signal during the high powered NBI indicated that the neutron and magnetic shielding of the IR camera were not adequate. Therefore the shielding was increased for the 2005-2006 campaign. Soft iron magnetic shielding was increased from 6 mm to 20 mm, a 15 mm lead shield was added for gamma rays, and the boron-doped polyethylene was increased from 3 cm to 9 cm.

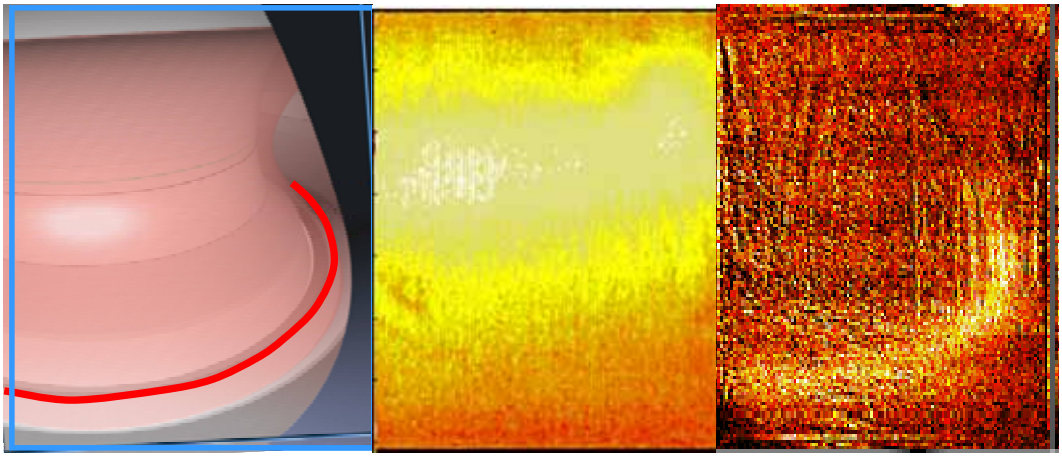

Figure 3 CAD image of field of view of imaging bolometer in JT-60U with divertor shown in red (left), IR camera images of core radiation at disruption (middle), and divertor radiation during Hydrogen discharges (right).

In addition other improvements were made to enable triggering of the IR camera and 14 bit data acquisition.

3. Foil testing on an ion beam facility

Tests have been carried out on an ion beam facility using a simple prototype IRMFTD shown schematically in Figure 4 [10]. Three types of stopping foils were tested; nickel

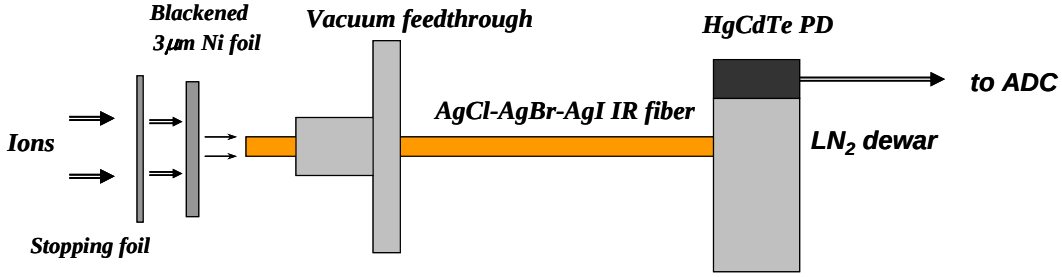

Figure 4 Schematic of prototype IRMFTD [10].

(1 μm), diamond-like carbon film (150 nm), CVD damond membrane (155 nm). The results of the transmitted power fraction versus beam energy are shown in Figure 5. The discrepancy at low energies is attributed to scattering.

4. Conclusion

Preliminary work has been done on the development of an infrared multifoil thermal detector for measuring energetic charged particles in fusion devices. This work has

basically demonstrated the proof of principle of using foils to discriminate ion energy and the durability and operability of an imaging bolometer in a tokamak environment. However, much work remains to demonstrate the viability of the diagnostic for ITER. Work on JT-60U will continue to demonstrate the applicability of an imaging bolomter in a tokamak reactor environmentwith high neutron fluxes. Experiments with a prototype IRMFTD will be extend to investigate a prototype IRMFTD using multiple foil layers and an IR camera and its application to an existing fusion device. In addition consideration of integration issues for ITER and detector locations have begun.

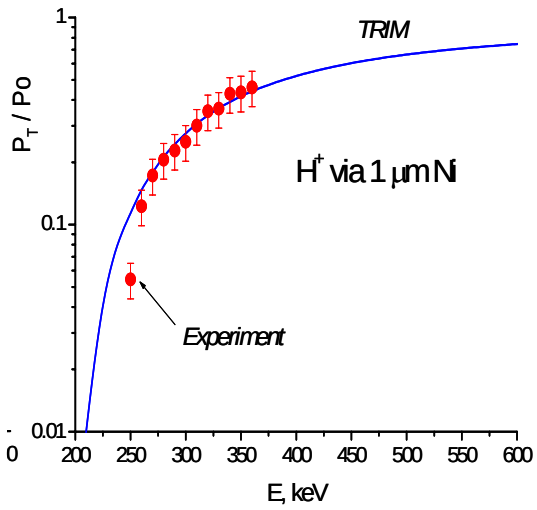

Figure 5 Transmitted power fraction versus H^+ beam energy for .a one micron Ni foil compared with the prediction of the Monte Carlo calculation, TRIM (in blue) [10].

This work is partly supported by Grants-in-Aid for Scientific Research of the JSPS, Nos.16560729 and 16082207.

References

[1] K.M. Young, 4th ITPA Topical Group Meeting on Diagnostics, February 19, 2003, Padua, Italy.
[2] S. Baeumel et al., Rev. Sci. Instrum. **75** (2004) 3563.
[3] D. S. Darrow et al., Rev. Sci. Instrum. **75** (2004) 3566.
[4] A.G. Alekseyev et al., proc. 30th EPS CCFPP 2003, ECA **27A** P-1.171 (2003).
[5] B.J. Peterson et al., Rev. Sci. Instrum. **74(3)** (2003) 2040.
[6] G.A. Wurden and B.J. Peterson, Rev. Sci. Instrum. **70(1)** (1999) 255.
[7] B.J. Peterson et al., Plasma Phys. Cont. Fusion **45(7)** (2003) 1167.
[8] B.J. Peterson et al., 30th EPS CCFPP 2003, ECA **27A** P-4.067 (2003).
[9] S. Konoshima et al., proc. 32nd EPS CCFPP 2005, ECA **29A** P-4.092 (2005).
[10] A. G. Alekseyev et al., proc. 23rd SOFT (2004) P2C-D-220.

Agenda

9th IAEA Technical Meeting on Energetic Particles in Magnetic Confinement Systems.

9-11 November 2005, Hida Earth Wisdom Center, Takayama, Japan

organized by National Institute for Fusion Science, Toki, Japan

	9 Nov. 2005(Wed.)	**10 Nov. 2005 (Thu.)**	**11 Nov. 2005 (Fri.)**
Bus depart.	8:05 for the conference site*	8:05 for the conference site*	8:05 for the conference site*
	8:30-8:50 **Registration****		
	8:50-9:20 **Opening A. Malaquias** **Welcome O. Motojima** **Logistics K. Toi**		
Morning session 1	***Tokamak experiments & theories 1 (Alfvén cascade & frequency sweeping)*** **Chair : D. Borba** 9:20-10:00 **IT01 (S.Sharapov)** 10:00-10:20 OT01 (B.Breizman)*** 10:20-10:40 OT02 (R.Vann)	***Theories (AE physics & wave-particle interaction)*** **Chair : W. Heidbrink** 8:40-9:20 **IT07 (H.L. Berk)***** 9:20-10:00 **IT08 (T. Bergkvist)** 10:00-10:20 OT09 (Y. Todo)	***Diagnostics*** **Chair: S. Pinches** 8:40-9:20 **IT14 (V. Kiptily)** 9:20-10:00 **IT15 (W. Heidbrink)** 10:00-10:20 OT11 (M. Sasao)
	Coffee break 10:40-11:00	Coffee break 10:20-10:40	Coffee break 10:20-10:40
Morning session 2	***Tokamak experiments & theories 2 (AE studies)*** **Chair: M. Sasao** 11:00-11:40 **IT02 (M.Van Zeeland)** 11:40-12:00 OT03 (Ph. Lauber)	***Tokamak experiments & theories 4 (Runaway electrons & Wave-Particle interactions)*** **Chair : E. Fredrickson** 10:40-11:20 **IT09 (P. Savrukhin)** 11:20-12:00 **IT10 (L. Eriksson)** 12:00-12:20 OT10 (T. Hellsten)	***ITER & New Trend & PD*** **Chair: T. Hellsten** 10:40-11:20 **IT16 (A.Fukuyama)** 11:20-11:40 OT12 (G. Fu) 11:40-12:00 OT13 (D. Spong)
	Group photo Lunch 12:00-13:20	Lunch 12:20-13:40	Lunch 12:00-13:30 **IAC meeting 13:05-13:25**
Afternoon session 1	***Helical/stellarator experiments & theories*** **Chair: J. Van Dam** 13:20-14:00 **IT03 (M.Osakabe)** 14:00-14:40 **IT04 (M. Isobe)** 14:40-15:00 OT04 (G. Matsunaga) 15:00-15:20 OT05 (A. Koenies) 15:20-15:40 OT06 (S. Murakami)	***Spherical Torus experiments & theories*** **Chair: N. Nakajima** 13:40-14:20 **IT11(E. Fredrickson)** 14:20-15:00 **IT12(M.Gryaznevich)** 15:00-15:40 **IT13(N. Gorelenkov)**	***Summary Session& discussions*** **Chair: K. Toi** 13:30-14:00 **Summary1 (S. Sharapov)** 14:00-14:30 **Summary2 (G. Fu)** 14:30-15:30 Discussions "Toward ITER and future" (Commentators: J. VandDam, D. Borba, M. Sasao)
	Coffee break 15:40-16:00	Coffee break 15:40-16:00	Closing 15:30-15:45
Afternoon session 2	***Tokamak experiments & theories 3 (Fast ion transport & Fishbones)*** **Chair: L. Eriksson** 16:00-16:40 **IT05 (M. Ishikawa)** 16:40-17:20 **IT06 (S. Pinches)** 17:20-17:40 OT07 (F. Nabais) 17:40-18:00 OT08(V. Marchenko)	***Poster Session (16:00-18:15)*** Poster presentations : P01- P24	
Bus depart.	18:15 for hotel	18:30 for hotel	16:04 for Takayama station
		Banquet at ***"Art & Festa Forest in Takayama"*** 19:00-20:45	

*A bus leaves for the conference site from the bus terminal at JR Takayama station.

** Pre-registration is arranged at the restaurant "Roen" of the *Hida Takayama Washington Hotel Plaza*,

from 17:00 to 20:30 on 8 Nov., 2005.

*** Presentation with TV conference link.

List of Participants

T. Bergkvist	Alfven Laboratory, Euratom-VR, Sweden	tommy.bergkvist@alfvenlab.kth.se
H.L. Berk	University of Texas, Austin, USA	hberk@mail.utexas.edu
B. Breizman	University of Texas, Austin, USA	breizman@mail.utexas.edu
D. Borba	EFDA Close Support Unit, Culham, UK	duarte.borba@jet.efda.org
L. Eriksson	CEA-Cadarache, France	Lars-Goran.Eriksson@cea.fr
E. Fredrickson	Princeton Plasma Physics Laboratory, USA	efredrickson@pppl.gov
G. Fu	Princeton Plasma Physics Laboratory, USA	fu@pppl.gov
A. Fukuyama	Kyoto University, Japan	fukuyama@nucleng.kyoto-u.ac.jp
P. Goncharov	National Institute for Fusion science, Japan	pavel@nifs.ac.jp
N. Gorelenkov	Princeton Plasma Physics Laboratory, USA	ngorelen@pppl.gov
K. Goto	National Institute for Fusion Science, Japan	goto.kazuyuki@LHD.nifs.ac.jp
M. Gryaznevich	UKAEA, Culham, UK	mikhail.gryaznevich@ukaea.org.uk
N. Hayashi	National Institute for Fusion Science, Japan	naho@nifs.ac.jp
W. Heidbrink	Univ. of Calif. Irvine, USA	wwheidbr@uci.edu
T. Hellsten	Alfven Laboratory, Euratom-VR, Sweden	torbjorn.hellsten@alfvenlab.kth.se
M. Ishikawa	Japan Atomic Energy Agency, Japan	ishikawm@fusion.naka.jaeri.go.jp
M. Isobe	National Institute for Fusion Science, Japan	isobe@nifs.ac.jp
V. Kiptily	UKAEA, Culham, UK	Vasili.Kiptily@jet.uk
A. Koenies	Max-Planck-Institut f' Plasmaphysik, Greifswald, Germany	axel.koenies@ipp.mpg.de
T. Kondoh	Japan Atomic Energy Agency, Japan	kondoh@naka.jaeri.go.jp
A. V. Krasilnikov	Troitsk Institute for Innovating and Fusion Research, Russia	anatoli@triniti.ru
N. Kubo	Tohoku Univ., Japan	naoki.kubo@ppl2.tohoku.ac.jp
R. Kumazawa	National Institute for Fusion Science, Japan	kumazawa@nifs.ac.jp
Ph. Lauber	Max-Planck-Institut fuer Plasmaphysik , Garching, Germany	pwl@ipp.mpg.de
A. Malaquias	International Atomic Energy Agency	a.malaquias@iaea.org
V. Marchenko	Institute for Nuclear Research, Ukraine	march@kinr.kiev.ua
G. Matsunaga	Japan Atomic Energy Agency, Japan	matsunaga.go@jaea.go.jp
H. Matsushita	The Graduate University for Advanced Studies, Japan	matusita@nifs.ac.jp
V. Moiseyenko	UPPSALA UNIVERSITY, Sweden	moiseenk@ipp.kharkov.ua
O. Motojima	National Institute for Fusion Science. Japan	motojima.osamu@lhd.nifs.ac.jp

S. Murakami	Kyoto University, Japan	murakami@nucleng.kyoto-u.ac.jp
F. Nabais	EURATOM/IST, Portugal	fnabais@cfn.ist.utl.pt
K. Nagaoka	National Institute for Fusion Science, Japan	nagaoka@nifs.ac.jp
N. Nakajima	National Institute for Fusion Science, Japan	nakajima@nifs.ac.jp
H. Nishimura	Tohoku University, Japan	hidetoshi.nishimura@ppl2.qse.tohoku.ac.jp
T. Nishitani	JAEA, Japan	nishitani.takeo@jaea.go.jp
M. Nishiura	National Institute for Fusion Science, Japan	nishiura@nifs.ac.jp
K. Ochiai	Japan Atomic Energy Agency, Japan	ochiai.kentaro@jaea.go.jp
S. Ohdachi	National Institute for Fusion Science, Japan	ohdachi@nifs.ac.jp
A. Okamoto	Tohoku University, Japan	atsushi.okamoto@qse.tohoku.ac.jp
M. Osakabe	National Institute for Fusion Science, Japan	osa@nifs.ac.jp
T. Ozaki	National Institute for Fusion Science, Japan	ozaki@nifs.ac.jp
B. Peterson	National Institute for Fusion Science, Japan	peterson@lhd.nifs.ac.jp
S. Pinches	Max-Planck-Institute for Plasma Physics, Garching, Germany	Simon.Pinches@ipp.mpg.de
H. Sakakita	Natational Inst. of Advanced Industrial Science and Technology, Japan	h.sakakita@aist.go.jp
M. Sasao	Tohoku University, Japan	mamiko.sasao@qse.tohoku.ac.jp
P. Savrukhin	Kurchatov Institute, Russia	psavrukhin@nfi.kiae.ru
S. Sharapov	UKAEA, Culhamm UK	sershar@jet.uk
K. Shinohara	Japan Atomic Energy Agency, Japan	shinohara.koji@jaea.go.jp
K. Shinto	Tohoku University, Japan	katsuhiro.shinto@qse.tohoku.ac.jp
T. Shoji	Nagoya University, Japan	shoji@ees.nagoya-u.ac.jp
D. Spong	Oak Ridge National Laboratory, USA	spongda@ornl.gov
M. Takechi	Japan Atomic Energy Agency, Japan	takechi.manabu@jaea.go.jp
K. Tani	Japan Atomic Energy Agency, Japan	tani.keiji@jaea.go.jp
K. Tobita	Japan Atomin Energy Agency, Japan	tobita.kenji@jaea.go.jp
Y. Todo	National Institute for Fusion Science, Japan	todo@nifs.ac.jp
K. Toi	National Institute for Fusion Science, Japan	toi@lhd.nifs.ac.jp
T. Tokuzawa	NIFS, Japan	tokuzawa@nifs.ac.jp
J. Van Dam	University of Texas, Fusion Studies, USA	vandam@physics.utexas.edu
M. Van Zeeland	General Atomics, USA	vanzeeland@fusion.gat.com
R. Vann	University of York, UK	rglv500@york.ac.uk
E. Veshchev	Graduate Univ. for Advanced Studies, Japan	veshchev.evgeny@lhd.nifs.ac.jp
T. Watari	National Institute for Fusion Science, Japan	watari@nifs.ac.jp